DOTTORATO DI RICERCA IN INGEGNERIA CIVILE E INDUSTRIALE

University of Calabria

DIMEG – Department of Mechanical, Energy and Management Engineering

Ph.D. Thesis

XXX Cycle (2014-2017)

Ph.D. in Civil and Industrial Engineering

Surface Integrity enhancement of aerospace components produced by subtractive and additive manufacturing processes

Candidate

Stano Imbrogno

Ph.D. Coordinator:

Prof. Franco Furgiuele

Supervisor:

Prof. Domenico Umbrello

Dottorato in Ingegneria Civile e Industriale

DOTTORATO DI RICERCA IN INGEGNERIA CIVILE E INDUSTRIALE

University of Calabria

DIMEG – Department of Mechanical, Energy and Management Engineering

Ph.D. Thesis

XXX Cycle (2014-2017)

Ph.D. in Civil and Industrial Engineering

Surface Integrity enhancement of aerospace components produced by subtractive and additive manufacturing processes

Candidate

Stano Imbrogno

Ph.D. Coordinator:

Prof. Franco Furgiuele

Supervisor:

Prof. Domenico Umbrello

To my Family

Index

Lists of Figures 3
Lists of Tables 9
Abstract 10
Abstract (lingua italiana) 11
Acknowledgments 13
CHAPTER I 14
Introduction 14
1.1. Research objectives 17
1.2. Dissertation outline 18
CHAPTER II 20
Advanced and conventional manufacturing processes of aerospace metal components 20
2.1 Aerospace materials for engine, structural and engine components 20
2.1.1 Titanium alloy – *Ti6Al4V* 24
2.1.2 Aluminum alloy – *AA7075-T6* 27
2.2 Additive and subtractive manufacturing processes of aerospace metal components 29
CHAPTER III 39
Machinability and surface integrity investigation of additive manufactured and wrought parts of Ti6Al4V alloy in semi-finishing conditions 39
3.1 Experimental work – semi-finishing operations on Ti6Al4V EBM, DMLS and wrought 40
3.1.1 Design of Experiments and experimental set-up 41
3.1.2 Cutting forces 41
3.1.3 Temperature analysis 45
3.2 Surface Integrity analysis of Ti6Al4V EBM, DMLS and wrought 47
3.2.1 Topography - Surface Roughness 47
3.2.2 Affected Layers and microstructure deformation 50
3.2.3 X-Ray Diffraction analysis (XRD) 59
3.2.4 Surface and Subsurface hardness 62
CHAPTER IV 68
High speed machining of the aluminum alloy AA7075-T6 and the application of a severe plastic deformation (SPD) process 68
4.1. Experimental work – high speed machining of AA7075-T6 under dry and cryogenic conditions 68
4.1.1 Design of Experiments and material selections 69
4.1.2 Cutting Forces 70
4.1.3 Temperature analysis 72
4.2 Surface Integrity analysis 73

4.2.1 Topography – Surface Roughness 73
4.2.2 Affected Layers and microstructure analysis 74
4.2.3 X-Ray Diffraction analysis (XRD) 79
4.2.4 Surface and Subsurface hardness 81
4.3 Equal Channel Angular Pressing and machining process on aluminum alloy 86
4.3.1 Design of the ECAP die 87
4.3.2 ECAP tests on AA7075 88
4.3.3 Orthogonal cutting tests of AA7075 89
4.4 Comparison of the experimental results 90
4.4.1 Microstructure and hardness measurements 90
4.4.2 X-Ray Diffraction analysis 93
CHAPTER V 96
Finite element modeling and analysis to investigate the surface integrity characteristics during machining processes 96
5.1 Numerical Simulation of manufacturing processes – State of the art 97
5.1.1 Material constitutive modeling in machining simulation 97
5.2 3D FE model of semi-finishing of Ti6Al4V produced via EBM and DMLS technology 108
5.2.1 Material constitutive model 108
5.2.2 3D FE model of Ti6Al4V semi-finishing machining process 118
5.2.3 FE Calibration 121
5.2.4 FE Validation 122
5.2.5 Surface Integrity Analysis 125
5.3 3D FE model of high speed machining of AA7075-T6 129
5.3.1 Material constitutive model 129
5.3.2 FE Calibration 135
5.3.3 FE Validation 136
5.3.4 Surface Integrity Analysis 138
Concluding Remarks 142
Future research directions 143
References 144

Lists of Figures

Figure 1: Different mechanical and structural aircraft components and the materials employed. 14
Figure 2: Representative scheme of the research activities developed in this Ph.D. thesis 16
Figure 3: Flow chart of the Ph.D. thesis 19
Figure 4: Materials and their weight percentages used in the airframes of civilian and military aircrafts (adapted from Mouritz 2012). 21
Figure 5: Different mechanical and structural groups of aircraft components and the materials employed. 21
Figure 6: a) Yield strength of aluminum alloys and the year of introduction into civils transport services; b) Titanium content % used in military and civils transport aircrafts (adapted from Mouritz 2012) 22
Figure 7: a) Boeing 787 fuselage under construction; b) wing and its internal structures made by wing ribs; c) Aluminum alloys used on Boeing 777 (adapted from Starke and Staley 1996) 23
Figure 8: a) blades material at different temperature operative conditions into a representative aerospace jet engine; b) economy of weight achieved in the case of using titanium for engines: 1, large-size; 2, medium-size; 3, small-size (Rolls-Royce Trent 700). 23
Figure 9: a) Rutile, b) Ilmenite. 24
Figure 10: Appearance of crystal structures of titanium at atomic level (Donachie 2000) 25
Figure 11: Effect of cooling rate on the microstructure of an alpha-beta alloy (*Ti6Al4V*); (a) α' + β; prior beta grain boundaries; (b) Primary α and α' + β; (c) Primary α and α' + β; (d) Primary α and metastable β; (e) Acicular α + β; prior beta grain boundaries; (f) Primary α and acicular α + β; (g) Primary α and acicular α + β; (h) Primary α and β; (i) Plate-like α + β; prior grain boundaries; (j) Equiaxed α and intergranular β; (k) Equiaxed α and intergranular β; (l) Equiaxed α and intergranular β (adapted from Donachie 2000). ... 26
Figure 12: Bauxite. 27
Figure 13: a) Microstructure of *AA7075-T6* (MacKenzie 2006); b) FCC crystal structure. 28
Figure 14: Al Matrix, η' dispersed into the matrix and η grain boundaries precipitates ($MgZn_2$) 7xxx series aluminum alloy aged at 180°C (adapted from Flower 1995). 28
Figure 15: Thin Wall Ribs of Boeing aircraft structural part: High Speed vs. Conventional Machining (adapted from Campbell 2006) 30
Figure 16: a) and b) SEM micrographs of machined surface; c) and d) SEM micrographs of fracture surface morphology of machined parts (adapted from Wang and Liu 2016) 30
Figure 17: a) TEM and b) HAADF-STEM images showing the microstructure of the surface deformation layer in the machined 7055 aluminum alloy (Chen et al. 2017) 31
Figure 18 : Microstructure on the cross section of the machined samples (dry) and b (cryogenic); c) measured microhardness (Adapted by Rotella 2013) 32
Figure 19: a) aircraft duct example; b) Seat buckle produced using DMLS technology (Adapted from Gibson et al. 2010, Dutta and Froes 2016). 33
Figure 20: Life cycle of a product from production to the use-phase and recycling (Schmidt et al. 2017). 34
Figure 21: Effect of different manufacturing technologies on "buy-to-fly" ratio. 34
Figure 22: *Ti6Al4V* image compositions corresponding to test block sections. Numbers in horizontal and vertical reference planes at left are Vickers micro-indentation hardness in GPa. Numbers 2 and 4 at right refer to test block (focus offset) numbers. B indicates the build direction (Murr et al. 2012) 35
Figure 23: a) roughness surface obtained on AM titanium alloy; b) detailed zone of the surface (Greitemeier et al. 2016). 36
Figure 24: Fatigue limit (at 5 × 106 cycles) compared to surfaces roughness. R_v = maximum profile valley depth, AB = as-built (adapted by Kahlin et al. 2017). 37
Figure 25: Tool wear analysis by SEM images of the tool used to machine a) and b) wrought titanium alloy, c) and d) AM titanium alloy (Bordin et al. 2014). 37

Figure 26: a) Experimental set-up used to perform machining test under dry conditions; b) Cryogenic delivery system detail. 40
Figure 27: Elaboration of the main cutting force (F_z) signal acquired by the piezoelectric dynamometer during dry turning operation on the titanium bars (V_c 80m/min, f=0.2mm/rev, a_p=0.2mm, *Ti6Al4V* DMLS)..... 42
Figure 28: Main cutting forces a) and Feed forces b) at varying cutting speed and feed rate equal to 0.1mm/rev (dry conditions). 42
Figure 29: Main cutting forces a) and Feed forces b) at varying cutting speed and feed rate equal to 0.2mm/rev (dry conditions). 43
Figure 30: Main and feed cutting forces obtained during machining of *Ti6Al4V* DMLS at feed rate 0.1mm/rev (dry conditions). 43
Figure 31: Main cutting forces a) and Feed forces b) at varying cutting speed, feed rate and cooling conditions. 44
Figure 32: a) Cryogenic machining; b) dry machining. 44
Figure 33: Thermal gradient signal acquired by the infrared camera during turning operation on the titanium bars and elaborated (V_c =110m/min, f=0.1mm/rev, a_p=0.2mm, *Ti6Al4V* DMLS). 45
Figure 34: Average value of the maximum temperature at varying cutting speed, feed rate and material machined under dry conditions; a) 0.1mm/rev; b) 0.2mm/rev. 46
Figure 35: Comparison of average maximum temperature acquired under dry and cryogenic machining of *Ti6Al4V* EBM; a) 0.1mm/rev; b) 0.2mm/rev. 46
Figure 36: Average maximum temperature acquired under cryogenic machining of *Ti6Al4V* EBM at varying cutting speed and feed rate. 46
Figure 37: Topographic parameter R_a (Mean Roughness). 48
Figure 38: ConScan Surface Profilometer (Anton-Paar) employed to evaluate the surface roughness. 48
Figure 39: Roughness R_a measured at varying cutting speed and feed rate for different tested materials... 49
Figure 40: Roughness R_a measured on *Ti6Al4V* EBM machined under dry and cryogenic conditions at varying cutting speed and feed rate. 50
Figure 41: Experimental procedure to prepare the samples for metallographic analysis and optical microscopy. 51
Figure 42: a) Sever Plastic Deformed layer on machined *Ti6Al4V* DMLS; b) bended lamellae due to the deformation imposed by the tool action; c) Measure representative of the plastic deformation within the deformed layer ($\varepsilon = tang\theta = a/b$). 51
Figure 43: Affected Layer thickness (AL) at varying cutting speeds, feed rate and materials in dry conditions. 52
Figure 44: Affected Layer thickness (AL) at varying cutting speeds, feed rate and cooling condition measured on the *Ti6Al4V* EBM. 52
Figure 45: Plastic deformation at varying cutting speed and feed rate on different machined material under dry conditions. 53
Figure 46: Plastically deformed layer thickness of machined materials at cutting speed 110m/min, feed rate 0.2mm/rev and a_p=0.2mm: a) *Ti6Al4V* EBM; b) *Ti6Al4V* DMLS. 53
Figure 47: Plastic deformation at varying cutting speed, feed rate and cooling conditions on machined *Ti6Al4V* EBM. 54
Figure 48: Yield stress depending on α-lamellae thickness (Adapted from Al-Bermani et al. 2010). 55
Figure 49: Variation of the α-lamellae thickness due to the tool action on machined surface (cross section). 55
Figure 50: Initial microstructure of the *Ti6Al4V*; a) EBM; b) DMLS; c) Wrought. 56
Figure 51: SEM analysis of the machined surface of a) *Ti6Al4V* EBM; b) *Ti6Al4V* DMLS (V_c=110m/min, f=0.2mm/rev, dry conditions). 56
Figure 52: Optical micrographs and AFM microstructure analysis (V_c = 110 m/min, f = 0.2 mm/rev); (a) wrought; (b) EBM; (c) DMLS machined samples. 57

Figure 53: Degree of Grain Refinement at varying cutting speed and feed rate for different machined materials in dry conditions. 58
Figure 54: Degree of Grain Refinement at varying cutting speed, feed rate and cooling conditions for machined *Ti6Al4V* EBM. 58
Figure 55: Experimental set-up and sample used to perform the XRD analysis. 59
Figure 56: XRD pattern of as produced *Ti6Al4V* samples. 59
Figure 57: XRD pattern of the *Ti6Al4V* EBM machined under dry condition (f=0.2 mm/rev). 60
Figure 58: XRD pattern of the *Ti6Al4V* DMLS machined under dry condition (f=0.2 mm/rev). 60
Figure 59: XRD pattern of the *Ti6Al4V* wrought machined under dry condition (f=0.2 mm/rev). 60
Figure 60: XRD pattern of the *Ti6Al4V* EBM machined under cryogenic condition (f=0.2 mm/rev). 61
Figure 61: Nano-hardness measurement set-up and procedure. 62
Figure 62: a) Micrograph in dark field of the matrix spot for the nano-indentation test; b) vertical line of tips; c) nano-indentation test results. 63
Figure 63: Nano-hardness measurements on the cross section of the samples. 63
Figure 64: Nano-hardness at varying cutting speed, feed rate and materials. 64
Figure 65: Nano-hardness measured on *Ti6Al4V* EBM machined under dry and cryogenic conditions at varying cutting speed and feed rate. 65
Figure 66: Hardness profile through the dry machined surface; a) V_c=50m/min and f=0.2mm/rev; b) V_c=110m/min and f=0.2mm/rev. 65
Figure 67: Hardness profile through the cryogenic machined surface of the *Ti6Al4V* EBM; a) V_c=50m/min and f=0.2mm/rev; b) V_c=110m/min and f=0.2mm/rev. 66
Figure 68: Experimental set-up to perform High Speed Machining. 69
Figure 69: Cutting force components in turning operation, F_f feed force, F_c tangential force or main cutting component (adapted by Laperrire 2014). On the right, the two components acquired during the tests. 70
Figure 70: Main cutting (a) and feed (b) forces at varying cutting speeds, feed rate and cooling conditions. 71
Figure 71: Chip obtained at cutting speed of 1250m/min and feed rate 0.1mm/rev; a) dry conditions, b) cryogenic conditions. 71
Figure 72: Rake face and worn edge at cutting speed 1000m/min and feed rate 0.1mm/rev; a) dry conditions, b) cryogenic condition. 72
Figure 73: Cutting temperatures at varying cutting speeds and cooling conditions a) f=0.1mm/rev; b) f=0.3mm/rev. 73
Figure 74: R_a measurements at varying cutting speed, feed rate and cooling strategy. 73
Figure 75: Flank wear at cutting speed 1500m/min and feed rate 0.3mm/rev; a) cryogenic conditions, b) dry conditions. 74
Figure 76: Grain size variation from the machined surface through the depth of the specimens manufactured under dry conditions at varying cutting parameters. 75
Figure 77: Grain size variation from the machined surface through the depth of the specimens manufactured under cryogenic conditions at varying cutting parameters. 76
Figure 78: Thickness of the material layers where the microstructure changes due to the machining process. 76
Figure 79: Optical micrographs of the cross section at cutting speed 1000m/min and varying feed rate and cooling strategy. 77
Figure 80: Optical micrographs of the cross section at cutting speed 1500m/min and varying feed rate and cooling strategy. 78
Figure 81: X Ray diffraction profiles at varying cutting speed; a) feed rate 0.1mm/rev; b) feed rate 0.3mm/rev (Dry conditions). 79
Figure 82: X Ray diffraction profiles at varying cutting speed; a) feed rate 0.1mm/rev; b) feed rate 0.3mm/rev (Cryogenic conditions). 80

Figure 83: Micro-hardness measured on the machined surface at varying cutting parameters and cooling conditions. 81
Figure 84: Micro-hardness variation from the surface through the depth of the machined parts at varying cutting speed and feed rate under dry conditions. 84
Figure 85: Micro-hardness variation from the surface through the depth of the machined parts at varying cutting speed and feed rate under cryogenic conditions. 84
Figure 86: Principle of ECAP (Sahai et al 2017). 86
Figure 87: Schematic illustration of dies used at varying corner angles (adapted from Nakashima et al. 1998. 87
Figure 88: a) the designed ECAP components in CAD environment; b) 50ton press and experimental set-up with pc acquisition data system; c) The ECAP experimental set up realized. 88
Figure 89: The prismatic sample used to perform ECAP test and the as received microstructure. 88
Figure 90: Not deformed and deformed sample by ECAP process. 89
Figure 91: Experimental set up, workpiece and tool holder detail used to perform the orthogonal cutting. 89
Figure 92: Microstructure analysis of the ECAP deformed sample; microstructure of section 1 (x-z plane, not deformed part); microstructure of section 1 (x-y plane, not deformed part); microstructure of longitudinal section 2 (deformed part); microstructure of cross. 91
Figure 93: a) Frame of the machining test, b) longitudinal section of the machined sample; c) cross section of the machined sample and the related microstructure. 91
Figure 94: Hardness measurements on the deformed ECAP sample (a) and on the longitudinal section of the machined sample (b). 92
Figure 95: Microstructure analysis of the ECAP deformed and machined sample. 93
Figure 96: X-Ray Diffraction patterns of the as received and the deformed cross section of the ECAP sample. 94
Figure 97: X-Ray Diffraction patterns of the machined sample and the deformed cross section of the ECAP sample. 94
Figure 98: Schematic representation of dynamic recovery (DRV) effect on work hardening flow stress... 98
Figure 99: Schematic representation of the FE prediction of failure phenomenon in cutting simulation by flow stress coupled and not coupled with damage model (adapted by Li and Hou 2014) 99
Figure 100: Johnson-Cook model and Modified Johnson-Cook model proposed by Calamaz et al. 2008. 100
Figure 101: Prediction strategy of the microstructural changes and FE numerical results obtained in *AA7075-T6* turning simulation (Adapted from Rotella and Umbrello 2014). 101
Figure 102: Numerical prediction of microstructural changes on machined *Ti6Al4V*; a) grain size, b) hardness (Adapted from Rotella and Umbrello 2014). 102
Figure 103: Comparison of simulated a), and experimental results b) of chip morphology and shear plane deformation at low speed machining (V_c =100 m/min, f=0.25 mm/rev) (Paturi et al. 2014). 103
Figure 104: Comparison of measured and simulated chip shapes (Melkote et al. 2015). 104
Figure 105: a) optical micrograph of the chip microstructure in shear band region and simulated b) grain size and c) dislocation density distribution (Melkote et al. 2015). 104
Figure 106: Comparison between the measured and predicted cutting-induced hardness changes (Liu et al. 2014). 105
Figure 107: Cutting simulation of OFHC CU, dislocation density and grain size evolutions (Atmani et al. 2016). 105
Figure 108: Adapted by Ding and Hing 2013, simulation flow chart and numerical prediction of temperature, phase transformation, dislocation density, grain size and microhardness. 106
Figure 109: Strain rate predicted and comparison between experimental and numerical cutting forces (Adapted from Svodoba et al. 2010). 107
Figure 110: Comparison of the material constitutive flow stress with different numerical constants. The red pictures represent the microstructures. 109

Figure 111: a) *Ti6Al4V* DMLS microstructure of the as received material, b) Mower Todd and Long 2016. 110
Figure 112: True Stress-True Strain experimental curve of Ti6Al4V DMLS (Mower Todd and Long 2016). 110
Figure 113: Comparison between all the empirical models and the experimental curve, a) Calamaz et al.2011, b) Calamaz et al. 2008, c) Sima and Özel. 2010 (Model 1), d) Sima and Özel. 2010 (Model 2), e) Sima and Özel. 2010 (Model 3). 113
Figure 114: a) Flow stress at vary temperatures and fixed strain rate, b) flow stress at vary strain-rate and fixed temperature. 114
Figure 115: a), b), c), d) measurements of the α-lamellae thickness (or β-interspacing) and correlation between the yield stress and α-lamellae thickness on *Ti6Al4V* produced by EBM (Adapted by Tan et al. 2015). 115
Figure 116: Numerical strategy to predict the α-lamellae thickness, the nano-hardness and to update the flow stress during the machining simulation. 117
Figure 117: a), b) CAD models and c) FE domain of the turning process (adapted by DEFORM SFTC MANUAL). 118
Figure 118: Dimensions of the workpiece and position of the tool in the space simulation; b) α=8°; c) β=7°; d) γ=5°. 118
Figure 119: Kinematic and thermal boundary conditions. 119
Figure 120: Customized heat exchange windows to model the thermal effect of liquid nitrogen during machining simulation. 120
Figure 121: a) heat transfer coefficient implemented in the FE software, b) Nitrogen properties at 10^5 Pa isobar (Pušavec et al. 2016). 120
Figure 122: Representation of the sticking-sliding hybrid friction model used in machining simulation. . 121
Figure 123: Calibration procedure to determine the friction coefficients of the hybrid friction model. ... 122
Figure 124: Numerical prediction of temperature and area of interest in which the data were collected. 123
Figure 125: Comparison between experimental and numerical cutting forces; a) main cutting force (Fz) and b) feed forces (Ft) of turning tests on Ti6Al4V EBM under dry conditions. 123
Figure 126: Comparison between experimental and numerical cutting forces; a) main cutting force (Fz) and b) feed forces (Ft) of turning tests on Ti6Al4V EBM under cryogenic conditions. 124
Figure 127: Comparison between experimental and numerical cutting forces; a) main cutting force (Fz) and b) feed forces (Ft) of turning tests on Ti6Al4V DMLS under cryogenic conditions. 124
Figure 128: Comparison between experimental and numerical maximum temperature; a) Ti6Al4V EBM dry machining, b) Ti6Al4V EBM cryogenic machining, c) Ti6Al4V DMLS dry machining. 125
Figure 129: a) α-lamellae thickness predicted by FE simulation on *Ti6Al4V* EBM; b) micrograph of *Ti6Al4V* EBM microstructure in which α-lamellae is deformed due to the machining operation (V_c= 80m/min, f=0.1mm/rev dry conditions) 126
Figure 130: Comparison between numerical prediction and experimental measurements of α-lamellae thickness of machined *Ti6Al4V* EBM; a) dry conditions, b) cryogenic conditions 127
Figure 131: Comparison between numerical prediction and experimental measurements on *Ti6Al4V* EBM; a) nano-hardness dry condition; b) nano-hardness cryogenic condition; c) plastic deformation dry condition; d) plastic deformation cryogenic condition 127
Figure 132: Comparison between the experimental and predicted true stress-strain curves of the aluminum alloy *7075-T6* at varying temperature and strain rate; a) strain-rate $0.1s^{-1}$ T= 200°C, b) strain-rate $0.5s^{-1}$ T= 150°C. 133
Figure 133: Numerical strategy developed to model the mechanical behavior of the *AA7075-T6* through physically based modeling approach. 135
Figure 134: Calibration procedure to determine the friction coefficients of the hybrid friction model. ... 135
Figure 135: Comparison between experimental and numerical cutting forces; a) main cutting force (F_z) and b) feed forces (F_t) under dry conditions. 137

Figure 136: Comparison between experimental and numerical cutting forces; a) main cutting force (F_z) and b) feed forces (F_t) under cryogenic conditions. 137
Figure 137: Comparison between experimental and numerical temperature; a) dry machining and b) cryogenic machining 137
Figure 138: Comparison between the numerical and experimental chip shape (V_c=1000m/min, f=0.3mm/rev, dry conditions) 138
Figure 139: Predicted microstructure under dry conditions (V_c=1500m/min, f=0.3mm/rev); a) comparison of numerical and experimental grain size measured on machined surface (dry conditions); b) comparison of numerical and experimental grain size measured on machined surface (cryogenic conditions). 139
Figure 140: Grain refinement and dislocation density variations from the machined surface and in depth into the part (V_c=1500m/min, f=0.3mm/rev, dry condition) 140
Figure 141: Recrystallized grain size prediction at varying cooling conditions (f=0.3mm/rev). 141
Figure 142: Dislocation density prediction at varying cooling conditions (f=0.3mm/rev). 141

Lists of Tables

Table 1: Alloying titanium elements and their effects (Donachie 2000). 25
Table 2: Chemical composition of 7075 aluminum alloy (Mouritz 2012). 27
Table 3: Mechanical properties of *Ti6Al4V* produced via different production processes (Facchini et al. 2010, Bruschi et al. 2016). 40
Table 4: Design of Experiments (24 full factorial experimental plan). 41
Table 5: Grinding and polishing procedure to prepare the *Ti6Al4V* samples to metallographic analysis. . 50
Table 6: Mechanical properties of the aluminum alloy *AA 7075-T6* (Kaufman 2000). 69
Table 7: Design of Experiments (12 full factorial experimental plan). 70
Table 8: Grinding and polishing procedure to prepare the *AA7075-T6* samples to metallographic analysis. 75
Table 9: Precipitates and grain refinement contributions to hardness at varying cutting parameters and cooling strategy. 83
Table 10: Cutting parameters 90
Table 11: Work hardening material constitutive laws (Arrazola et al. 2013). 98
Table 12: Modified material constitutive model developed for the *Ti6Al4V* alloy (Calamaz et al. 2008, Sima and Özel 2010, Özel et al. 2010, Karpat 2010). 100
Table 13: Material constitutive model proposed by Rotella and Umbrello for modeling the *AA7075-T6* and *Ti6Al4V* mechanical behavior (Rotella and Umbrello 2014). 101
Table 14: Material constitutive model proposed by Zerilli and Armstrong 1987, Follansbee and Kocks 1988. 103
Table 15: Set of coefficient for the material constitutive model adopted in the FE analysis for the *Ti6Al4V* EBM (Lee and Lin 1998, Özel et al. 2010). 109
Table 16: Mechanical properties of Ti6Al4V DMLS (Mower Todd and Long 2016). 110
Table 17: Material constitutive model of Ti6Al4V tested. 111
Table 18: Material constants used in the models reported in Table 17. 112
Table 19: Comparison between numerical and experimental results, total average error. 114
Table 20: Coefficients of the selected model to simulate the material behavior of the Ti6Al4V DMLS. . 114
Table 21: Numerical constants of the physics based model developed (calibrated or reported in literature). 134
Table 22: Friction coefficients calibrated at varying cutting parameters and cooling conditions. ...**Errore. Il segnalibro non è definito.**

Abstract

The growing interest in the opportunity of increasing the production rate and introducing new functional products in the aerospace industries is becoming significant. The possibility to produce geometrically complex products without operating numerous manufacturing steps is attracting both academia and industry attention. In fact, these new design techniques bring new products with higher performance, reducing the buy-to-fly ratio and consequently, the waste of material. Therefore, the Additive Manufacturing (AM) techniques are becoming the protagonists in this last decade, especially in the production of parts made by difficult-to-cut materials. However, the AMed products, although they show higher complex shapes that are impossible to achieve by the conventional subtractive processes, post-process treatments are still necessary to improve their surface quality. Nowadays, the research, in order to improve the mechanical properties of the AM products affected by external (poor surface roughness) and internal defects (voids and pores), is developing specific thermal, mechanical and chemical treatments. On the other side, the reduction of production time and the possibility to produce aircraft structural components (thin geometry) are also important. Indeed, the incorrect manufacturing process parameters usually lead to the production of parts with inaccurate tolerances or distorted geometry, especially when aluminum alloys are employed, compromising their mechanical performances. In the contests previously mentioned, the surface integrity plays a key role because it permits to understand the overall quality of the products depending on the process parameters and manufacturing strategies adopted. In aerospace fields the designed components must satisfy high quality requirements in safety/fatigue performance, thus the knowledge of the effects of metallurgical modifications induced by manufacturing processes is very important. Therefore, the produced components can be improved in terms of performance and mechanical resistance just improving the surface integrity, hence optimizing the manufacturing process.

The scope of this Ph.D. thesis is **to evaluate the machinability and study the surface integrity of the materials used in aerospace applications.**

In particular, the main objectives are:

- to investigate the machinability and study the surface integrity of the *Ti6Al4V* titanium alloy parts additively manufactured after semi-finishing machining processes at different cutting parameters and cooling strategies (dry and cryogenic);
- to investigate the machinability and study the surface integrity of the *7075-T6* aluminum alloy used to produce structural aircraft parts performing the high speed machining process at different cutting parameters and cooling strategies (dry and cryogenic);
- to employ a severe plastic deformation (Equal Channel Angular Pressing) process to better understand the physical reasons of the metallurgical changes during severe plastic deformations induced by machining on aluminum alloy;
- to define the mechanical behavior flow stress of the additively manufactured titanium parts in order to simulate the semi-finishing machining operations;
- to develop a physically-based material behavior model of the aluminum alloy to predict the metallurgical transformation induced by high speed turning operation at different cutting parameters and cooling conditions;
- to describe the physical reasons of the microstructural variations and to understand the hardening or softening governing phenomena;
- to predict the main fundamental variables such as cutting forces and temperature and to describe the surface integrity in terms of microstructural deformed shapes and hardness changes;

Abstract (lingua italiana)

Oggigiorno, il crescente interesse da parte delle industrie aerospaziali sulle opportunità di poter aumentare il tasso di produzione così come l'introduzione sul mercato di prodotti performanti è significativo. Infatti, la possibilità di produrre componenti meccanici dalle geometrie particolarmente complesse senza dover ricorrere a numerose operazioni manifatturiere sta attirando l'attenzione della comunità scientifica e delle aziende. Le recenti metodologie di progettazione permettono di produrre componenti sempre più performanti riducendo allo stesso tempo il buy-to-fly ratio e conseguentemente gli sfridi di materiale. Pertanto, in questa ultima decade le tecniche di manifattura additiva (AM) stanno diventando le protagoniste soprattutto nella realizzazione di componenti caratterizzati da materiali difficili da lavorare alle macchine utensili quali le leghe di titanio e a base nickel. Tuttavia questi manufatti, sebbene posseggono geometrie molto complesse e funzionali difficilmente realizzabili con i classici processi sottrattivi di materiale, necessitano di successivi trattamenti per migliorarne la qualità superficiale. Oggigiorno, il cuore ricerca industriale in campo aeronautico è anche impegnato nello sviluppo di nuove tecniche meccaniche, termiche e chimiche per trattare i manufatti realizzati con tecniche additive in modo da ridurne le difettosità superficiali (scarsa rugosità superficiale) e interne (vuoti e pori) in modo da migliorarne le performance meccaniche. D'altra parte, la ricerca mira anche a raggiungere ulteriori obiettivi quali la riduzione dei tempi ciclo di produzione o la possibilità di produrre componenti di piccolo spessore sempre più performanti per applicazioni in campo aeronautico. Difatti, questi ultimi vengono principalmente realizzati tramite processi di sottrazione di materiale e pertanto i parametri di processo giocano un ruolo fondamentale nell'ottenimento di prodotti di elevata qualità. Ad ogni modo, è chiaro che l'integrità superficiale rappresenta il fattore di maggior rilievo in quanto permette di stimare in generale la qualità del prodotto finito in funzione della strategia di manifattura definita. Nelle applicazioni aeronautiche i prodotti devono possedere un'elevata accuratezza dimensionale ed elevate proprietà meccaniche, pertanto conoscere gli effetti dei cambiamenti di natura metallurgica indotte dai processi manifatturieri quali l'asportazione di materiale è oltremodo importante. Di conseguenza, le proprietà meccaniche dei componenti realizzati possono essere migliorate migliorando l'integrità superficiale, ovvero ottimizzando il processo manifatturiero.

Lo scopo di questa tesi di Dottorato è **studiare la lavorabilità alle macchine utensili e l'integrità superficiale di manufatti realizzati con materiali principalmente utilizzati in ambito aeronautico**.

Nel dettaglio, i principali obiettivi sono:

- investigare la lavorabilità alle macchine utensili e studiare l'integrità superficiale a valle dei processi di semi-finitura (in condizioni di lavorazione a secco e criogeniche) della lega di titanio *Ti6Al4V* realizzata mediante tecniche additive;
- investigare la lavorabilità alle macchine utensili e studiare l'integrità superficiale a valle dei processi di taglio ad alta velocità (in condizioni di lavorazione a secco e criogeniche) della lega di alluminio *7075-T6*;
- impiegare un processo di deformazione plastica severa (Equal Channel Angular Pressing) per investigare la natura dei fenomeni metallurgici che si innescano durante tali processi e quelli in cui viene asportato materiale tramite operazioni di taglio;
- sviluppare un modello che descrive il comportamento meccanico della lega di titanio durante il processo di semi-finitura;
- sviluppare un modello fisico che descriva il comportamento meccanico della lega di alluminio esaminata durante i processi di taglio ad elevata velocità;
- Prevedere le principali variabili di interesse industriale quali forze di taglio e temperature, descrivere l'integrità superficiale attraverso la previsione di cambiamenti metallurgici e delle proprietà meccaniche quali la microstruttura e capire i fenomeni che governano l'incrudimento o il softening.

Acknowledgments

I want to express a sincere gratitude to my supervisor Prof. Domenico Umbrello for giving me the possibility to work in his research group. His continuous help, positive encouragement throughout these years were a strong support and inspiration that allowed me to reach the main goals and present the main outcomes at International Conferences.

I would also like to express my gratitude to Dr. Ing. Giovanna Rotella for her valuable support during the experimental activities in laboratory and for helping me with the very long measurement procedures. Her time spent in helping and guiding me was enormously useful to improve my research skills.

I also thank Professor Fortunato Crea and Dr. Ing. Sebastiano Candamano for their help and strong support during the metallurgical analysis through SEM and XRD techniques.

I am grateful to Professor Stefania Bruschi and her research group from the University of Padova for their valuable contribution in sharing and performing the experimental tests on additively manufactured materials. I am also very grateful to Dr. Ing. Alberto Bordin for having continuously inspired and motivated me during my research activities, especially at the Conferences and for the strong friendship established.

I special thanks goes to Dr. Ing. Antonio Rotella who shared with me all the hardest moments of the academic carrier. I am grateful for his sincere friendship, which always gave me the right motivation to overcome every problem. A special thank goes also to all my friends that made these three years less stressful.

I would also like to express a sincere gratitude to Professor Volker Schulze and the research team of WBK of the Karlsruhe Institute of Technology for allowing me to spend a considerable part of my Ph.D. in their Institute. During the year spent in Germany, He guided me to improve and develop new research skills.

I would like also to express my thankfulness to Ing. Eric Segebade for having guided and motivated me during the activity researches in developing the experimental and numerical activities.

Last but not the least, I want to express my infinite gratitude to my parents and my family for their fundamental support that always helped me to achieve important goals and make the right decisions. Finally, a special thought goes to Martina, her special emotional support always contributed to reach important goals in this period of my life.

CHAPTER I

Introduction

The overall quality of a component, its mechanical performance and reliability during all its life cycle depends on several characteristics. The engineer involved in the design of new parts has to face the structural computations in order to guarantee the functionality of the products that usually operate under complex loading conditions. The choice of the material plays an important role in satisfying the requirements and usually it makes the difference between failed and not failed products. Consequently, the importance of materials science and technology in engineering advanced fields, such as aerospace, cannot be overstated. Several structural parts, mechanical components and joining elements constitute the fundamental frame of an aircraft. Furthermore, the materials used in airframe structures and in jet engine components are crucial to the successful design, construction, certification, operation and maintenance of the aircraft (Figure 1). Materials have an impact through the entire life cycle of aircraft, from the initial design phase to manufacture and certification of the aircraft, to flight operations and maintenance and, finally, to disposal at the end-of-life (Mouritz 2012).

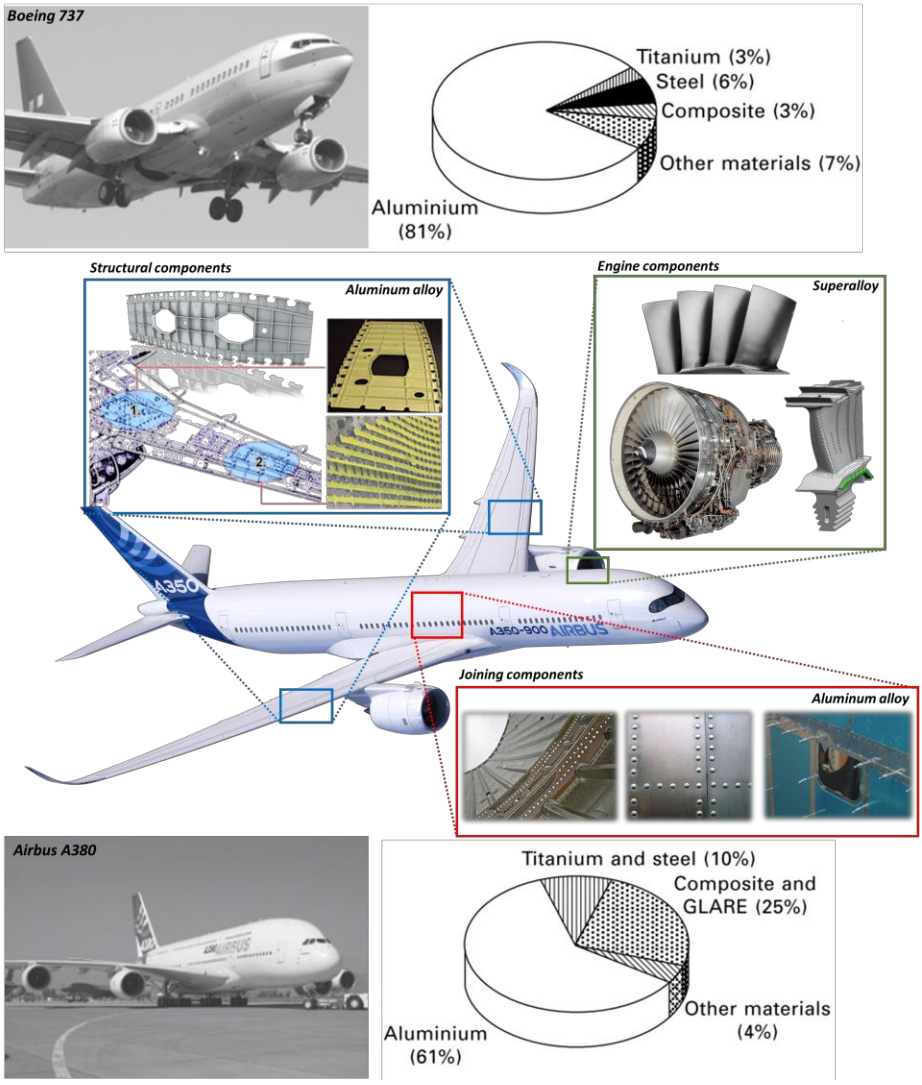

Figure 1: Different mechanical and structural aircraft components and the materials employed.

Focusing on engines and structural parts of the aircrafts, these require materials that are lightweight, high strength, damage tolerant, high temperature strength, oxidation and corrosion resistant with robust and repeatable mechanical properties. These materials can be readily manufactured into components that are inspectable to ensure the required level of quality and mechanical capability. These requirements are also bounded by the absolute need for lowest possible cost and greatest possible availability (Ott et al. 2010). The main groups of materials used in aerospace structures are aluminum alloys, titanium alloys, steels and composites. In addition to these materials, nickel-based alloys are important structural materials for jet engine applications. Many other materials are also used in aircraft: copper for electrical wiring; semiconductors for electronic devices; synthetic fabrics for seating and other furnishing. The structural and mechanical metal components are essentially produced by manufacturing processes such as machining. However, nowadays the innovative processes, namely additive manufacturing, allow to produce a part simply adding melted material layer-upon-layer, avoiding to remove material but adding it where it is required. Although these processes are able to produce components with very complex shape and geometrically close to the final product (near-net-to-shape), there are some drawbacks related to the production volume as well as the tolerance and surface quality. Due to the high requirements safety/fatigue performance of the aerospace components, the additively produced parts still require secondary manufacturing steps (semi-finishing processes) in order to achieve the surface quality required and match the geometric designed tolerances (Bordin et al. 2015, Bordin et al. 2014, Gibson et al. 2010). In literature, the titanium alloys produced by AM technologies were mechanically characterized and the outcomes clearly showed different mechanical response if compared with the wrought titanium alloy commonly used. Consequently, the machinability is expected to be different from that investigated by several researchers. A part of this Ph.D. thesis aims to fill this lack of knowledge investigating the machinability of AMed titanium alloy under semi-finishing condition in order to define the surface integrity varying the cooling conditions and cutting parameters (Figure 2). The choice to adopt different cooling strategies, in particular the cryogenic fluid, is because of the positive effects of coolants when low thermal conductivity difficult-to-cut material are machined (Jawahir et al. 2016, Grzesik et al. 2012, Bermingham et al. 2011, Hong 2006). As previously mentioned the aircraft is also characterized by structural and joining components that are usually realized with high performance aluminum alloys (7xxx and 2xxx series coupled with T3 or T6 treatments). Considering the structural components, the aircraft industries are attracted by the possibility to manufacture the aluminum alloy by high speed machining conditions. The advantages compared with the conventional machining are numerous: tremendous reduction of production time, lower cutting forces due to the increase of thermally induced ductility of the material , possibility to reach better tolerances, reduction of the number of parts that need to be assembled (Campbel 2008). Moreover, Chen et al. 2017 highlighted the formation of nanograins during high speed machining of aluminum 7xxx series and the positive effects on mechanical response due to the formation of subsurface nanograins layers. No comprehensive researches are available on high speed turning of the aluminum alloy *7075-T6* under cryogenic conditions. The delivering of liquid nitrogen during machining of aluminum alloy was observed to positively affect the material in terms of mechanical properties due to its ability to preserve the recrystallized grains and prevent their growth (Rotella et al. 2013). Consequently, the mainly applied structural material aluminum alloy *7075-T6* under high speed machining conditions was investigated in order to assess the machinability level and to investigate how the high removal rate affects the surface integrity of the machined parts (Figure 2). The high performance aluminum alloys are also employed to produce rivets and joining components to link and assembly some parts of the aircraft structures (de Rijck et al. 2007). The fatigue strength of these mechanical joining elements plays a key role during the thousand hours of work accomplished by the aircraft during its lifetime; therefore, the mechanical properties of the selected materials are extremely important. Chan 2010 demonstrated that the microstructural and metallurgical changes drastically affect the fatigue life and, in particular, the grain refinement leads to positive effect increasing fatigue strength.

In literature, there are a certain number of processes known as severe plastic deformation (SPD) that lead to an important microstructural refinement and consequently an increment of the work hardening of the processed material. In this Ph.D. thesis, the process known as ECAP (Equal Channel Angular Pressing) was chosen as a SPD process to study the microstructural changes of the aluminum alloy and to find some correlations with the metallurgical variations induced by machining operations. The aim of this research activity is to define new techniques in order to investigate the microstructural modifications when high thermo-mechanical loads are involved during the material forming. From the literature analysis, most of the experimental activities, in which ECAP is used, are designed to induce ultra or nano crystals formations to produce high performance materials. This thesis aims to discover a new scientific application of this SPD process to understand and study the evolution of the metallurgical changes in the deformed material. Subsequently, these phenomena could be modeled and used to predict the microstructural variation in the machining simulation once the links between the deformation mechanisms and material changes are assessed (Figure 2).

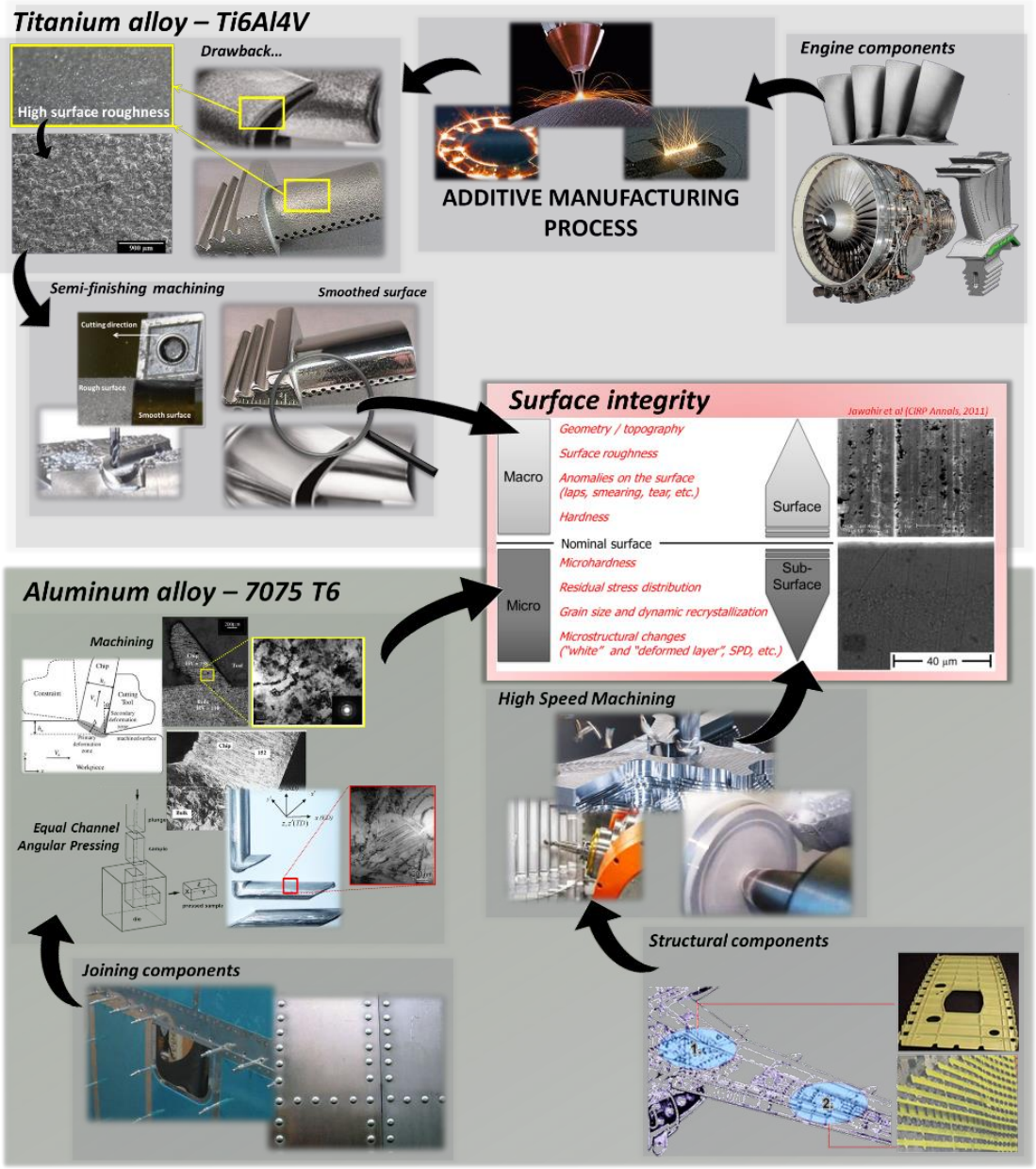

Figure 2: Representative scheme of the research activities developed in this Ph.D. thesis.

1.1. Research objectives

The literature review has highlighted the increasing trends in researching innovative high performance materials as well as new production processes of aerospace components (engine, structural and joining parts). The more complex geometry of the newest produced parts of the aircraft engine: blades, valves, stator/rotor components produced by the innovative additive manufacturing techniques demonstrated to be stronger than the same materials produced by conventional subtractive processes. Moreover, the materials used to produce engine parts (e.g. titanium alloy *Ti6Al4V*) are extremely difficult to machine due to their higher thermo-mechanical performance, therefore the AM is becoming important. The differences in mechanical performances between the machined and the AMed parts are mainly due to their different metallurgical aspects. However, the geometrical tolerances and surface quality obtained on the additively manufactured parts do not satisfy the requirements defined during the designing phase. Therefore, semi-finishing machining operations are still necessary to improve the geometry, reduce the distortions and the roughness, improving the surface quality. The literature analysis showed a lack of knowledge about the machinability strategy to improve the surface quality of these new materials produced via AM. Further investigations are also necessary to assess the mechanical behavior of AMed parts under machining conditions. The literature analysis has also highlighted the importance to improve the production rate through the increment of the cutting speed to extreme values (high speed machining conditions), when aircraft structural parts made by aluminum alloy are produced. In fact, the aluminum alloy particularly shows a refining of the microstructure, more evident at high plastic deformation rate, and this usually leads to enhancement of the mechanical properties and the fatigue strength. The presence of finer grain layers on the produced components leads to extend their duration during the operative conditions. The aluminum alloy *AA7075-T6* has been usually employed in producing structural aircraft parts, such as wings ribs, fuselages etc. and the parts are usually produced by machining processes. In literature, interesting results in terms of grain refinement and improved mechanical properties induced by machining on this kind of alloy are reported but the process parameters used (cutting speed lower than 800m/min) did not permit to achieve high production rates. The aluminum series (7xxx) is also employed in producing joining parts such as rivets. Several research articles based on applications of severe plastic deformation processes to the *7075-T6* alloy are reported but no comparison studies with the metallurgical changes machining induced are provided. In detail, the evolution of the thermo-mechanical loads induced by the SPD processes, such as ECAP, and their effects in metallurgical changes are not employed to investigate the same phenomena that occur during the machining processes. Taking into account the main lacks of knowledge highlighted by the literature analysis, the main objectives of this research are:

- to investigate the machinability and study the surface integrity of the additively manufactured titanium (*Ti6Al4V* alloy) machined parts after semi-finishing machining processes at different cutting parameters and cooling strategies;
- to investigate the machinability and study the surface integrity of the aluminum alloy (*7075-T6*) used to produce structural aircraft parts performing the high speed machining conditions at different cutting speed and cooling strategies;
- to employ and adapt the ECAP process to better understand the physical reasons of the metallurgical changes during severe plastic deformation induced by machining on aluminum alloy;
- to define the mechanical behavior flow stress in order to simulate the semi-finishing machining operations on the additively manufactured titanium parts To perform further investigations to assess the surface integrity in terms of microstructure deformation shape and hardness changes;
- to develop a physically-based model of aluminum alloy to simulate high speed turning operation at different cutting parameters and cooling conditions;
- to describe the physical reasons of the microstructural variations and to understand the hardening or softening governing phenomena;
- to predict the main fundamental variables such as cutting forces and temperature.

1.2. Dissertation outline

The schematic representation of this Ph.D. thesis is reported in Figure 3. The flow chart represents the organization of the analyzed topics (state-of-the-art), the experimental and numerical activities that are discussed in this work.

Chapter II is a literature review that aims to analyze and compare the new advanced production process techniques, namely the Additive Manufacturing, and the conventional material removal processes used to produce the aircraft components (in detail structural and engine components). Further attention has been paid in the manufacturing process used to realize aircraft structural parts. The analysis focuses on the new challenges, advantages and drawbacks introduced by these new techniques and the efforts done to date in order to overcome the problems and to improve the quality of the produced products. In detail, two materials mainly used in aerospace field, titanium and aluminum alloy, have been considered in this analysis due to the high industrial and scientific interest.

Chapter III describes the experimental activity devoted to the analysis of the machinability of the titanium alloy *Ti6Al4V* produced by AM processes. In particular, the main fundamental variables such as cutting forces and temperatures as well as the surface integrity have been assessed comparing these results to the ones obtained by machining the wrought titanium alloy. The innovative cooling technique, namely cryogenic fluid delivery, has been also investigated in order to analyze its effect on the machinability and surface integrity as well. Moreover, a final discussion that relates the obtained results with the mechanical performance of the material is also reported.

In *Chapter IV*, the experimental investigation on the aluminum alloy *7075-T6* under high speed machining operation and SPD process is reported. In detail, the machinability and the surface integrity of the aluminum alloy at different cutting parameters and cooling conditions have been assessed. Furthermore, a SPD process (ECAP) on the *7075-T6* alloy has been carried out to understand the metallurgical changes and to find possible links between the microstructural variations induced by machining and SPD processes.

Chapter V reports the numerical study of the titanium and aluminum alloy subjected to machining operation. In detail, the mechanical behavior of the titanium alloy post AM process has been defined and implemented into FE software to simulate the machining process. Subsequently, the metallurgical changes have been modelled and implemented to study their evolution during the cutting process. The mechanical behavior of the aluminum alloy, due to the machining processes and the several physical phenomena involved into the deformation process, has been described by a customized physics based model. Subsequently, this model has been implemented in a FE software in order to simulate and study the metallurgical changes such as dislocation density and grain sizes during the machining process.

Finally, the conclusion remarks summarizes the obtained results and highlights the probable future improvements that should be done by future works.

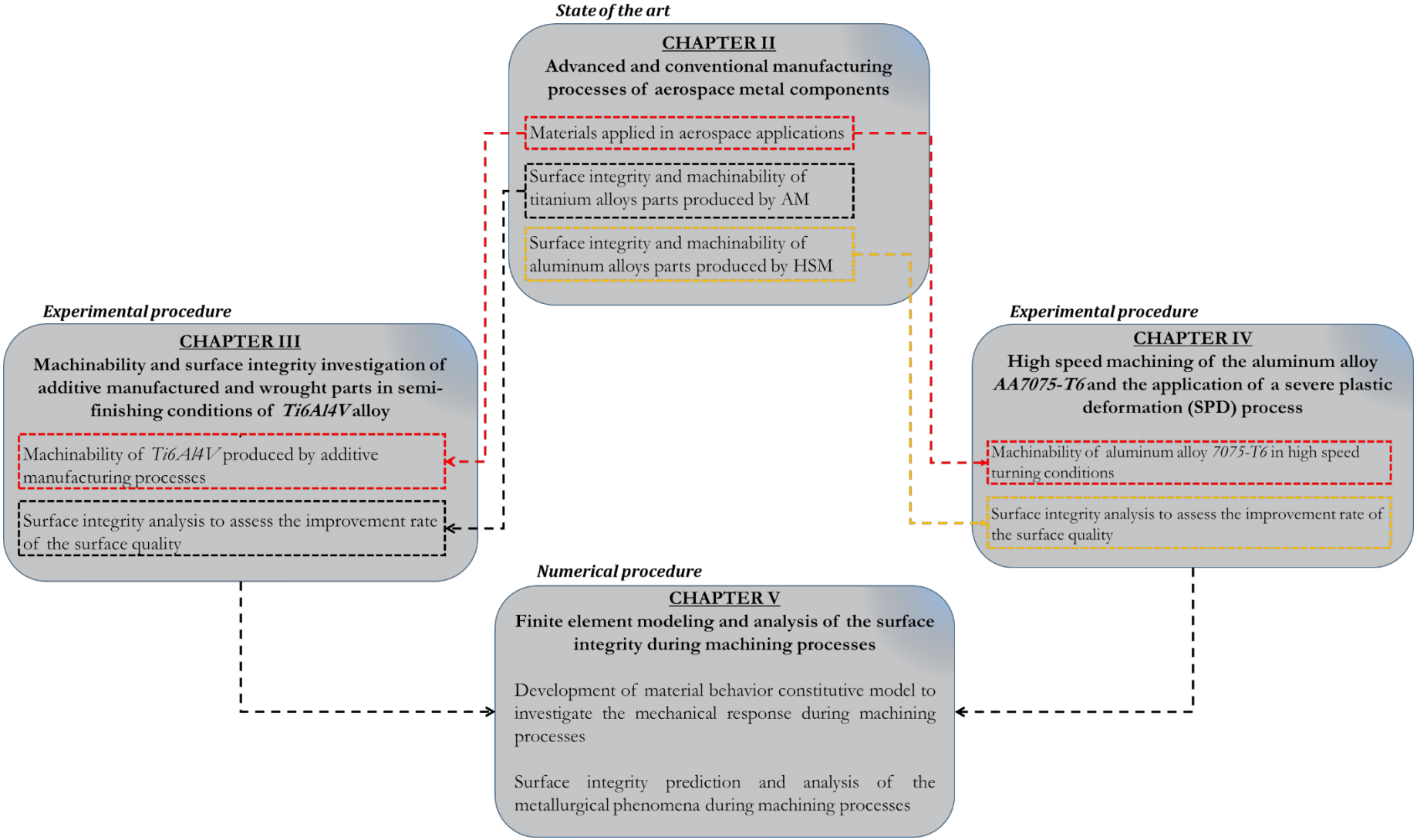

Figure 3: Flow chart of the Ph.D. thesis.

CHAPTER II

Advanced and conventional manufacturing processes of aerospace metal components

This chapter provides a brief literature review on aerospace materials focusing on the metal ones (titanium and aluminum alloys) and in particular, the alloys employed to produce engine, structural and joining parts. Subsequently, a brief state-of-the-art of the manufacturing processes used to build the aerospace mechanical components is also reported. The new outcomes and challenges introduced by the conventional and advanced manufacturing processes in fabricating the innovative mechanical components are highlighted. A detailed state-of-the-art on metallurgical aspects coupled with thermo-mechanical properties of the analyzed metal materials when manufactured are described and used in Chapter , Chapter IV and Chapter V as a support in understanding the experimental results and build up new material behavior constitutive models.

2.1 Aerospace materials for engine, structural and engine components

The aircraft structural design is driven by two design philosophies namely fail-safe and safe-life. Fail-safe design (denoted also as damage tolerant design) ensures that between two consecutive inspection intervals the overall structural integrity and function are not affected by failure or damage of some parts of the structure. Safe-life design implies that the structure and its components will function without any failure during the prescribed lifetimes of the components. It is clear that the design technique of structural or engine parts have in common the word "safe". In general, the typical functions of a structural component are primarily to resist and transmit the forces, while the engine parts have to resist to high pressure and temperature and drastic operative conditions in total "safe". Besides strength and general damage tolerance, aircraft structures must also be resistant to degradation from fatigue, corrosion, and stress corrosion; and in elevated temperature applications the materials must be resistant to creep and thermal instability. To respect the design requirements and satisfy the "safe" conditions, not only the geometry but also the selection of the best material for an aircraft structure or engine component is an important task for the aerospace engineer. The success or failure of any new aircraft is partly dependent on using the most suitable materials. The cost, flight performance, safety, operating life and environmental impact from engine emissions of aircraft is also dependent on the types of materials that aerospace engineers choose to use in the airframe and engines. Generally, the aerospace materials must be light, stiff, strong, damage tolerant and durable. These requirements aim to increase the airframe durability that is one of the main target for commercial and military aircraft production enterprises. However, most of the materials lack one or more of the essential properties that are strongly required by the aerospace structures and engine applications. Consequently, there is always a continuing demand for high-quality materials and metal alloys with closely controlled chemistries, cleanliness and homogeneity in mechanical response and statistically controlled reproducibility of the thermo-mechanical properties (Prasad and Wanhill 2017 – Volume 1). Other demands on aerospace materials are emerging as important future issues. These demands include the use of renewable materials produced with environmentally friendly processes and materials that can be fully recycled at the end of the aircraft life. Sustainable materials that have little or no impact on the environment when produced, and the reduction of the environmental impact of the aircraft by lowering fuel burn (usually through reduced weight), will become more important in the future (Prasad and Wanhill 2017 – Volume 2, Mouritz 2012).

As an example, the long-term strategic objectives of "Flightpath 2050" foresee the 75% reduction in CO_2 per passenger kilometer, the 90% reduction in NO_x emissions and the 65% reduction in noise.

This means the lightweight designs and new advanced materials on airframes and engines, advanced aerodynamic performances, advanced turbine materials for aero engines (disc and blades) (M' Saoubi et al. 2015). Consequently, as showed by Figure 4, the fundamental requirements previously explained are satisfied by several class of materials such as aluminum alloys, titanium alloys, steels and composites. In addition to these materials, nickel-based alloys are important structural materials for jet engines. Many other materials are also used in aircraft: copper for electrical wiring; semiconductors for electronic devices; synthetic fabrics for seating and other furnishing.

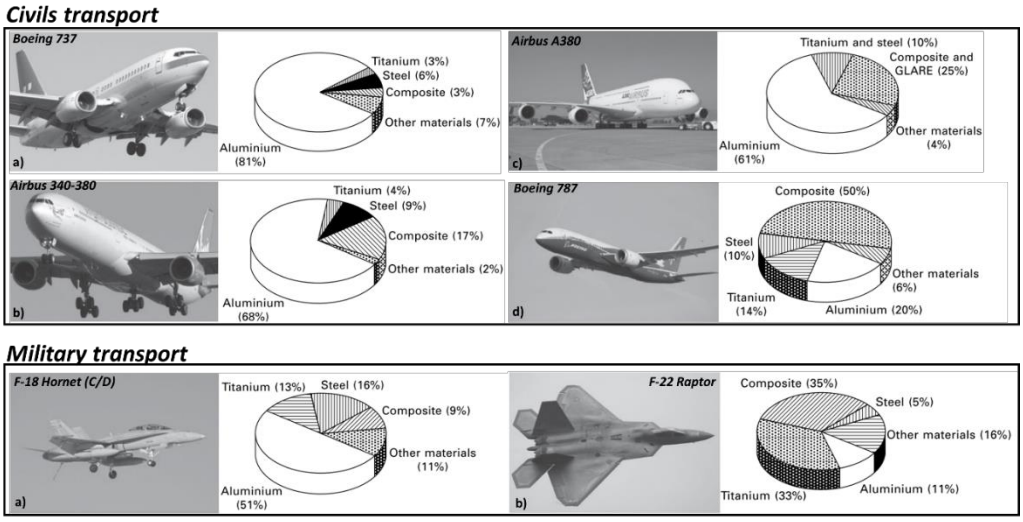

Figure 4: Materials and their weight percentages used in the airframes of civilian and military aircrafts (adapted from Mouritz 2012).

Taking into account the group of materials referred to aluminum and titanium alloys; these are mainly used to produce the mechanical and structural components of the functional groups showed in Figure 5.

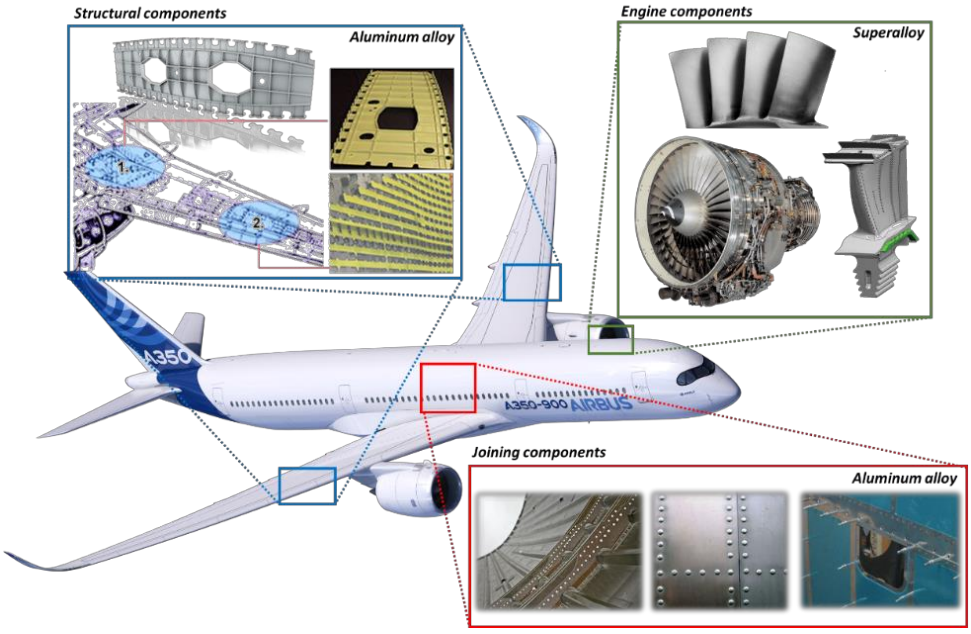

Figure 5: Different mechanical and structural groups of aircraft components and the materials employed.

As showed by Figure 4, although the presence of the composite material is constantly growing in aerospace field, the titanium and aluminum alloy usually represent the highest percentage of the material employed. The trends showed by Figure 6 suggest an increasing tendency to employ titanium alloy in military sector as well as a constant improvement of the mechanical properties of the aluminum alloys in order to increase their performance in aerospace applications. Therefore, due to the high interests in improving the mechanical performances of the aluminum and the increasing demand of titanium in aerospace applications, the material investigated by this Ph.D. thesis are in detail the aluminum alloy *7075-T6* and the titanium alloy *Ti6Al4V*.

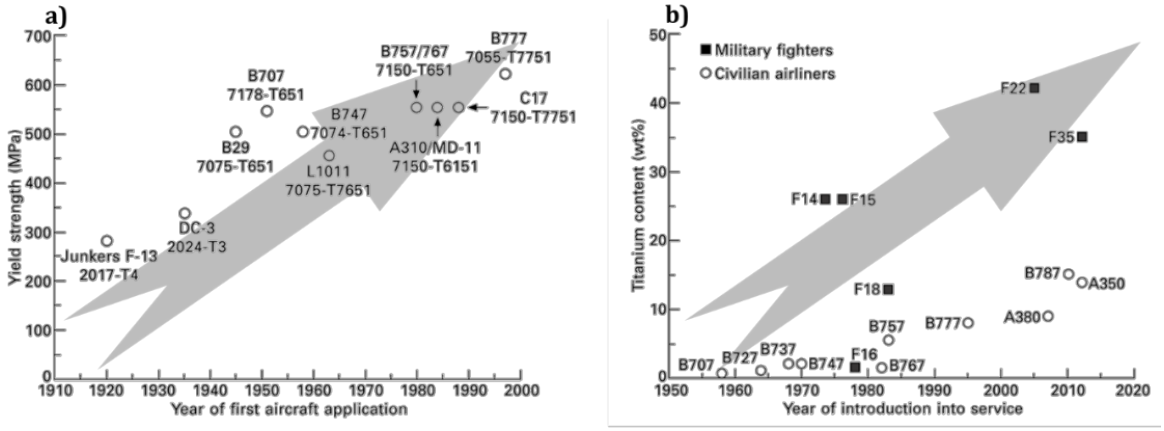

Figure 6: a) Yield strength of aluminum alloys and the year of introduction into civils transport services; b) Titanium content % used in military and civils transport aircrafts (adapted from Mouritz 2012).

The structural and joining components are mainly produced in aluminum alloy. This latter accounts for 60-80% of the airframe weight of most modern aircraft and this result is justified by its specific weight that make this material the lightest metal, being about 2.5 times lighter than steel. In addition, aluminum can be easily fabricated into thin skin panels and readily machined into spars, stiffeners and beams for the fuselage and wings. Around 400000 tons of aluminum each year are used in building military and civil aircrafts. Aluminum is used in the main structural sections of the Boeing B747 and B777, including the wings, fuselage and empennage (tail assembly). The fuselage of the civilian aircrafts is characterized by a semi-monocoque structure. A semi-monocoque fuselage consists of a thin shell stiffened in the longitudinal direction with stringers and longerons and supported in the radial direction using transverse frames or rings (Figure 7a). The strength of a semi-monocoque fuselage depends mainly on the longitudinal stringers (longerons), frames and pressure bulkhead. The skin carries the cabin pressure (tension) and shear loads, the longitudinal stringers carry the longitudinal tension and compression loads, and circumferential frames maintain the fuselage shape and redistribute loads into the airframe. During the flight, the upward loading of wings coupled with the tail plane loads usually generates a bending stress along the fuselage. The lower part of the fuselage experiences a compressive stress whereas the upper fuselage (called the crown) is subject to tension. Therefore, it is possible to understand that the structural parts experience very complex loads combinations in critic environmental conditions. Concerning the wings (Figure 7b), the main function is to pick up the air loads to maintain flight and transmit the load to the fuselage (via wing-box and wing connections). In military combat aircrafts the fluctuating loads are generally higher than commercial aircraft owing to the need for frequent and fast maneuvering. These fluctuating loads can induce fatigue damage. Therefore, the necessity to research high performance materials with high fatigue strength to resist damage and failure from fluctuating loads and turbulence is an important requirement as well. Furthermore, it is known that fatigue damage does not occur in compression, and therefore the lower (tension) and upper (compression) wing surfaces have different material requirements. For this reason, several materials are also used in a single aircraft wing.

For example, subsonic aircraft wings have traditionally been made using two types of aluminum alloys: high compressive strength alloy (such as *2024 Al*) for the upper wing surface and high tensile strength alloy (e.g. *7075 Al*) for the lower surface. It is imperative use high performance and lightweight materials to produce wings because they account the 20-25% of the structural weight of an aircraft.

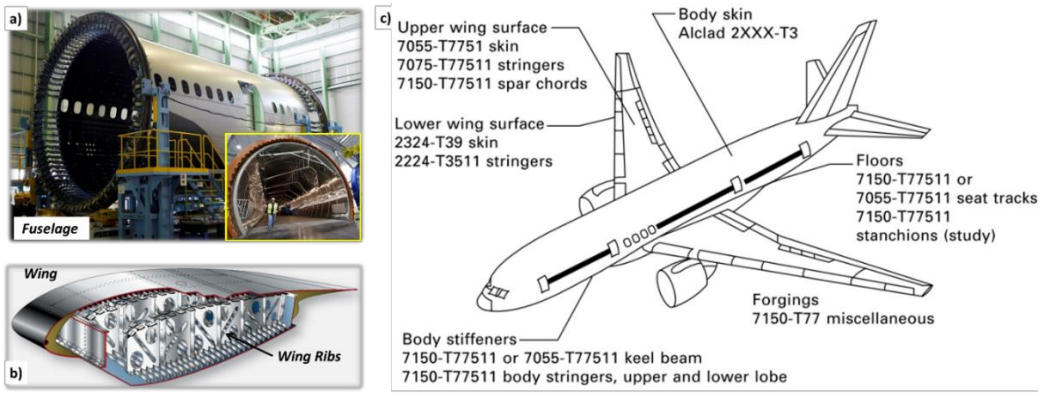

Figure 7: a) Boeing 787 fuselage under construction; b) wing and its internal structures made by wing ribs; c) Aluminum alloys used on Boeing 777 (adapted from Starke and Staley 1996).

In Figure 7c, the typical aluminum alloys used to produce various parts of the Boeing 777 are reported. Referring to Figure 4, the second most important material used in building aircrafts is the titanium alloy. This percentage is mainly referred to the material used to produce mechanical components of the engines, especially for aircraft intended to civilian transportation. This material finds also structural and covering applications in military aircraft as showed by Figure 6b (in this latter the percentage is higher if compared with the civilian aircraft). The material used in jet engines are subjected to the most arduous working temperature in an aircraft. In fact, the turbines compress the air to high pressure and this air is then heated to extreme temperature by burning fuel to produce hot, high-pressure gases which are expelled from the engine exhaust thus propelling the aircraft forward. The engine materials must perform for long periods under high temperatures and stresses while exposed to hot corrosive and oxidizing gases generated by the burning fuel. Jet engine materials must possess high tensile strength, toughness, fatigue strength and creep resistance together with excellent resistance against corrosion and oxidation at high temperature (Mouritz 2012). An example of different materials applied into the aerospace jet engine depending on the temperature working conditions is showed in Figure 8.

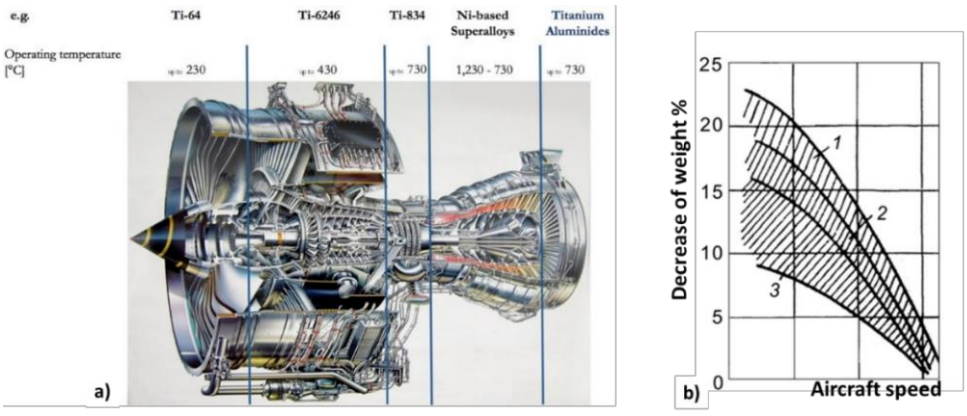

Figure 8: a) blades material at different temperature operative conditions into a representative aerospace jet engine; b) economy of weight achieved in the case of using titanium for engines: 1, large-size; 2, medium-size; 3, small-size (Rolls-Royce Trent 700).

Generally, the titanium and nickel alloys are preferred due to their ability to meet higher strength and corrosion resistance required at high temperature.

Titanium alloys, such as *Ti6Al4V*, are mainly used in fan and compressor assemblies – disks, blades, guides, spacer rings, engine body, various engine-body parts, air collectors, and other items. Moreover, in military applications, the titanium alloy is also used in the region of the aircraft in which the temperature reaches values up to 300-350 °C. Titanium is used as a replacement material for steel in landing gear to eliminate the problems of corrosion and hydrogen embrittlement as well as to achieve a significant weight saving. The use of titanium alloys in aircraft-engines instead of steel reduces the weight of components by 30-40% leading considerable benefits in terms of reduction of fuel consumption (Mouritz 2012, Moiseyev 2006). Moreover, titanium has the ability to form a thin oxide surface layer, which is resistant and impervious to most corrosive agents and which provides excellent corrosion resistance.

The work materials investigated in this Ph.D. thesis are the most common used aluminum and titanium alloy; in detail the *AA7075-T6* and the *Ti6Al4V* respectively. The metallurgical aspects of these materials permit to understand their properties that make them suitable for aerospace applications.

2.1.1 Titanium alloy – *Ti6Al4V*

Titanium was discovered in 1790 but not purified until the early 1900s. Nowadays it has the accumulated experience of some 50 years of modern industrial practice and design application to support its use (Donachie 2000). Titanium is the ninth most-abundant element on the planet and the fourth most-abundant structural metal. Mineral sources of titanium are rutile, ilmenite and leucoxene, an alteration product of ilmenite (Figure 9).

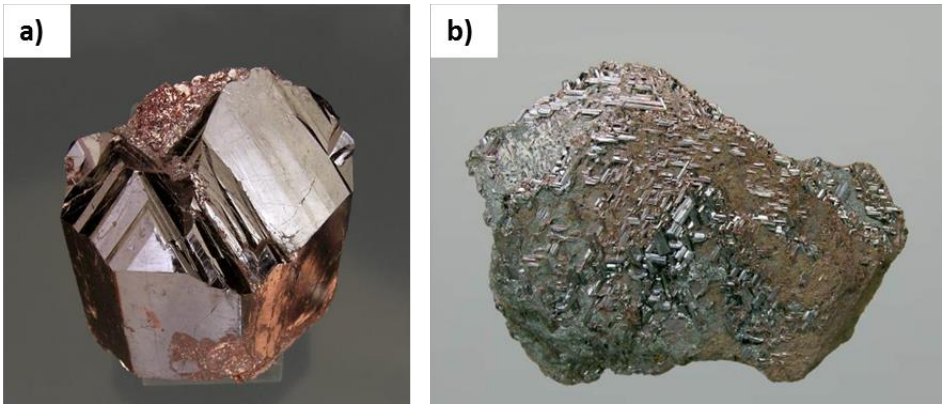

Figure 9: a) Rutile, b) Ilmenite.

A metallurgical property of titanium alloys that is important in their use in aircraft is allotropy, which is defined as different physical forms of the same material that are chemically very similar. Many metals, including the aluminum, magnesium and nickel alloys used in aircraft, can only occur in one crystalline phase at 20 °C. For instance, aluminum can only have a face-centered-cubic (FCC) crystal structure at room temperature, and no other. As another example, the crystal structure of magnesium is always hexagonal close packed (HCP) at 20 °C. Titanium alloys, on the other hand, can have two elemental crystal structures namely hexagonal-close-packed (HCP) crystal structure, which is known as alpha (α-Ti), and a body-centered-cubic (BCC) structure, which is called beta (β-Ti), at room temperature (Figure 10).

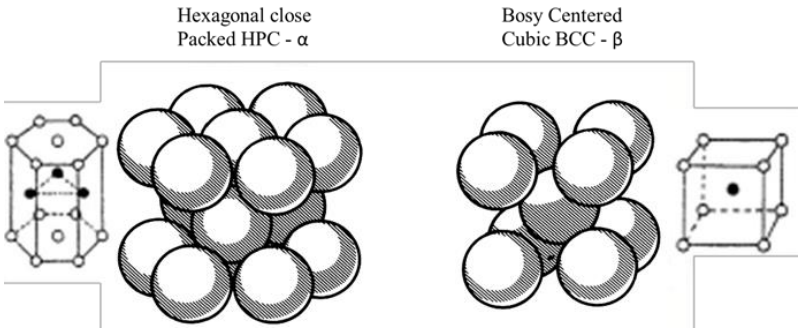

Figure 10: Appearance of crystal structures of titanium at atomic level (Donachie 2000).

The single cubic structure is found only at high temperatures, unless the titanium is alloyed with other elements to maintain the cubic structure at lower temperatures. The alpha and beta "structures"—sometimes called systems or types are the basis for the generally accepted four classes of titanium alloys: alpha, near-alpha, alpha-beta, and beta. These categories denote the general type of microstructure after processing (microstructure refers to the phases and grain structure present in a metallic component). Alloying elements can be generally classified as α or β stabilizer as reported in Table 1. Alpha stabilizers as aluminum or oxygen increase the temperature at which the alpha phase is stable. On the other hand, Vanadium or Molybdenum which are beta stabilizer allow the beta phase to be stable at lower temperatures (Donachie 2000).

Table 1: Alloying titanium elements and their effects (Donachie 2000).

Alloying element	**Range [wt%]**	**Effect on structure**
Aluminum	2 to 7	Alpha stabilizer
Tin	2 to 6	Alpha stabilizer
Vanadium	2 to 20	Beta stabilizer
Molybdenum	2 to 20	Beta stabilizer
Chromium	2 to 12	Beta stabilizer
Cooper	2 to 6	Beta stabilizer
Zirconium	2 to 8	Alpha and beta strengthening
Silicon	0,2 to 1	Improves creep resistance

The *Ti6Al4V* (α+β category) is the most widely used in aerospace industries. *Ti6Al4V* alloy contains 6 wt% Aluminum stabilizing the α phase and 4 wt% Vanadium which stabilizes the β phase. The equilibrium at room temperature consists of α phase (HCP) in a retained β phase (BCC). As it is possible to see in Figure 11, the transformation temperature from *alpha-plus-beta* or from *alpha* to all *beta* is known as the *beta transus* temperature (995 °C). The *beta transus* is defined as the lowest equilibrium temperature at which the material is 100% *beta*. Below the *beta transus*, titanium is a mixture of *alpha-plus-beta* if the material contains some *beta* stabilizers; otherwise it is all *alpha* if it contains limited or no *beta* stabilizers. The *beta transus* is important because processing and heat treatment often are carried out with reference to some incremental temperature above or below the *beta transus*. In relation to the chemistry of the selected alloy, the microstructure is produced depending on the heat treatment selected (Lütjering and Williams 2007). Taking into account that the *Ti6Al4V* is an α+β alloy, the microstructure that results at room temperature is a function of the way in which the transformation of beta to alpha phase occurs. For the commercial *Ti6Al4V* alloy, there are some commonly used heat treatments that produce different microstructures. Figure 11 shows some microstructures formed during solution temperature and cooling rate variations. The microstructure formed from beta region, depending on the cooling rate can evolve in equiaxed or acicular also known as Widmanstätten (Figure 11).

This latter microstructure consists of parallel plates of α delineated by the β phase between them. Depending on the quenching temperature and chemistry of the alloy, different types of martensite can form. These are designated α prime and α double prime.

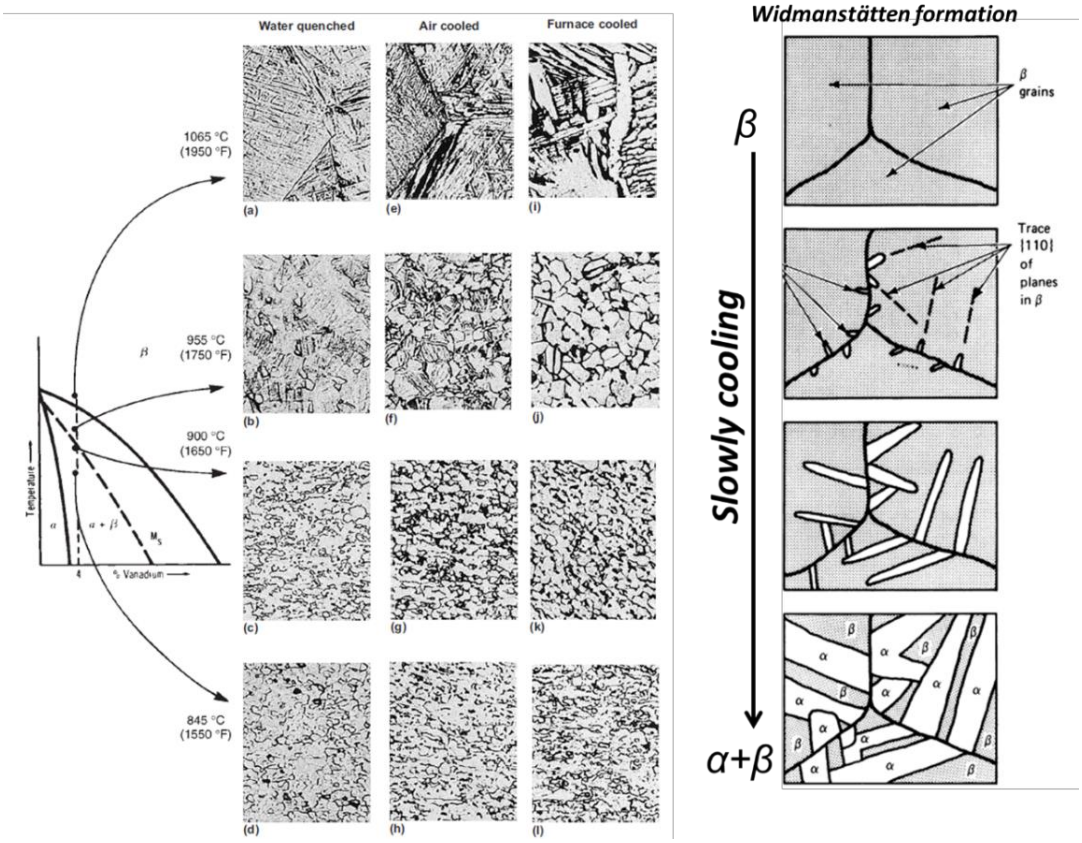

Figure 11: Effect of cooling rate on the microstructure of an alpha-beta alloy (*Ti6Al4V*); (a) α' + β; prior beta grain boundaries; (b) Primary α and α' + β; (c) Primary α and α' + β; (d) Primary α and metastable β; (e) Acicular α + β; prior beta grain boundaries; (f) Primary α and acicular α + β; (g) Primary α and acicular α + β; (h) Primary α and β; (i) Plate-like α + β; prior grain boundaries; (j) Equiaxed α and intergranular β; (k) Equiaxed α and intergranular β; (l) Equiaxed α and intergranular β (adapted from Donachie 2000).

There are some significant facts and / or important benefits offered by titanium alloys that illustrate the basis for the widespread use of titanium today:

- The density of titanium is only about 60% than that of steel or nickel-base superalloys.
- The tensile strength (as an alloy) of titanium can be comparable to that lower-strength martensitic stainless and is better than that of austenitic or ferritic stainless.
- The commercial alloys of titanium are useful at temperature to about 538 °C to 595 °C, dependent on composition.
- Titanium is exceptionally corrosion resistant. It often exceeds the resistance of stainless steel in most environment, and it has outstanding corrosion resistance in the human body.
- Titanium can be forged or wrought by standard techniques.
- Titanium is castable and the investment cast titanium alloy structures have a lower cost than conventional forged / wrought fabricated titanium alloy structures.
- Titanium is available in a wide variety of types and forms.

Due to its good compromise between mechanical resistance and tenacity, together with its low density and excellent corrosion resistance, *Ti6Al4V* titanium alloy is often used in two areas of application: corrosion-resistant service and strength-efficient structures that normally are representative of the aerospace field.

2.1.2 Aluminum alloy – *AA7075-T6*

Aluminum comprises 8% of the earth's crust and is, therefore, the most abundant structural metal. In the manufacture of aluminum, there are two main stages. The first embraces the production of pure Al_2O_3 from bauxite (Figure 12), and the second is the reduction of this Al_2O_3 to the metal in a bath of fused cryolite.

Figure 12: Bauxite.

Pure aluminum and its alloys have the face centered cubic (FCC) (Figure 13b) structure, which is stable up to its melting point at 657 °C. Since the FCC structure contains multiple slip planes, this crystalline structure greatly contributes to the excellent formability of aluminum alloys. Only a few elements have sufficient solid solubility in aluminum to be major alloying elements. These include copper, magnesium, silicon, zinc, and more recently lithium. Important elements with lower solid solubility are the transition metals chromium, manganese, and zirconium, which normally form compounds that help to control the grain structure (Mouritz 2012, Campbell 2006). In Table 2 is reported the chemical composition of the alloy.

Table 2: Chemical composition of 7075 aluminum alloy (Mouritz 2012).

Alloying element	**[wt%]**
Zn	5.1-6.1
Mg	2.1-2.9
Cu	1.2-2
Mn	0.3
Cr	0.28
Fe	0.4
Si	0.4

In general, the main alloying elements in series 7xxx alloys are Copper and Zinc, with the Zinc content being three to four times higher than the Copper. Magnesium is also an important alloying element and for these reasons, the 7xxx series is known as Al-Zn-Mg alloys. Addition of Copper to the Aluminum–Zinc–Magnesium system, together with small but important amounts of Chromium and Manganese, results in the highest strength aluminum-base alloys. The equilibrium phases are $MgZn_2$ (η), Mg_3Zn_3Al (T) and Mg_5Al_3 (β). If the quantity of Zn is higher than the Mg (the case of *7075* alloy), than the precipitation sequence to equilibrium $MgZn_2$ is predominant. In Figure 13a is showed the microstructure of the wrought *AA7075-T6*. It is possible to see small grains precipitates of $MgZn_2$ dispersed in the Al matrix.

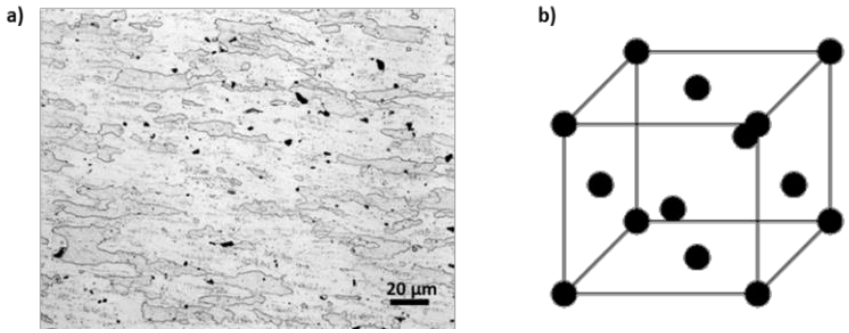

Figure 13: a) Microstructure of *AA7075-T6* (MacKenzie 2006); b) FCC crystal structure.

The aluminum alloys show different mechanical properties depending on the heat treatment and ageing. In detail, the wrought *AA7075* has better performance than the other aluminum alloys due to the precipitation hardening that lead to high strength. In general, precipitation hardening consists of three steps: (1) solution heat treating, (2) rapidly quenching to a lower temperature, and (3) aging. In solution heat treating, the alloy is heated to a temperature that is high enough to put the soluble alloying elements in solution. After holding at the solution treating temperature for a certain interval time, the alloy is quenched to a lower temperature (e.g., room temperature) to keep the alloying elements trapped in solution. During aging, the alloying elements trapped in solution precipitate to form a uniform distribution of very fine particles. This fine distribution of precipitates strengthens and hardens the alloy by creating obstacles to dislocation movements. Some aluminum alloys will harden after a few days at room temperature – a process called natural aging, while others are artificially aged by heating to an intermediate temperature. Taking into account the aluminum 7xxx series, and in particular the *7075* aluminum alloy, the precipitation hardening due to the aging transformation starts with the Guinier-Preston (GP) zones formation. The normal precipitation sequence during aging of the supersaturated solid solution is: GP zones → η' ($MgZn_2$) → η ($MgZn_2$). The GP zones are ordered, solute-rich clusters resulting from phase separation that nucleate and grow. The GP zones are the first to nucleate, because of their small size and coherency with the matrix. The semi-coherent intermediate metastable phase η' nucleates and grows from the GP zones while the incoherent equilibrium phase η (hexagonal crystal structure) grows from η' phase. Generally the metastable η' is homogeneously distributed in the alloy matrix. This may nucleate from the spherical GP zones which form during the earliest stages of ageing below the GP zone solvus (~ 150 °C for most alloys of commercial importance) (Figure 14). The equilibrium η phase nucleates and grows at the grain boundaries and its presence indicates over-aging and results in decreased strength properties (Campbell 2008, Zhao et al. 2004, Flower 1995).

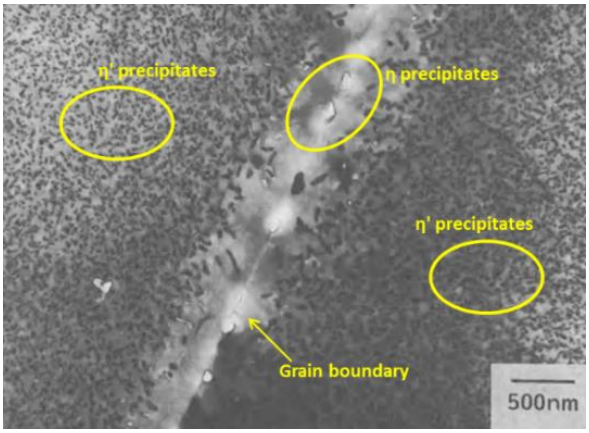

Figure 14: Al Matrix, η' dispersed into the matrix and η grain boundaries precipitates ($MgZn_2$) 7xxx series aluminum alloy aged at 180°C (adapted from Flower 1995).

The major characteristics that make the *7075-T6* suitable for aerospace applications are:

- the alloy is suitable for heat treatments;
- high conductivity, strength and hardness;
- high ultimate tensile strength;
- high corrosion resistance;
- good machinability;
- good mechanical properties at cryogenic temperatures, it is suitable to be employed as structural material in pressure cells at low temperatures.

2.2 Additive and subtractive manufacturing processes of aerospace metal components

During the design of a component, another important issue is to properly decide and define all the steps to produce the specified part with the appropriate specific requirements. *Manufacturing* is the term used to describe the making of the products. Metalshaping operations are of particular importance because metallic materials are most often the load-bearing components of many engineered products and structures. Although most of the previously mentioned products (blades made of titanium alloy or aluminum structural components) are primarily produced by casting or forming processes, these latter do not permits to achieve the dimensional tolerances as well as the required surface and sub-surface quality. Therefore, these issues can be overcome if the desired shape is finally obtained by incrementally removing excess material by machining processes. The most common machining operations rely on relative motion between the workpiece and a cutting tool that mechanically removes material in the form of chips. These include, among others, the processes of turning, planing, shaping, drilling, milling and grinding (Beddoes and Bibby 1999). The production processes of structural parts of the aircraft frame are mainly represented by forging process. However, the possibility to perform high speed machining permits to produce in a short time parts with complex shapes directly from heavy rolled plates. This improvement in production represents an additional threat to expanded use of forgings. Therefore, reduced set up time, machine tools of greater rigidity, precision computerized controls, and new cutting tool materials have made high speed machining a viable contender for producing complex shapes that are ordinarily made by forging. The aerospace industry has invested enormous amounts of money in new high speed machining technologies that allow fast machine feed rate without machine tool vibration, and allow production of thinner machined webs. Moreover, in conventional machining, roughing is usually followed by finishing using lighter depths of cut at much slower speeds. In high speed machining, it is often possible to combine the roughing and finishing cuts in the same operation. An enabler for high speed machining has been the development of porosity-free thick plate in the 7XXX series of alloys (Campbell 2006, Totten and MacKenzie 2003). The high speed machining is a fast growing technology very closely related to the machining of light metal alloys due to the different advantages apart of the obvious increase in machining productivity: i) increased machining accuracy, especially in the manufacture of parts containing; ii) better surface finish and reduction in the damaged layer; iii) reduced burr formation and better chip disposal; iv) possibility of higher stability due to superposition of stability lobes against chatter vibration (Schulz and Moriwaki 1992).

High speed machining (HSM) has been used very effectively in the production of thin web aluminum alloys stringers which assemble onto the Boeing 737 aircraft (Figure 15). The high material removal rate also changes the design of the aerospace parts. In fact, the HSM permits to machine extremely thin walls and webs allowing to produce parts lighter leading to an additional cost saving (Prasad and Wanhill 2017, Volume 1). In Figure 15, two components representative of thin Wall Ribs made of *7075-T6* machined by conventional process and HSM process are reported. This latter does not show critical regions and no deflected part (especially the walls) results. Moreover, the thickness of the walls was reduced leading to a reduction of the weight (Campbell 2006).

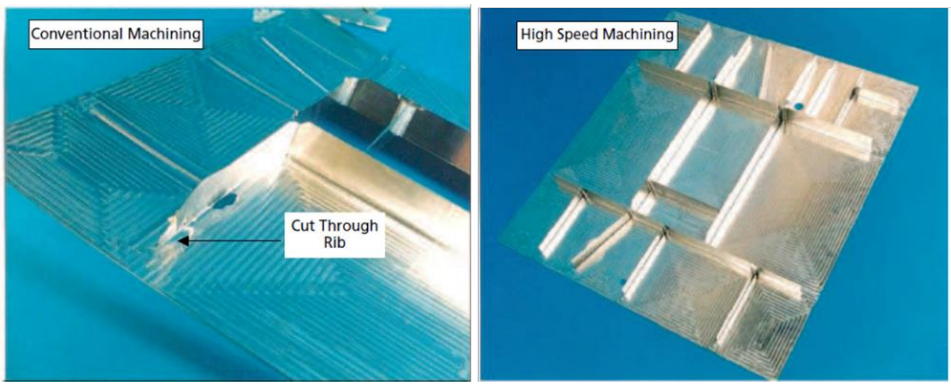

Figure 15: Thin Wall Ribs of Boeing aircraft structural part: High Speed vs. Conventional Machining (adapted from Campbell 2006).

Machining the material at high material removal rate clearly produces different results in terms of surface integrity compared to the machining processes at conventional cutting speed. Wang and Liu 2016 showed that the material deformation and fracture behavior of aluminum alloy *7050-T7* during high speed machining changed greatly and this affected the material removal mechanism and the surface quality of the machined parts. They reported that the surface roughness increased when increasing the cutting speed from 2500m/min up to 7000m/min. The poor surface roughness at ultra-high cutting speed was provoked by the material behavior characterized by brittle fracture (the chip material is undergone to brittle fracture) leading to chip fragmentation.

The chip brittle fracture mechanism was also justified by the presence of brittle tearing and fragment adhesion observed on the machined surface (Figure 16).

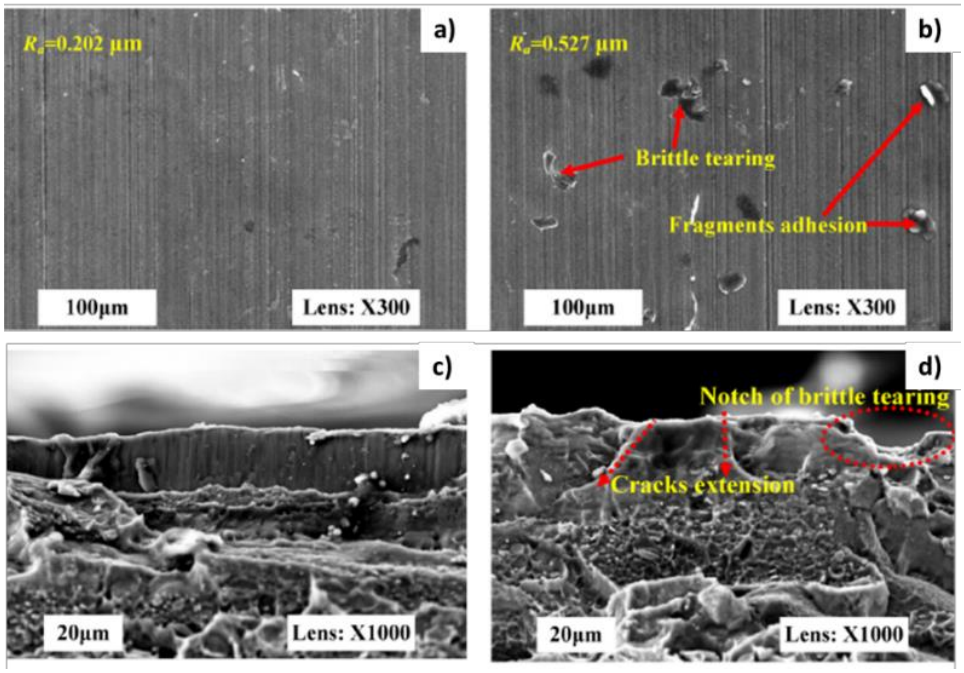

Figure 16: a) and b) SEM micrographs of machined surface; c) and d) SEM micrographs of fracture surface morphology of machined parts (adapted from Wang and Liu 2016).

The authors also affirmed that because the chip material undergone brittle fracture under ultra-high cutting speed, the energy consumption could be reduced substantially due to hardly plastic deformation occurred during fragmented chip formation. Therefore, the ultra-high speed machining (UHSM) is recommended to be used in rough machining and semi-finishing, while the HSM is recommended to be used in the finishing process. This combined manufacturing process can take full advantage of the merits of both HSM and UHSM. Chen et al. 2017 studied the formation of surface gradient nanostructures induced by high speed machining on *7055* aluminum alloy. They used sophisticated analysis and mixed the results provided by transmission electron microscope (TEM) and other advanced analysis techniques to study the microstructural and crystallographic features on the machined surfaces. The results showed that the surface and sub-surface material under thermo-mechanical loads induced by machining was characterized by gradient nanostructured layer (equiaxed and lamellar nanograins) (Figure 17). Moreover, some low angle dislocation boundaries and recrystallized nanograins and ultrafine grains were observed, providing the direct evidence that dislocation activities and dynamic recrystallization were two dominant approaches for grain refinement. Compared with the coarse grained matrix, the large size and density differences between grain boundaries precipitates and grain interior precipitates showed a prominent precipitate redistribution, which could be accomplished via the thermally and mechanically induced precipitate dissolution, solute diffusion and reprecipitation.

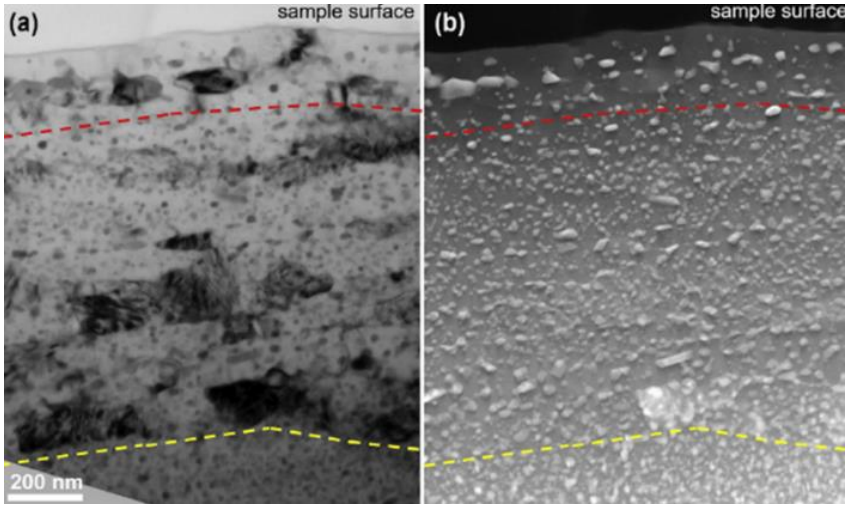

Figure 17: a) TEM and b) HAADF-STEM images showing the microstructure of the surface deformation layer in the machined 7055 aluminum alloy (Chen et al. 2017).

Although this work shows a deep comprehensive study of the metallurgical phenomena induced by the high speed machining process, the material behavior and the mechanical properties changes due to the microstructural alteration were not investigated. Most of the works based on sever plastic deformation of aluminum alloys clearly show that the plastic deformation caused an accentuated increase of the alloy hardness, tensile strength resulted from precipitation and grain refinement as well as work hardening (Ma et al. 2014, Cardoso et al. 2011). The cooling strategy that was used during the machining process was demonstrated to have interesting benefits, improving the surface integrity of the produced components. As reported by Rotella and Umbrello 2014 and Rotella et al. 2013, the increasing of the cutting speed coupled with very low temperature (cryogenic conditions) led to very small grain size on surface and into the subsurface of the machined parts. The grain refinement and the work hardening provoked an increment of the hardness improving the surface integrity of the components (Figure 18). The authors affirmed that the main responsible of the higher surface hardness was the grain refinement phenomenon and they modeled the hardness by the Hall-Petch relation. Moreover, they reported that the effect of cryogenic machining on fatigue performance was beneficial because the grain refinement led to increasing the fatigue life and strength.

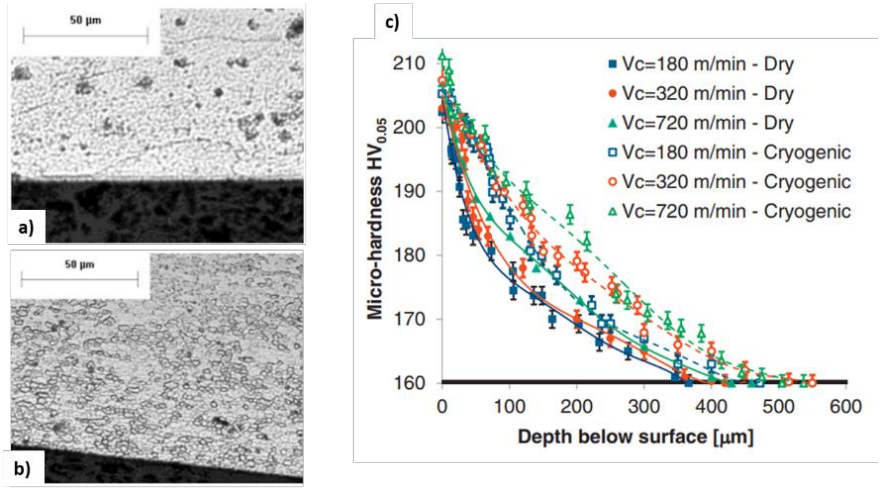

Figure 18 : Microstructure on the cross section of the machined samples (dry) and b (cryogenic); c) measured microhardness (Adapted by Rotella 2013)

However, further investigations to understand the role of the precipitates and their evolution during machining process and under cryogenic conditions and the role of dislocation densities were not investigated by the authors. The possibility to improve the mechanical properties as well as the performance of the manufactured parts, in particular aluminum, and the process under cryogenic conditions is well reported in literature. In fact, Pušavec et al. 2011 conducted an experimental study on the influence of cryogenic cooling on process stability in turning operations, in which coarse-grained entropy rate (CER) method was used for detection of chatter in cutting tests. A higher machining stability limit achieved during cryogenic machining was observed due to the reduction of specific cutting force components. Huang et al. 2014 conducted some milling test on *7075-T6* aluminum alloy under cryogenic conditions. They concluded that cryogenic cooling enhanced stability limits in end milling because the LN_2 jet helped to take away the chips leading to a significant reduction of the cutting force.

From the literature analysis, the positive impact in production introduced by HSM is obviously evident; furthermore, the aerospace industries are strongly motivated to improve this production technology to enhance the final quality of the products. On the other hand, the research and the industry are also motivated to introduce the aluminum alloy in the AM world. However, the number of different Al alloys available for AM is still rather limited. Indeed, the 7xxx series usually contain highly volatile elements such as Zn, leading to turbulent melt pools, splatter and porosity and are therefore not easy and suite to use in AM. Moreover, the Al alloys, compared to Ti alloys are easy to machine and the cost of machined parts are lower (Herzog et al. 2016). Therefore, the high speed machining still represent a good strategy to improve the production process of aerospace components and it has been investigated in this Ph.D. thesis taking into account the aluminum alloy *7075-T6*. The aim of the work is to suggest new optimized process strategies to improve the quality and surface integrity of the machined parts. The role of the microstructural and metallurgical alterations is not clearly investigated for the aluminum alloy *7075-T6* during high speed machining; therefore, another important goal is to assess the surface integrity in terms of microstructure, phase and hardness changes at varying cutting parameter and cooling strategy.

Focusing on the manufacturing processes devoted to produce smaller parts for aircraft engine applications, during the last years due to progress in computation power and systems technology laser based, the Additive Manufacturing has advanced to a technology with high potential for industrial applications (Schmidt et al. 2017). Contrarily to what observed during the machining processes where a certain volume of material is removed to achieve the desired shape, the AM is a computer-driven layer-by-layer construction process in which the part is built-up without use of tooling.

The AM technology permits also to rebuild the damaged expensive aerospace titanium components, such as bearing housing, flanges, fan blades, casings, vanes, and landing gears (Dutta and Froes 2016). From the sustainability point of view, this new production technology is strongly preferred from the aircraft industries because it holds great potential for improving material efficiency, reducing life-cycle impacts, enabling greater engineering functionality compared to conventional manufacturing processes such as machining (Huang et al. 2016). Furthermore, the AM techniques permit to satisfy the design standard rule. In fact, in general the design for assembly aims to minimize the number of part and fasteners when it is possible to reduce the assembly cost. In Figure 19a is reported an example of two very different approaches to designing ducts for aircraft (Conventional vs. AM). This example represents a design concept for conveying cooling air to electronic units in military aircraft. The first design (conventional) is a typical approach using parts fabricated by conventional manufacturing processes (stamping, sheet metal forming, assembly using screws, etc.).

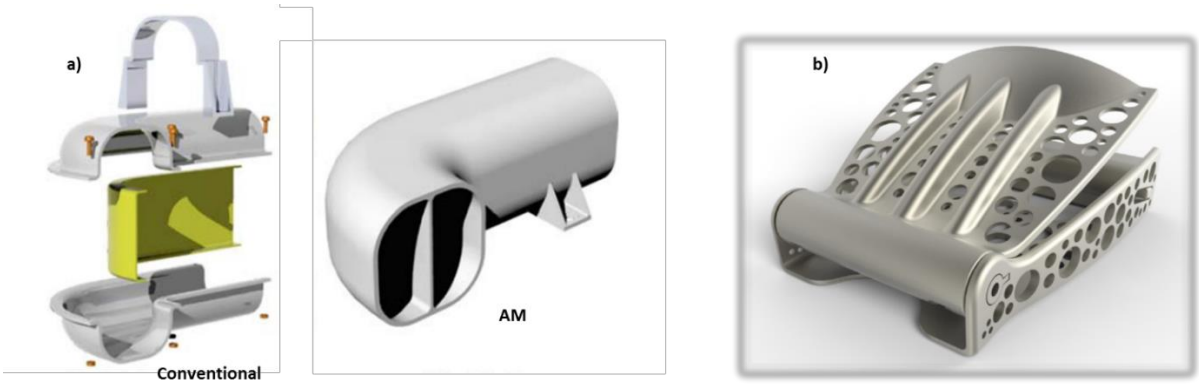

Figure 19: a) aircraft duct example; b) Seat buckle produced using DMLS technology (Adapted from Gibson et al. 2010, Dutta and Froes 2016).

In contrast, the approach on the right (Figure 19a, AM) illustrates the benefits of taking design for assembly guidelines to their extreme: the best way to reduce assembly difficulties and costs is to eliminate assembly operations altogether. The resulting design replaces 16 parts and fasteners with 1 part that exhibits integrated flow vanes and other performance enhancing features. However, this integrated design cannot be fabricated using conventional manufacturing techniques and is only manufacturable using AM (Gibson et al. 2010) .

If Computer Numerical Control (CNC) machine is being used to create a part directly in a single piece, then some geometric features cannot be fabricated. Since a machining tool must be carried in a spindle, there may be certain accessibility constraints or clashes preventing the tool from being located on the machining surface of a part. AM processes are not constrained in the same way and undercuts and internal features can be easily built without specific process planning. Certain parts cannot be fabricated by CNC unless they are broken up into components and reassembled at a later stage. AM machines essentially break up a complex, 3D problem into a series of simple 2D cross-sections with a nominal thickness. In this way, the connection of surfaces in 3D is removed and continuity is determined by how close the proximity of one cross-section is with an adjacent one. Such geometry can become extremely difficult to produce with CNC, even with 5-axis control or greater. Undercuts, enclosures, sharp internal corners and other features can all fail if these features are beyond a certain limit. The redesign of the seat buckle with lighter geometry (Figure 19b) is another interesting example of potential application of AM in aircraft industry. The part was produced using Direct Metal Laser Sintering (DMLS) *Ti6Al4V* alloy and their replacement permit to save 85g weight per buckle that represent a 55% of weight reduction. In an Airbus A380 with 853 seats will result in a possible weight saving of 72.5 kg.

According to the project sponsor, Technology Strategy Board, UK, this weight saving translates to 3.3 million liters of fuel savings over the life of the aircraft that is equivalent to US$3 million, while the cost of making all the buckles using DMLS is only US$256,000 (Gibson et al. 2010, Dutta and Froes 2016).

The AM can provide benefits during different steps of the whole life cycle of a product and hence, additively manufactured parts can outperform conventionally manufactured parts. In Figure 20 a comparison of total energy consumption is shown. During the production phase, significant benefits can be realized if a redesign of the whole system is undertaken or if expensive tools can be avoided. During the use phase, savings are due to enhanced part performance, energy savings, and reduced delivery times, whereas the end of life phase requires less energy input due to the reduced amount of material per part (Schmidt et al. 2017).

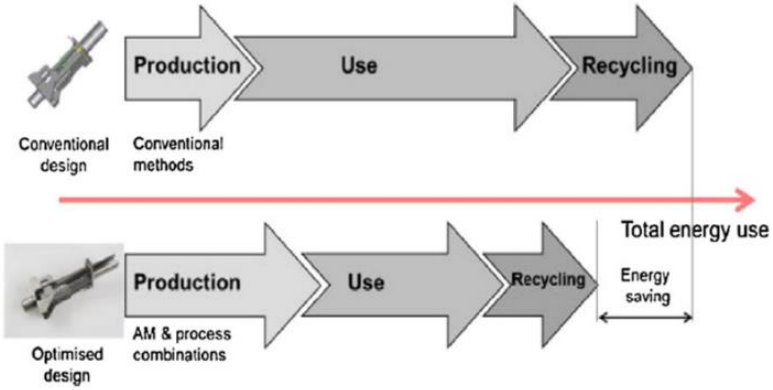

Figure 20: Life cycle of a product from production to the use-phase and recycling (Schmidt et al. 2017).

Focusing the attention on the production process effectiveness, in aerospace industry the "buy-to-fly" ratio is the most common index used. This index represents the mass of raw material needed per unit mass of the finished part.

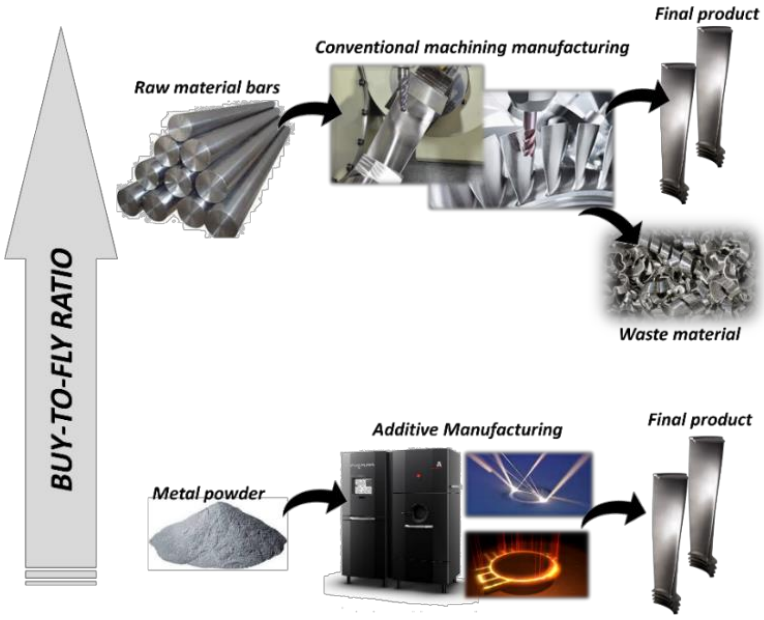

Figure 21: Effect of different manufacturing technologies on "buy-to-fly" ratio.

The conventional machining processes lead to produce finished parts but these processes yield a "buy-to-fly" ratio that ranges from 12:1 to 25:1 (Huang et al. 2016). This implies that up to 96% of the original material may be removed to end up as formed chips. The higher waste material rate is clearly evident and the time used to remove the material adds a significant cost to the process in terms of machining time,

tool life and raw material. This motivates the researchers and industries to develop more efficient and sustainable manufacturing processes. Therefore the use of AM techniques demonstrates to yield buy-to-fly ratios closer to 1:1 component reducing the waste material rate and energy required to remove the raw material (Figure 21) (Gebler et al. 2014).

Nevertheless, although the AM processes are able to produce components known as near-net-to-shape (the shape is very close to final product) and with very low waste material rate, the part accuracy and surface finish as well as the geometric tolerances are inferior to those obtained by machining processes. Consequently, the mechanical parts produced by AM usually do not satisfy the aerospace standards for finished components. Additionally, porosity, residual stresses and crack growth behavior associated with AM processes may affect the mechanical characteristics of the component if not used with post treatments (Gibson et al. 2010). In general, the metal parts produced by AM techniques are post-processed by machining operation in order to improve the surface quality. In general, the wrought titanium conventionally used to produce aerospace components usually shows an equiaxed microstructure. Instead, the additively manufactured products made by powder of titanium alloy are characterized by different microstructure, in detail acicular when produced by Electron Beam Melting (EBM) and martensitic when produced by DMLS. This latter is submitted to other thermo-mechanical processes as Hot Isostatic Pressing (HIP) to reduce the porosity and the voids inside the part, contributing also to transform martensite to lamellar α+β microstructure (Facchini et al. 2010). The AM parts always show different microstructure characterized by different features. Indeed, during AM, a defined volume element of the material is usually subjected to a complex thermal cycle. This thermal cycle involves rapid heating above melting temperature due to the absorption of the energy of the laser or electron, a rapid solidification of the molten material after the heat source has moved on, and numerous re-heating and re-cooling processes when the following layers are welded and the volume element is still exposed to heat. Consequently, the microstructure of the AM fabricated parts results of meta-stable or non equilibrium composition of the result phases (Figure 22). Concerning the dependence of yield strength on average grain size, AM specimens were found to follow the Hall-Petch relationship, as shown by Xu et al. 2015 and Al-Bermani et al. 2010 for lamellar α+β microstructures of *Ti6Al4V* manufactured with different AM techniques. Aboulkhair et al. 2015 reported the same for *AlSi10 Mg*. The AM process produces parts with a density usually of the 99.5%.

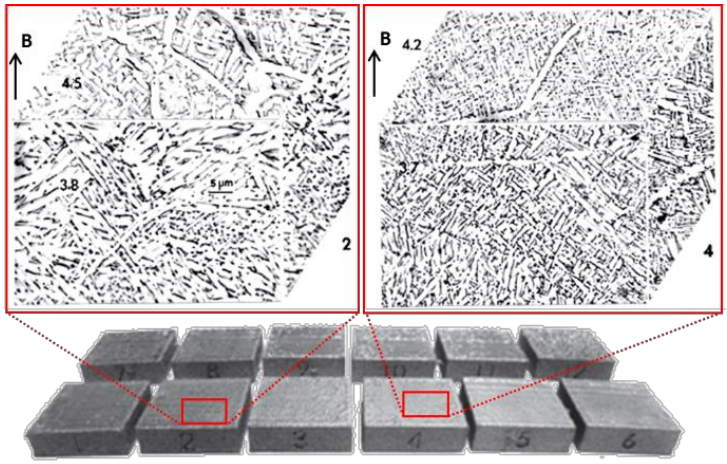

Figure 22: *Ti6Al4V* image compositions corresponding to test block sections. Numbers in horizontal and vertical reference planes at left are Vickers micro-indentation hardness in GPa. Numbers 2 and 4 at right refer to test block (focus offset) numbers. B indicates the build direction (Murr et al. 2012).

The pore distribution and their shape have a significant influence on mechanical properties. It has been observed that the elongation at break is significantly affected by pores. Moreover, the pores tend to be aligned in the plane of the powder layers facilitate the brittle fracture upon perpendicular tensile load. Therefore, anisotropic pore formation usually occurs and leads to anisotropic mechanical behavior of the part (Stichel et al. 2017, Herzog et al. 2017). Another significant aspect related to the mechanical properties is characterized by the surface roughness. The AM process uses powder as a building material inducing at least two kinds of surface defects, one is due to the steps caused by successive addition of layers and the other is due to the partially molten particles on surface (Vetterli et al. 2014). Greitemeier et al. 2016 studied the effect of surface roughness generated by EBM and DMLS, two powder bed fusion processes, on fatigue life of parts produced by *Ti6Al4V* powder. They affirmed that the processes produced parts that showed two types of roughness: primary roughness induced by solidification of the melt pool; secondary roughness induced by partly melted powder particles (Figure 23). They confirmed that the fatigue life of the AM parts not post-processes and characterized by poor surface roughness showed low fatigue performance. They compared their result with those obtained on post-processed AM part and these latter showed higher fatigue life, therefore the surface roughness plays an important role in determining the mechanical performance of an additively manufactured product. Therefore, it is clear that post-process techniques are necessary to improve the surface quality and the mechanical response of the produced parts.

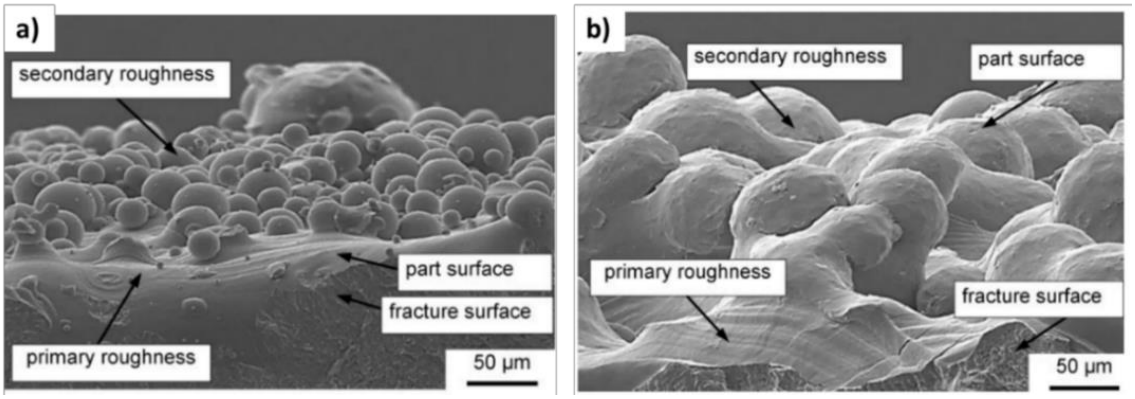

Figure 23: a) roughness surface obtained on AM titanium alloy; b) detailed zone of the surface (Greitemeier et al. 2016).

The authors produced another interesting study (Greitemeier et al. 2017) in which they also observed the influence of the heat treatment to the microstructure, surface roughness and defects and they linked the results to the fatigue life. They observed that the HIP treatment did not improve the fatigue life since the effect on the fatigue life of the decrease of inner defects was negligible compared to the poor surface roughness. On the other hand, in absence of poor roughness, the inner defects dominated the fatigue performance. To improve the fatigue performance it is necessary to reduce the defects and this result was obtained by HIP process. Similar results were reported by Kahlin et al. 2017 (Figure 24) affirming that the HIP post heat treatment gave no improvement in fatigue life for AM materials with rough as-built surface since poor surface roughness was mainly responsible of crack initiation than the internal defects.

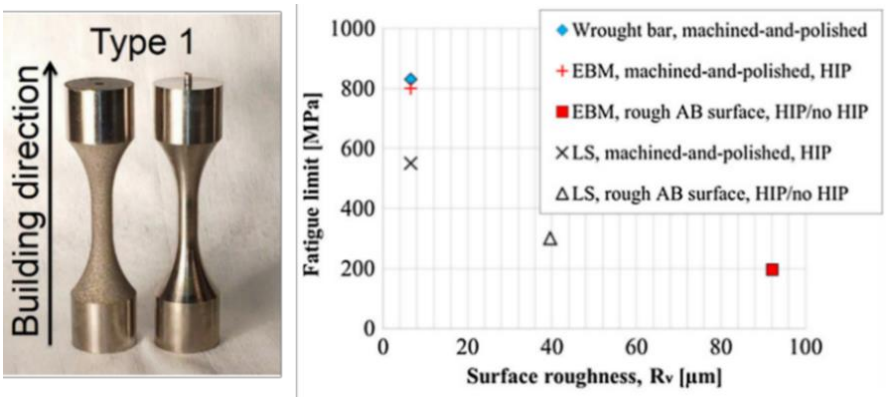

Figure 24: Fatigue limit (at 5 × 106 cycles) compared to surfaces roughness. R_v = maximum profile valley depth, AB = as-built (adapted by Kahlin et al. 2017).

Moreover, the heat treatment process induced coarsening phenomenon of the lamellar microstructure. The coarse lamellar microstructure decrease the fatigue performance (Leyens and Peters 2003), therefore it is necessary to develop a smart strategy to improve the surface roughness, decreasing the inner defect and avoiding the grain growth. Fatemi et al. 2017, evaluated the surface finish and heat treatment effect on the torsional fatigue behavior of *Ti6Al4V* produced via EBM. They observed that longer torsion fatigue lives were achieved for machined annealed AM specimens, as compared to as-built annealed specimens. The effectiveness of surface finish was mainly due to the removal of stress concentration effect of surface defects. For what concerning the mechanical properties, it is clear that the additively manufactured parts mechanical behavior is also different from the wrought one and this can affect the machinability of the titanium alloys. Bordin et al. 2014 made a comparison of machinability between *Ti6Al4V* wrought and EBM one in order to analyze the tool wear and the surface integrity. They observed crater wear formation on the tool used to machine the titanium EBM and its formation was favorited by higher feed rate. The *Ti6Al4V* EBM had higher hardness than the wrought one and even if showed an affected layers similar to those observed on the wrought, the hardness values were higher and tend to increase with higher feed rate values. However, the cutting speed range adopted were up to 80m/min and the technical information such as cutting forces and thermal gradients were not reported by the authors (Figure 25).

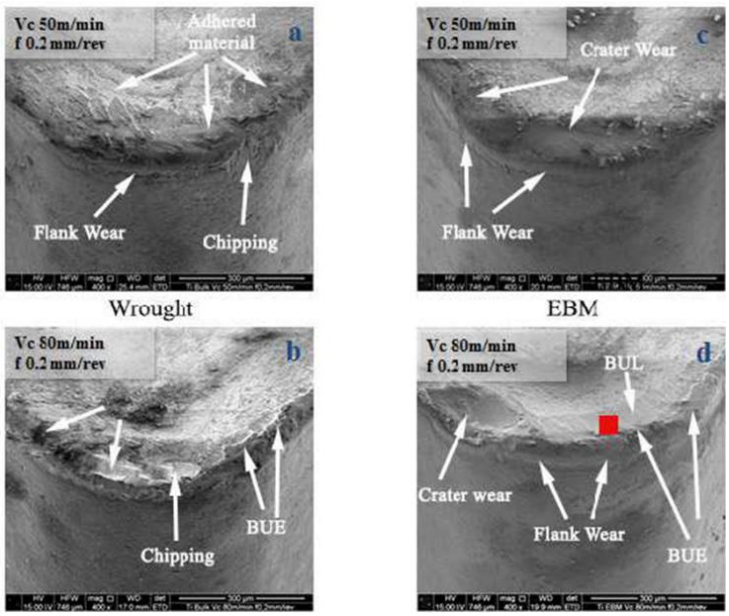

Figure 25: Tool wear analysis by SEM images of the tool used to machine a) and b) wrought titanium alloy, c) and d) AM titanium alloy (Bordin et al. 2014).

Subsequently, Bordin et al. 2015 investigated the effect of liquid nitrogen delivered into the cutting zone during machining of titanium bars produced via AM. They observed that the main tool wear mechanism during machining of *Ti6Al4V* produced by EBM was the adhesive both in dry and cryogenic turning. However, the liquid nitrogen led to a reduction of the thickness of the adhered layer on the rake face of the tool. The positive effects of the liquid nitrogen are evident also with the new class of metal material produced by AM technology. Another interesting study is reported by Conradie et al. 2017 in which they investigated the combination of an additive manufacturing process Selective Laser Melting (SLM) and machining (5-axis CNC milling) to produce a component. They evaluated if the aerospace surface quality requirements were achieved after the manufacturing process. The AM process permitted to reduce the production time of 21% compared with the conventional machining and the deviation of the geometrical shape was low and adequate to ensure no surface defects. However the roughness (R_a) was equal to 10μm while the aerospace requirement was 1.6μm confirming the need for final machining. After the machining process, the SLM parts finished by milling and the part obtained by only machining processes showed very low roughness, lower than 1μm. However, the tool wear when the SLM part were finished was drastically higher due to the martensitic microstructure and higher hardness of the SLM part.

Subsequently, the two components were fatigue tested and the wrought one showed better results in terms of fatigue life due to lower inner defects, better surface quality and reduced residual stresses. However, the authors did not carried out a detailed analysis to properly establish the machinability of the titanium alloy after AM process and the aim of the work is far from providing outcomes of the surface quality. It is clear that the mechanical properties, as well as the fatigue life, are affected by several aspects that need to be carefully considered during the design of mechanical or structural components and their production processes. Although the AM processes bring numerous advantages in producing high performance aircraft components, the produced parts show different characteristics than those produced by conventional materials. The literature analysis showed that even though the different type of microstructure (lamellar) are better than the equiaxed one in terms of strength and more complex geometry can be achieved by AM processes, the post-processing procedures are an important step into the production process that should not be neglected. A detailed study of the finishing or semi-finishing process on *Ti6Al4V* parts produced by different AM techniques taking into account the surface and subsurface features is not completely addressed by the researches available in literature. Moreover, in these studies fundamentals information about the machining process, such as the tool geometry or the cooling/lubricant effect are not investigated.

Therefore, because new production strategies to improve the surface parts are becoming one of the new focus of the future research activities, this Ph.D. thesis aims also to study the post-process operations necessary to enhance the surface and subsurface quality of the printed parts. Probably, different mechanical properties and metallurgical characteristics will affect the post-processing parameters conventionally suggested by the literature to finish the surface of the wrought material. This research activity will contribute to suggest an operative machining guideline (cutting parameters, tool and cooling strategy) to significantly improve the surface integrity of the additively manufactured titanium alloys parts that require post-processing treatments.

CHAPTER III

Machinability and surface integrity investigation of additive manufactured and wrought parts of *Ti6Al4V* alloy in semi-finishing conditions

This chapter provides a detailed description of the experimental work conducted on the *Ti6Al4V* titanium alloy and a comprehensive analysis of the obtained results. These latter are discussed and their variation is investigated through material changes study in order to understand the physical reasons that brought the different results. As stated in the earlier chapters, the *Ti6Al4V* is well known and employed in aerospace and aeronautic field due to its superior thermo-mechanical properties. The samples investigated were additively manufactured by two kinds of additive manufacturing processes, namely Electron Beam Melting (EBM) and Direct Metal Laser Sintering (DMLS). The AM samples were provided as rough bars, 3D printed having their symmetrical axis parallel to the beam direction (normal to the layers melting direction) with diameter and length equal to 40mm and 150mm, respectively. The same amount of samples were provided as wrought material, produced via conventional production techniques in order to compare the final results. The as-built cylindrical specimens showed an external surface characterized by high porosity due to the AM process. As reported by Wang et al. 2017 the roughness of the AM *Ti6Al4V* parts by EBM is between 40μm and 50μm depending on the scanning strategy with the electron beam. The DMLS technology permits to reach lower roughness than the one obtained by EBM. As reported by Longhitano et al. 2015, Mower and Long 2016, the surface roughness is between 9μm and 11μm, but the value is still outside the aerospace limits required. Although, the AM technology permits to drastically reduce the production time and the waste of materials compared to the machining conventional process, the surface quality does not satisfy the strictly requirements of roughness and tolerances for aerospace components (Conradie et al. 2017). Therefore, additional surface treatment techniques such as semi-finishing turning and finishing operations are still necessary to achieve the quality requirements. Consequently, the main goal of the experimental tests were to improve the surface integrity quality via semi-finishing machining operation, in detail external turning, using as process variables the cutting speed and feed-rate. The machinability of these new metal printed materials was investigated measuring the main fundamental process output data as cutting forces and temperature. The surface integrity of the machined bars was analyzed through several investigation techniques in order to characterize the surface (roughness) and particular material alterations in sub-surface (micro and nano-hardness, microstructure and phase changes). At the end of the outcomes analysis, the material produced via EBM showed the highest surface and sub-surface hardness, microstructural refinement and other interesting results. For this reason, in order to understand if further improvements in surface integrity could be achieved, additional tests delivering a cryogenic fluid (LN_2) during the machining process were carried out on *Ti6Al4V* EBM bars. Several researches available in literature described the positive effects of the cryogenic fluids applied during the machining operations. Indeed, the tool life is tremendously increased due to the combination of embrittlement of the material and cooling of the cutting zone. Furthermore, the very low temperatures on the fresh-machined surface prevent the dynamic recrystallization or recovery, preserving the work hardening effect provoked by the cutting tool. Consequently, not only the tool but also the machined material benefits of the positive effects of the LN_2 when delivered into the cutting zone during the machining operations.

3.1 Experimental work – semi-finishing operations on *Ti6Al4V* EBM, DMLS and wrought

The experimental machining tests were performed under dry conditions on the EBM, DMLS and wrought specimens and under cryogenic conditions on the EBM specimens. The workpieces were cylindrical bars of 40mm diameter and 150mm length. The material was supplied in the as-built condition (as produced by the metal 3D printer). In detail, the EBM material was used without any post-processing or heat treatment according to the industrial standard, while the DMLS one, due to the martensitic microstructure was heat treated by the supplier in order to achieve a stable microstructure. Moreover, to compare and understand the difference regarding the machinability between the additively manufactured materials and the conventionally produced, some cylindrical bars of Ti alloys produced via standard processes (ASTM B348 thermo-mechanical treatments procedure) (from now on it will be referred as wrought material) were machined using the same cutting parameters and set-up. The mechanical properties of the initial materials are given in Table 3.

Table 3: Mechanical properties of *Ti6Al4V* produced via different production processes (Facchini et al. 2010, Bruschi et al. 2016).

Material	Elastic modulus [GPa]	Yield Stress [MPa]	Ultimate Stress [MPa]	Breaking elongation [%]
Ti6Al4V EBM	120+/-5	950	1020	9.1+/-0.4
Ti6Al4V DMLS	117+/-1	870	990	11.0+/-0.5
Ti6Al4V Wrought	104+/-2	790	870	18.1+/-0.8

Each experiment consisted of an external turning operation and each test lasted almost 25 seconds in order to achieve the cutting temperatures and forces steady state conditions. The turning tests were performed on a Mori Seiki NL 1500 CNC lathe, equipped with a system aimed at supplying the LN_2 directly into the cutting zone (Figure 26). The LN_2 was carried through a vacuum insulated pipe and a system composed by two cooper nozzles with an internal diameter of 0.9mm (Figure 26b) that directed the flow towards the tool rake face and the primary cutting edge with an inclination of 45°, the pressure of the coolant was equal to 12 bar.

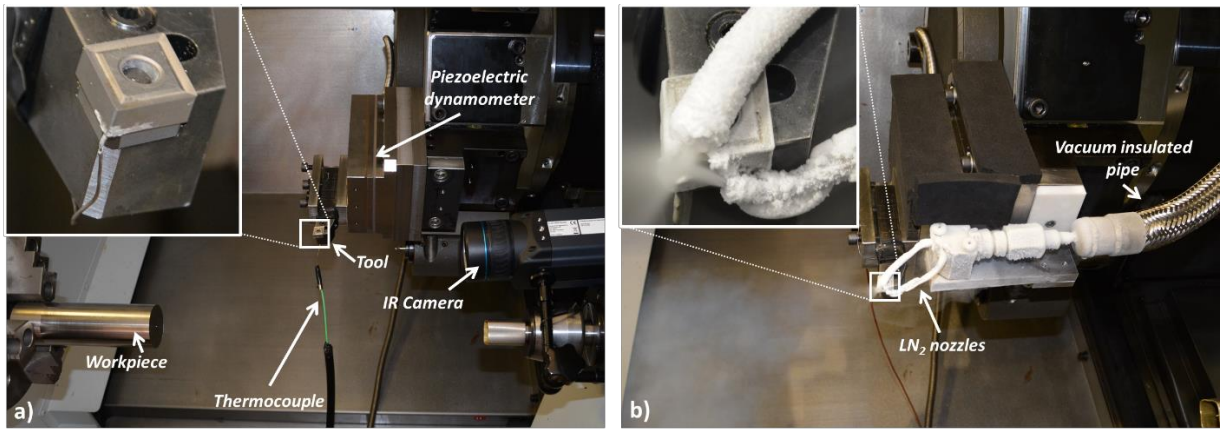

Figure 26: a) Experimental set-up used to perform machining test under dry conditions; b) Cryogenic delivery system detail.

The utilized cutting tool inserts were uncoated carbide, Sandvik Coromant® CNMG 120404-23 H13A, mounted on a PCLNR/L 2020k12 tool holder supplied by the same manufacturer.

The effective cutting angles and the tools geometry were measured with an optical profilometer (Sensofar Plu-Neox) by scanning the tool insert fixed on the tool holder. At the end of the procedure, the effective cutting angles, namely rake and clearance angles were identified and they were equal to 7° and 8° respectively. During each cutting test, a fresh cutting edge was adopted in order to avoid the tool wear effect on the results. Moreover, for each test the depth of cut (a_p) was kept constant and equal to 0.2mm according with the suggestion of the tool makers to perform semi-finishing machining operations.

3.1.1 Design of Experiments and experimental set-up

To understand the effect of each cutting parameters on the overall quality of the machined part, the tests were carried out following a Design of Experiments (DOE). An experimental plan of 2x3 for each material (*Ti6Al4V* EBM, *Ti6Al4V* DMLS, *Ti6Al4V* Wrought) was adopted. In detail, there is qualitative level that is referred to the cooling conditions (dry) and two quantitative levels that are related to the feed rate (0.1 mm/rev and 0.2 mm/rev). The last part of the experimental plan is referred to one factor, the cutting speed, characterized by three levels (50 m/min, 80 m/min and 110 m/min). The total experimental tests conducted with each material is equal to 6, but this number was increased to 12 to guarantee the statistical repeatability of the results. Moreover, as reported above, due to the interesting results showed by the *Ti6Al4V* EBM machined parts, 12 tests under cryogenic conditions were additionally performed only on the EBM material in order to assess possible further enhancement in terms of surface integrity. In Table 4 is reported the experimental plan (DOE) defined for this research activity.

Table 4: Design of Experiments (24 full factorial experimental plan).

Material			Test n°	V_c [m/min]	f [mm/rev]	Cooling condition
Ti6Al4V Wrought	*Ti6Al4V* DMLS	*Ti6Al4V* EBM	**1**	50	0.1	Dry / Cryogenic (EBM)
			2	80	0.1	Dry / Cryogenic (EBM)
			3	110	0.1	Dry / Cryogenic (EBM)
			4	50	0.2	Dry / Cryogenic (EBM)
			5	80	0.2	Dry / Cryogenic (EBM)
			6	110	0.2	Dry / Cryogenic (EBM)

Once defined the machining parameters and strategy, the material selection of the tools was carried out following the tool supplier's guidelines. Regarding the tool type used during the tests, the CNMG is suggested by Sandvik Coromant for semi-finish to medium turning operations. The tool made in Tungsten Carbide (WC) is particularly used to machine difficult-to-cut materials as titanium. Its features and benefits are that permit to achieve a good chip control, long length of cut and it is able to keep sharp edge line for long time in according with the cutting parameters suggested. These characteristics make this tool one of the most suitable for the experimental tests planned. The tool holder was selected once the tool was chosen. Finally, the workpiece geometry was designed in order to achieve at least 20 seconds of machining test for the most critical cutting parameters selected (higher cutting speed and feed rate). In these conditions, the possibility to reach the thermo-mechanical steady state was guaranteed.

3.1.2 Cutting forces

The components of the cutting forces (feed F_a and main component F_z), represented in Figure 27, were acquired by a KISTLER type 9257 B three components piezoelectric dynamometer mounted on the lathe revolver (Figure 26a). In Figure 28 and Figure 29 are reported the two cutting components measured during the tests under dry conditions depending on the cutting speed, feed rate and the machined material.

It is worth pointing out that the cutting forces were acquired during all the machining operations and the reported results represent the average value of the steady-state signal, obtained as reported in Figure 27. The cutting force signal acquired as well as the average value evaluated were processed by a spreadsheet program.

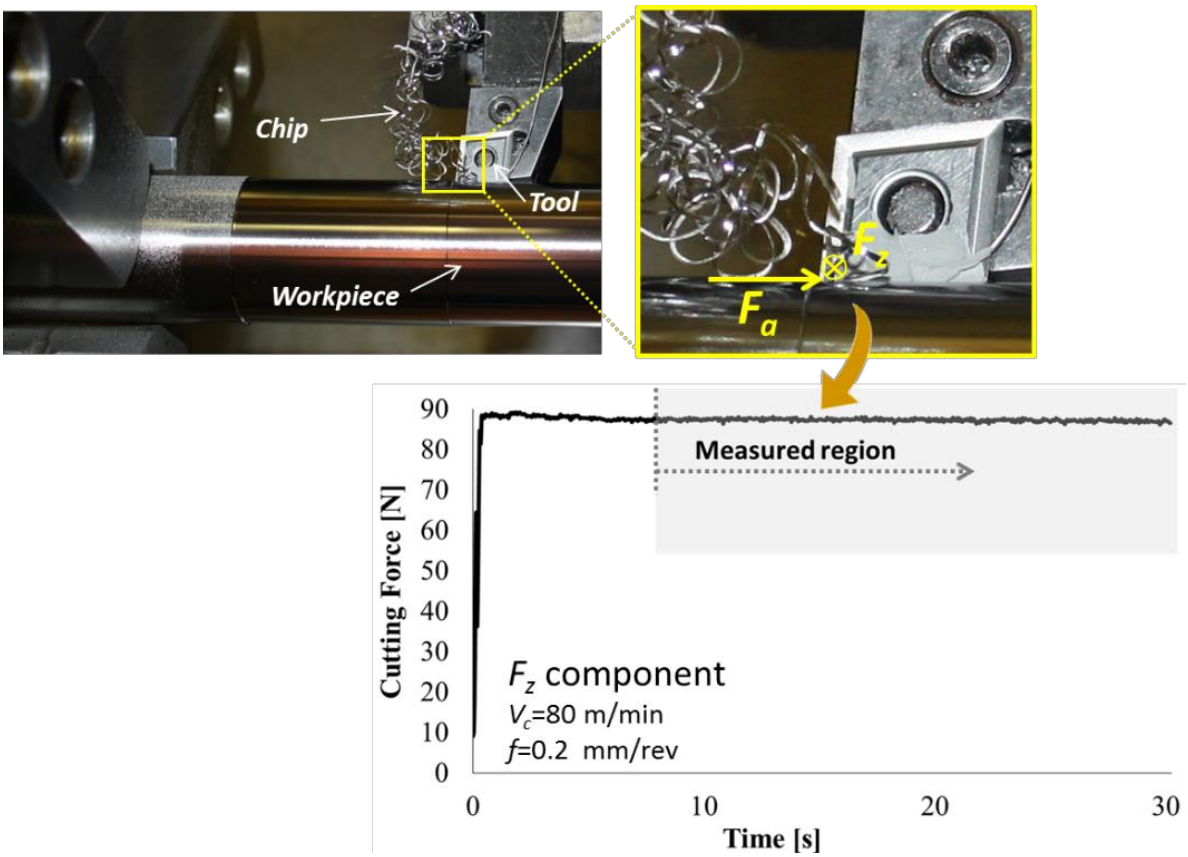

Figure 27: Elaboration of the main cutting force (F_z) signal acquired by the piezoelectric dynamometer during dry turning operation on the titanium bars (V_c 80m/min, f=0.2mm/rev, a_p=0.2mm, *Ti6Al4V* DMLS).

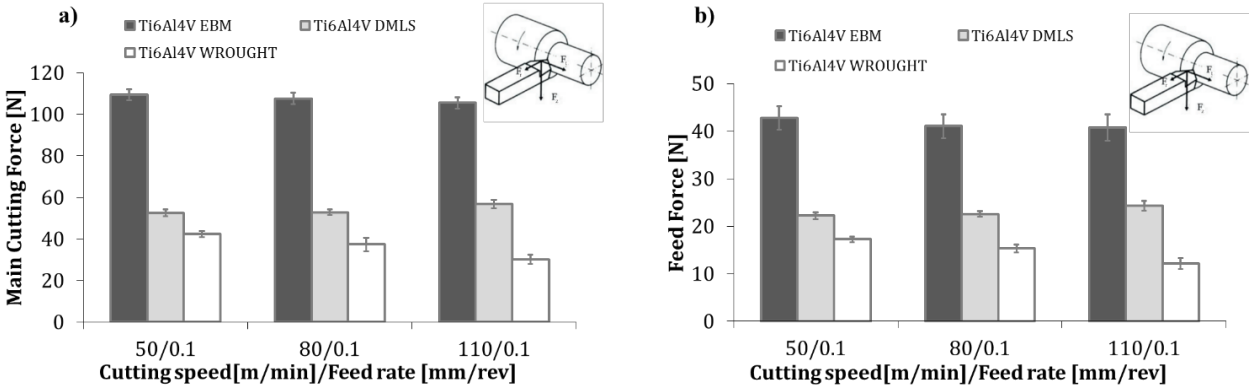

Figure 28: Main cutting forces a) and Feed forces b) at varying cutting speed and feed rate equal to 0.1mm/rev (dry conditions).

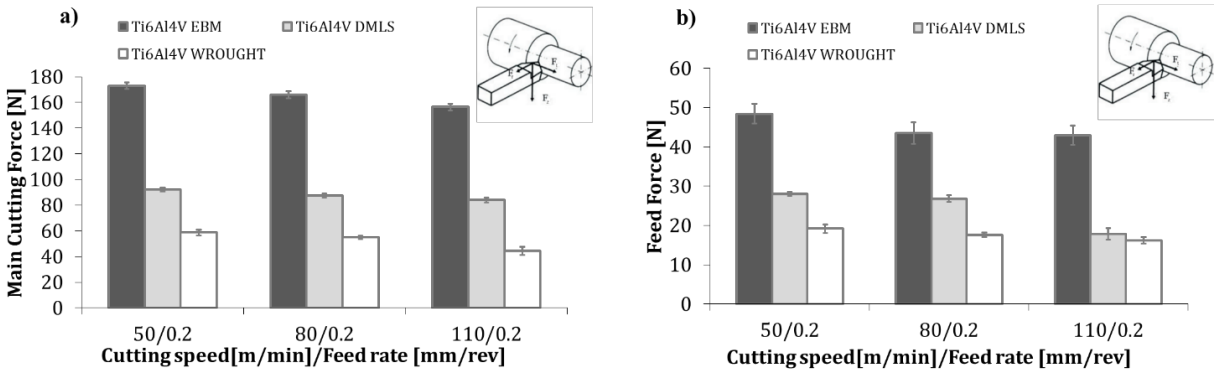

Figure 29: Main cutting forces a) and Feed forces b) at varying cutting speed and feed rate equal to 0.2mm/rev (dry conditions).

In general, for both the components of the cutting force, a progressive decrement was observed when the cutting speed increased for all the tested materials (Figure 28 and Figure 29). An exception is showed by the force components (main and feed cutting component) measured during the machining test of the *Ti6Al4V* DMLS at feed rate equal to 0.1 mm/rev, indeed, the trend increased (Figure 30). Generally, the decreasing trend of the cutting forces was due to the thermal softening of the *Ti6Al4V* alloy that was provoked by the major heat generated into the cutting zone when increased the cutting speed (Davim et al. 2014, Takeyama et al. 1963). This is certainly visible in Figure 28a and Figure 28b with the materials Ti6Al4V wrought and EBM and in Figure 29a and Figure 29b with all the three materials, but the *Ti6Al4V* DMLS machined with a feed rate equal to 0.1 mm/rev (Figure 30), showed an inverse trend when the cutting speed increased. This result shows that the material behavior of the *Ti6Al4V* DMLS is clearly different when it is machined at low feed rate (0.1mm/rev). This phenomenon was normally attributed to the predominant strain-rate hardening behavior because of lower thermal gradient. On the contrary, at higher feed rate (0.2mm/rev), the thermal softening phenomenon predominated on the strain-rate hardening. (Sun et al. 2009).

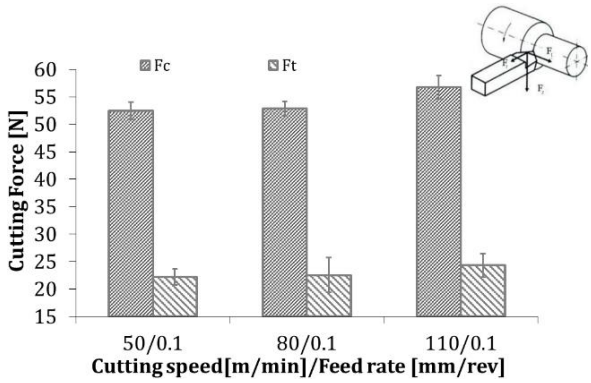

Figure 30: Main and feed cutting forces obtained during machining of *Ti6Al4V* DMLS at feed rate 0.1mm/rev (dry conditions).

It is also important to highlight the role played by the mechanical properties of the material. Despite the machined material was chemically the same, the different production processes led certainly to produce parts that are very different from the metallurgical point of view (microstructure, hardness etc.). Taking into account Table 3, the yield and ultimate stress among the three material were different. These diversities in mechanical properties are reflected in the differences between the cutting force components. Indeed, the *Ti6Al4V* EBM has the highest values of yield and ultimate strength, consequently it is harder to machine compared with the *Ti6Al4V* DMLS and the wrought one; therefore, the forces were the highest for each conditions.

From the machinability point of view, it is important to take into account the mechanical properties of the material produced by different production processes, such as additive manufacturing, because although the working material is the same, the mechanical response is completely different as shown by Figure 28, Figure 29 and Figure 30. Considering the results of the cutting forces acquired during machining tests on *Ti6Al4V* EBM, the machinability of this material under cryogenic conditions was also investigated to check possible benefits due to the presence of LN_2. The cutting parameters were kept constant in order to perform comparisons with the results obtained during dry operations (Figure 31).

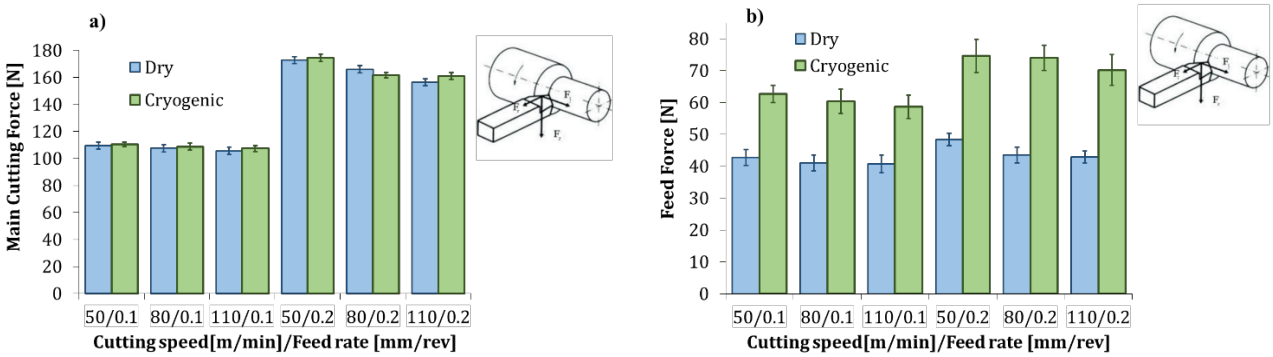

Figure 31: Main cutting forces a) and Feed forces b) at varying cutting speed, feed rate and cooling conditions.

As showed by Figure 31a, the application of cryogenic fluid during machining of *Ti6Al4V* EBM did not provide any obvious positive benefits in terms of cutting force reductions as well as power consumption. The main cutting force was slightly higher when liquid nitrogen was delivered into the cutting zone, only a small reduction was observed with cutting speed of 80m/min and feed rate of 0.2mm/rev. The difference between the cutting forces under dry and cryogenic conditions became more evident observing Figure 31b. Both the cutting components showed a decreasing trend when the cutting speed was increased. Hong et al. 2001 and Bermingham et al. 2011 also observed higher cutting forces during cryogenic machining compared with the ones measured without any coolant applied. The difference in machinability under dry and cryogenic conditions can be explained considering the ductility of the material coupled with the heat generated due to the plastic deformation. It is well known that *Ti6Al4V* is characterized by poor thermal conductivity compared to other metal alloys, as a consequence higher temperature is concentrated into the cutting zone where high plastic deformation rate is generated. Consequently, if no coolants are applied, higher temperature is reached at the workpiece-tool interface making the material softer. On the contrary, when LN_2 is applied into the cutting zone, the temperature drastically decreases and the surrounded surface of the machined material is frozen (Figure 32a and Figure 32b).

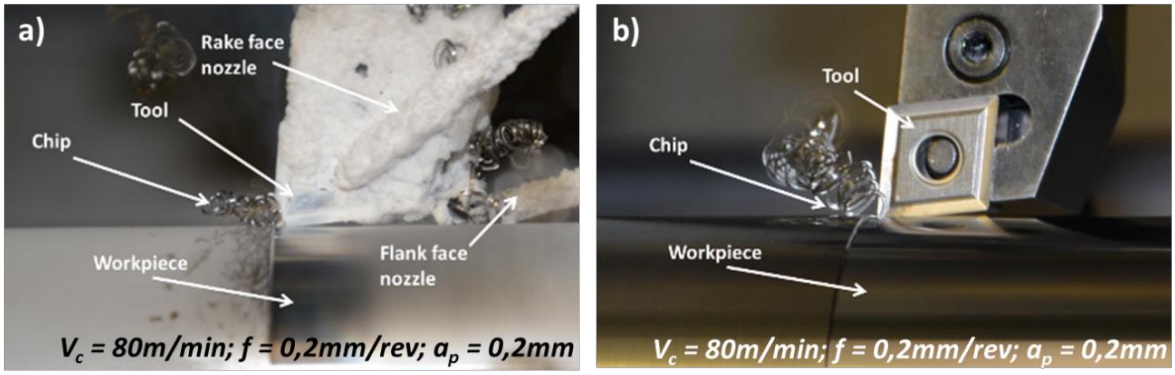

Figure 32: a) Cryogenic machining; b) dry machining.

As a result, the plasticity of the alloy under these working conditions is outstandingly reduced as well as the strain-thermal softening effect, leading to a more brittle behavior and thus harder material that is more difficult to machine (strain-hardening dominant effect). This working condition led to an increasing of the cutting forces at very low temperatures. Krämer et al. 2014 observed similar results during turning of *Ti6Al4V* wrought delivering LN_2.

3.1.3 Temperature analysis

The temperature gradients were evaluated by an infrared thermo-camera FLIR A6000-series. The camera was fixed on a rigid bracket on the tool-holder. This solution permitted to keep the focus directly on the cutting zone following the movement of the tool during the entire duration of each test (Figure 26a). The workpiece material emissivity (equal to 0.46) was calibrated comparing the measurements carried out with a thermocouple and with the infrared camera when a dummy sample was warmed on a plate at fixed steps of temperature. As previously explained with the cutting forces, the signal acquired by infrared camera representative of the thermal gradient into the cutting zone was plotted and the average value was computed considering the steady-state region (Figure 33). In Figure 34a and Figure 34b are reported the averaged maximum temperature measured during the tests under dry conditions depending on the cutting speed, feed rate and the machined material. Generally, it is possible to see that the increase of the cutting speed led to an increasing of the temperature into the cutting zone. The maximum temperature was significantly affected by the value of the feed rate when the *Ti6Al4V* EBM was machined. Although, a variation of the feed rate led to temperature changes also considering the other two materials, namely the DMLS and the wrought one, the variation was not as evident as in the EBM material. Moreover, from the physical point of view, the lower temperatures when machining EBM were related to the more brittle behavior of the material if compared with the DMLS and wrought. Indeed, the wrought and DMLS have lower value of yield stress, ultimate stress and young modulus suggesting a higher capability to accumulate plastic deformation before reaching failure.

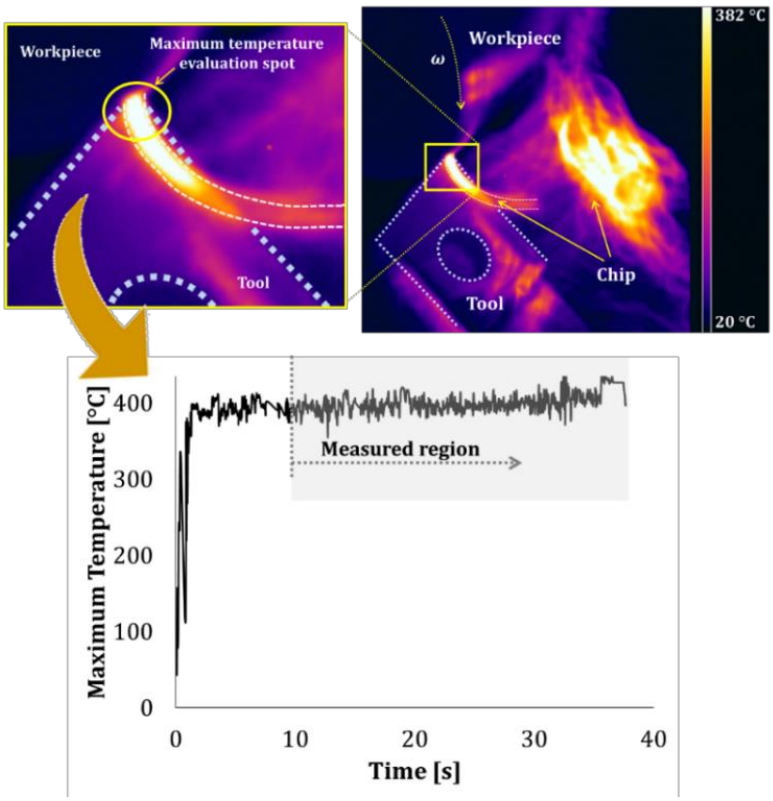

Figure 33: Thermal gradient signal acquired by the infrared camera during turning operation on the titanium bars and elaborated (V_c =110m/min, f=0.1mm/rev, a_p=0.2mm, *Ti6Al4V* DMLS).

Therefore, the higher temperature showed when machining *Ti6Al4V* DMLS and wrought was due to the more plastic deformation accumulated and dissipated as heat. Consequently, the higher temperature led to more thermal softening effect and thus lower cutting forces as showed previously by Figure 28 and Figure 29. Finally, it is possible to assert that the material plays an important key role also for what concern the thermal gradient, because it affects not only the surface and subsurface quality of the machined parts but also the tool life and the related wear rate and mechanisms (Sartori et al. 2016, Bordin et al. 2015). As previously showed with the cutting forces, also the temperature were acquired during cryogenic machining of *Ti6Al4V* EBM (Figure 35) and elaborated as suggested by Figure 33.

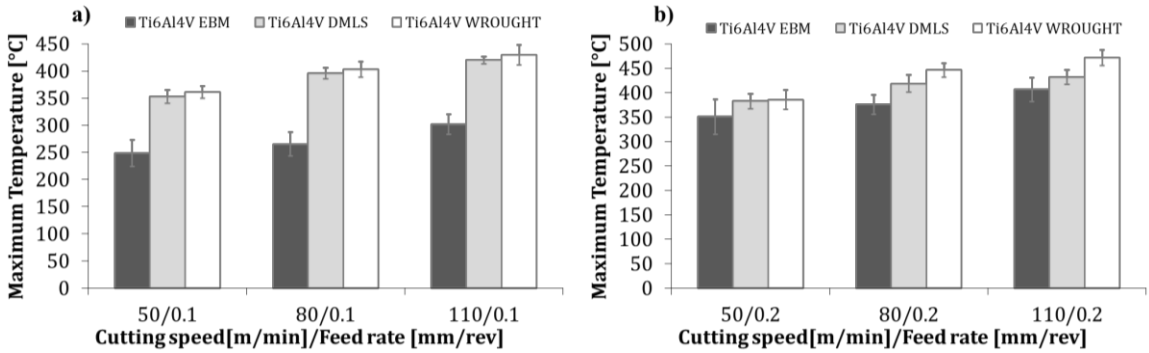

Figure 34: Average value of the maximum temperature at varying cutting speed, feed rate and material machined under dry conditions; a) 0.1mm/rev; b) 0.2mm/rev.

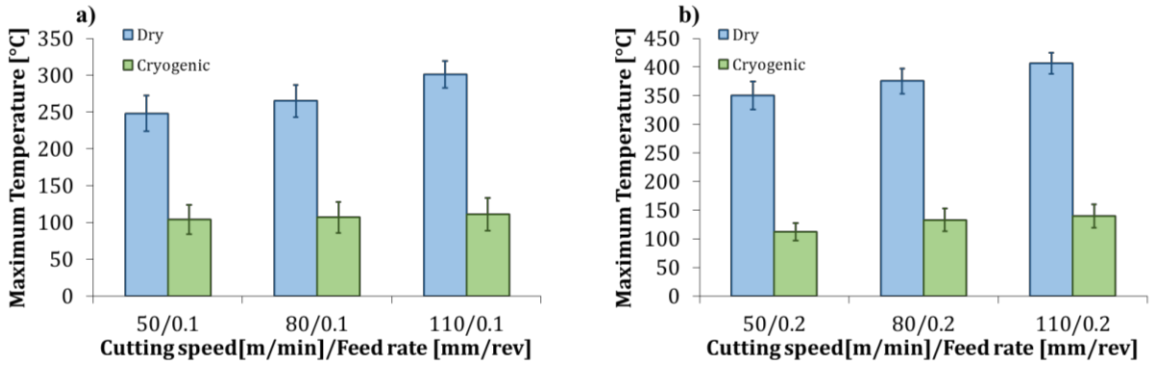

Figure 35: Comparison of average maximum temperature acquired under dry and cryogenic machining of *Ti6Al4V* EBM; a) 0.1mm/rev; b) 0.2mm/rev.

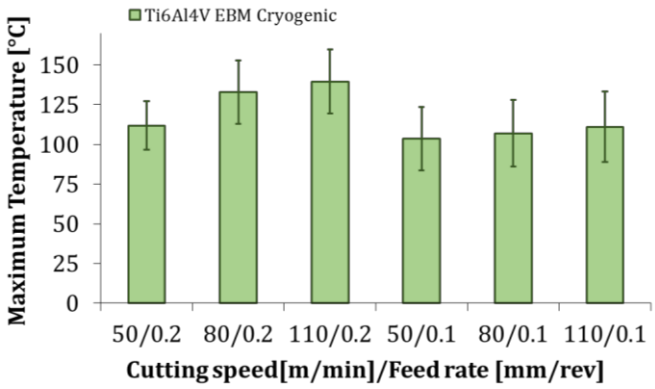

Figure 36: Average maximum temperature acquired under cryogenic machining of *Ti6Al4V* EBM at varying cutting speed and feed rate.

As previously mentioned, in machining difficult-to-cut materials, where the thermal conductivity of the workpiece material is very low, the generated heat at the cutting zone cannot be effectively dissipated through the workpiece or chips. This would result in very high-localized temperatures at the cutting zone and the tool rake face. The high temperature developed under dry machining, as reported in Figure 35a and Figure 35b, compared with the results obtained under cryogenic conditions suggested that the concentration of the heat into the cutting zone was not properly evacuated by the chip, thus the LN_2 was the main protagonist in the cooling effect. Therefore, the LN_2 as a coolant in machining operations can drastically reduce the temperature during semi-finishing machining operations even with additively manufactured materials (Figure 36). As also observed by Sun et al. 2010, the delivering of the cryogenic fluids during machining of *Ti6Al4V* led to lower cutting temperatures into the cutting zone compared with the machining operations in dry conditions and the cutting forces measured under cryogenic conditions were higher than the ones measured under dry conditions. Moreover, Sartori et al. 2017 analytically calculated the cooling capacity as thermal power of the cryogenic coolant and they discovered that the LN_2, compared with other coolant, has the maximum cooling capacity leading to lower thermal gradients into the cutting zone during machining of Ti alloy. These results are in agreements with those obtained in this study confirming that the material shows low ductility due to freezing effect (lower temperature into the cutting zone) of LN_2 and consequently it is more difficult to machine (higher cutting forces). These results were also observed by other researchers, testing the cooling effect of liquid nitrogen during machining of others materials (Ambrosi et al. 2014).

3.2 Surface Integrity analysis of *Ti6Al4V* EBM, DMLS and wrought

Generally, in manufacturing context the surface can be defined as a border between a machined workpiece and its environment. It describes the state and attributes of a machined surface and its relationship to functional performance. In this Ph.D. thesis, the surface integrity of different machined parts has been analyzed taking into account the main two aspects in which commonly the surface integrity is divided, i.e. external topography of surface and metallurgy of the internal sub-surface layers (Davim 2010, Laperrière 2014). In general, from an industrial perspective, surface integrity assumes the greatest importance in relation to highly stressed components, especially where safety is paramount, but also with high cost items. With dynamic loading and cyclical stresses, the fatigue characteristics are a prime consideration in determining component failure. Consequently, surface integrity issues are to the fore in aerospace applications, but also for biomedical implants and automotive engine, transmission and wheel component etc. In detail, the material used to produce aerospace engine parts and wing structures which are under constant development to be optimized, are understandably the main focus of machinability and surface integrity research (Jawahir et al. 2011).

3.2.1 Topography - Surface Roughness

Surface topography and texture are the foremost characteristics among the surface integrity magnitudes and properties imparted by the tools used in the processes, machining mostly, and especially their finishing versions. Generally, for the specification of surface topography, a multitude of different roughness parameters have been defined: the most common being the mean roughness R_a (Equation 1) (Figure 37), the average peak-to-valley height or roughness depth R_z and the maximum roughness depth R_{max}. In this Ph.D. thesis, the R_a was measured and taken into account in order to estimate the state of surface topography depending on the cutting parameters, material and cooling conditions. The mean roughness R_a is able to detect gradual changes in surface topography, e.g., as a result of tool wear. It is calculated as suggested by Equation (DIN EN ISO 4287).

$$R_a = \frac{1}{l}\int_0^l |Z(x)|\, dx \quad (1)$$

Where *l* means the evaluated fraction of the measured length and *Z* is the distance of the profile from the centerline within the measured length.

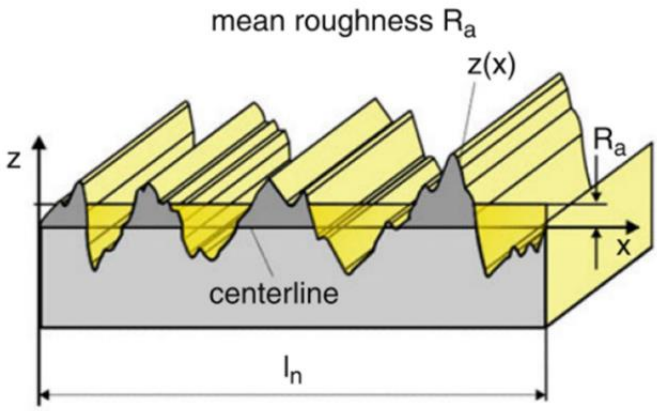

Figure 37: Topographic parameter R_a (Mean Roughness).

To perform the surface topography measurements, a surface profilometer (ConScan Surface Profilometer Anton-Paar) was employed (Figure 38). The concept behind confocal profilometry involves the use of the chromatic aberration principle. By directing a white light source through a filtering optical component towards a sample surface, it is possible to use the chromatic aberration to separate the light with a dispersive lens into its component wavelengths, each of which corresponds to a different z-coordinate in the optical axis. Therefore, the visible light spectrum is now encoded with z-coordinate data as a function of varying focal distance from the end of the lens. As the focus point of each wavelength is represented at a different distance from the lens, the returning light waves will be different according to the height characteristics of a specific region of the sample. Therefore, the returning spectrum at any given point can be regarded as the spectrophotometric signature of z-height, where strong spectral response is indicative of a defined distance away from the lens at a given focal point (Randall 2010).

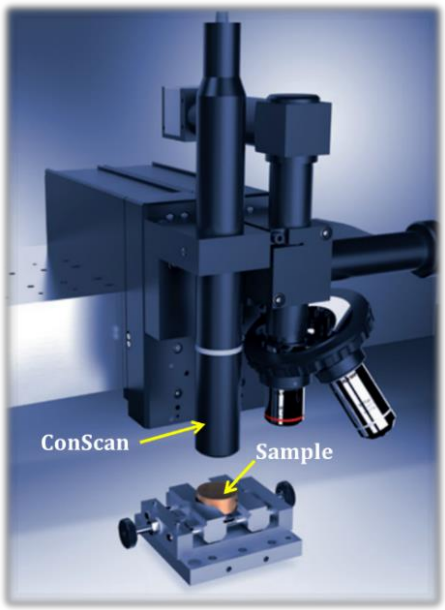

Figure 38: ConScan Surface Profilometer (Anton-Paar) employed to evaluate the surface roughness.

The obtained results for all the materials machined at varying cutting speed and feed rate are reported in Figure 39a and Figure 39b. Very smooth surface with low roughness values, always lower than 1μm were obtained when the lowest feed rate (0.1mm/rev) was set during the tests. The *Ti6Al4V* DMLS and wrought showed almost the same value of roughness at varying cutting speed without the increasing or decreasing of the values. In that case, at low feed rate, lower or equal than 0.1mm/rev the cutting speed did not affect the surface roughness. The *Ti6Al4V* EBM showed higher surface roughness than the *Ti6Al4V* DMLS and the wrought one. The reason is due to the higher mechanical properties; in fact, the material showed more brittle behavior and consequently less ductility. Higher surface roughness with higher value of feed rate (0.2mm/rev) was measured (Figure 39b). The R_a value measured on the three materials was always higher than 1μm and this resulted far from the aerospace requirements (generally, very smooth surface with roughness lower than 1μm are required). With higher feed rate (0.2mm/rev) the roughness showed a trend depending on the cutting speed. In fact, as showed by Figure 39b, as the cutting speed increased the roughness increased as well for all the machine materials. Moreover, the *Ti6Al4V* EBM showed similar roughness value in relation with the *Ti6Al4V* DMLS and wrought. In general, it is possible to affirm that better smoothed surface are produced with low feed rate under dry machining conditions. Similar results on different material were reported in the research works of Bordin et al. 2014 (CrCoMo alloy additively manufactured) and Sartori et al. 2016 (*Ti6Al4V* DMLS). Figure 40a and Figure 40b show the surface roughness of the *Ti6Al4V* EBM machined under cryogenic conditions and the measured results are compared with those obtained from the dry machined bars. It is clear that the LN_2 has a negative effect regarding the surface roughness due to its ability to reduce the ductility of the material that shows a brittle behavior. These results can be justified by the lower temperature measured into the cutting zone during cryogenic machining. The temperature reduction due to the LN_2 application is between the 60% and 70% compared with the data registered during the dry tests. Taking into account that for each cutting test a new fresh tool was employed (the tool wear did not affect the tests) and the duration of each test was the same, the higher roughness value measured on the cryogenic machined parts was only due to the embrittlement of the material. This latter affects the material removal process leading to low surface roughness. Grzesik et al. 2012 also observed higher surface roughness during machining and burnishing of precooled hardened AISI 5140 steel concluding that the cryogenic treatments increased the hardness and the strength of the material affecting the material behavior under machining and then the resulting surface roughness.

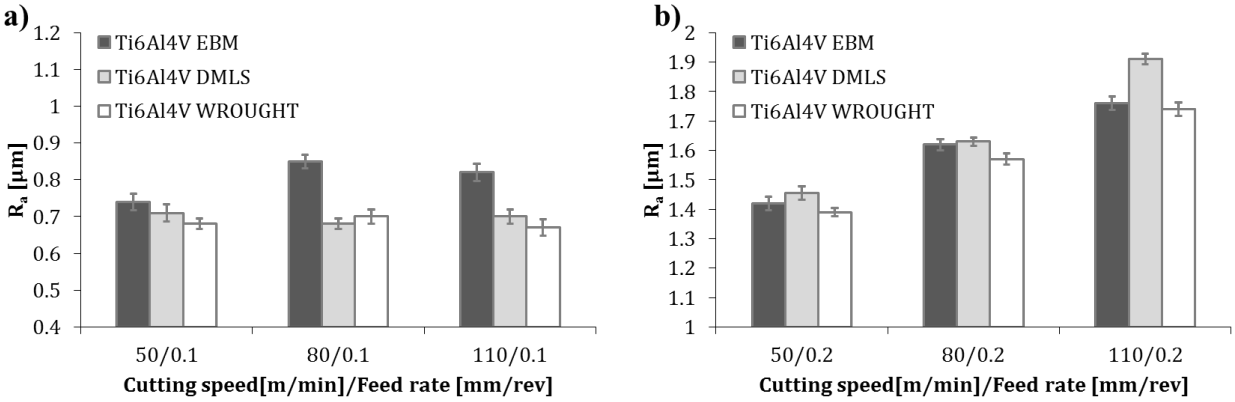

Figure 39: Roughness R_a measured at varying cutting speed and feed rate for different tested materials.

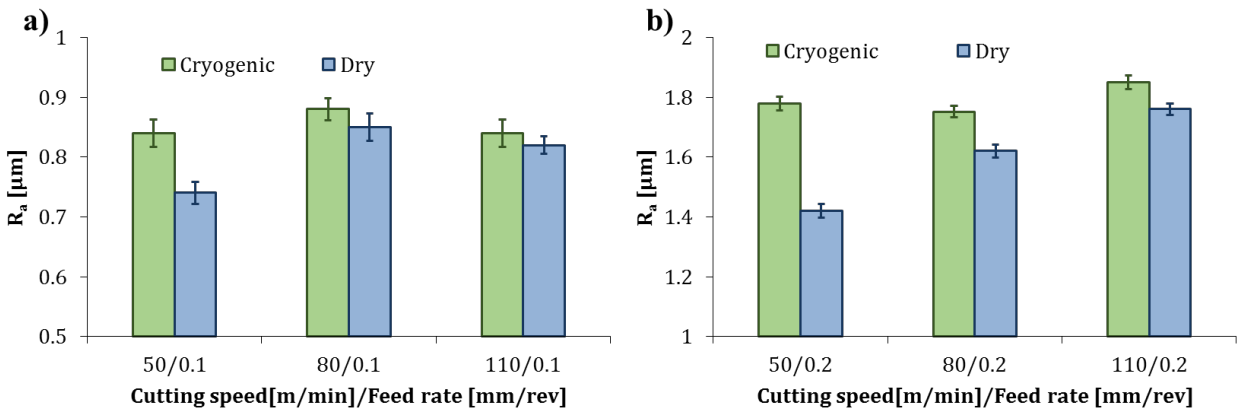

Figure 40: Roughness R_a measured on *Ti6Al4V* EBM machined under dry and cryogenic conditions at varying cutting speed and feed rate.

3.2.2 Affected Layers and microstructure deformation

The microstructure analysis was conducted collecting some samples close to the surfaces of the machined samples (Figure 41). Each sample was embedded in phenolic resin (MultiFast provided by Struers). Subsequently, the samples were grinded and polished following the procedure reported in Table 5.

Table 5: Grinding and polishing procedure to prepare the *Ti6Al4V* samples to metallographic analysis.

Type of material	Fluid	Time [s]	Force [N]
SiC Foil 180	Water	230	10
SiC Foil 320	Water	70	10
SiC Foil 500	Water	70	5
SiC Foil 1200	Water	120	5
SiC Foil 2000	Water	90	5
MD-Largo	DiaPro Largo 9µm	360	5
MD-Dac	DiaPro Dac 3µm	360	5
MD-Chem	OP-S 0.04µm	180	5

After the polishing step, the samples were chemically treated by etchant (Kroll's reagent: 1-3mL HF, 2-6mL HNO_3, 1000 mL of H_2O) (Gammon et al. 2004) in order to show the microstructure under light optical microscope (OM) (LEICA DFC 320). Several images of the machined parts cross sections (Figure 41) were acquired via OM and the dimension of the affected layers (several plastic deformed layer) and grain size changes (lamellae thickness or average diameter of the equiaxial grains) were measured. In Figure 42a, Figure 42c and Figure 46 are represented the metallurgical parameters measured that are quantitatively showed from Figure 43 to Figure 47 (average value of the Affected Layer Thickness (AL), the Plastic Deformation (PD) of the bended lamellae) and in Figure 53 and Figure 54 (the Degree of the Grain Reduction (DGR)).

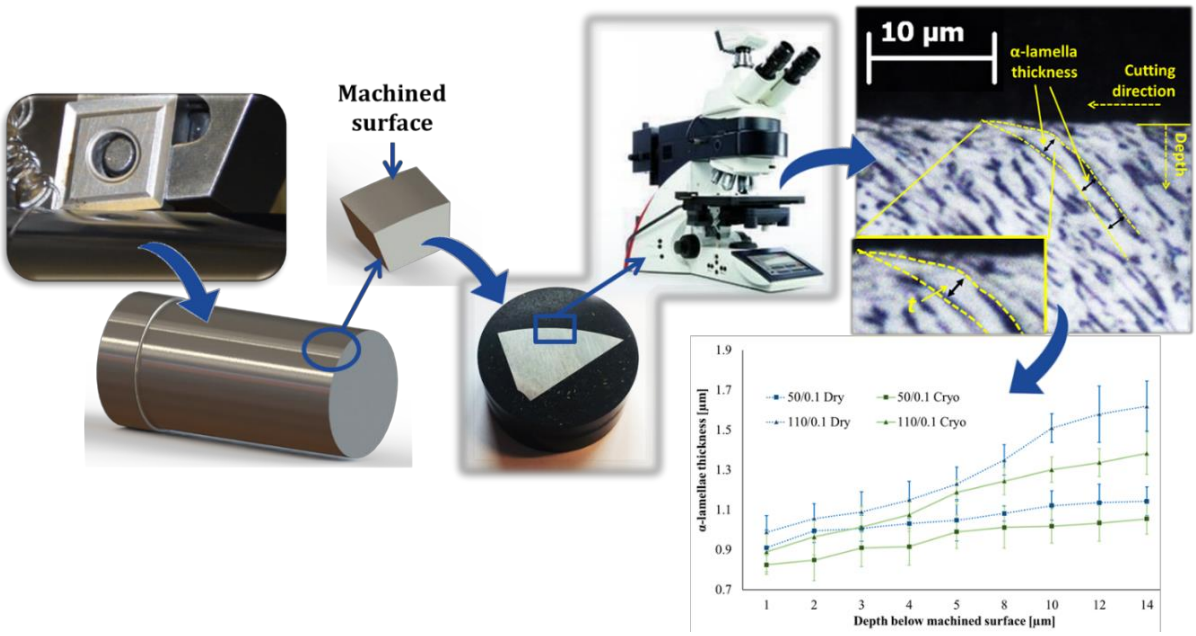

Figure 41: Experimental procedure to prepare the samples for metallographic analysis and optical microscopy.

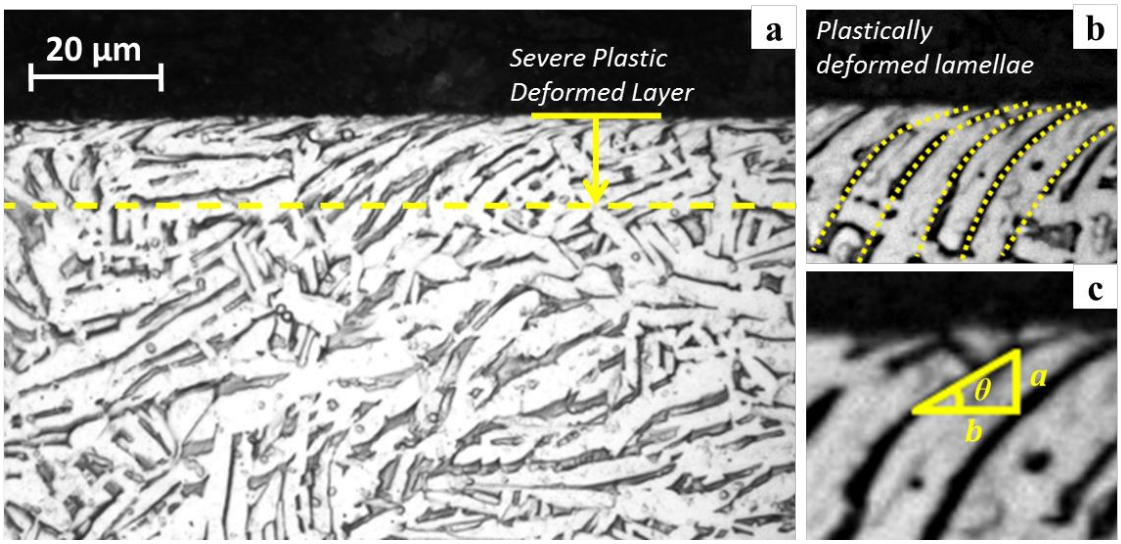

Figure 42: a) Sever Plastic Deformed layer on machined *Ti6Al4V* DMLS; b) bended lamellae due to the deformation imposed by the tool action; c) Measure representative of the plastic deformation within the deformed layer ($\varepsilon = tang(\theta) = a/b$).

The micrographs acquired via optical microscope under light field permitted to evaluate the depth of the plastically deformed material due to the manufacturing operation (Figure 42a). To better estimate the altered material thickness, further analysis such as nano-hardness measurements and X-Ray Diffraction (XRD) analysis as well as SEM observation were carried out and will be described in details in the next sections (Section 3.2.3). The results of the AL depending on the cutting parameters, cooling conditions and machined material are reported in Figure 43 and Figure 44. It is clear that the cutting speed had a predominant effect in increasing the AL of the *Ti6Al4V* produced via AM, unlike the wrought one that was also affected by the feed rate. Despite, the increase of the cutting speed permitted to achieve in *Ti6Al4V* wrought remarkable ALs and higher feed rate exacerbated them.

Consequently, the combination of the cutting speed and feed rate has to be properly set when the wrought alloy is machined, unlike what was observed for the AM ones, which were mostly affected only by cutting speed. It is known that higher cutting speeds lead to higher temperature and stress-strain field into the cutting zone and beneath the machined surface justifying the growing trends of the ALs of the three materials. However, the different microstructure (equiaxed, lamellar) affected the behavior of the material during the plastic deformation and then the capability to be deformed before reaching the failure at high shear stress (Telrandhe et al. 2017).

Figure 44 reports the ALs measured on the *Ti6Al4V* EBM machined under dry and cryogenic conditions. Taking into account what has been previously affirmed regarding the effect of temperature on the ALs depth, the highest AL was expected when the material was machined under dry condition but deeper deformed layer were measured on the cryogenically machined parts. Although, the temperatures during the cryogenic machining were lower, (Figure 35a and Figure 35b) compared with the ones measured during dry turning, the LN_2 in contact with the material being deformed into the cutting zone, froze locally the material and locked any thermal-induced recovery effect. Consequently, the very low temperature froze the deformed material preserving its deformed shape (bended lamellae). This latter result was in agreement with the nano-hardness results reported in Section 3.2.4. In fact, the altered material was more evident also in depth while the cryogenic fluid was adopted.

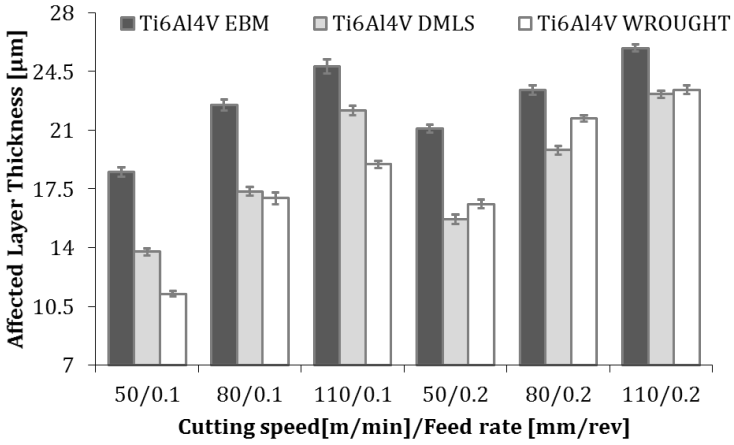

Figure 43: Affected Layer thickness (AL) at varying cutting speeds, feed rate and materials in dry conditions.

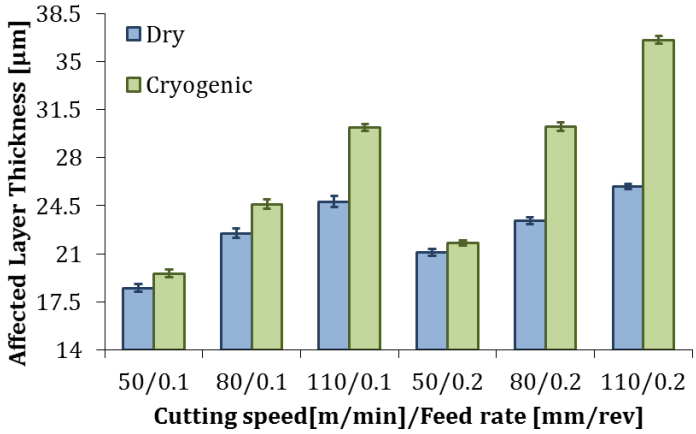

Figure 44: Affected Layer thickness (AL) at varying cutting speeds, feed rate and cooling condition measured on the *Ti6Al4V* EBM.

Referring to Figure 42b and Figure 42c, due to the shape of the microstructure (lamellar or acicular), the Equation 2, suggested by Joshy et al. 2014 permitted to estimate the PD of the deformed grains. Since the equiaxial microstructure of the wrought material did not change the almost circular shape, contrary to what observed for the acicular ones, it was not possible to evaluated the PD by Equation 2. Consequently, only the PD of the additively manufactured machined parts was measured (Figure 45 and Figure 47). In Equation 2, *a* and *b* are the components of the lamellae deformation of the α lamellae phase along and across the machined surface, as illustrated in Figure 42c. These values were measured approximately between 1µm and 2µm far from the machined surface within the cross section. The measurements were repeated five times in order to achieve a statistical repeatability.

$$\varepsilon = tang(\theta) = \frac{a}{b} \tag{2}$$

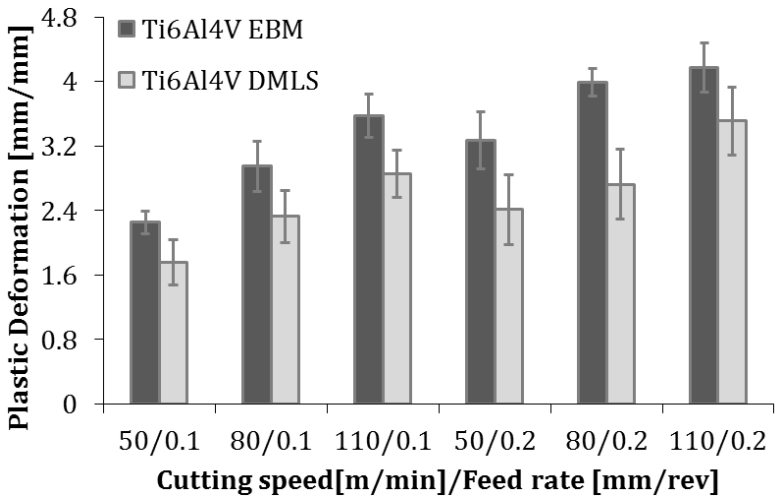

Figure 45: Plastic deformation at varying cutting speed and feed rate on different machined material under dry conditions.

Figure 46 shows the comparison between the PD measured through the bended lamellae on the *Ti6Al4V* produced by EBM and DMLS. It is evident that the increasing of the cutting speed led to an increment of the plastic deformation. The lamellae of the EBM machined parts were more bended than the DMLS ones at higher feed rate while at lower feed rate they were almost comparable (Figure 45).

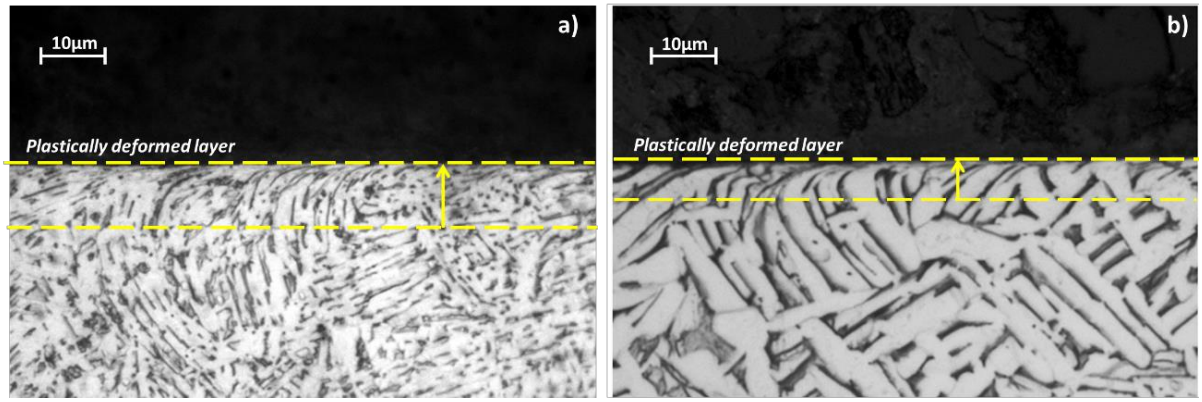

Figure 46: Plastically deformed layer thickness of machined materials at cutting speed 110m/min, feed rate 0.2mm/rev and a_p=0.2mm: a) *Ti6Al4V* EBM; b) *Ti6Al4V* DMLS.

The reason of that is related to the capability of the material to accumulate elastic strain before the plastic one, that is permanent and then visible under microscope. In fact, the Young Modulus of the EBM (Table 3) is slightly higher than the DMLS one, as a result since the strain at a certain cutting speed is almost the same; the EBM material has accumulated more plastic deformation energy than the DMLS one. Consequently more stretched and bended lamellae following the cutting direction are visible, as showed in Figure 46. Moreover, higher thermal gradient measured during *Ti6Al4V* EBM machining surely made the material more deformable under tool action. Moreover, the feed rate together with the cutting speed affect the plastic deformation only on the EBM machined material, as reported by Figure 45. Indeed, comparing the plastic deformation with different feed rate value and fixed cutting speed, some differences are evident only on the EBM material.

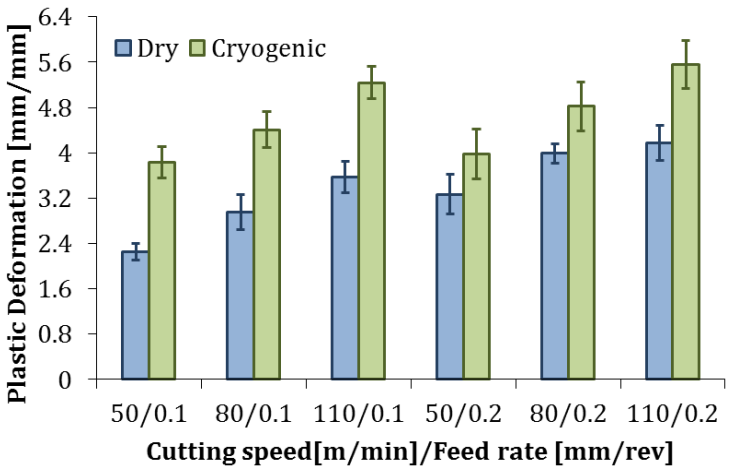

Figure 47: Plastic deformation at varying cutting speed, feed rate and cooling conditions on machined *Ti6Al4V* EBM.

Figure 47 represents the PD evaluated on *Ti6Al4V* EBM machined under dry and cryogenic conditions. It is clear that, as previously discussed for the ALs, the very low temperature of the cryogenic fluid prevented any thermal-induced recovery effects, preserving the plastic deformation field and the microstructure-deformed shape. Rotella et al. 2014 also highlighted the ability of the LN_2 in interrupting the thermal-induced microstructural modifications (static recovery). The authors affirmed that the LN_2 cooling process prevents grain growth after the dynamic recrystallization (DRX), which in turn was the result of the severe plastic deformation process. The possibility to prevent any recovery effect can drastically increase the mechanical strength of the worked material not only in surface but also for few microns (usually between 10μm and 50μm but it depends on the material) under the machined surface.

Regarding to the microstructure analysis, the measurements of the α phase lamellae thickness (t) were carried out along the radial direction in fifteen positions setting a fixed pitch equal to 1μm (Figure 42, Figure 49). This microstructural parameter has an important role in terms of mechanical response. In fact, as reported from many researchers (Xu et al. 2017, Tan et al. 2015, Xu et al. 2015, Al-Bermani et al. 2010, Baufeld et al. 2010) the yield strength, as well as the ultimate stress and some fatigue life performance, are strongly affected by the dimensions of the lamellae size or lath size of lamellae width (Figure 48).

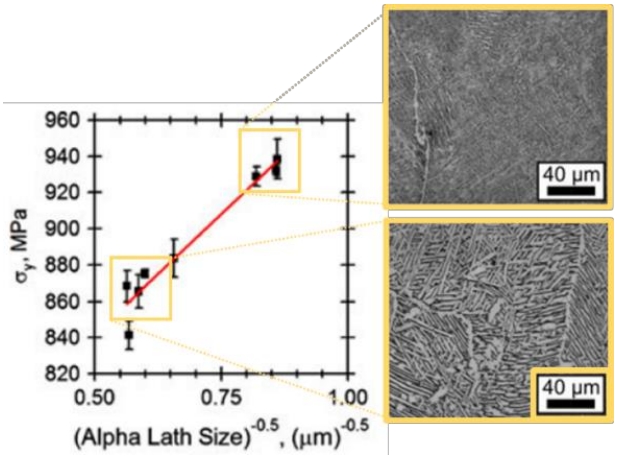

Figure 48: Yield stress depending on α-lamellae thickness (Adapted from Al-Bermani et al. 2010).

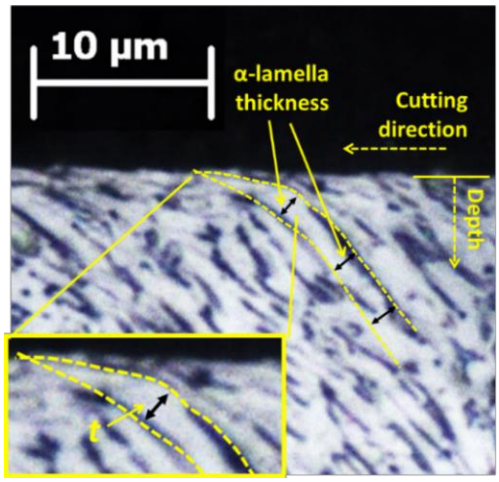

Figure 49: Variation of the α-lamellae thickness due to the tool action on machined surface (cross section).

As a result, due to the fundamental role that the lamellae thickness plays in describing the mechanical performance, the average value of the lamellae thickness was also evaluated in the same region where the deformation was measured.

In order to compare the microstructural dimensions due to the different value of the initial grain size of each material, the parameter Degree of Grain Reduction (DGR) was computed as reported in Equation 3. The experimental results are reported in Figure 53 and Figure 54.

$$DGR\% = \frac{t_0 - t}{t_0} \times 100 \quad (3)$$

To understand the amount of the reduction, the initial grain size of the as-received material was measured. The grain size of the wrought was equal to 4.29 +/- 0.44 μm, while the lamellae thickness of the EBM and DMLS was equal to 1.68+/- 0.25 μm and 3.46 +/- 0.29 μm respectively (Figure 50).

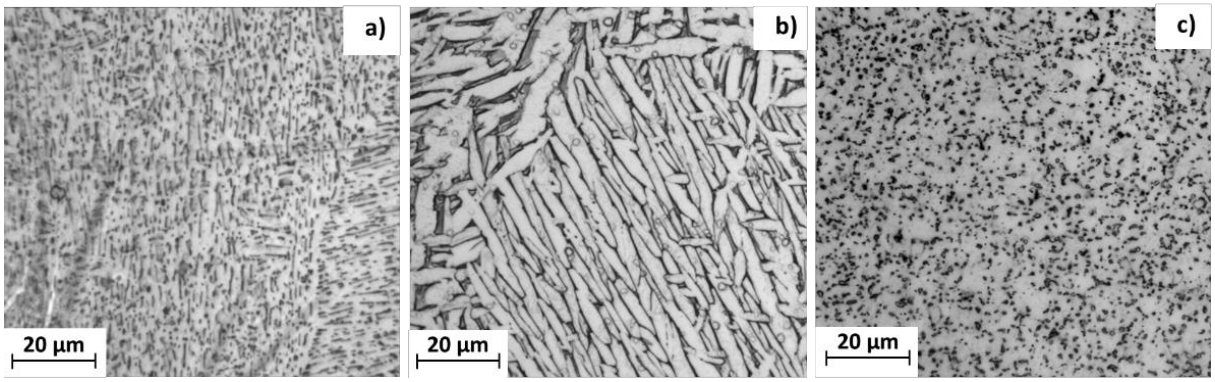

Figure 50: Initial microstructure of the *Ti6Al4V*; a) EBM; b) DMLS; c) Wrought.

It is important to point out that after different analyses (e.g. SEM and X-Ray inspections) no phase changes or metallurgical phenomena such as dynamic recrystallization were observed, but some grain shape variations were revealed (Figure 51). Furthermore, in Figure 51 are clearly visible the peculiar microstructure of the additively manufactured *Ti6Al4V* characterized by α lamellae (acicular shape produced by EBM) and the β phase that is inside the α phase matrix. To better analyze the region of plastically deformed material close to the machined surface, the Atomic Force Microscopy (AFM) (Figure 52) analysis was carried out on the sample collected by the specimens machined at higher cutting speed and feed rate. It is clearly visible that only severe plastic deformed material was present into the affected layers of the three kinds of material, therefore no recrystallized grains were visible.

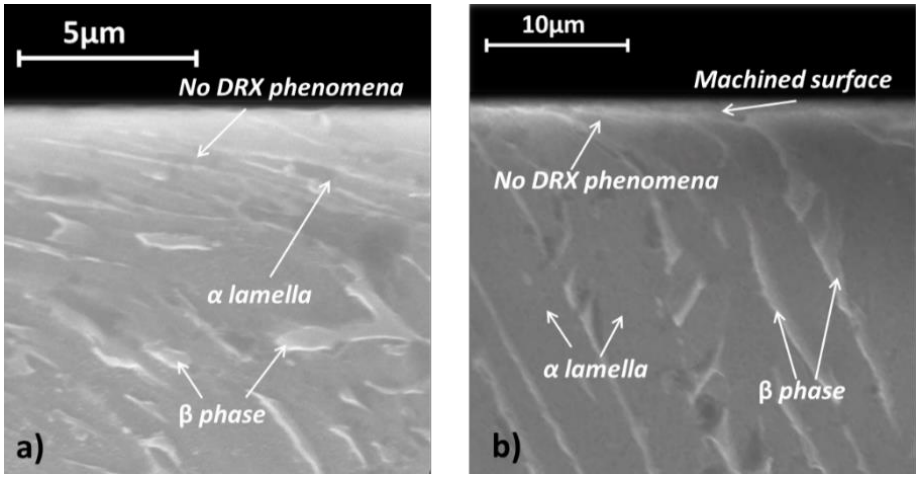

Figure 51: SEM analysis of the machined surface of a) *Ti6Al4V* EBM; b) *Ti6Al4V* DMLS (V_c=110m/min, f=0.2mm/rev, dry conditions).

This particular result was also confirmed by the low temperature measured that coupled with plastic deformation could not trigger microstructural phenomena. Therefore, the decreasing in grain size was mainly attributed to shape changes due to the deformation imposed by the tool action. It is still of paramount importance to evaluate the microstructural changes because it suggests the deformation rate imposed by the machining processes.

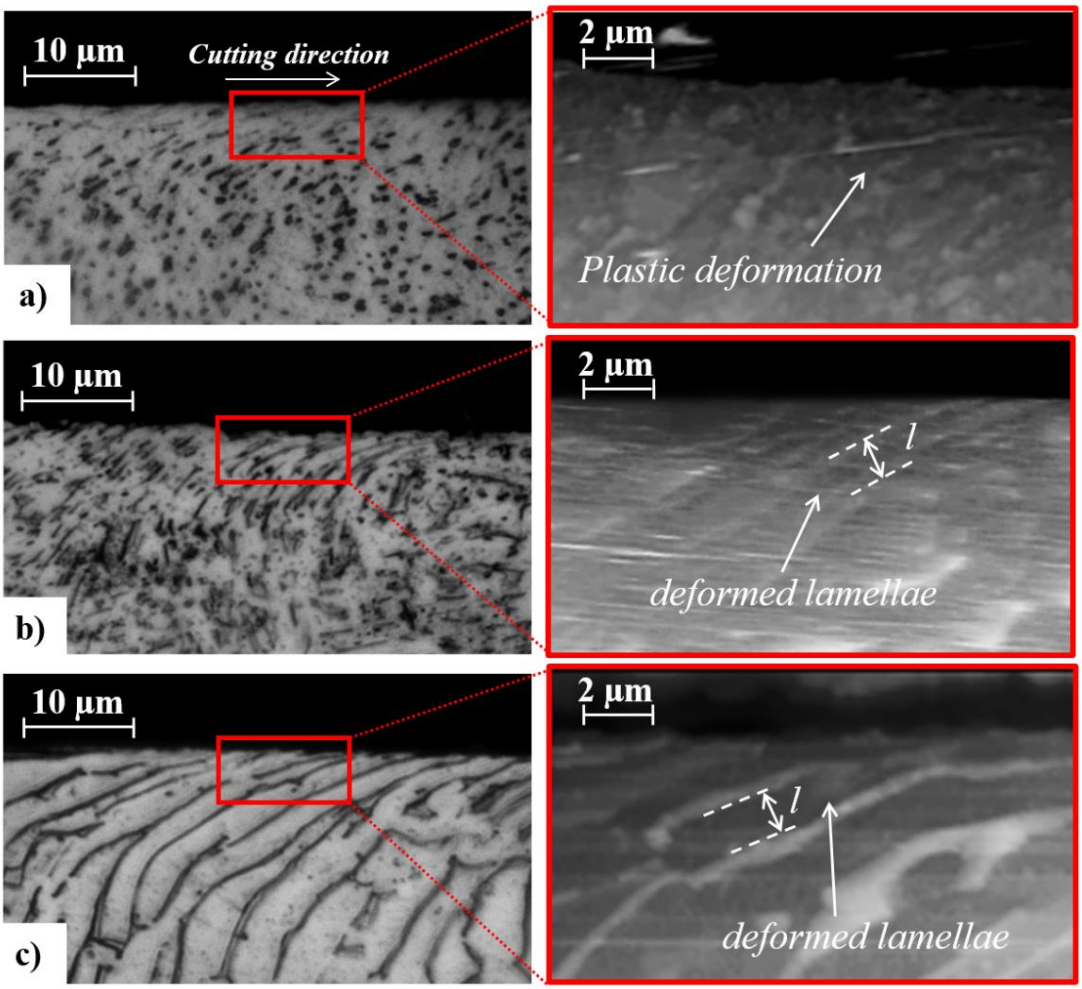

Figure 52: Optical micrographs and AFM microstructure analysis (V_c = 110 m/min, f = 0.2 mm/rev); (a) wrought; (b) EBM; (c) DMLS machined samples.

The materials additively manufactured, as reported in Figure 52 and Figure 53, did not show significant variation among the DGR at varying cutting speed and feed rate. Particularly, at cutting speed of 80m/min and feed rate equal to 0.1mm/rev, as well as 50m/min and feed rate of 0.2mm/rev, the DGR measured was almost the same. Furthermore, at low feed rate when the cutting speed increased, the DGR of the DMLS started to increase overcoming the one measured on the EBM. With a feed rate equal to 0.2 mm/rev this result was more evident. However, although the DGR between the EBM and the DMLS was almost similar, taking into account the initial value of the lamellae thickness, the EBM showed lower lamellae thickness because the initial value was smaller than the DMLS. Regarding the *Ti6Al4V* wrought, the DGR measured was lower if compared to the EBM and DMLS except when the cutting speed and feed rate were equal to 110m/min and 0.2mm/rev respectively. In this case, the DGR of wrought and EBM are comparable. In general, as observed for the ALs and PD, the increase of the cutting speed and the feed rate leads to an increase of the grain refinement (smaller grains).

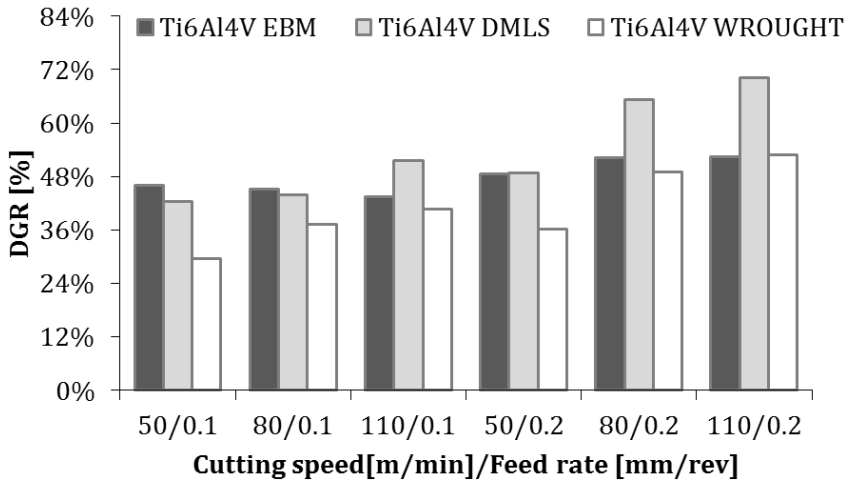

Figure 53: Degree of Grain Refinement at varying cutting speed and feed rate for different machined materials in dry conditions.

Figure 54 reports the DGR of machined Ti6Al4V EBM under dry and cryogenic condition. The highest DGR was obtained under cryogenic conditions. All the reported results confirm that the lower temperature achieved during cryogenic machining can prevent the static grain growth caused by high thermal gradient reached during machining. The lower temperature also permitted to preserve the deformation field and grain refinement induced by manufacturing processes. Moreover, the lower grain size means higher yield stress limit induced by work hardening of the machining process. As suggested by Figure 48, smaller grain size or lamellae thickness leads to higher hardness value on the surfaces. These results are confirmed by hardness measurements as reported in Section 3.2.4. Similar results were observed on the *Ti6Al4V* specimens cryogenically machined by Rotella et al. 2014 and by Pu et al. 2012 on cryogenic machining *AZ31B Mg* alloy.

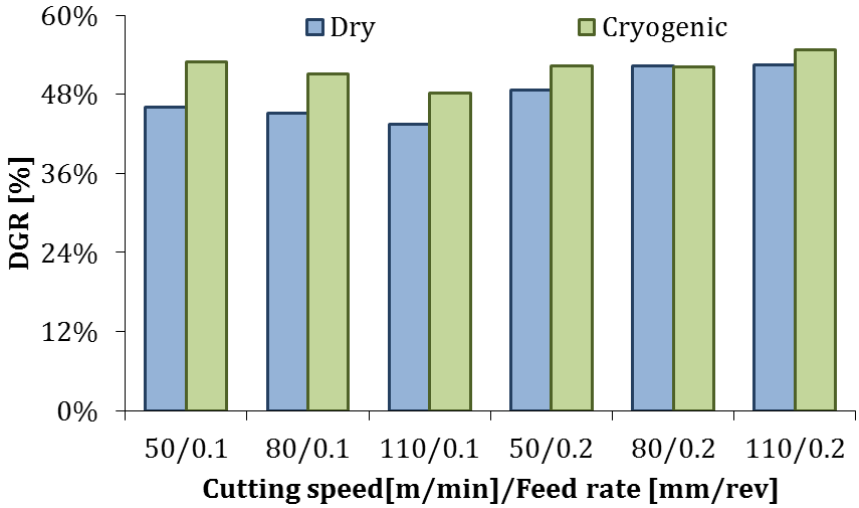

Figure 54: Degree of Grain Refinement at varying cutting speed, feed rate and cooling conditions for machined *Ti6Al4V* EBM.

3.2.3 X-Ray Diffraction analysis (XRD)

The X-Ray Diffraction (XRD) analysis can give important information on crystallite size, micro-strain phase changes or formation of new precipitates (Guinebretière 2007). The XRD experiments were performed for all the experimental tests in order to better understand the surface modifications taking place during the machining process. In Figure 55 is reported the experimental instrument Rigaku© MiniFlex 600 X-Ray Diffractometer with CuKα radiation and a representative sample collected by the machined bars.

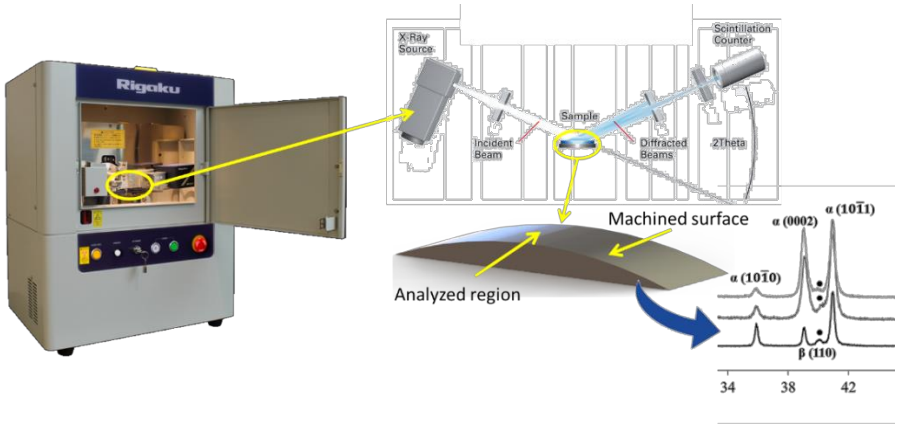

Figure 55: Experimental set-up and sample used to perform the XRD analysis.

The X-Ray scanned by angle/step of 0.2 in a range from 20° to 110° on the machined surface penetrating the sample in depth (up to 50μm). The registered patterns represented the peaks due to the diffracted beams from the crystallographic planes oriented orthogonally to the incident beam. The *Ti6Al4V* is susceptible to the development of strong textures during thermo-mechanical processing, thus, the XRD analyses were carried out on the as produced material to understand the texture generated by the different production methods (additive and conventional production processes). After the preliminary crystallographic characterization of the as produced materials, other investigations were carried out on the machined samples. The different patterns were normalized in order to make possible a comparison among them (Figure 56).

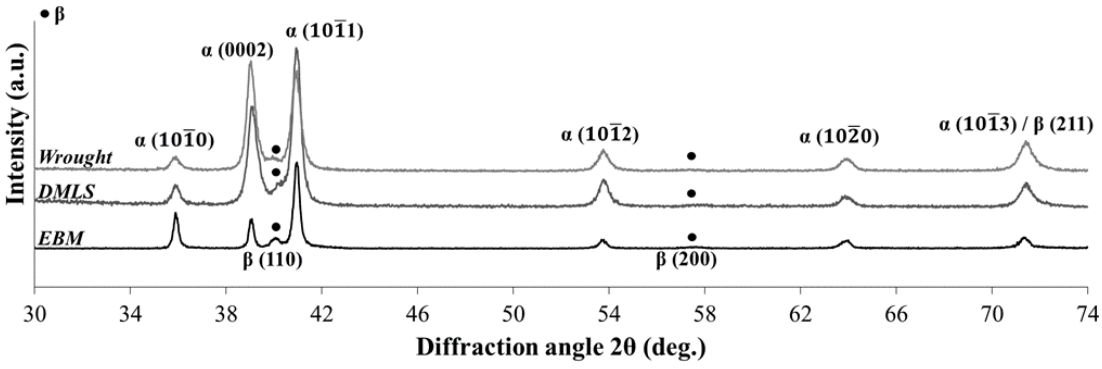

Figure 56: XRD pattern of as produced *Ti6Al4V* samples.

X-Ray Diffraction scans reveal that HCP α phase was textured on the (10$\bar{1}$0) prism plane, (0002) basal plane and (10$\bar{1}$1) pyramidal plane in *Ti6Al4V* EMB manufactured and on (0002) basal plane and (10$\bar{1}$1) pyramidal plane in DMLS and wrought manufactured *Ti6Al4V* alloys. Furthermore, while in EMB manufactured alloy β phase had a (100) preferred orientation and its relative peak was clearly distinguished,

in DMLS and wrought alloys it was partially overlapped by (10$\bar{1}$1) Ti-α peak, that consequently, resulted dissymmetric. All the samples showed a weak peak at 2θ≈58° corresponding to (200) reflection of β phase. The patterns obtained (Figure 56) were in agreement with the ones reported in literature and that characterize the standard peaks profiles (Xu et al. 2017, Li et al. 2008 and Velàsquez et al. 2007).

Subsequently, the machined surfaces under dry conditions were analyzed and the results are reported in Figure 57, Figure 58 and Figure 59.

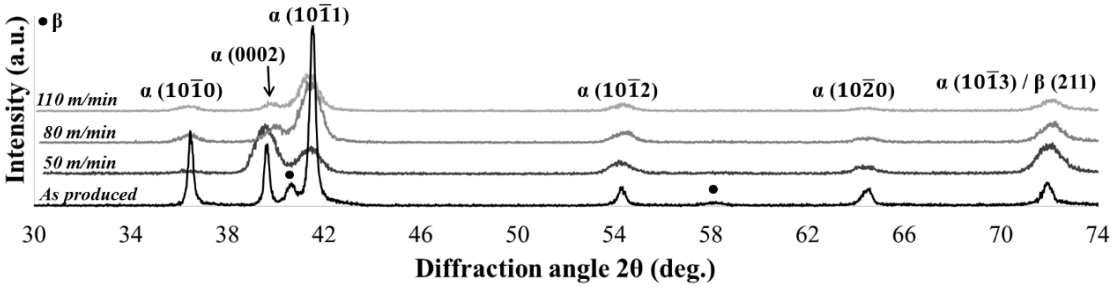

Figure 57: XRD pattern of the *Ti6Al4V* EBM machined under dry condition (*f*=0.2 mm/rev).

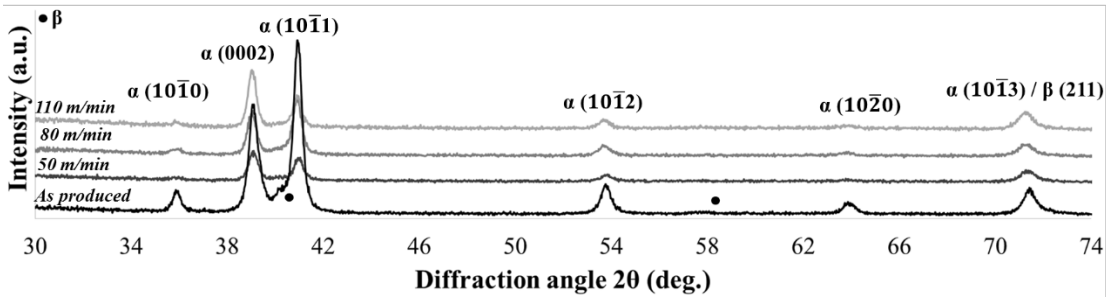

Figure 58: XRD pattern of the *Ti6Al4V* DMLS machined under dry condition (*f*=0.2 mm/rev).

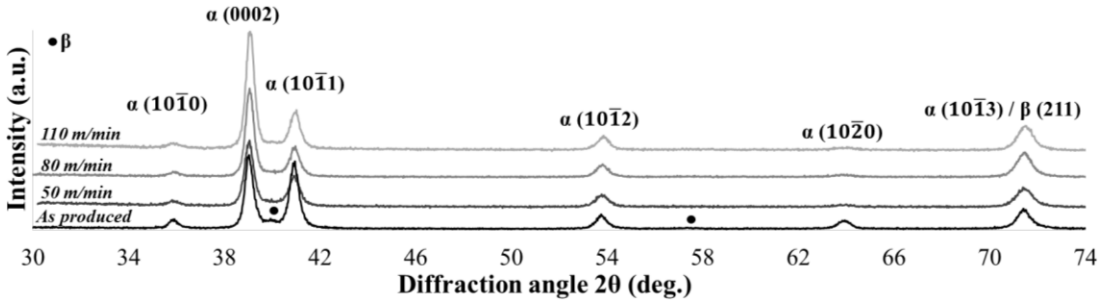

Figure 59: XRD pattern of the *Ti6Al4V* wrought machined under dry condition (*f*=0.2 mm/rev).

Only the samples collected by the machined parts with feed rate equal to 0.2mm/rev were analyzed via XRD due to the higher ALs observed. In this case, the results represent clearly the altered material inside the affected region. In fact, the patterns obtained on the samples machined with lower feed rate did not show important variations compared with the as-built material. Generally, this suggests that probably the semi-finishing operation on titanium alloy did not induce severe metallurgical changes, such as recrystallization or phase changes. In the results reported in this work, all the XRD pattern of the machined surfaces exhibited a broadening of the peaks, usually ascribed to nano-crystals formation or lattice strain (Guinebretière 2007), and all the planes related to β–phase were weaker because of cutting.

Since the SEM and the micrographs (Figure 51 and Figure 52) did not reveal any dynamic recrystallized grains, it is possible to assume that the peak broadening was mainly induced by plastic strain of the lattice. Furthermore, no phase transformations or precipitate formations were identified by the XRD analysis and these results were in agreement with the monitored temperatures since during the turning process the β–transus was never reached. The crystallographic orientation of the α–phase, that is characterized by a limited number of active slip systems, determines the ease of which slip occurs during turning process. In the case of the *Ti6Al4V* wrought machined sample, the cutting speed influenced both the peak broadening and intensity ratio. The turning process deeply affected the texture of the *Ti6Al4V* EBM machined samples. In fact, as shown in Figure 57, as the cutting speed increased the peaks broadening also increased, while the peak intensities decreased. The variation of the intensity ratios in XRD patterns as well as high peak broadening indicated that grain refinement (shape changes) existed in the plastically deformed layers. Finally, considering the *Ti6Al4V* DMLS machined samples the peak broadening in the obtained XRD patterns affected mainly $(10\bar{1}0)$ Ti-α plane (Figure 58). Furthermore, as the cutting speed increased the intensity shifts from $(10\bar{1}1)$ Ti-α peak to (0002) Ti –α peak, thus resulting in a change of texture. Moreover, as the cutting speed increased a greater decrease of the intensity of the $(10\bar{1}0)$ prism plane, and $(10\bar{1}1)$ pyramidal plane of HCP Ti-α was observed, while (0002) Ti-α peak intensity correspondingly increased (Figure 59). Furthermore the more pronounced peak broadening observed in XRD patterns on EBM machined samples confirmed the higher plastic deformation imposed by turning processes compared with the other machined samples (wrought and DMLS), supporting also the microstructural observation via micrographs.

Subsequently, the XRD analysis on the *Ti6Al4V* EBM cryogenically machined was also carried out. The results are reported in Figure 60. The average beta phase fraction of the as-built material resulted equal to 5%, whereas the machined samples showed values ranging from 4.7 to 5.3%, proving that the machining process and cooling strategy did not provoke any phase variations. In contrast, both the machining cooling strategies affected the subsurface layer of the machined *Ti6Al4V* EBM; in fact, the XRD patterns, acquired on the dry and cryogenically machined surfaces at different cutting speeds, clearly showed broader peaks with respect to the as-built material. This aspect was more evident on samples that were cryogenically machined. The peaks broadening mainly arise from the decreased size of the crystallites and micro-strains, which can be attributed to the plastic deformation induced by the process. The turning process also produced variation in the texture distribution of the alpha phase, with a more pronounced weakening of the alpha peaks. Furthermore, all the peaks corresponding to the beta phase disappeared. This can be ascribed to the β→α phase transformation and/or to residual beta peaks being hidden by broadened neighboring alpha peaks.

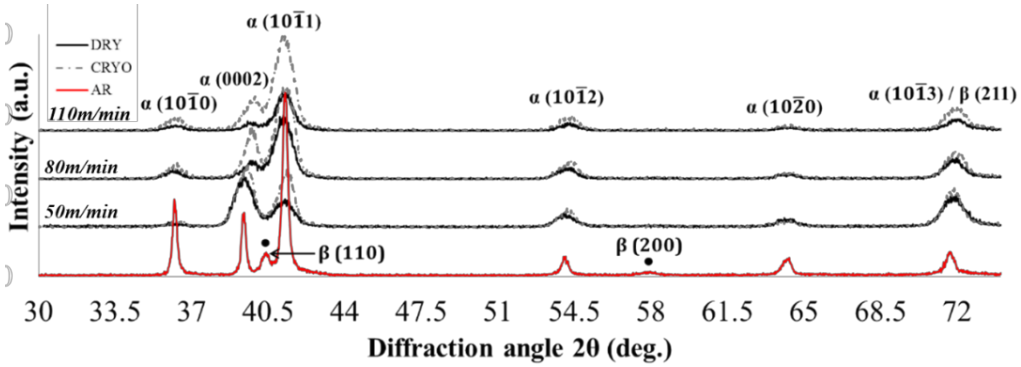

Figure 60: XRD pattern of the *Ti6Al4V* EBM machined under cryogenic condition (*f*=0.2 mm/rev).

3.2.4 Surface and Subsurface hardness

The measurements of hardness allow to understand the changes in mechanical properties due to the applied loads that usually lead to plastic deformation and hardening of the material. Indeed, during the manufacturing processes, such as machining, the cutting tool action induces high compressive loads beneath the machined surface leading to high stresses and then plastic deformations. In some cases, the combination of the high strains with the high temperatures gives rise to favorable conditions to trigger metallurgical phenomena. Therefore, the hardness measurements permit to catch all these alterations in the machined material and to understand their effects on the mechanical properties.

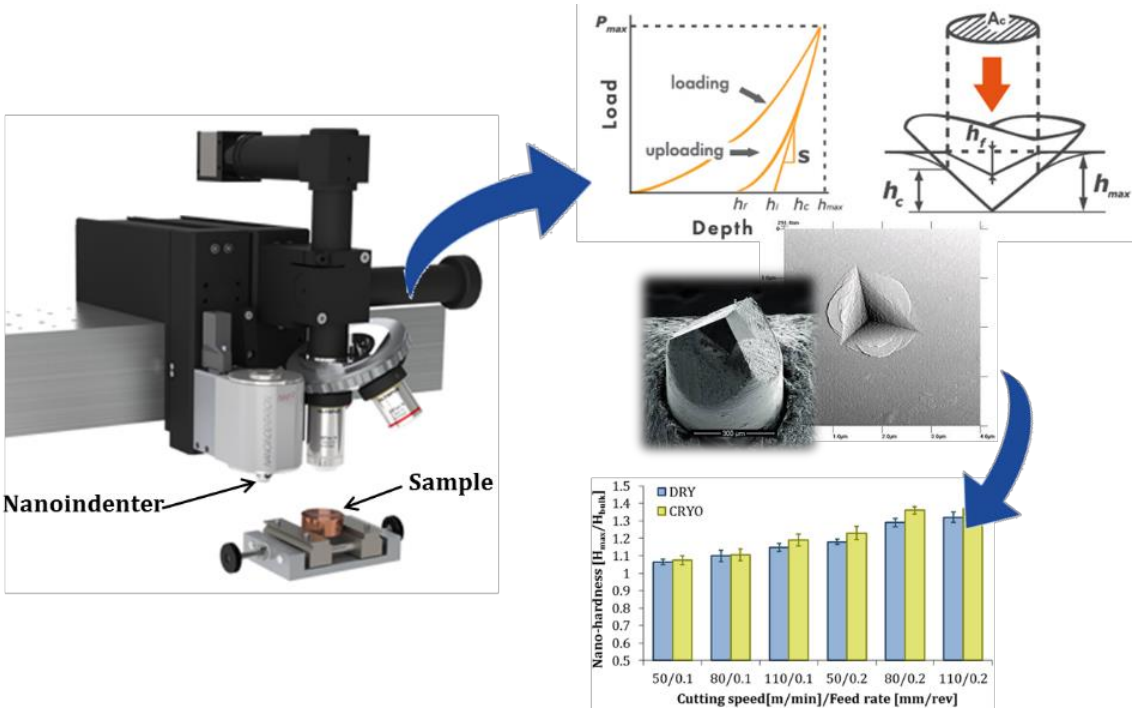

Figure 61: Nano-hardness measurement set-up and procedure.

The nano-hardness measurements were carried out due to the very small size of the microstructure and affected layers. The procedure employed is reported in Figure 61. The nano-hardness was measured by nano-indentation tests with a Berkovic tip. The parameters (dwell time and load) set for measuring the nano-hardness were chosen after some preliminary tests. The load and dwell time were respectively varied from 10mN to 200mN and from 5s to 30s respectively. Three matrix spots composed by fifty indentations were sampled for each test piece. In Figure 62a are shown the spots where the indentation tips are visible through microscope in dark field light condition. Figure 62c reports the typical graph obtained from a nano-indentation test. This procedure was executed for each combination of load and dwell time tested within the ranges previously mentioned. The best and more reliable results (very low scatter of value) were obtained setting the values of 20mN and 15s of load and dwell time respectively. These parameters were applied to perform all the nano-indentation tests. Preliminarily, the nano-hardness values referred to the as produced EBM, DMLS and wrought samples are, 4.29 ± 0.27 GPa and 4.46 ± 0.31 GPa and 3.54 ± 0.14 GPa were measured respectively. There were no appreciable differences in nano-hardness values of AM parts, meanwhile the wrought material was clearly softer as also suggested by the lower mechanical properties reported in Table 3. It is worth noting that the mechanical properties, including hardness, are strictly related to the microstructure features (equiaxed, lamellar), their dimensions (coarse or fine) and texture (Tan et al. 2015, Kar et al. 2006). Thus, the slightly higher value of hardness on DMLS sample was not expected.

However, although the DMLS microstructure was coarser than the EBM one (Figure 50), the thermal history of DMLS process induced a martensite to alpha transformation that contributed to raise the overall hardness of the material (Facchini et al. 2010).

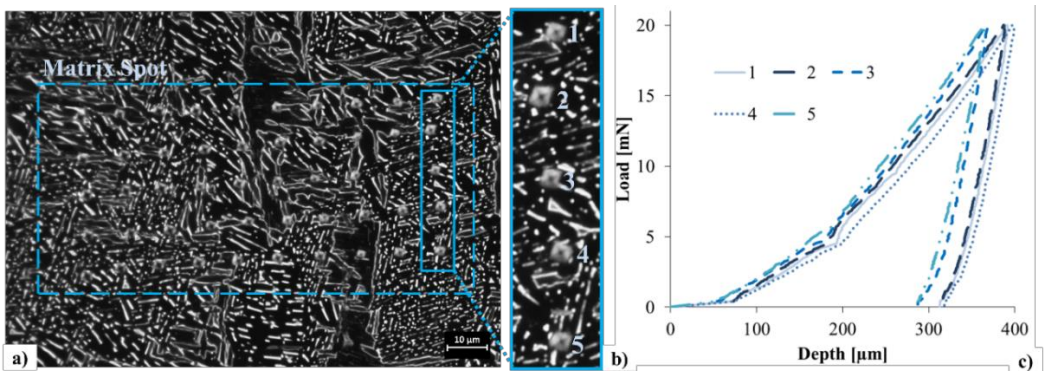

Figure 62: a) Micrograph in dark field of the matrix spot for the nano-indentation test; b) vertical line of tips; c) nano-indentation test results.

Subsequently, the nano-hardness on the machined surface and in the cross section of the machined bars were measured (Figure 63). Several tips were done close to the machined surface and into the depth in order to estimate the hardness variation and to compare the affected layer thickness already evaluated by micrographs. The results of the nano-hardness measured on the machined surfaces are reported in Figure 64. The average value of the hardness obtained by the tips close to the machined surface (a region of 5µm thick) was computed and then divided by the nano-hardness value of the as-built material. Depending on the cutting speed and feed rate, the hardness of the material close to the machined surface was always higher than the as-built suggesting that the semi-finishing operation slightly induced a small amount of work hardening. Moreover, as observed by the micrographs and according to the temperature reached, no metallurgical phenomena such as DRX occurred, in fact, as showed by literature, higher values of surface hardness are provoked by ultra-fine grains layers (Rotella et al. 2014, Pušavec et al. 2011, Pu et al. 2011). On the contrary, during the semi-finishing turning operations the increasing of the hardness was induced only by high strain leading to high hardening of the material inside the altered layers.

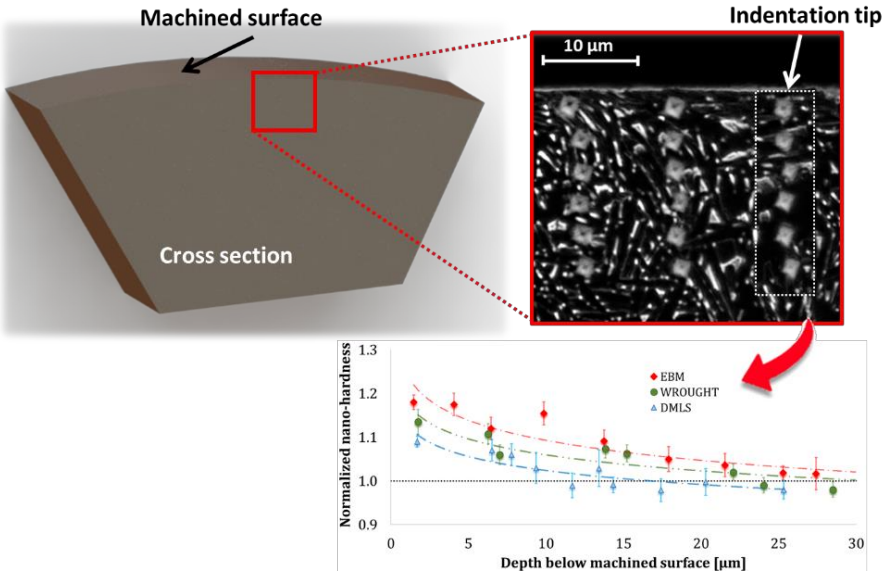

Figure 63: Nano-hardness measurements on the cross section of the samples.

Analyzing Figure 64, at lower value of the feed rate (0.1 mm/rev), the hardness showed a slight increase and the AM materials were harder than the wrought one. This result can be justified by the lamellar microstructure that is smaller (thickness) than the equiaxed one, as a results more grain boundaries able to act as obstacle to the mobile dislocations are located into the deformed region increasing the hardness. The cutting speed started to affect the hardness when the feed rate increases to 0.2 mm/rev. In this case, increasing the cutting speed a strong variation of the nano-hardness was clearly visible, especially considering the AM materials. The *Ti6Al4*V EBM was the most affected in terms of surface hardness changes with the higher value of feed rate. In particular, increasing the cutting speed it was possible to induce more work hardening leading to higher hardness value. The *Ti6Al4V* wrought reached always smaller or comparable surface hardness than the *Ti6Al4V* DMLS suggesting its low ability to accumulate work hardening machining induced. The *Ti6Al4V* DMLS showed hardness value almost comparable with the EBM ones. In general, the *Ti6Al4V* additively manufactured showed higher surface hardness value than the wrought one and this result was expected since the initial microstructure of the wrought was slightly bigger. At higher feed rate and cutting speed, the *Ti6Al4V* EBM was able to accumulate more work hardening as suggested by the higher surface hardness values (Figure 64).

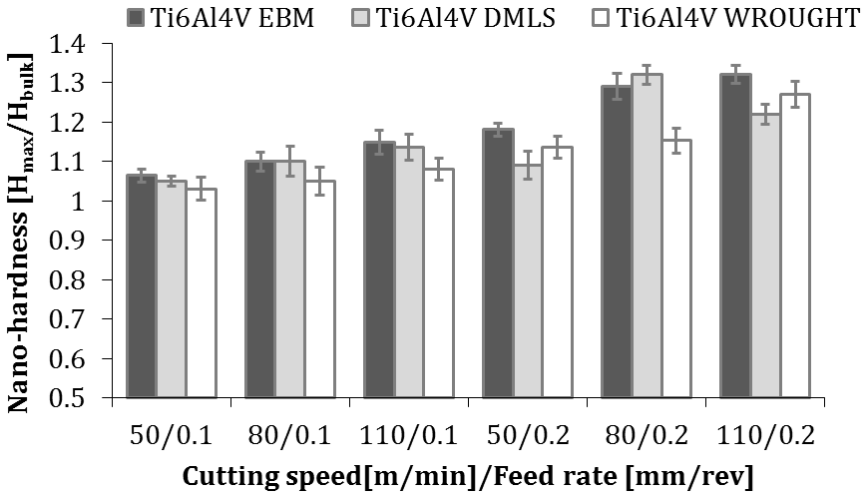

Figure 64: Nano-hardness at varying cutting speed, feed rate and materials.

Figure 65 reports the comparison of the nano-hardness measured close to the surface of the *Ti6Al4V* EBM machined under dry and cryogenic conditions at varying cutting speed and feed rate. As suggested by the previous results (affected layer, plastic deformation) the cryogenic is expected to lead higher hardening effect due to the miss recovery phenomenon. This aspect is confirmed by the yellow histograms that are always higher than the ones obtained on the dry machined parts (blue color). Higher value of feed rate led to higher value of hardness and in that case, the cutting speed had further positive effect in increasing the hardness as well. Taking into account the surface hardness changes, the delivering of cryogenic fluids had a positive effect also during semi-finishing machining operation. The surface hardness at the highest cutting speed and feed rate the machined part showed was increased of the 37% that represented the highest increment measured.

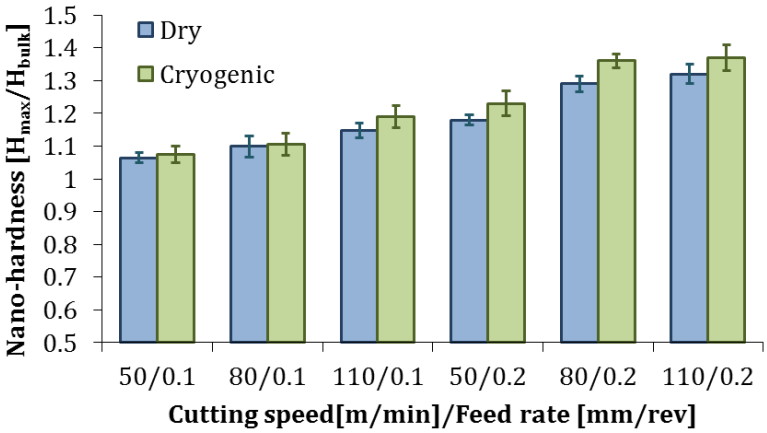

Figure 65: Nano-hardness measured on *Ti6Al4V* EBM machined under dry and cryogenic conditions at varying cutting speed and feed rate.

The mechanical response in terms of nano hardness measurements was analyzed into the affected layers in order to understand the cutting speed and cooling effects on the machined materials. In Figure 66a, Figure 66b, Figure 67a and Figure 67b are reported the hardness profiles at higher value of feed rate (0.2mm/rev) and at cutting speed of 50m/min and 110m/min respectively. The three kind of alloys, namely the EBM, the DMLS and the wrought showed different nano-hardness values from the machined surface through the depth. The work hardening induced by semi-finishing operation was remarked by the higher hardness value close to the surface. However, the manufacturing process induced alterations also in the subsurface regions where higher values of nano-hardness were measured. The EBM titanium showed higher hardness profile than the DMLS and the wrought. When the cutting speed was equal to 50 m/min (Figure 66a), the AM and wrought machined samples showed a slight increment of hardness at the machined surface (16%, for EBM, 12% for wrought, 9% for DMLS). This increment was more remarked when a higher cutting speed was used (110m/min) as showed by Figure 66b. In particular, at the highest cutting speed the EBM machined samples were the most affected with the 32% of nano-hardness increment followed by the 27% for the wrought and 22% measured on the DMSL.

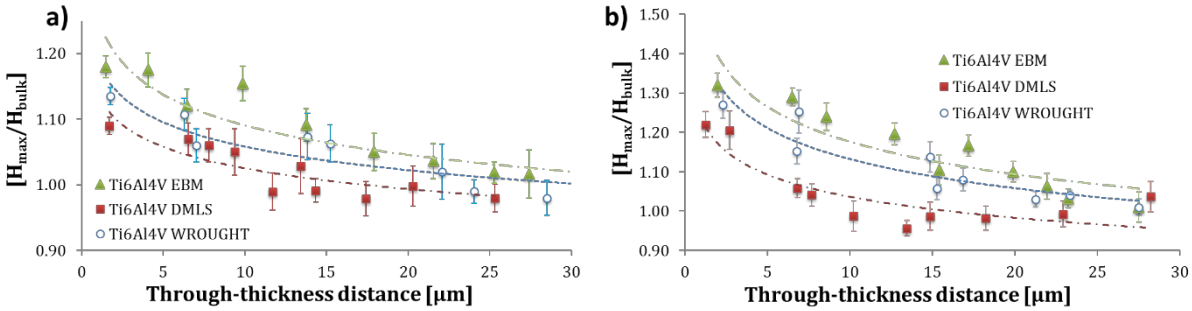

Figure 66: Hardness profile through the dry machined surface; a) V_c=50m/min and f=0.2mm/rev; b) V_c=110m/min and f=0.2mm/rev.

Subsequently, the nano hardness measurements were carried out on the EBM cryogenically machined samples. Figure 67a and Figure 67b show the comparison between dry and cryogenic EBM machined samples at cutting speed equal to 50m/min and 110m/min respectively. The trends were almost similar but the cryogenic machined sample showed higher hardness both with low and high cutting speed. The possibility to induce higher hardness on surface by machining operations leads to fatigue life benefits as massively reported in literature by Jawahir et al. 2016.

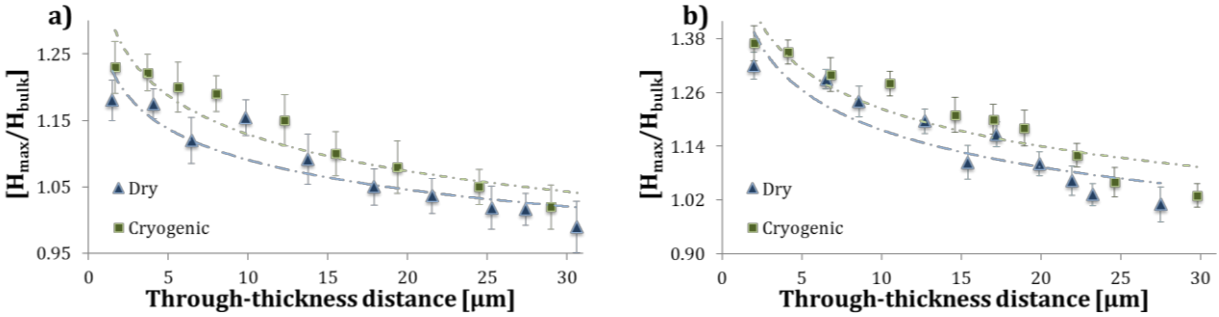

Figure 67: Hardness profile through the cryogenic machined surface of the *Ti6Al4V* EBM; a) V_c=50m/min and f=0.2mm/rev; b) V_c=110m/min and f=0.2mm/rev.

The highest hardness values reached in the EBM machined samples are also justified by the smallest α – lamellae thickness. Tan et al. (2015) highlighted similar observations between mechanical properties (yield stress) and microstructure produced by EBM process. These trends were also obtained in the works produced by Collins et al. (2009) and Al-Bermani et al. (2010). As overall, in all the three tested materials, the decreasing grain size or lamellae thickness coupled with the plastic deformation (strain-hardening) led to an increment of the hardness. Finally, the nano-hardness profiles also permitted to estimate the affected layer induced by dry semi-finishing turning; it was always contained within 15-25µm depth and it slightly increased when the cutting speed increased. This affected layer increased up to 25-30 µm when cryogenic fluid during the manufacturing process was used. These results confirm the experimental observations done by optical, SEM and AFM inspections.

The AM technology has great potentials in producing components with very complex geometry in few steps avoiding very long designing phases and manufacturing procedures. As reported by the literature and more in detail in this Ph.D. thesis, the AM produced parts still require post-processing procedures to be able to work in safety under complex loading conditions to which aircrafts are exposed. The cutting parameters investigated in this Ph.D. thesis for performing semi-finishing turning of *Ti6Al4V* alloy are in the range suggested by the toolmakers, however a higher cutting speed not conventionally adopted to machine Ti alloy, namely 110 m/min, was also studied to understand its effect on surface integrity. Taking into account the cutting forces, high cutting speed can provide some benefits because it provokes thermal softening and consequently lower cutting forces. On the other hand, the temperature will be higher leading to the reduction of tool life. However, focusing on the material, the parts produced by EBM showed lower thermal gradient with respect to the ones produced by DMLS or conventional processes; therefore, the choice to use higher cutting speed at lower feed rate on EBM does not drastically affect the tool life. Moreover, the possibility to use liquid nitrogen can provide a significant temperature drop into the cutting zone and this results in longer tool life while the cutting forces remain almost unaltered. From the surface integrity point of view, the literature shows that the microstructure, the hardness and surface roughness affect the mechanical performance as well as the fatigue resistance. It is important to emphasize that it is not in the scope of this Ph.D. thesis to suggest which titanium part (additive manufactured or wrought) achieved the best surface integrity because even though the specimens (EBM, DMLS and wrought) are chemically the same; they have different metallurgical aspects in as-built conditions. Therefore, this work aims to show that the same cutting process on these materials produced different results in terms of surface integrity.

Taking into account the highest cutting speed, at feed rate equal to 0.2mm/rev the volume of the material removed is higher than the one removed with feed rate 0.1mm/rev. Therefore, higher feed rate could represent an initial condition to rapidly clean and smooth the surface of the AM parts. In this case, the surface roughness will assume values higher than 1µm; therefore, further machining steps will be required.

At lower feed rate the surface roughness improves on EBM and DMLS materials machined, however the EBM still shows higher roughness value than DMLS, therefore other finishing operations are still required. Moreover, the use of liquid nitrogen did not show better results, due to the embrittlement of the material inside the cutting zone during the machining process. As explained by Kahlin et al. 2017 and Kasperovich et al. 2015, the possibility to reduce the porosity as well as the roughness on surface of the AMed parts leads to improve the fatigue resistance and to increase the fatigue life. For what concerns the microstructural changes, the thermo-mechanical loads were not critical to trigger important metallurgical phenomena such as dynamic recrystallization. Therefore, the microstructure refinement was mainly characterized by a shape change, thickness lamellae variations (AM) and grain diameter changes (wrought) induced by severe plastic deformation processes. The outcomes provided by Tan et al. 2015, Xu et al. 2015 and Al-Bermani et al. 2010, show that the reduction of lamellae thickness and in general of grain size, leads to higher mechanical properties. In this contest, the higher cutting speed and feed rate produced the higher degree of grain reduction; therefore, it is possible to affirm that the material resistance on surface and few microns beneath the machined surface is improved. This latter result was also confirmed by the nano-hardness measurements. It is possible to affirm that the semi-finishing operation not only remove the surface porosity improving the surface roughness but also contribute to improve the surface integrity of the machined parts. All the results produced by this research activity can be used as a guideline, depending on the printed material, to set the post-process machining strategy in order to optimize the surface integrity.

CHAPTER IV

High speed machining of the aluminum alloy *AA7075-T6* and the application of a severe plastic deformation (SPD) process

In this Chapter all the details and outcomes related to the experimental work conducted on the aluminum alloy *AA 7075-T6* are reported. Different metallurgical investigations were carried out to comprehensively understand the physical reasons of the result variations. Moreover, the surface quality of the manufactured parts is discussed and further comparison crossed with the literature information to describe the modified mechanical performance are also reported. The material used in this experimental activity is the aluminum alloy *AA 7075-T6*. This kind of alloy is particularly used to produce the main structural components of the aircraft frames such as fuselage and wing ribs (inner structural parts of the wings). The wrought materials were provided by the suppliers as extruded bars (diameter 100mm and 3000mm length). The total number of the bars employed was four and different samples were produced. Generally, the aerospace industry interests are moving towards producing parts of improved quality and performance in short period of time. Therefore, due to the strong interest in reducing the production time and improving the quality of the manufactured components, as observed in the literature review (Chapter II), the high speed machining and Equal Channel Angular Pressing (ECAP) tests were carried out. Therefore, the machinability during high material removal rate of the aluminum alloy were assessed in terms of cutting forces and temperature developed into the cutting zone. In detail, different cutting speeds and feed rates during the turning tests were used as process variables and the cooling conditions were also investigated. In fact, the delivering of cryogenic fluids during the machining process were investigated to understand the advantages or drawbacks on the manufacturing process in terms of machinability and surface integrity. This latter was evaluated by micro-hardness measurements on the machined surface and subsurface, optical microscopy and X-Ray Diffraction (XRD) analysis. Regarding the mechanical performance enhancements, the well known severe plastic deformation process named ECAP was performed and the deformed specimens were analyzed. This latter process was used to study the microstructural variation induced by plastic deformations due to very high shear stress field. These latter also appear during the machining process into the cutting zone, therefore the ECAP was employed as an analysis instrument to better understand the microstructural refinement into the cutting zone and in the deformed material. In fact, the possibility to correlate the surface integrity with the quality of the products and functional performances of the manufactured components is becoming significant (Jawahir et al. 2011), therefore making easier and more accurate the surface integrity analysis is one of the targets of this research activity. As a result, one of the aims of this Ph.D. thesis is to find the possible affinities between the ECAP and machining process in terms of surface and subsurface alterations. These affinities will permit to use the ECAP process to produce microstructural altered material similar to the ones produced near machined surface in order to easily study and characterize the metallurgical and mechanical changes that occur inside the affected layers during the plastic deformations.

4.1. Experimental work – high speed machining of *AA7075-T6* under dry and cryogenic conditions

The experimental activity consists of High Speed Machining (HSM), in detail turning process, adopting two different cooling strategies during the manufacturing operations, namely dry and cryogenic. The aim of the experimental work is to increase the material removal rate without compromising the surface quality of the machined parts. A right machining strategy developed and coupled with optimized and more sustainable cooling techniques can bring some advantages to the producers and their products. The choice to adopt the cryogenic fluid as a cooling medium during the turning tests is justified by some particular effects on the metallurgy of the manufactured parts.

In detail, the liquid nitrogen helps to reduce the recovery phenomenon and preserve the grain refinement into the affected layers (Rotella and Umbrello 2014, Rotella and Umbrello 2014, Yang et al. 2013, Pu et al. 2013, Jawahir et al. 2016). The workpiece material is an aluminum alloy *AA 7075-T6*. This kind of alloy undergoes a heat treatment, namely *T6* that consists of two-phases process to increase the strength of the material. The first phase is the quenching, the alloy is usually heated to 500°C for 9-10 hours to dissolve the copper in the aluminum matrix and then rapidly cooled with water to obtain a supersaturated aluminum with cooper. The second phase is the ageing that consists of heating the alloy between 150 °C - 180 °C for 9-10 hours and then cooled by air allowing the precipitation hardening. In Table 6 are reported the mechanical properties.

Table 6: Mechanical properties of the aluminum alloy *AA 7075-T6* (Kaufman 2000).

Material	Elastic modulus [GPa]	Yield Stress [MPa]	Ultimate Stress [MPa]	Breaking elongation [%]
AA 7075 T6	71	505	570	11

4.1.1 Design of Experiments and material selections

To understand the effect of each cutting parameters on the overall quality of the machined part, different experiments were carried out following a Design of Experiments (DOE). Unlike to the tests performed with titanium alloy, in this case the aluminum alloy was provided by the supplier with T6 treatment. Consequently, there are two qualitative levels referred to the cooling condition (dry and cryogenic), two quantitative levels referred to the feed rate (0.1mm/rev and 0.3mm/rev) and three quantitative levels related to the cutting speed (1000m/min, 1250m/min and 1500m/min). Finally, the DOE can be expressed as a plan of $3x2^2$ experiments. The cutting parameters as well as the depth of cut (2mm) were chosen in according with the parameters suggested by the toolmakers for machining the aluminum alloy.

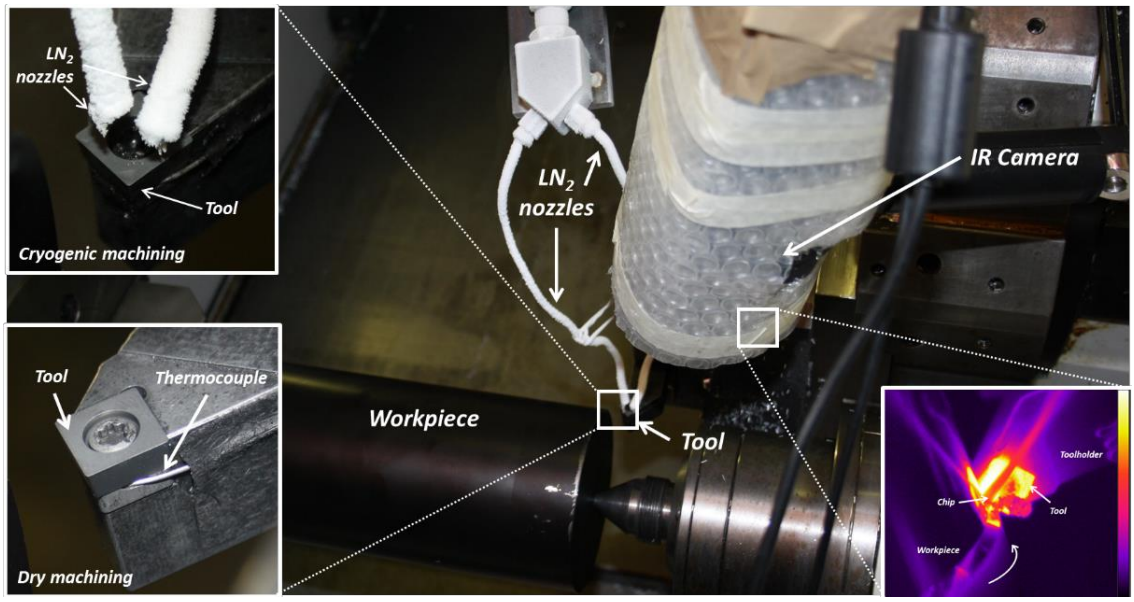

Figure 68: Experimental set-up to perform High Speed Machining.

Table 7 summarizes the DOE used in this experimental activity. The selected tools and tool holder are particularly suggested to machine the aluminum alloy. In detail, the model of the tool holder was SSDCL 2020K 09 and the tool was SCMW 09 T3 04 H13A both provided by Sandvik Coromant©.

In Figure 68 is reported the experimental set-up to perform HSM. In detail, the picture shows the region close to the tool equipped with/without the liquid nitrogen delivery system.

Table 7: Design of Experiments (12 full factorial experimental plan).

Material	Test n°	Vc [m/min]	f [mm/rev]	Cooling condition
AA 7075 T6	**1**	1000	0.1	Dry
	2	1250	0.1	Dry
	3	1500	0.1	Dry
	4	1000	0.3	Dry
	5	1250	0.3	Dry
	6	1500	0.3	Dry
	7	1000	0.1	Cryogenic
	8	1250	0.1	Cryogenic
	9	1500	0.1	Cryogenic
	10	1000	0.3	Cryogenic
	11	1250	0.3	Cryogenic
	12	1500	0.3	Cryogenic

4.1.2 Cutting Forces

The component of the cutting forces (axial and main component), as represented in Figure 69, were acquired by a KISTLER type 9257 B three components piezoelectric dynamometer mounted on the lathe revolver. In Figure 70a and Figure 70b are reported the two cutting components (feed and main cutting forces) measured during the tests under dry and cryogenic conditions depending on the cutting speed and feed rate. It is worth to point out that the cutting forces were acquired and analyzed as explained by Figure 27. Between each turning tests, the cutting tool was changed in order to provide a fresh cutting edge and avoid any wear effect on the cutting forces and thermal gradients.

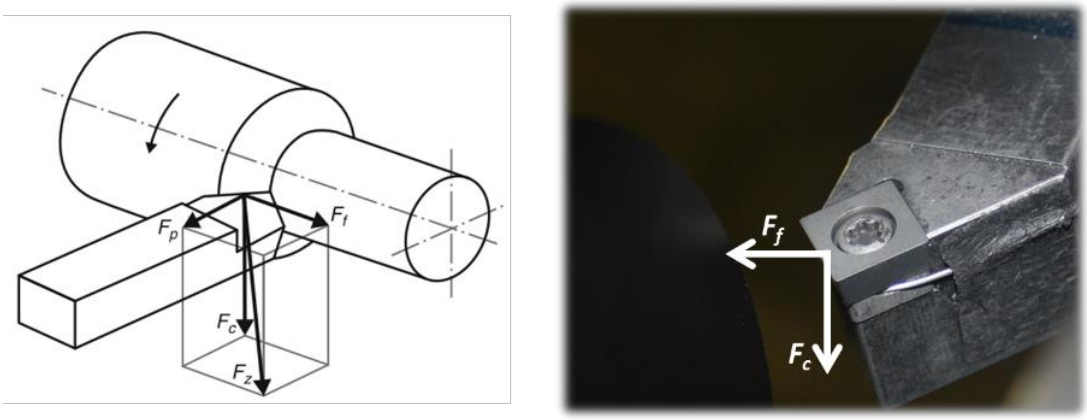

Figure 69: Cutting force components in turning operation, F_f feed force, F_c tangential force or main cutting component (adapted by Laperrire 2014). On the right, the two components acquired during the tests.

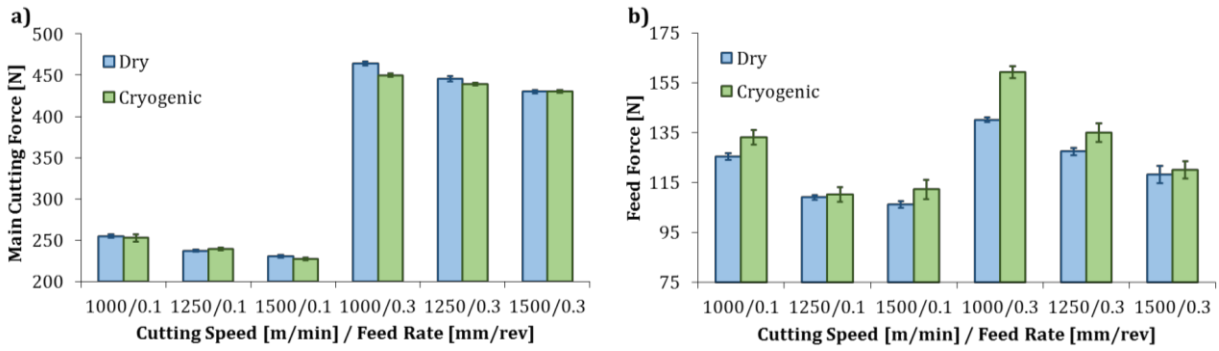

Figure 70: Main cutting (a) and feed (b) forces at varying cutting speeds, feed rate and cooling conditions.

When the feed rate was equal to 0.1mm/rev and 0.3mm/rev, increasing the cutting speed the main cutting force showed a decreasing trend both under dry and cryogenic condition. This result was due to the thermal softening induced by the higher plastic deformation rate. In detail, the main cutting forces measured during dry machining were slightly higher than the ones measured under cryogenic conditions. These differences were more evident with higher feed rate at cutting speed equal to 1000m/min and 1250m/min, while at 1500m/min were comparable. When the cutting speed was equal to 1000m/min the main cutting force was the highest. Focusing on feed force component, the trends obtained depending on the cutting speed and feed rate were similar to the ones related to the main component. Higher values of the feed forces measured under cryogenic conditions were due to the lower temperature reached into the cutting zone. The lower temperature led to predominate the work hardening effect instead of the thermal softening and this result was justified by the discontinuous chip formation (Figure 71) suggesting that the material was more brittle under cryogenic conditions.

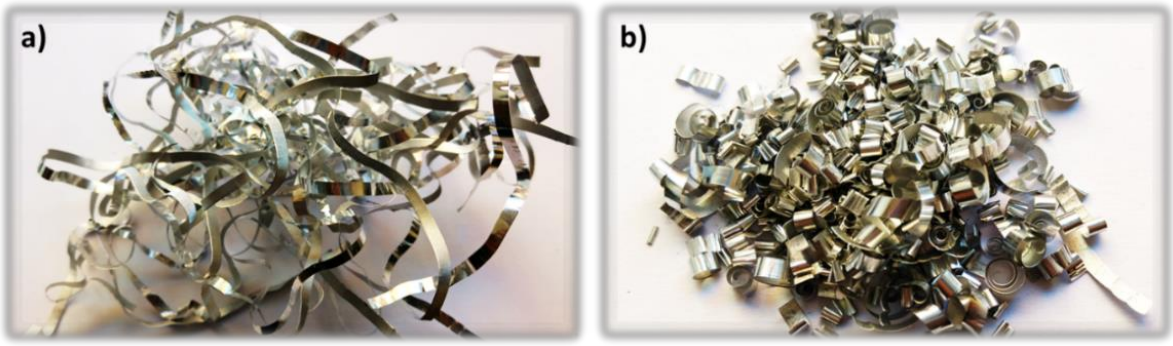

Figure 71: Chip obtained at cutting speed of 1250m/min and feed rate 0.1mm/rev; a) dry conditions, b) cryogenic conditions.

On the other hand, taking into account the main cutting force component the lower value may contradict what has been already affirmed. However, into the tool-chip contact region the cryogenic condition provided better machining conditions because the cheap breakability was better than the turning tests under dry conditions (prevails the sticking effect and burr formation due to the higher temperature). Moreover, as suggested by Figure 72, the cutting length measured on the tool used in cryogenic machining was smaller than the one showed by the rake face of the tool used under dry condition.

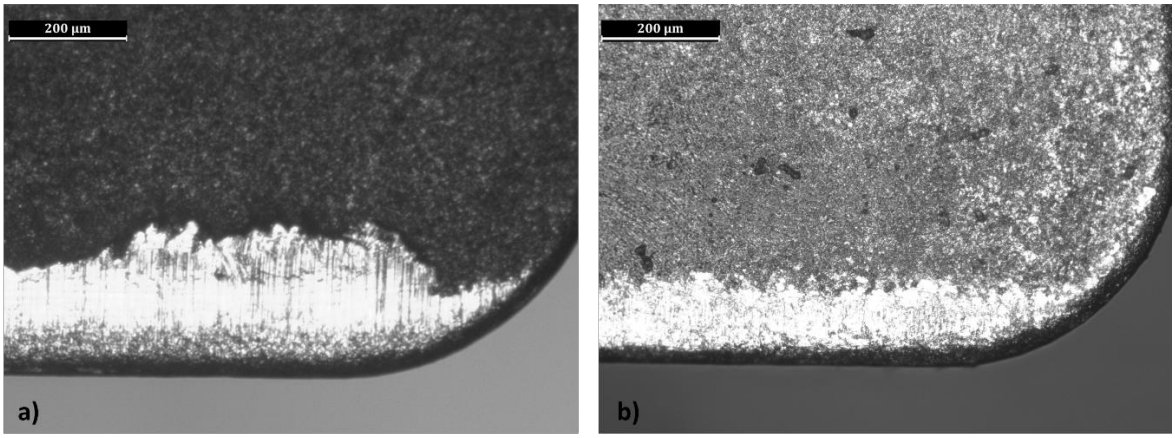

Figure 72: Rake face and worn edge at cutting speed 1000m/min and feed rate 0.1mm/rev; a) dry conditions, b) cryogenic condition.

Consequently, the lower main cutting forces measured under cryogenic condition were also due to the reduced tool-chip contact region, therefore lower pressure and forces on the tool. Sadik et Lindström 1993 based on their numerous experimental tests affirmed that reduction of the contact length led to a reduction of tool wear (as showed by Figure 72b) and cutting forces. Therefore, the cryogenic fluid played an important role in main cutting forces reductions. Bermingham et al. 2011 obtained smaller value of main cutting force during *Ti6Al4V* cryogenic machining compared with the ones measured under dry conditions and they claim that these results were due to the "cushion effect". This latter appeared when the liquid nitrogen was immediately in contact with a high temperature region that provoked the liquid to gas transition of the cryogenic fluids (Hong 2006). This cushion of gas formed between the tool and chip contact zone reducing the contact length and then the chip surface that was in contact with the tool. Consequently, as showed by Figure 72b, the wear rate was lower than the one observed on the tool employed under dry conditions (Figure 72a); therefore the friction phenomena was obviously less evident during cryogenic machining. It is now clear that the position of the nozzles as well as the liquid nitrogen delivery pressure are very important in reducing the tool-chip contact zone contributing to reduce the friction heat generation and the wear rate as well as the main cutting forces. Rotella and Umbrello 2014 and Rotella 2013 obtained similar results regarding the main cutting forces during cryogenic machining of aluminum alloy *7075-T651*. The authors affirm that the lower main cutting forces compared with the ones measured during dry tests were due to the minimal lubricant effect of the liquid nitrogen into the cutting zone in which the reduction of friction mechanisms were previously explained (Bermingham et al. 2011 and Hong 2006).

4.1.3 Temperature analysis

The temperature gradients were evaluated by an infrared thermo-camera FLIR A6000-series (Figure 68). The camera was fixed on a rigid bracket on the tool-holder. This solution permitted to keep the focus directly on the cutting zone following the movement of the tool during the entire duration of each test. Differently to the procedure used with titanium, in this activity the workpiece surface was painted with a special black tint in order to take an emissivity value close to 1 (Rinaldi et al. 2017). The signals acquired by infrared camera representative of the thermal gradient were plotted and the average values were computed in the region in which the signals reached the steady-state (Figure 33). In Figure 73a and Figure 73b are reported the averaged maximum temperatures measured during the tests at varying cutting speeds, feed rates and cooling conditions. It is clearly visible that the cryogenic machining was characterized by lower temperature compared with the dry conditions. Moreover, at lower feed rate (0.1mm/rev) the cutting speed did not influence the thermal gradient since the differences among the measured results are negligible, especially the ones referred to cryogenic machining. On the contrary, the cutting speed affected the thermal gradient when the feed rate was higher (0.3mm/rev).

The highest temperature value, namely 238 °C, was measured at cutting speed equal to 1500m/min and feed rate 0.3mm/rev under dry conditions and 82 °C under cryogenic conditions. The 65% reduction in temperature led positive benefits in terms of wear rate and tool life. When the feed rate was equal to 0.1mm/rev the 79% of reduction in temperature was measured at higher cutting speed. Reduction in thermal gradient inside the cutting zone when liquid nitrogen was delivered were also observed by Danish et al. 2017, Rotella and Umbrello 2014, Rinaldi et al. 2017.

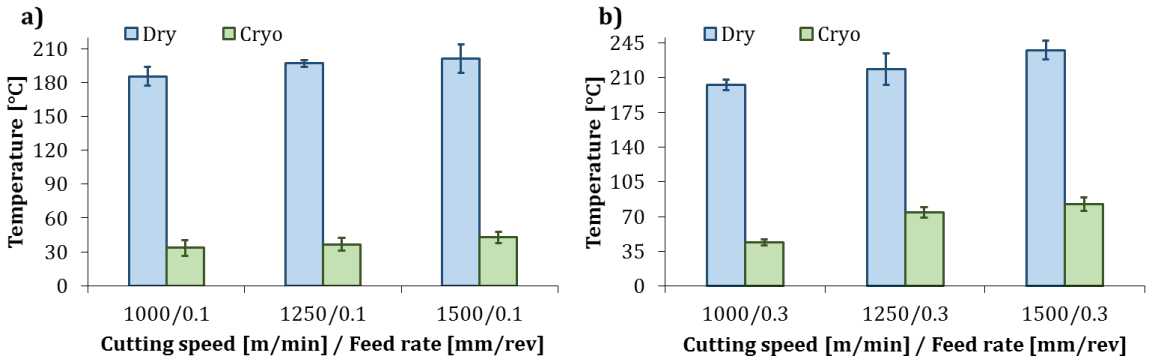

Figure 73: Cutting temperatures at varying cutting speeds and cooling conditions a) *f*=0.1mm/rev; b) *f*=0.3mm/rev.

4.2 Surface Integrity analysis

Large contribution from the researchers in studying the application of HSM to various machining processes as turning, milling, and so on of aluminum alloys was done. The high speed machining is generally able to positively affect the surface integrity of the machined parts. In fact, HSM, apart from increasing productivity, also offers the advantage of better surface finish, better chip disposal, reduction in the damaged layer, reduced burr formation, and increased machining accuracy. (Zhang and Zhao 2013). The surface integrity of the different machined parts was analyzed taking into account the two main aspects in which commonly the surface integrity is divided, i.e. external topography of surface (surface roughness) and metallurgy of the internal subsurface layers (micro-hardness, grain size analysis, phase changes or precipitation formation analysis).

4.2.1 Topography – Surface Roughness

To perform the surface topography measurements, a surface profilometer was employed (Figure 38). In Figure 74 are reported the R_a measurements carried out on the machined surface of the samples.

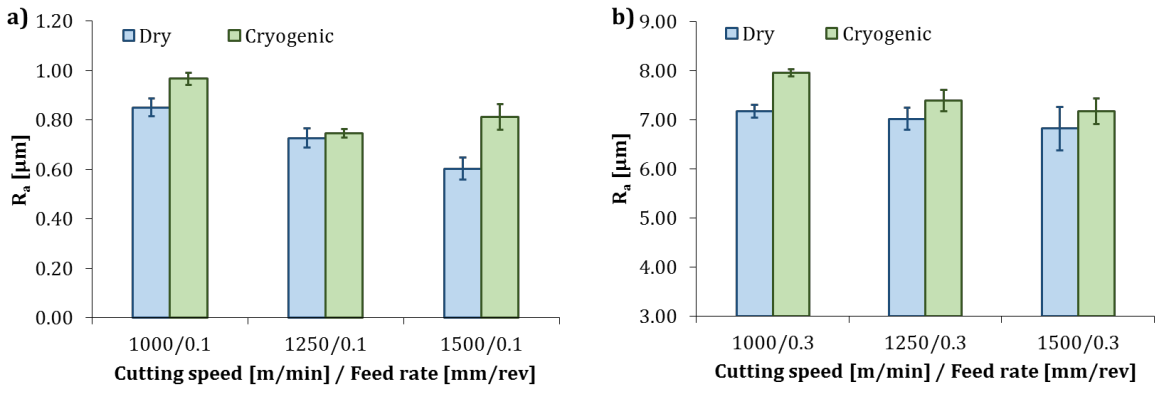

Figure 74: R_a measurements at varying cutting speed, feed rate and cooling strategy.

As showed by the results, the delivering of cryogenic fluid during machining raised the roughness surface. The feed rate equal to 0.1mm/rev provided the better surface quality in terms of surface roughness; in fact, the maximum R_a value was 0.85µm during dry machining that was lower than 1µm. Therefore, low feed rate provided very good results because low value of surface roughness, close to the semi-finishing results were almost achieved at very high cutting speeds. Moreover, further improvements were achieved just increasing the cutting speed to 1500m/min that permitted to reach a surface roughness value of 0.6µm under dry machining condition. At higher feed rate (0.3mm/rev), the surface roughness was clearly higher than the one obtained at lower feed rate. Under dry machining, the higher cutting speed permitted to reach slight improvement but the roughness was still high, therefore, the machined components need more post-process operations to improve the surface quality. Adopting the cryogenic fluid during high speed machining of *7075-T6* did not provide any improvement compared with the results obtained by dry machining. The high value of cutting speed still led to a decrease of surface roughness under cryogenic conditions but the R_a measured was higher than that measured on the dry machined samples. The reason of poor surface roughness was surely due to the very low temperature achieved during machining under cryogenic conditions. The material behavior was thermally modified moving from ductile to brittle. Moreover, as showed by Figure 75, the flank wear under cryogenic conditions was more pronounced at higher feed rate, probably due to the embrittlement of the tool at lower temperature. It is clear that the flank wear was responsible of poor surface roughness under cryogenic machining at high cutting speed regime.

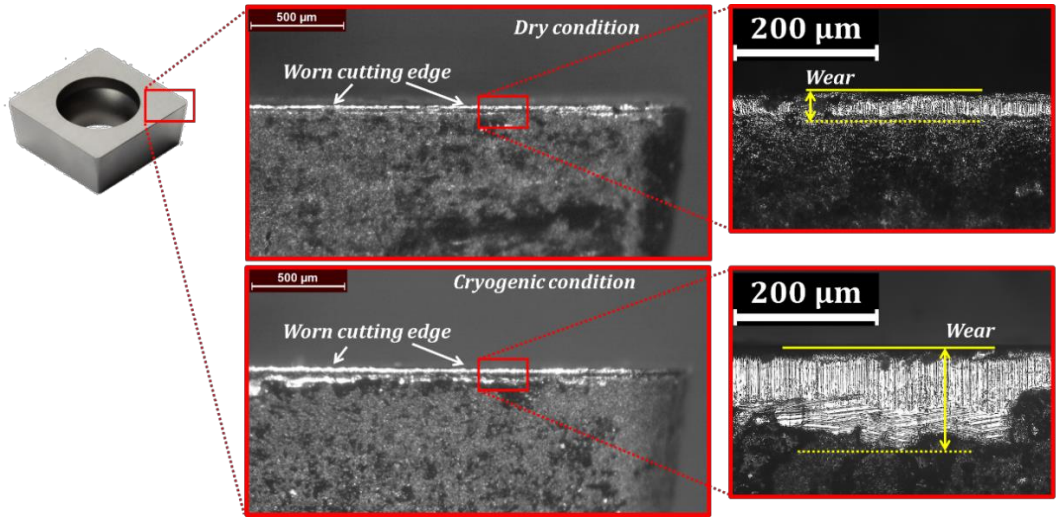

Figure 75: Flank wear at cutting speed 1500m/min and feed rate 0.3mm/rev; a) cryogenic conditions, b) dry conditions.

The obtained trends of surface roughness with different cutting parameters were also observed by Rao and Shin 2001 during high speed milling operation. Therefore, it is possible to affirm that the higher cutting speed and lower feed rate without coolant can provide lower surface roughness and therefore lower defects rate on the machined surface due to the better plastic flow of the material induced by thermal softening.

4.2.2 Affected Layers and microstructure analysis

Generally, the amount of plastic strain as well as microstructural change below the machined surface can vary significantly, depending on the machined material, the tool geometry, the cutting parameters and the presence or absence of a coolant or lubricant (Davim 2010). In this Ph.D. thesis, taking into account that the tool geometry, the tool position, the material were fixed, the thickness of the affected layer (qualitative level of plastic strain on surface and subsurface) and the grain size changes are modified only by cutting parameters (cutting speed and feed rate) and cooling strategy (dry and cryogenic).

The literature shows that the surface considerably improves when the cutting speed is high, but it is fundamental and necessary to understand the influence of the cutting parameters combinations (cutting speed and feed rate) on the surface and especially in subsurface of the machined components (Laperriere 2014). The microstructure was analyzed through optical micrographs; several samples were collected from the cross section of the machined bars (similar procedure described in Section 3.2.2, and were cold embedded in a phenolic resin (ClaroCit) provided by Struers. The advantage to use cold embedding is the possibility to avoid a thermal effect due to the metallographic preparation that can modify the metallurgy of the samples. Generally, this procedure is suggested with the materials that could be easily modified by heat source, such as aluminum alloy. After the embedding steps, the specimens were grinded and polished following the procedure reported in Table 8.

Table 8: Grinding and polishing procedure to prepare the *AA7075-T6* samples to metallographic analysis.

Type of material	Fluid	Time [s]	Force [N]
SiC Foil 180	Water	60	25
SiC Foil 320	Water	60	25
SiC Foil 500	Water	60	25
SiC Foil 1200	Water	60	25
SiC Foil 2000	Water	60	25
MD-Largo	DiaPro Largo 9µm	240	25
MD-Mol	DiaPro Mol R 3µm	180	25
MD-Chem	OP-U 0.04µm	60	15

After the polishing step, the samples were chemically treated by etchant (Keller's reagent: 10mL HF, 25mL HNO_3, 15mL HCl, 50mL distilled H_2O) (Warmuzek 2004) in order to show the microstructure under light optical microscope (OM) (LEICA DFC 320). Several images of the machined cross sections parts were acquired via OM and the dimension of the layer thickness where the microstructure drastically changes and grain size variations (equiaxial grains) were measured. In Figure 76 and Figure 77 are reported the grains size variations measured from the machined surface into the depth of the dry and cryogenic machined samples.

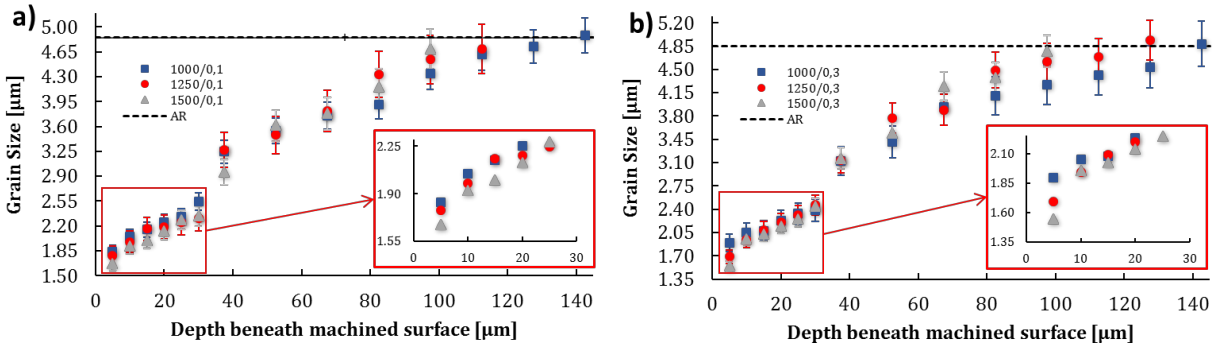

Figure 76: Grain size variation from the machined surface through the depth of the specimens manufactured under dry conditions at varying cutting parameters.

The average value of the grain size of the as-built material (not machined) was equal to 4.85µm. As showed by Figure 76, the high speed machining led to an important grain refinement. The grain size was very small close to the machined surface and increase going into the bulk material. Observing Figure 76a and Figure 76b, it is clearly visible that the cutting speed governs the grain refinement rate and the variation of the layers thickness where the microstructure changes.

In both cases, at high and low feed rate, the increase of the cutting speed led to decrease the grain refinement layers. In detail under dry machining conditions, this layer varied from 97µm to 142µm and slightly increased when the feed rata increased (Figure 78). Moreover, when the feed rate was equal to 0.3mm/rev the cutting speed variation led to different grain refinement rate as showed by Figure 76b, in fact, increasing the cutting speed the grain size near the machined surface was smaller.

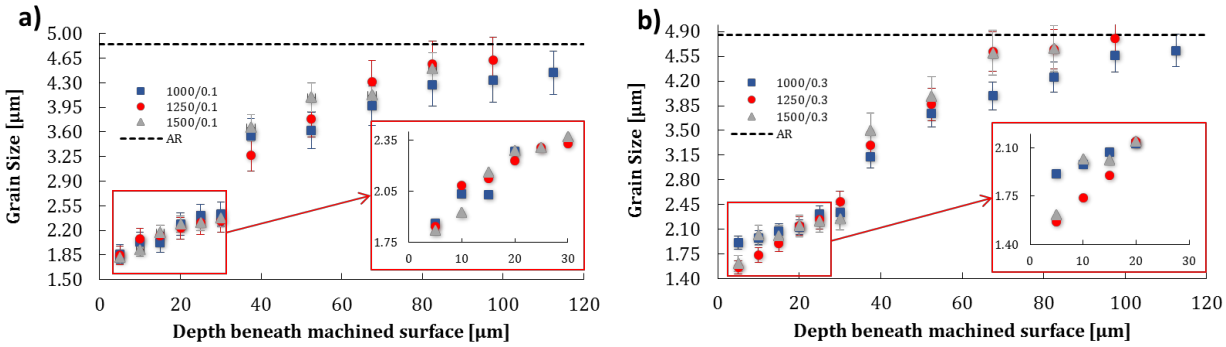

Figure 77: Grain size variation from the machined surface through the depth of the specimens manufactured under cryogenic conditions at varying cutting parameters.

In Figure 77 the grain size variation measured on the cryogenic machined samples are reported. The trends are almost equal to those reported in Figure 76; however, some considerations can be done. In fact, it is clearly visible that the cryogenic fluids delivered on the fresh-machined surface and into the cutting zone affected the material layers and the microstructure changes. Indeed, as showed by Figure 78, the altered layers provoked by cryogenic machining were smaller than those measured on the dry machined specimens. Mohan et al. 2016 studied the *7075-T6* mechanical behavior at room temperature and after shallow cryogenic treatments. The experimental results showed high ductility (% elongation ≈ 11%) at room temperature but after cryogenic treatments the ductility decreased (≈ 7%) while the strength increased. Based on Mohan's results, it is possible to affirm that the material behavior under cryogenic machining is more brittle than ductile, consequently, the material fails under tool action easily being able to absorb lower plastic deformations before reaching the fracture. This result is also justified by the lower main cutting force measured under cryogenic machining (Figure 70a).

At lower feed rate, the altered layer varied from 82µm to 112µm and increasing the feed rate, the altered layer thickness did not change drastically but was slightly higher.

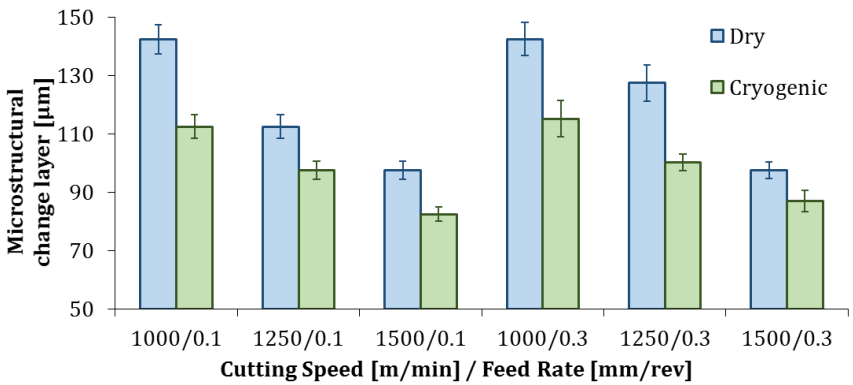

Figure 78: Thickness of the material layers where the microstructure changes due to the machining process.

The optical micrographs analysis permitted to obtain the grain size distributions graphs showed in Figure 76 and Figure 77. In detail, in Figure 79 some micrographs of the microstructure are reported. They are related to the cross section of the machined workpiece at cutting speed 1000m/min and different feed rate and cooling conditions. Focusing on Figure 79a, the machining operation led to the formation of new recrystallized grains (green box labeled with the letter A) that surrounded the plastically deformed old grains (red box labeled with letter B). The green box that is visible in all the micrographs, is representative of the regions where dynamic recrystallization (DRX) occurred close to the machined surface. The micrographs show also the pancake-type grains (white grains) and the dispersed second phase (dark grains). The very small grains indicated by the green box show slight differences in dimensions depending on the cutting parameters (cutting speed and feed rate) and cooling conditions (dry and cryogenic). At lower feed rate 0.1mm/rev and cutting speed equal to 1000m/min (Figure 79a and Figure 79b), the grains inside the green box were slightly smaller in the cryogenic machined sample than the ones obtained under dry machining. These new grains, under cryogenic machining nucleated and grew around the grain boundary. On the other hand, the recrystallized grains inside the green box of the dry machined sample (Figure 79b and Figure 79d) nucleated and grew into the prior plastically deformed grains and they were more equiaxed shape suggesting the grain growth thermally induced. This suggests that the very low temperature permitted to avoid any local grain growth and recovery thermally induced phenomena. Focusing on Figure 80a and Figure 80b, although the cutting speed was equal to 1500m/min and then higher than 1000m/min, the small grains and their size inside the green box were almost comparable to those showed by Figure 79a and Figure 79b. However, it is important to highlight that the density of the smaller grains considerably changed. In fact, the number of small grains (inside the green box) in the micrographs related to cryogenic machining was higher than the ones related to dry machining (Figure 79 and Figure 80).

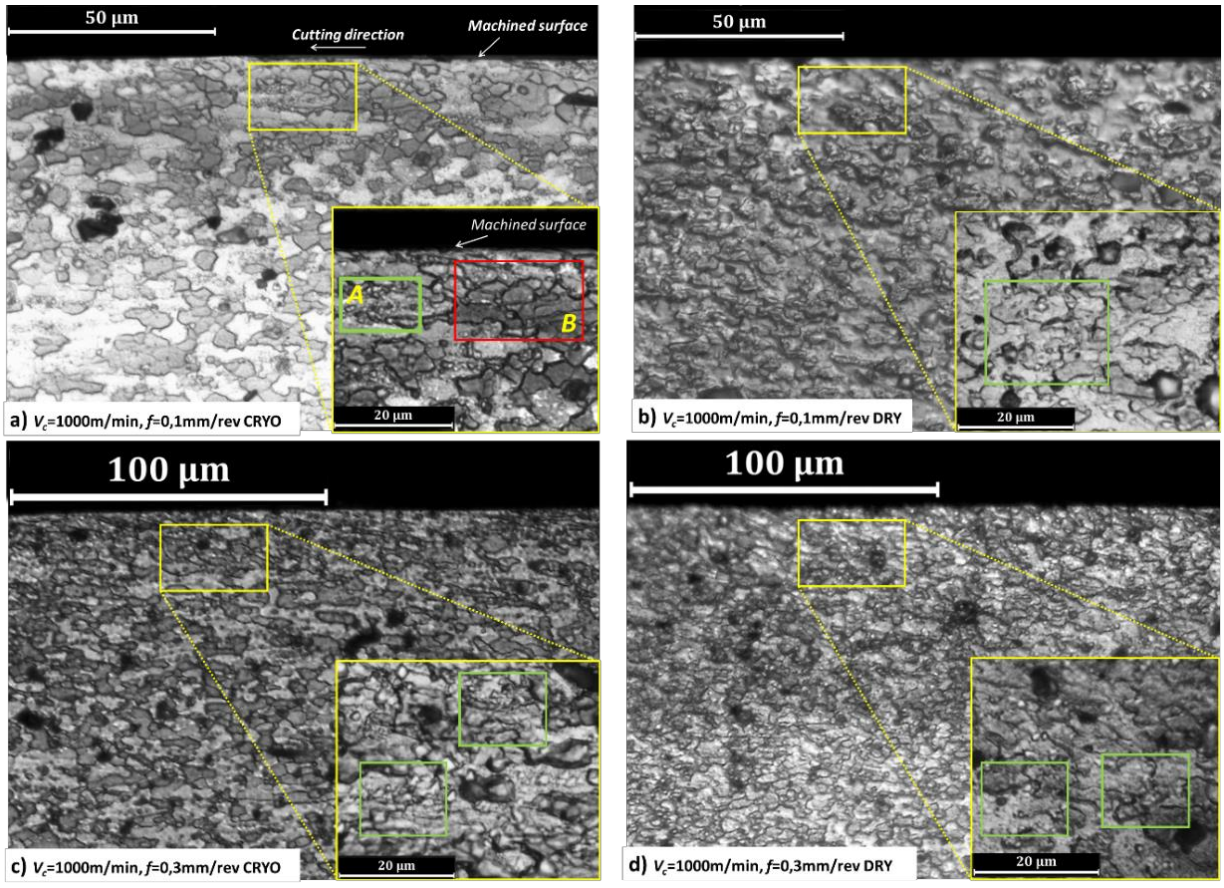

Figure 79: Optical micrographs of the cross section at cutting speed 1000m/min and varying feed rate and cooling strategy.

As reported by Lee and Lin 2016, at very low temperature, the increase of dynamic load (range of strain rate $1000s^{-1}$-$5000s^{-1}$) during impact tests on *7075-T6* samples provoked a decreasing of the grains size and their dimensions were slightly lower at -196 °C than those measured after the tests at 0°C. However, the grain size reduction is mainly governed by the strain-rate. In machining, the increase of the cutting speed can be considered as an increment of the strain-rate on the workpiece due to the tool action; therefore, at high cutting speed a higher grain refinement is expected. Rotella et al. 2013 analyzed the machined surface at varying cutting parameters founding that at higher cutting speed the grains size was smaller than that machined at lower cutting speed. They found that the higher strain rate and temperature developed at high cutting speed led to high Zener-Hollomon parameter that means lower grain size. This experimental evidence based on calculation of Zener-Hollomon parameter was also confirmed by Tsuji and Maki 2009.

In the presented graphs (Figure 76 and Figure 77), the machining operation led to a grain size reduction that was slightly higher at high cutting speed. The possibility to modify the entity of the microstructural changes depending on the cutting speed and feed rate during dry turning machining was also reported by Tabei et al. 2016. The authors also provided a finite element model to describe the microstructure evolution during the machining process. Moreover, the cryogenic liquid delivered on the fresh machined surface avoided the recovery phenomena (Figure 79a, Figure 79c, Figure 80a and Figure 80c), therefore, smaller grains and a greater grain boundary numbers were present.

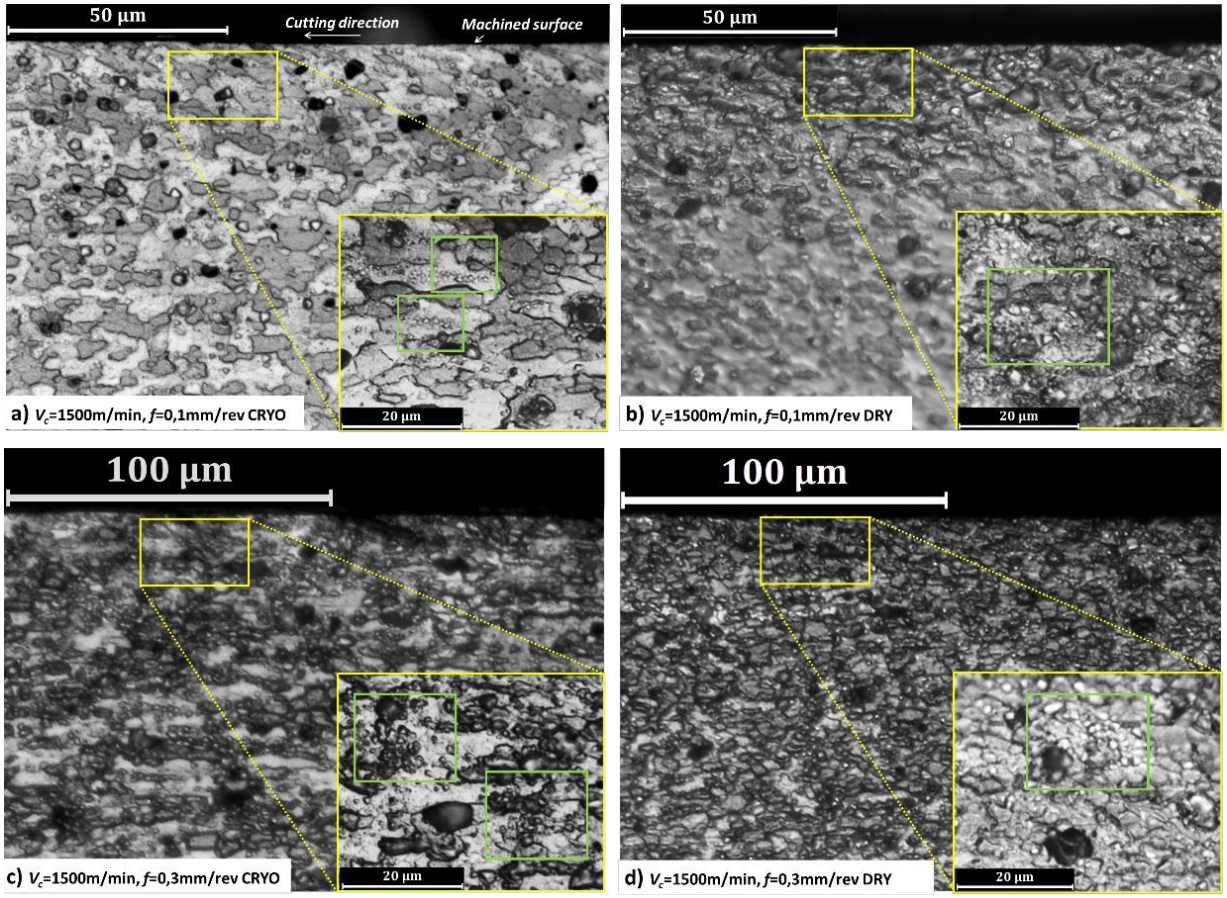

Figure 80: Optical micrographs of the cross section at cutting speed 1500m/min and varying feed rate and cooling strategy.

The ability of the low temperature, generally in cryogenic range, to avoid any dynamic recovery phenomena was observed in other manufacturing process such as cryorolling and ECAP (Abbasi-Baharanchi et al. 2017, Mohan et al. 2016, Fritsch et al. 2012).

In their work was observed that the deformation process in cryogenic condition led to higher amount of smaller grains due to the lack of dynamic or static recovery phenomena induced by high temperature. Furthermore, higher accumulation of dislocation density as well as precipitates were also observed by TEM and XRD analysis.

4.2.3 X-Ray Diffraction analysis (XRD)

The XRD analysis was carried out following the same procedure explained in Section 3.2.3. The X-Ray scanned by angle/step of 0.05 in a range from 15° to 100° on the machined surface penetrating the sample in depth (almost 70µm) within the AL zone. The registered patterns represent the peaks due to the diffracted beams from the crystallographic planes oriented orthogonally to the incident beam. Since in high performance aerospace Al-alloys, the precipitation-hardening and microstructure play a key role in the final properties, through the XRD analysis it is possible to better understand and study their evolution and changes depending on the process parameters (cutting speed, feed rate and cooling conditions). In Figure 81 and Figure 82 are reported the XRD profiles obtained analyzing the machined surface of the samples taking also into account the as-built XRD profile.

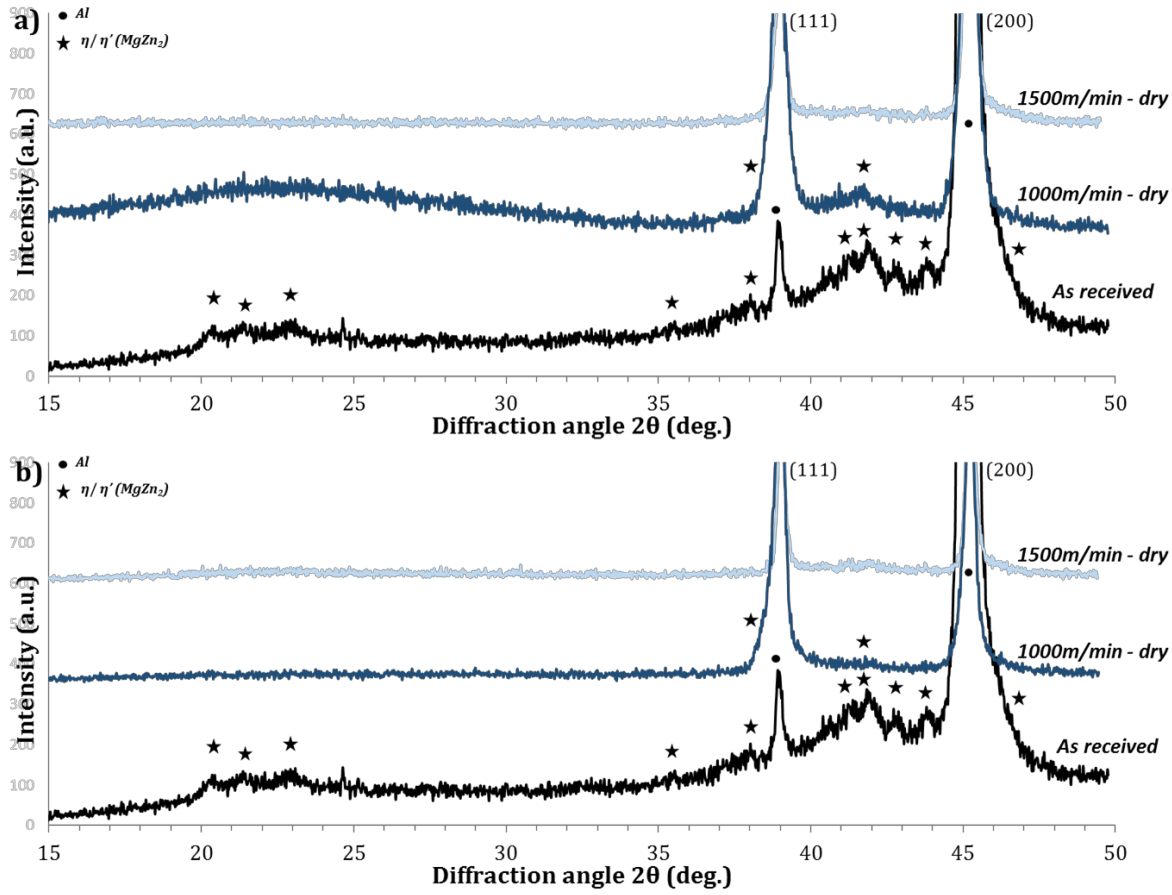

Figure 81: X Ray diffraction profiles at varying cutting speed; a) feed rate 0.1mm/rev; b) feed rate 0.3mm/rev (Dry conditions).

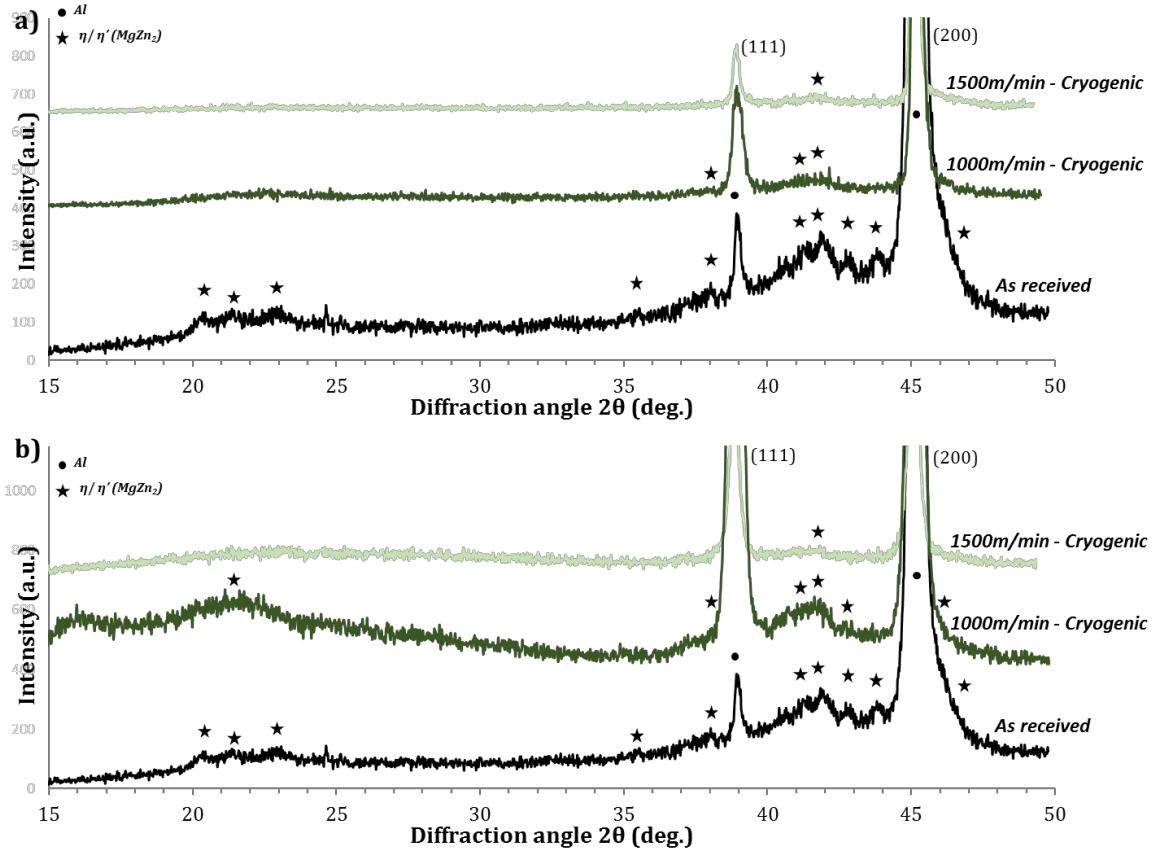

Figure 82: X Ray diffraction profiles at varying cutting speed; a) feed rate 0.1mm/rev; b) feed rate 0.3mm/rev (Cryogenic conditions).

Even though the analysis was performed between 2θ angles of 15°-110°, only the range of the patters where some variations were observed are reported in this Ph.D. thesis. Taking into account the XRD profile of the as-built material (black line), the material provided by the supplier was characterized by broad peaks at about 2θ = 20° correspond to the GP zones. In this region, weak peaks were slightly pronounced and they represented the metastable precipitates η' that were gradually moving to stable precipitates η. The same results were shown by the region between 2θ angles of 40°-45°. A similar pattern was also reported by Zhao et al (2004). Taking into account Figure 81 and Figure 82, the machining process clearly induced some metallurgical changes in terms of precipitates. Considering the machining tests performed under dry conditions with low feed rate (Figure 81a), the cutting speed 1500m/min produced higher thermal gradient (temperature close to 200°C) than that produced at cutting speed of 1000m/min. Therefore, the GP zones were dissolved (DeIasi and Adler 1977) and the precipitation from metastable η' to η did not appear due to the very small time exposition of the alloy to these temperatures. In fact, as reported by DeIasi and Adler 1977, at a temperature close to 200°, the Differential Scanning Calorimetry (DSC) provided a first peak temperature (endothermic) and coupled with TEM observations concluded that the GP zone dissolution was the predominant reaction. Moreover, the (111) aluminum peak appeared slightly broadened and this suggested the microstructure refinements as well as high distortion of the lattice. At lower cutting speed, namely 1000m/min, the temperature did not reach 200°C and the GP zone into the matrix was not dissolved, indeed the small peak at 20° was still captured by XRD. On the contrary, at higher feed rate (0.3mm/rev, Figure 81b), the higher temperature reached in both cases at 1000m/min and 1500m/min induced the dissolution of the GP zone.

Similar results, but different in intensity are shown in Figure 82. During the machining test under cryogenic conditions, at low and high feed rate, the cutting speed still has a predominant role in metallurgical modifications.

Taking into account the feed rate equal to 0.1mm/rev (Figure 82a), the amount of precipitate was higher than that observed under dry conditions. The lower temperature immediately avoided the material to be exposed to high thermal gradient and the very small amount of $MgZn_2$ was still evident also when cutting speed of 1500m/min was applied. The broadening of the peaks at 2θ angle between 40° and 45° suggested that the precipitates had very small size (sub micrometer). When higher feed rate (0.3mm/rev) was used (Figure 82b), even though higher temperature were developed, the liquid nitrogen helped to not overcome the 200°C, therefore, the GP zones were still evident at 20° (1000m/min of cutting speed). The $MgZn_2$ amount was higher compared to that qualitatively observed in Figure 82a. Even though higher temperature were induced by higher feed rate, the very low temperature induced by cryogenic fluid helped to delay the dynamic aging. As stated by Abbasi-Baharanchi et al. 2017, on the cryogenically treated sample, the precipitate still remained while in the heat treated one no precipitate peaks were evident suggesting that the complete dissolution happened. Similar results were also confirmed by Mohan et al. 2016 on their samples treated by shallow cryogenic technique. They observed second-phase intermetallic particles in the treated and not treated sample but the higher amount of precipitated second-phase particles on the cryogenically treated samples were confirmed by the XRD and Electron Back Scattered Diffraction analysis.

4.2.4 Surface and Subsurface hardness

The micro-hardness measurements were carried out on the cross section and on the surface of the samples collected from the machined bars. The type of micro-hardness measured was Vickers ($HV_{0.01}$) and the measurement parameters used were dwell time of 15s and a load of 10g. The same experimental set-up showed in Figure 61 was employed. Initially, some matrix of 50 points into the bulk material were set in order to measure the as received micro-hardness. Subsequently, the measurements on the machined surface and into the cross sections were carried out.

The as received micro-hardness was equal to 165 $HV_{0.01}$ that is in agreement with the one suggested by the enterprises for aerospace applications.

To provide insight into the relationship between the mechanical response modification induced by machining operation and the grain size and precipitation phenomena, it is necessary to observe and report in a comprehensive manner the similarities and differences between the data obtained (X-Ray diffraction and grain size analysis). In Figure 83 the micro-hardness measurements carried out on the machined surface depending on cutting parameters and cooling strategy are shown.

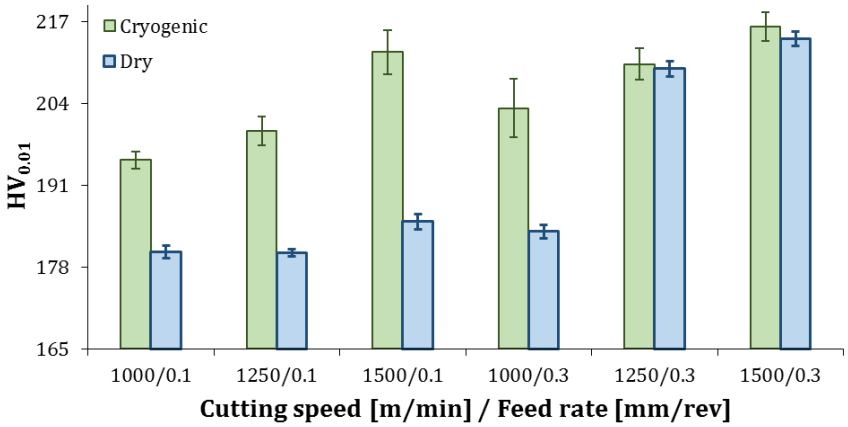

Figure 83: Micro-hardness measured on the machined surface at varying cutting parameters and cooling conditions.

The machining process clearly enhances the surface hardness in all the case analyzed. Taking into account the dry machining, the surface hardness did not show a prominent variation at varying cutting speed with low feed rate (0.1mm/rev), on the contrary, the cutting speed was mainly responsible of this variation when the feed rate was increased to 0.3mm/rev.

In fact, varying the cutting speed from 1000m/min to 1500m/min at low feed rate, the difference in micro-hardness was equal to 2.5%, while at high feed rate this difference was equal to 17%. The cryogenic fluids delivered during machining permitted to increase the surface hardness also with low feed rate. Moreover, the highest cutting speed at lower feed rate permitted to reach almost the same hardness measured with the highest feed rate under cryogenic conditions. The highest increment of micro-hardness at low and high feed rate was provided by the highest cutting speed coupled with cryogenic fluids and was equal to 29% and 31% respectively. It is important to highlight that the high feed rate and cutting speed under dry conditions permitted to reach surface hardness similar to those measured on the cryogenically machined samples. Finally, the surface hardness measured on the sample cryogenically machined with low feed rate and cutting speed equal to 1500m/min, was high and comparable with the one obtained at higher feed rate. The advantage in this case was represented by the feed rate (very low) that permitted to obtain at the same time a better surface quality due to the low surface roughness (Figure 74a). Rotella et al. 2014 also reported the positive effect of the cryogenic machining. The authors ascribed the higher surface hardness mainly due to the evident grain refinement (dynamic recrystallization) induced by the cutting tool and the low temperatures avoid any grain growth phenomena.

To better understand the physical reasons about the hardness variations, the XRD results provided very interesting evidences. These latter were helpful to understand, for example the hardness differences measured on the machined samples under dry and cryogenic conditions at low and high cutting speed. Taking into account the low feed rate value, namely 0.1mm/rev, at cutting speed equal to 1000m/min, the higher hardness measured on the cryogenically machined sample was mainly due to the contribute of grain refinement and precipitates ($MgZn_2$), as suggested also by Figure 79a and Figure 82a. At higher cutting speed (1500m/min), the very small grains mainly contributed to the hardness changes but again, under cryogenic conditions some precipitates ($MgZn_2$) were still present even though in small amount.

This observation was more evident at higher feed rate (0.3mm/rev), in fact with cutting speed 1000m/min, the hardness differences between the dry and cryogenic machined samples were evident. In particular, the XRD of the cryogenically machined samples showed higher peak intensity in the precipitation region compared with the dry on (Figure 82b and Figure 81b). At higher cutting speed (1500m/min) the XRD profiles were almost the same even if in Figure 82b, a very small amount of precipitate was still evident justifying the slight higher hardness of the sample machined under cryogenic conditions. Therefore, it was possible to understand that the hardness changes was due to a double contribution represented by grain refinement and precipitation strengthening. At higher cutting speeds, under dry conditions the major contribution to the hardness was represented by the grain refinement due to the high thermal gradient that trigger the precipitates dissolution. This later did not happen when liquid nitrogen was delivered into the cutting zone, therefore higher hardness was measured because both grain refinement and precipitation strengthening were presents.

Generally, the grain refinement strengthening is usually described by the Hall-Petch relation while the precipitation strengthening results from the precipitate's ability to inhibit the dislocation motion (Zhao et al. 2004). Mohan et al. 2016 observed higher percentage of precipitates in the cryogenically treated sample and confirmed their presence by XRD and EDS analysis. They also affirmed that the dislocation density in the cryogenically treated sample was higher due to the suppression of recovery phenomena induced by very low temperatures. Fritsch et al. 2012 affirmed that the *7075* material behavior under cryogenic conditions was able to accumulate more plastic deformation due to the higher work hardening capability. This behavior led to higher accumulation of density dislocation during the severe plastic deformation processes leading to stronger material.

Moreover, at higher feed rate, the precipitation strengthening was more evident on the cryogenically machined sample than the dry ones. In these latter, the major contribution to the hardness was represented by grain refinement. In Table 9 are summarized these results.

Table 9: Precipitates and grain refinement contributions to hardness at varying cutting parameters and cooling strategy.

Feed rate	Cutting speed	Dry	Cryogenic
0.1mm/rev	**1000m/min**	$MgZn_2$ + Grain refinement	$MgZn_2$ + Grain refinement
	1500m/min	Grain refinement	$MgZn_2$ + Grain refinement
0.3mm/rev	**1000m/min**	(small contribute) $MgZn_2$ + Grain refinement	$MgZn_2$ + Grain refinement
	1500m/min	Grain refinement	$MgZn_2$ + Grain refinement

It is also important to highlight that the tool action induced severe plastic deformation into the machined material. Therefore, coupled with the grain refinement and precipitates, the accumulation of dislocation density was also a clear contribution to the hardness. Even though more sophisticated and advanced analysis, as TEM coupled with XRD, are required to assess the presence and to quantify the dislocation density variations, the literature clearly shows what previously affirmed. Chen et al. 2017 investigated the microstructural alterations induced by high speed machining of aluminum alloy *7055*. The results showed that under the thermomechanical effect of the high strain, high strain-rate and instantaneous high temperature shear deformation, the surface adjacent coarse-grained layer transformed to a gradient nanostructured layer characterized by equiaxed and lamellar nanograins and ultrafine grains surrounded by coarse grain boundaries precipitates. Moreover, in the region of material very close to the machines surface, the authors observed dislocation boundaries and nano recrystallized grains highlighting that the dislocation activities and dynamic recrystallization are two dominant approaches for grain refinement.

In Figure 84 and Figure 85 are reported the hardness profiles related to the hardness variation from the machined surface to the bulk material. The results clearly demonstrate that the high speed machining allowed the material to reach a high hardness also in depth beneath the machined surface up to almost 200μm. In general, the figures show that the increase of the cutting speed at fixed feed rate leads to a decrease of the altered hardness layers, however these variations are very small. On the contrary, the feed rate governs the altered layers thickness and at higher feed rate correspond deeper altered layers. Comparing Figure 84b and Figure 85b, the cryogenic machining permitted to reach stable altered layers that are almost independent from the cutting speed, moreover, the hardness close to the surface was higher than those measured on the dry machined samples. This latter result was more evident comparing the results related to the low feed rate (Figure 84a and Figure 85a). Generally, the decreasing of the altered layers at high cutting speed is normally due to the relative speed between the tool and the workpiece. When the cutting speed is increased, the temperature and the thermal gradient in the cutting tool (also in the chip) increases and the specific force decreases, therefore the affected depth of the workpiece subsurface is reduced due to the lower induced subsurface stress (Neugebauer et al 2011).

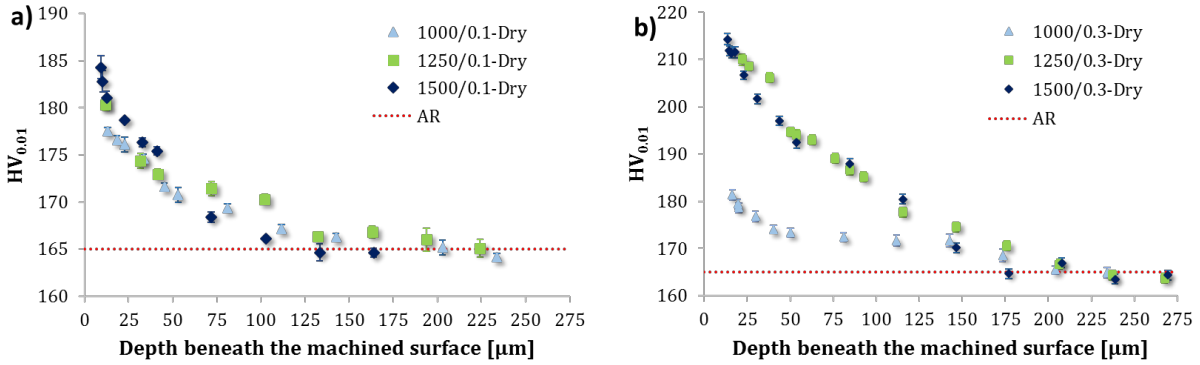

Figure 84: Micro-hardness variation from the surface through the depth of the machined parts at varying cutting speed and feed rate under dry conditions.

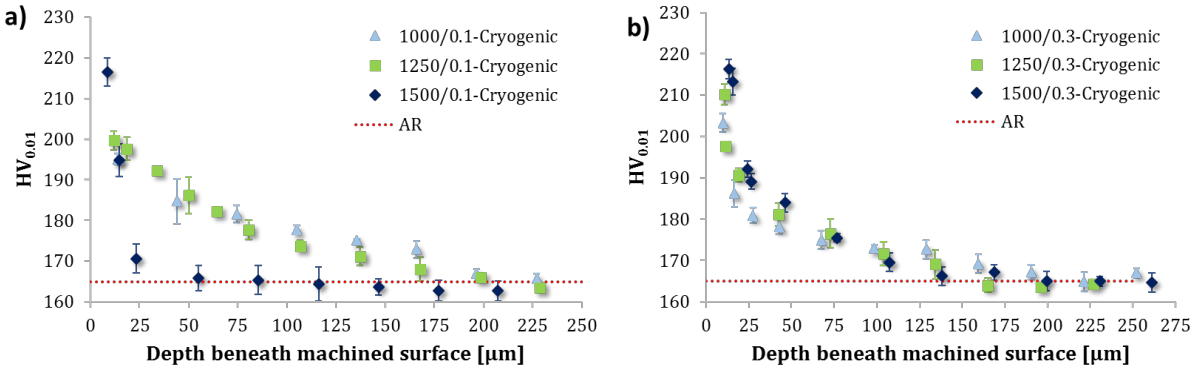

Figure 85: Micro-hardness variation from the surface through the depth of the machined parts at varying cutting speed and feed rate under cryogenic conditions.

The overall results obtained highlight the high feasibility to perform high speed machining on one of the stronger aluminum alloy, namely *7075-T6*, mainly applied to produce aircraft structural parts.

The Ph.D. thesis showed that the machining process, performed under dry and cryogenic conditions depending on the cutting parameters, permits to achieve interesting results that are useful to improve the machining process and the surface integrity. The application of high feed rate can surely reduce the time production due to the higher material removal rate but, as shown by the previous results, the surface integrity might be compromised. In particular, the machined sample at higher feed rate showed higher temperature favoring the precipitate dissolution and consequently the loss of hardness amount caused by the precipitate presence. However, a part of this hardness fault is compensated by the grain refinement phenomena. On the other hand, the machining process at lower feed rate permits to achieve smoother and higher quality surfaces characterized by very low surface roughness. Moreover, even though the grain size is not severely reduced, the presence of precipitate can contribute to keep the surface material harder than the not machined part. In addition, the use of liquid nitrogen during the machining process leads to a significant improvement of the surface hardness even at lower feed rate. In fact, as also reported by Fritsch et al. 2012 the cryogenic conditions make the material able to accumulate more density dislocations and consequently higher strength is expected. Moreover, the rake face of the tool resulted less worn than the one observed on the tool used during dry machining. This result suggests that the tool life is improved as well and the broken chips obtained under cryogenic conditions can reduce the entanglement of chips around the spindle that provokes useless delays in production and possible damage to people and products. The quality of the products, in according with the literature, could be also improved in terms of fatigue life and resistance.

The fatigue tests conducted on the cryogenically treated sample by Mohan et al. 2016 showed that higher fatigue life and strength were achieved thanks to the better structural rearrangements of the precipitates $MgZn_2$ and well refined microstructure.

Moreover, the literature highlighted the more accumulation of dislocation density in the aluminum alloy cryogenically treated; this result could justify the higher presence of precipitates when liquid nitrogen is delivered during machining. In fact, as reported by Gubicza et al. 2007, the regions with high dislocation density produced by plastic deformation accumulation represent nucleation sites for precipitates.

4.3 Equal Channel Angular Pressing and machining process on aluminum alloy

Recently, the study and understanding of surface integrity of various materials after machining is becoming an interpretative key to quantify a product's quality and life cycle performance. The possibility to provide fundamental details about the mechanical response and the behavior of the affected material layers caused manufacturing operations can help the designer to produce parts with superior quality (Jawahir et al. 2011). It is well known that during the severe plastic deformation processes the metal materials are subjected to high strain and stress conditions that often lead to several modifications of the mechanical properties. Among the numerous severe plastic deformation processes, the Equal Channel Angular Pressing (ECAP) was particularly preferred by the researchers due to its ability to induce high strain and grain refinements without modify the cross section and the shape of the workpiece (Figure 86). Segal and colleagues originated this process in the 1980s at Minsk in the former USSR (Langdon 2011, Sanusi et al. 2012). The dimensions of the ECAPed samples commonly range in the order of some centimeters (cross section), therefore the metallurgical analysis are quite easy to perform since the region of interest is wide.

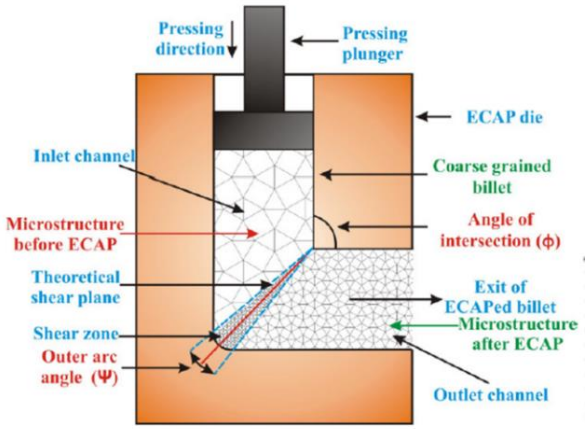

Figure 86: Principle of ECAP (Sahai et al 2017).

Recently, Klenosky et al. 2017 have performed a SPD processes known as Large Strain Extrusion Machining on *7050* aluminum alloy. The process consists to induce plastic deformation, similar to the ones imposed by ECAP, simply constraining the chip formation with an upper complementary tool. The main results are obviously a strong grain refinement with ultra-fine or nanograins, higher hardness than the one evaluated into the bulk material, higher yield and ultimate stress and higher corrosion resistance. From several researches available in literate it has been stated that the aluminum strengthening due to severe plastic deformation is a combination of some metallurgical phenomena such as solid solution, grain refinement, variation in density dislocations and precipitation (Shaeri and Ebrahimi 2016, Shaeri et al. 2015, Zhao et al. 2004). Although these phenomena could happen in machining, the possibility to investigate their nature, their evolutions and accurately quantify them in the very thin affected layers is usually very difficult. The research activity developed in this Ph.D. work aims to develop an ECAP experimental set-up to induce SPD on *7075-T6* in order to improve its mechanical properties. Subsequently, orthogonal cutting tests at speeds relatively similar to those adopted during ECAP tests were also performed in order to find possible links regarding induced microstructural and hardness changes between machined surface layer and SPD-bulk material.

This scientific investigation aims to establish the basis for an innovative method to study and to quantify metallurgical phenomena that occur beneath the machined surface of bulk material. This part of experimental activities were performed in cooperation with the KIT Karlsruhe Institute of Technology in Germany under the supervision of Prof. V. Schulze and the WBK research group.

4.3.1 Design of the ECAP die

The conventional ECAP die consists of two channels of equal cross section which intersect at 90° or 120°. The material is passed through one end of the channel and allowed to or pulled from the other end (Figure 87).

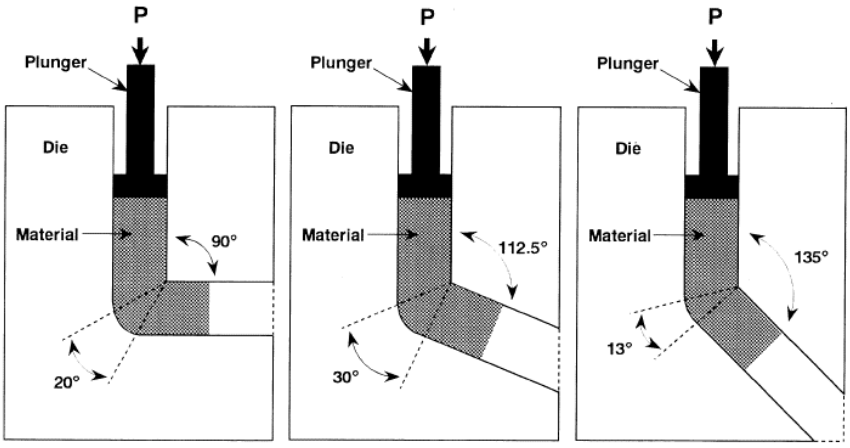

Figure 87: Schematic illustration of dies used at varying corner angles (adapted from Nakashima et al. 1998.

In this research activity, the ECAP die was formed from two channels of same cross-section and intersecting to form a 90° corner. The decision of the 90° angle is based on the results provided by Nakashima et al. 1998 in which they affirmed that the best ultrafine microstructure was achieved using a die having channel angle of 9°. Moreover, taking into account the Equation 3 proposed by Iwahashi et al. 1995, the strain is close to a value of 1.15 when the channel angle is equal to 90° and the imposed plastic strain decreases when this angle increases.

$$\varepsilon_N = N\left[\frac{2cot\left(\frac{\varphi}{2}+\frac{\theta}{2}\right)+\theta cosec\left(\frac{\varphi}{2}+\frac{\theta}{2}\right)}{\sqrt{3}}\right] \quad (3)$$

Where N represents the number of pass of the workpiece inside the ECAP die, φ is the inner angle and θ is the outer angle of the channel, ε is the plastic strain. In the adopted design, the inner angle was sharp and equal to 90° while the outer angle was equal to zero. The cross section of the channel was square with 14mm side. In Figure 88 are reported the single components of the die and the supports designed to keep it during the ECAP test. The ECAP die consisted of some components showed by Figure 88a. In detail, the ECAP die consisted of "1" that represented the pin where the sample, positioned inside it, was guided into the die; "2" was the frontal part of the die and was linked to the part "3" (back part) through high resistance screw 12.9. Part "4" was the named as "sandwich", it was linked to the part "3" and together with the pin was directly involved into the deformation process. The ECAP die was sustained by a bottom support showed in Figure 88c. Figure 88b represents the experimental set-up that consisted of the ECAP die, the 50ton press and a data acquisition system station. In detail, the load was monitored during the tests in order to understand if the process was in a steady state condition.

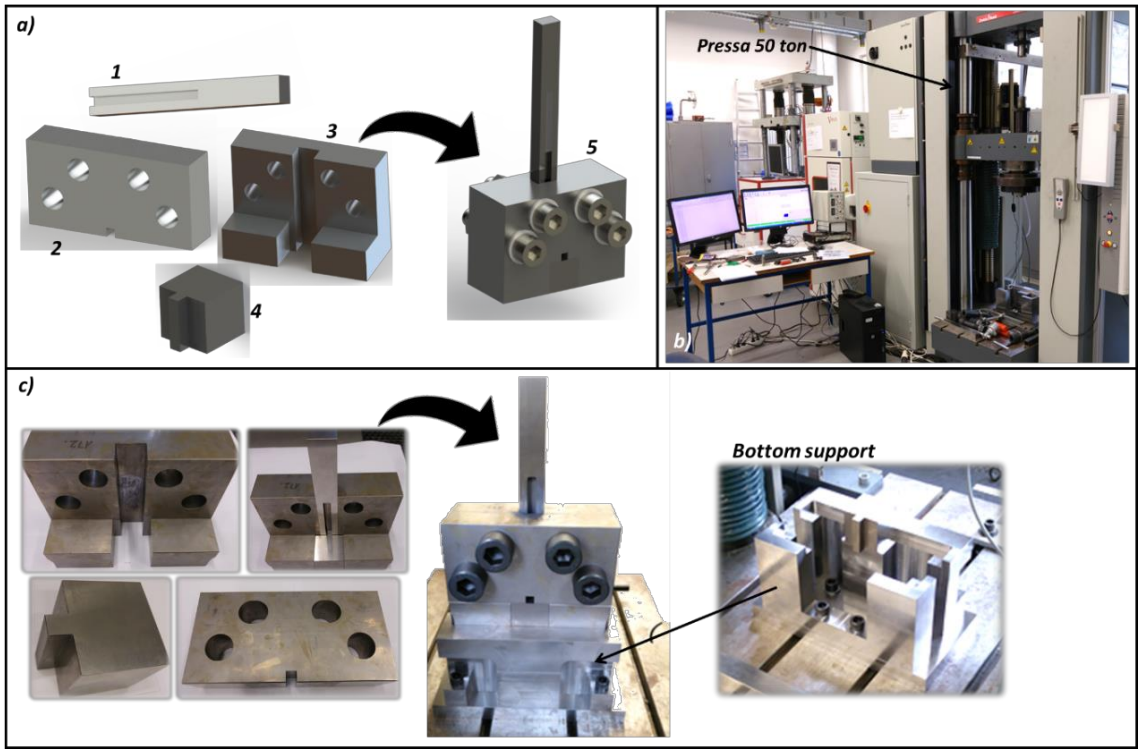

Figure 88: a) the designed ECAP components in CAD environment; b) 50ton press and experimental set-up with pc acquisition data system; c) The ECAP experimental set up realized.

4.3.2 ECAP tests on *AA7075*

The samples were characterized by prismatic shape with square cross section of 14mm side and 120mm length. The material investigated as previously mentioned was the aluminum alloy *AA 7075-T6*. Each sample was heated to 100 °C for 2 hours and cooled in furnace in order to reduce the residual stress induced by lamination and to homogenize the microstructure. The sample and its microstructure visible in cross section are reported in Figure 89.

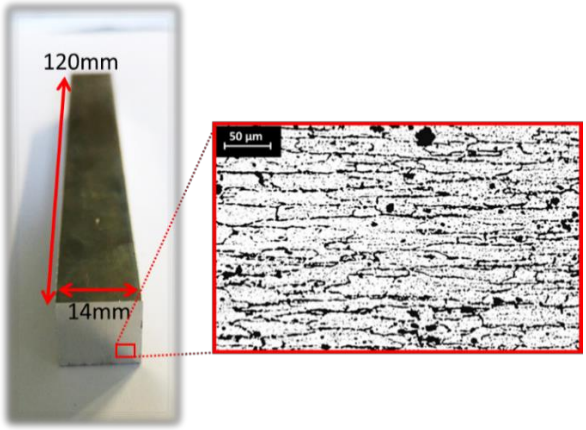

Figure 89: The prismatic sample used to perform ECAP test and the as received microstructure.

The ECAP test were performed at room temperature on a Zwick/Roell ZMART.PRO 50 ton (Figure 88b) press and each sample was processed one time in order to replicate the strain conditions that usually occur during the cutting process (chip formation).

A critical process parameter, once defined to perform the test at room temperature, was the stroke speed. For each test, the stroke speed was set to a moderate low speed equal to 6mm/min according to the value usually adopted in literature (Hussain et al. 2017, Estrin and Vinogradov 2013, Azushima et al. 2005). In order to drastically reduce the friction and to avoid any sticking effect and discontinuity into the deformation fields due to sticking of material against the die walls, the MoS_2 lubricant was employed. In Figure 90 the not deformed and deformed samples are reported. The tests were stopped before to deform the entire sample in order to preserve the microstructural transition between the deformed and not deformed region and to evaluate the effect of the shear strain on the microstructure.

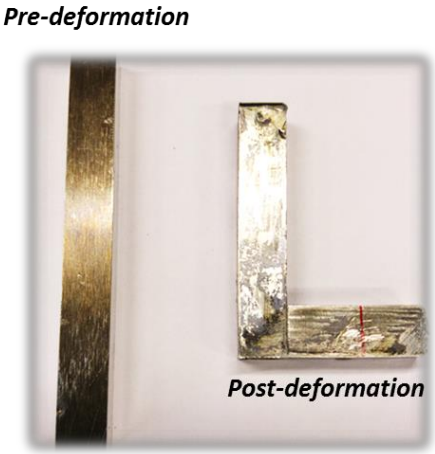

Figure 90: Not deformed and deformed sample by ECAP process.

4.3.3 Orthogonal cutting tests of *AA7075*

The orthogonal cutting tests were performed on a vertical broaching machine in dry conditions. In Figure 91 the experimental set up used to carry out the cutting tests is shown. The workpiece was shaped with a cross section of 14mm x 4mm and length of 110mm.

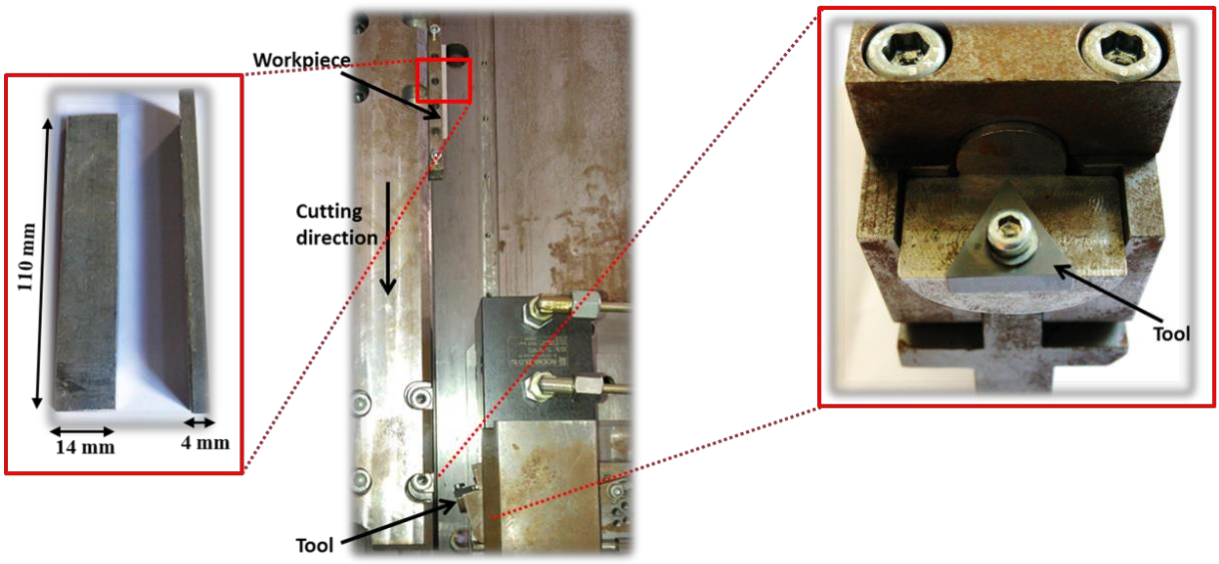

Figure 91: Experimental set up, workpiece and tool holder detail used to perform the orthogonal cutting.

Moreover, the same annealing treatments performed on the sample used during ECAP tests were carried out. Regarding the tool, a Walter Tool cutting insert type WKM P8TN 6028833 with a cutting edge angle of 90 degrees was utilized. The process parameters (summarized in Table 10) and the cutting speed were set in accordance with the process parameters set for the ECAP tests.

Table 10: Cutting parameters.

Cutting Parameters	Value
Cutting Speed V_c	6mm/min
Rake angle γ	-15°
Depth of cut h_c	0.1mm

The cutting speed set to perform the orthogonal cutting tests has no relevant industrial application since the aluminum alloy usually is machined at higher cutting speed (10^2 m/min to 10^3 m/min). In particular, the low value of cutting speed was set in order to reproduce a comparable stress-strain condition induced by the ECAP test on the aluminum samples.

4.4 Comparison of the experimental results

At the end of the experimental tests (ECAP and orthogonal cutting), the samples deformed by ECAP and the machined ones were collected in order to perform metallurgical analyses. The collected results were necessary to have a comprehensive understanding of the microstructural alterations and to find possible links in the plastically deformed materials. In order to understand the amount of microstructural and mechanical properties changes, the hardness, the metallographic and the XRD analysis were carried out on the specimens of the machined and deformed parts. The specimens collected for the analysis were obtained from the parts of the sample as shown in Figure 92 while the samples worked under orthogonal cutting were collected close to the machined surface and the longitudinal section were analyzed (Figure 93). Subsequently, the samples were grinded and polished following a specific metallographic procedure (Table 8) and they were chemically treated with Keller reagent (90 seconds) in order to reveal the microstructure. At the end of the metallographic analysis, the micro-hardness (Vickers $HV_{0.01}$) has been measured.

4.4.1 Microstructure and hardness measurements

Several micrographs were collected from the cross and longitudinal section of the deformed and not deformed regions as well as on the longitudinal section of the machined samples. As already mentioned, the ECAP samples were not entirely deformed in order to make a comparison in terms of microstructural variations of the deformed and not deformed region. In Figure 92 and Figure 93 are reported the micrographs of the not deformed and deformed part of the sample processed by ECAP and machining respectively.

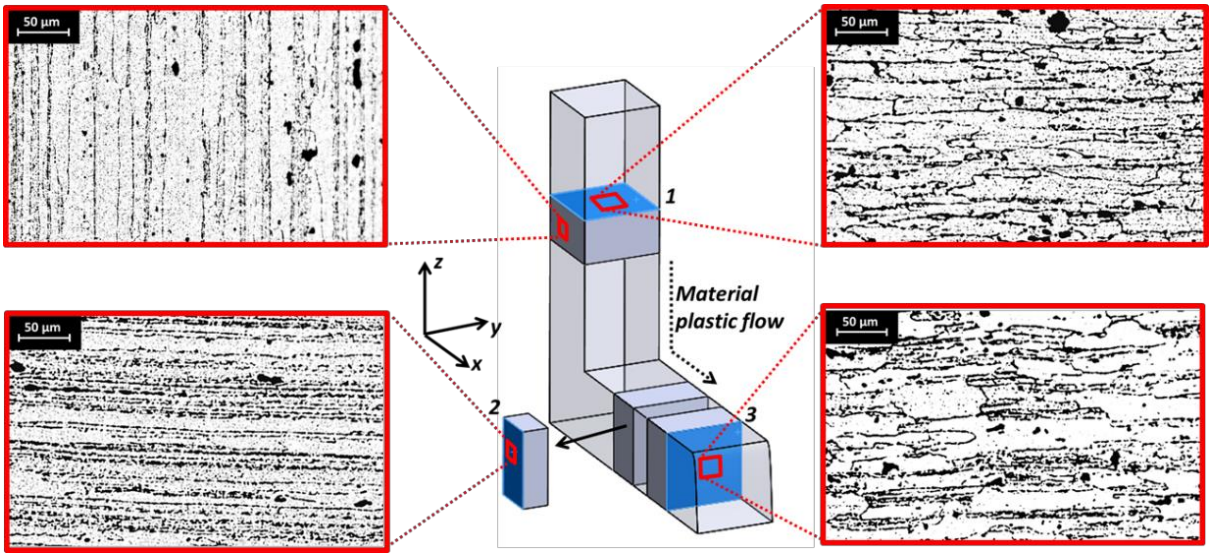

Figure 92: Microstructure analysis of the ECAP deformed sample; microstructure of section 1 (x-z plane, not deformed part); microstructure of section 1 (x-y plane, not deformed part); microstructure of longitudinal section 2 (deformed part); microstructure of cross.

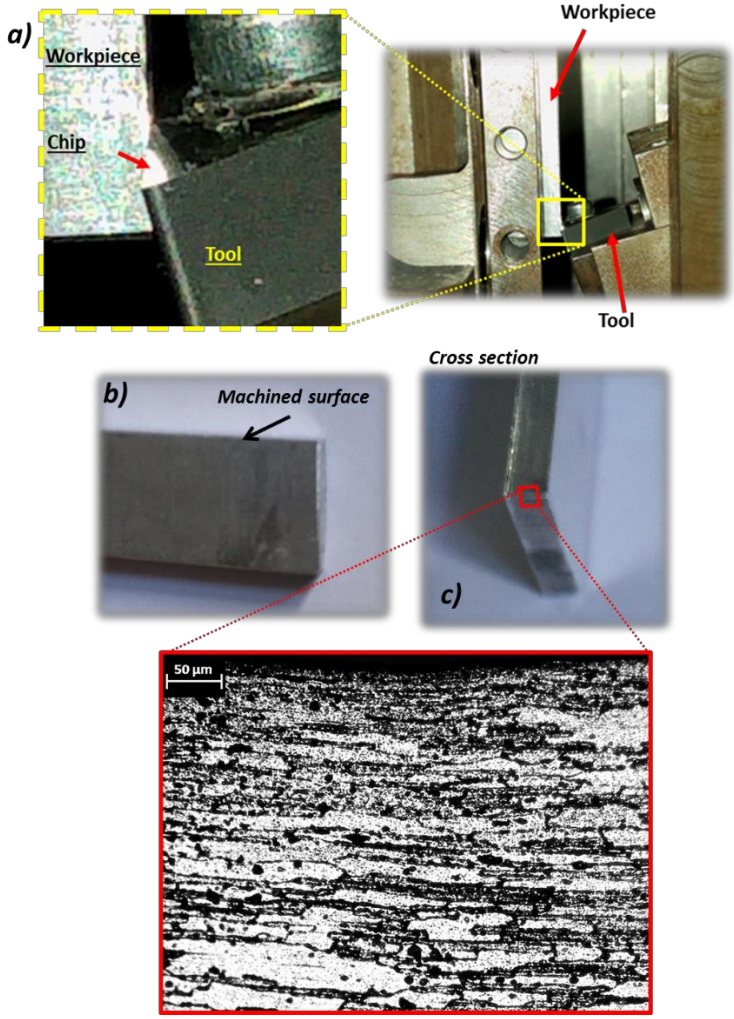

Figure 93: a) Frame of the machining test, b) longitudinal section of the machined sample; c) cross section of the machined sample and the related microstructure.

The compared measurements (hardness and microstructure) of the collected samples were carried out on different parts of the cross and longitudinal sections and the average values were taken into account (Figure 94 and Figure 95).

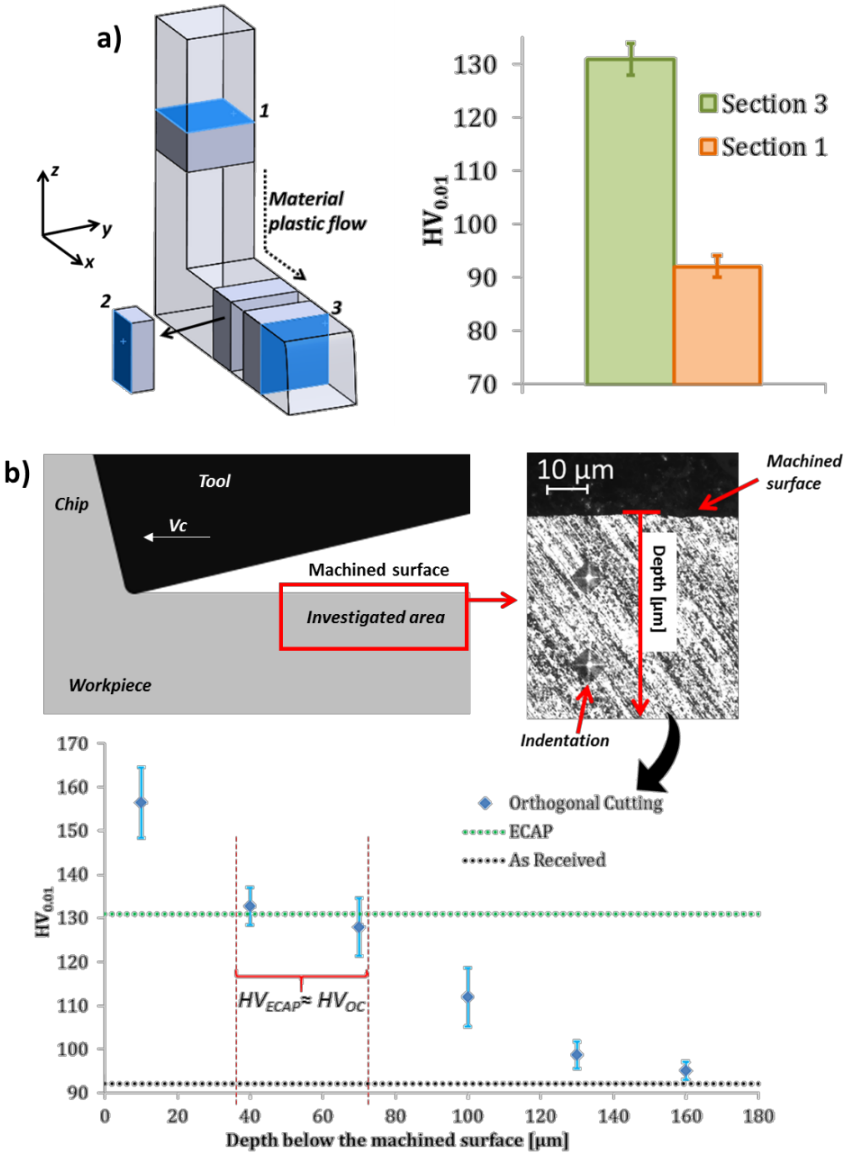

Figure 94: Hardness measurements on the deformed ECAP sample (a) and on the longitudinal section of the machined sample (b).

In detail, the hardness as well as the microstructure of the ECAP samples were evaluated on the cross section, namely Section 1 and 3 (Figure 94a). The samples obtained by the machined specimens were analyzed in the cross section for the metallographic analysis, and the longitudinal section to quantify the hardened layer (Figure 94b). The grain size measured from Section 1 of the as-built material was equal to 46.8 ± 3 µm (Figure 92). The longitudinal sections (Figure 92) referred to Section 1 and Section 2 were used only for a qualitative metallographic analysis to evaluate if the ECAP system provides components with constant deformation at the end of the process. Finally, the microstructure changes on the machined surface were evaluated on the cross and longitudinal sections but only the cross one (Figure 93c) was measured and compared with the grain changes observed into the cross section 3 of the deformed ECAP samples (Figure 92).

Initially, the micro-hardness changes between the deformed and not deformed material processed by ECAP was compared and an increase of 42% of hardness when section 3 and section 1 are considered (one pass of ECAP) was observed (Figure 94a). This increase of hardness was probably due to the high density of dislocations retained. Indeed, performing ECAP at room temperature on *AA7075* alloy allowed reaching high level of accumulation of dislocation density that initiated subgrain walls (Cepeda-Jiménez et al. 2012, Cepeda-Jiménez et al. 2011, E. A. El-Danaf 2008).

Subsequently, micro-hardness measurements on machined parts were carried out and the data are reported in Figure 94b. As highlighted in the graph (Figure 94b), a part of the material beneath the machined surface showed micro-hardness values very similar to those measured on the deformed samples by ECAP process. This represents a first important result since a part of affected material (almost 40 µm thick) manufactured by machining test showed similarity in terms of hardening with the ECAP sample, consequently there is a link in mechanical properties from the hardness point of view. Subsequently, once the similar material region was identified, a qualitative and quantitative microstructure analysis to verify possible analogies in terms of microstructure changes was carried out. Several micrographs between cross sections (Figure 92 section 3 and Figure 93c) and longitudinal sections (Figure 92 section 2 and Figure 93b) were analyzed. Comparing the cross section of the deformed sample by ECAP and the machining process (Figure 95) two kinds of deformed grains were distinguishable.

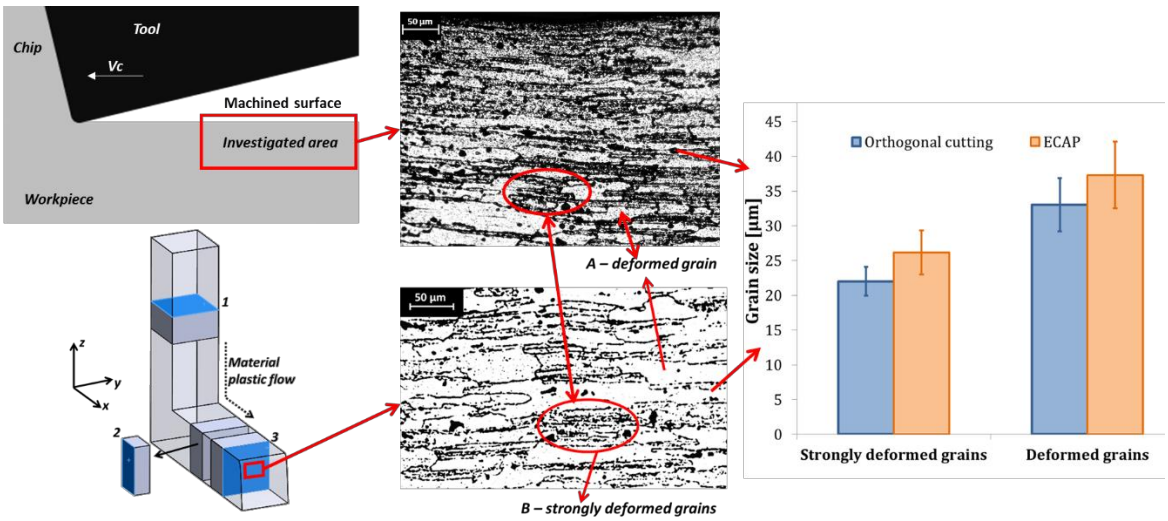

Figure 95: Microstructure analysis of the ECAP deformed and machined sample.

There were grains simply deformed (A) and zones in which the microstructure was strongly deformed (B) and in these parts of the material, the grain sizes were smaller than those surrounded (Figure 95). It is important to underline that the deformed microstructure in ECAP and machined samples was obtained by two different manufacturing processes. Comparing the grain sizes between the two cross sections, there are some analogies as shown in Figure 95.

4.4.2 X-Ray Diffraction analysis

From the previous reported results, it is clear that the possibility to have a link between the machining and ECAP process would be helpful in analyzing the metallurgical alterations and better characterize the material in terms of mechanical properties. To investigate the analogies between the machined and the material deformed by ECAP, the X-Ray Diffraction (XRD) analysis was conducted on the cross section of the deformed region, not deformed ECAP sample section and on the longitudinal section of the machined sample. In Figure 96 the XRD profiles of the ECAP sample and the not deformed one are reported.

The main peaks representative of the Al phase were clearly visible, moreover lot of small peaks representative of the η phase ($MgZn_2$) were also visible. The intensity of the peak are not reported because the pattern profiles were normalized in order to make a comparison among the different patterns.

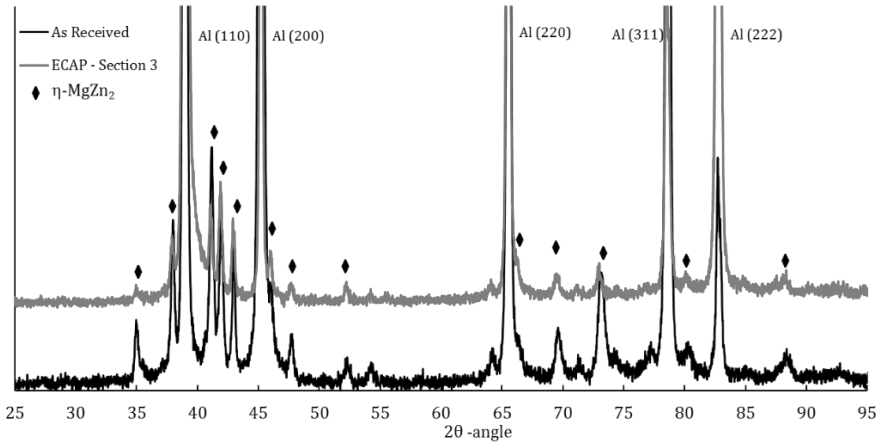

Figure 96: X-Ray Diffraction patterns of the as received and the deformed cross section of the ECAP sample.

It is important to highlight that the GP zones, usually observable as suggested by Shaeri and Ebrahimi 2016, were not visible because the annealing treatment provoked the diffusion of the GP zones to η' and finally to η phase as also confirmed by Zhao et al 2004. Comparing the two x-ray profiles, it was possible to state that there were few changes in peak intensities corresponding to the precipitation peaks. In detail, the peaks in correspondence of 2θ angle equal to 35°, 38°, 43°, 73° and 83° referred to the deformed section were smaller in intensity that indicated the peak broadening. This latter was usually visible when strain was induced into the texture undergone to refinement. In fact, the peak at 66° referred to Al phase (220) was slightly broadened, this result can be explained by the small refinement of the microstructure observed on the cross section 3 (Figure 95) in which the origin grains were divided into small subgrains as similarly observed by Gubicza et al. 2007. Furthermore, the peak at 73° was slightly shifted on the left; the peak shifting is another effect of the induced deformation into the Al matrix (Binesh and Aghaie-Khafri 2016). Taking into account the XRD profile obtained analyzing the longitudinal section of the machined samples and comparing with the XRD pattern of the ECAP deformed cross section sample, some interesting consideration can be done (Figure 97). The patterns are mostly the same and this result suggest that the crystallographic orientation as well as the metallurgical modification were doubtless comparable each other.

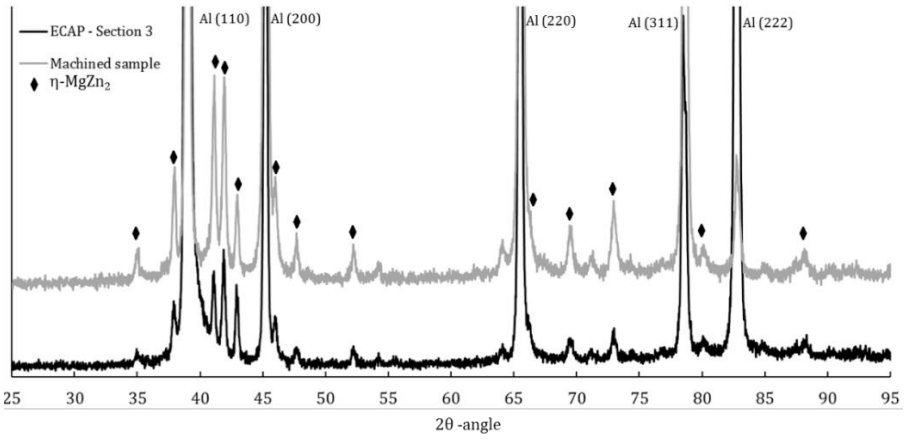

Figure 97: X-Ray Diffraction patterns of the machined sample and the deformed cross section of the ECAP sample.

In general, all the peaks referred to the η precipitates (machined sample) showed higher intensity suggesting that the amount of the precipitates was a bit higher than that related to the ECAP deformed sample. Moreover, the peaks referred to the Al phase, in detail the Al (200) and Al (311) showed a more pronounced broadening that suggested higher micro-strain into the texture and smaller grain size into the matrix. This result was in agreement with the grain size measurements, indeed as reported in Figure 95, the grain size measured on the machined sample were slightly smaller than the one measured on the cross section of the deformed ECAP sample. Finally, the grain refinement interested only the Al matrix, as suggested by Schiller et al. 2006, since the broadening of the η precipitates were negligible because the dislocations usually do not cut through precipitates. It is important to highlight that in both the manufacturing processes in which severe plastic deformation were involved; no phase transformation and formation of new precipitate were observed. Therefore, the deformed material of the ECAP sample and the machined ones were similar also in crystallographic distortion.

CHAPTER V

Finite element modeling and analysis to investigate the surface integrity characteristics during machining processes

This chapter aims to provide reliable models in order to simulate the main machining operations, as turning process, based on Finite Element Method (FEM). There are three main sections: Section 5.1 represents a state-of-the-art of the material behavior modeling and machining simulations; Section 5.2 concerns the development of the constitutive model of the *Ti6Al4V* mechanical behavior additively manufactured taking into account the experimental data available in literature. Section 5.3 describes the development and implementation of a physically based model of *AA7075-T6* aluminum alloy to simulate high speed machining under different cooling conditions.

It is known that the microstructural phenomena play an important role in defining the mechanical behavior. Therefore, the modification of the grain size evolution was investigated and modelled in order to take into account its effect into the material behavior. In particular, the yield stress (consequently the hardness) was modeled using the well-known Hall-Petch (Hall 1951 and Petch 1953) relation that links the microstructural changes and the mechanical response of polycrystals materials. Generally, the titanium alloys are considered metals having high efficiency of dynamic recovery; therefore, the new grains are not generated by nucleation mechanism but are obtained by accumulation of deformations that lead to subgrains progressive formations. In Section 5.2, which takes into account the material modeling of *Ti6Al4V*, the microstructural model was developed and customized to predict the lamellae thickness variation depending on the combination of effective strain-rate (numerically predicted) and temperature (experimentally measured). This model was based on an empirical formulation and did not take into account the metallurgical phenomena because no dynamic recrystallized grains were experimentally observed. Therefore, their changes were ascribed to the plastic deformation induced by tool action. Finally, the constitutive model developed was tested and validated by FE machining simulation of the experimental turning tests described in Chapter . Section 5.3 presents the development of the FE model of high speed machining of the aluminum alloy. Conversely to what has been done in Section 5.2, the material investigated under HSM was provided by the supplier as commercially available, namely in wrought conditions. The scientific literature already presents different interesting researches based on the material characterization, material behavior modeling coupled with physics model related to the metallurgical phenomena (dislocation density, grain changes, precipitations etc.) (Hu and Wang 2016, Ma et al 2014, Dixit et al. 2008, Baik et al 2003). Analyzing the previous cited works, the contribution to strengthening mechanism is characterized by different metallurgical phenomena. Therefore, a simplified empirical model cannot physically describe the mechanical behavior of the material, especially when extreme severe plastic deformation processes such as HSM are performed. Moreover, there are no clear formulation material constitutive model related to the aluminum alloy *7075-T6* except some empirical ones, which present few modifications to take into account the recrystallization phenomenon and its contribution to the strengthening (Rotella et al 2014). It is clear that the critical deformation imposed by the HSM process will trigger surface and subsurface metallurgical modifications thermo-mechanically induced, therefore the prediction of the dislocation density and grain size evolution are important to understand how to assess the surface quality after the machining process. Therefore, a physics based model was developed to properly simulate the turning tests and the metallurgical phenomena triggered by the severe plastic deformation induced by the turning process. The material modeling approach was based on the hypothesis of superposition of tensile single contributions generated by single physics phenomenon such as solid solution strengthening, precipitation hardening, density dislocation accumulation and recovery, grain size changes and dynamic recrystallization (Sabirov et al, 2013, Kimikawa et al. 2009).

The proposed model and its implementation into FE software aims to study the physical evolution of the state variables that contribute to modify the mechanical properties and quality of the surface and subsurface machined parts. The numerical models developed and proposed in Section 5.2 and Section 5.3 were calibrated and validated by detailed comparison with the experimental results.

5.1 Numerical Simulation of manufacturing processes – State of the art

The manufacturing enterprises face the growing demands of increasing product quality, greater products variability, reduced cost and global competition. In this contest, the understanding of the fundamental variables role (microstructural modification, phase changes etc.), their changes and effects on the overall quality of the products is important because it permits to plan, to control and optimize the functional design requirements and the production process. This fundamental understanding is the key to successfully designing and developing different metals and alloys to improve the performance and manufacturability. Generally, the industrial machining operations are among the most complex manufacturing processes to model and simulate, and the requirements of innovative and advanced predictive models are continuously growing in the industrial world. The great interest in modeling machining is justified by the fact that machining represents the most prevalent manufacturing operation. Nowadays, even though the industries are moving their interests in other innovative and promising processes such as the additive manufacturing, the machining operations still represent the biggest volume of work in the manufacturing environment. Consequently, although the new production frontiers are moving through more complex geometry products simply adding material instead of removing it, the post processes like surface finishing are still required (Schmidt et al. 2017). Predictive performance models could also be effectively used in adaptive control for machining processes, reducing and/or eliminating trial and error approaches. Therefore, the industrial and scientific fields are strongly interested in correctly modeling the manufacturing processes. In fact, these predictive models with simulation can be integrated into process planning systems to improve productivity and enhance product quality.

5.1.1 Material constitutive modeling in machining simulation

Numerical modeling and simulation of machining is a very effective approach for gaining fundamental insight into the complex material behavior during the metal cutting process. The simulations can be used for optimizing the cutting conditions and tool geometry without performing costly experiments. Due to the complexity of the machining processes, a reliable numerical modeling and simulation approach should consider all aspects including material deformation behavior, contact friction, heat generation and transfer (Arrazola et al. 2013). The development of a constitutive material model that accurately describes the deformation behavior during machining of metal materials produced by additive manufacturing processes is one of the goals of this Ph.D. thesis. During metal machining operation, the material undergoes severe plastic deformations leading to high thermal gradient. Therefore, this process is characterized by heterogeneous thermo-mechanical deformations that lead to the microstructural and material property changes (Jawahir et al. 2011). Consequently, constitutive models for metal machining require fundamental understanding of the deformation conditions and their mechanisms inside the plastically deformed zone, as well as, the thermal gradients and the metallurgical modifications. In general, a constitutive material model provides a mathematical description of the relationship between stress and strain at various strain-rate and temperature during different deformation mechanisms. Most of the earlier constitutive models, known as phenomenological models, describe macroscopically the material plastic stress-strain response in machining as a phenomenological function of strain, strain-rate and temperature. This means that the microstructure and its evolution as well as dislocations density modifications are not included into the model.

Phenomenological models are commonly used to describe the high strain-rate and temperature flow stress response of metals in machining and are usually preferred because of easy implementation into the simulation software (Melkote et al. 2017).

The general mathematical formulation of these models is represented by Equation 4:

$$\sigma = \sigma(\varepsilon_p, \dot{\varepsilon}_p, T \dots) \tag{4}$$

The easiest phenomenological formulation are reported in Table 11.

Table 11: Work hardening material constitutive laws (Arrazola et al. 2013).

Material constitutive model - Work hardening law
Power Law: $\sigma = \sigma_0 \left(\frac{\bar{\varepsilon}}{\bar{\varepsilon}_0}\right)^n \left(\frac{\dot{\bar{\varepsilon}}}{\dot{\bar{\varepsilon}}_0}\right)^m \left(\frac{T}{T_0}\right)^\tau$
Oxley: $\sigma = \sigma_0 \varepsilon^n$
Swift: $\sigma = \overline{K}(\varepsilon + \varepsilon_0)^n$

Generally, these models represent a material characterized by work hardening behavior at increasing strain. As a metal is deformed to large strains, it is expected that the dynamic recovery will attenuate the strain hardening leading to a saturation of the flow stress and as showed by Figure 98, the models reported in Table 11 do not fit the dynamic recovery phenomenon leading to a unique work-hardening response .

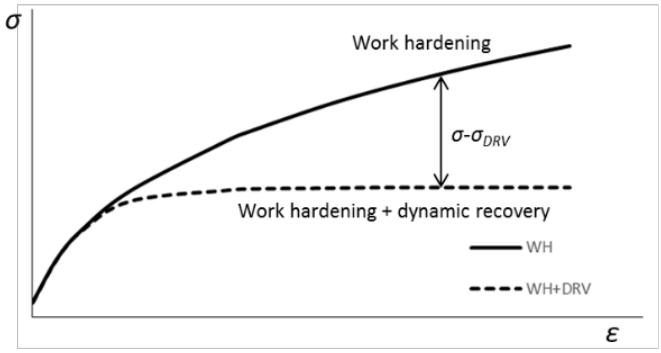

Figure 98: Schematic representation of dynamic recovery (DRV) effect on work hardening flow stress.

Another famous phenomenological model is the Johnson-Cook (JC) model. It is also the most widely used because of its simplicity and relative ease of calibration (Equation 5).

$$\sigma = \left(A + B{\varepsilon_p}^n\right)\left(1 + Cln\left(\frac{\dot{\varepsilon}_p}{\dot{\varepsilon}_0}\right)\right)\left(1 - \left(\frac{T - T_r}{T_m - T_0}\right)^m\right) \tag{5}$$

Where σ is the stress, *A*, *B*, *n*, *C* and *m* are numerical constants empirically calibrated by fitting experimental data, ε_p is the plastic strain, $\dot{\varepsilon}_p$ and $\dot{\varepsilon}_0$ are the plastic strain-rate and the reference plastic strain-rate respectively. T, T_r and T_m are the local temperature, room temperature and melting temperature of the material respectively (Johnson and Cook 1983).

As a phenomenological model, it is obviously better than the previous mentioned because it has a more complex mathematical formulation depending on strain-rate and temperature. Therefore, the JC is purely empirical and unfortunately has some limitations. In fact, one of its limitation is the unfeasibility to describe the constitutive behavior of the materials such as titanium or nickel based alloys that exhibit softening phenomena. Indeed, materials characterized by low thermal conductivity show a localized failure phenomenon into the primary shear zone due to shear banding formation when a certain combination of strain and temperature occurs (Pawade and Joshi 2011, Sun et al. 2009, Yang and Liu 1999, Komanduri and Turkovich 1981). Some researchers (Umbrello 2008, Guo and Yen 2004, Gene Ng and Aspinwall 2002, Chen et al 2011 and many others) have coupled the JC model with damage models (Brozzo's model, Usui's model or Johnson-Cook's model) in order to simulate the failure inside the cutting zone due to the tool action (Figure 99). The weakness of this modeling approach is characterized by unknown material constants, such as the damage limit value that usually needs to be calibrated.

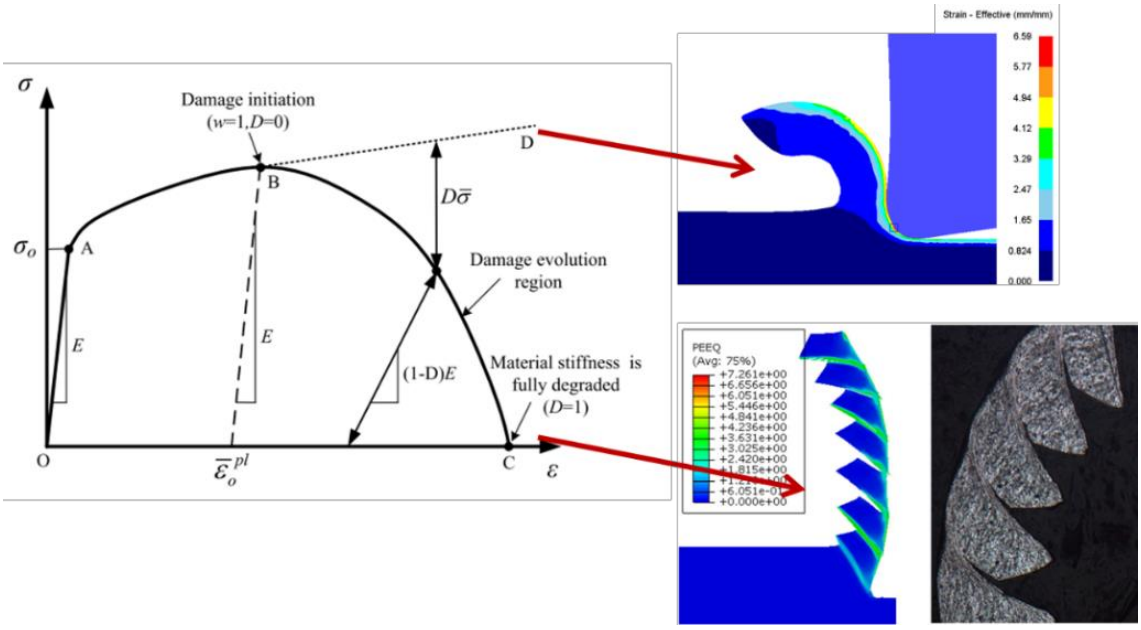

Figure 99: Schematic representation of the FE prediction of failure phenomenon in cutting simulation by flow stress coupled and not coupled with damage model (adapted by Li and Hou 2014).

The good prediction of the adiabatic shear bands and chip failure modes are very important due to their impact in the cutting forces and temperature prediction. In fact, the presence of serrated chip formation leads to high vibration and consequently not constant but fluctuant forces. Recently, Calamaz et al. 2008, Calamaz et al. 2010, Özel et al. 2010, Sima and Özel 2010 and Karpat 2010, proposed modified versions of the JC equation in order to empirically model the softening phenomena that characterize the superalloys as *Ti6Al4V* and *IN718*.

In the equations reported in Table 12 there are several terms that mathematically modify the flow stress trend at varying strain-rate and temperature. These modifications aim to model the failure phenomena previously mentioned. It is important to point out that in these last models, the failure criteria is already modeled by the flow stress rule, consequently no damage rules need to be coupled with the constitutive material models. This modeling approach leads to a reduction of the constants that need to be defined.

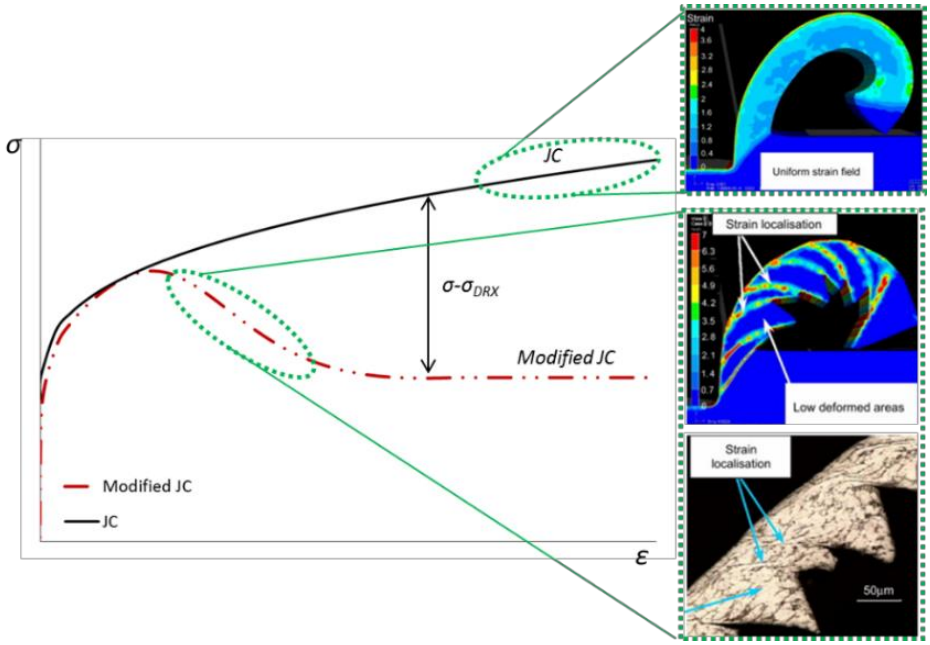

Figure 100: Johnson-Cook model and Modified Johnson-Cook model proposed by Calamaz et al. 2008.

Taking into account Figure 100, the new modified JC model proposed by Calamaz et al. 2008 is able to represent the drop stress (dashed curve) due to the concentration of thermal gradients as well as strain into a thin band known as adiabatic shear band. However, the trigger of the failure in the material is modeled by mathematical terms without physical meaning. Consequently, the physical reason of the drop in stress are not described by the model. Although, several models have been proposed by the scientific community, they are based on experimental activities carried out on the most common materials provided to laboratory tests in wrought conditions (as commercially available).

Table 12: Modified material constitutive model developed for the *Ti6Al4V* alloy (Calamaz et al. 2008, Sima and Özel 2010, Özel et al. 2010, Karpat 2010).

Material constitutive model - Modified Johnson-Cook
Calamaz et al. 2008: $\sigma = \left(A + B\varepsilon^n\left(\frac{1}{\exp(\varepsilon^n)}\right)\right)\left(1 + Cln\left(\frac{\dot{\varepsilon}}{\dot{\varepsilon}_0}\right)\right)\left(1 - \left(\frac{T - T_0}{T_m - T_0}\right)^m\right)\left(D + (1 - D)\,tanh\left(\frac{1}{(\varepsilon + S)^c}\right)\right)$ $S = \left(\frac{T}{T_m}\right)^b \qquad D = 1 - \left(\frac{T}{T_m}\right)^d$
Sima et Özel. 2010 (Model 1): $\sigma = (A + B\varepsilon^n)\left[1 + C\ln\left(\frac{\dot{\varepsilon}}{\dot{\varepsilon}_0}\right)\right]\left[1 - \left(\frac{T - T_0}{T_m - T_0}\right)^m\right]\left[D + D\left[\tanh\left(\frac{1}{(\varepsilon + p)^r}\right)\right]^S\right]$
Karpat: $\sigma = (A\varepsilon^n + B)(CT^{*2} + DT^{*2} + E)\left(1 - \left(1 - \left(\frac{\ln\varepsilon_0}{\ln\varepsilon}\right)^q\right)\right)\left(\frac{1}{L + \tanh(\varepsilon + p)}\right)$ $T^* = \frac{T}{T_m}$

Taking into account the models showed in Table 12, σ is the stress, *A, B, n, C, m, b, d, q, p, L, D, E, c, S, r,* are numerical constant empirically calibrated by fitting experimental data, ε_p is the plastic strain, $\dot{\varepsilon}_p$ and $\dot{\varepsilon}_0$ are the plastic strain-rate and the reference plastic strain-rate respectively. T, T_r and T_m are the local temperature, room temperature and melting temperature of the material respectively. Rotella and Umbrello 2014 showed new findings in modeling by empirical approaches the material behavior of the *Ti6Al4V* and *AA7075-T6* to simulate machining operation (orthogonal cutting and turning) taking into account the microstructural effects. The material constitutive models proposed are reported in Table 13. The flow stress was predicted by JC model and the *A* coefficients that is representative of the yield strength was modified in according with the grain size evolution.

Table 13: Material constitutive model proposed by Rotella and Umbrello for modeling the *AA7075-T6* and *Ti6Al4V* mechanical behavior (Rotella and Umbrello 2014).

Material constitutive model - Modified Johnson-Cook
Rotella and Umbrello 2014: Ti6Al4V
$\sigma = \left(\left(a + \frac{k}{\sqrt{d}}\right) + B\varepsilon^n\left(\frac{1}{\exp(\varepsilon^n)}\right)\right)\left(1 + Cln\left(\frac{\dot{\varepsilon}}{\dot{\varepsilon}_0}\right)\right)\left(1 - \left(\frac{T - T_0}{T_m - T_0}\right)^m\right)\left(D + (1 - D)\,tanh\left(\frac{1}{(\varepsilon + S)^c}\right)\right)$
Rotella and Umbrello 2014: AA7075-T6
$\sigma = \left(\left(a + \frac{k}{\sqrt{d}}\right) + B\varepsilon^n\right)\left(1 + Cln\left(\frac{\dot{\varepsilon}}{\dot{\varepsilon}_0}\right)\right)\left(1 - \left(\frac{T - T_0}{T_m - T_0}\right)^m\right)$

The differences between the models reported in Table 12 and in Table 13 are the constants *a* and *k* that are calibrated by fitting the experimental values of yield stress measured at varying grain sizes. The variable *d* represents the equivalent diameter of the equiaxed grain. The grain size change due to the dynamic recrystallization is numerically computed by Equation 6 as proposed by Yanagimoto and Karhausen 1998.

$$d_{DRX} = bZ^m \tag{6}$$

Where *b* and *m* are calibration constants and *Z* represents the Zener-Hollomon parameter. In Figure 101 the numerical prediction strategy developed and implemented in the FE code is reported.

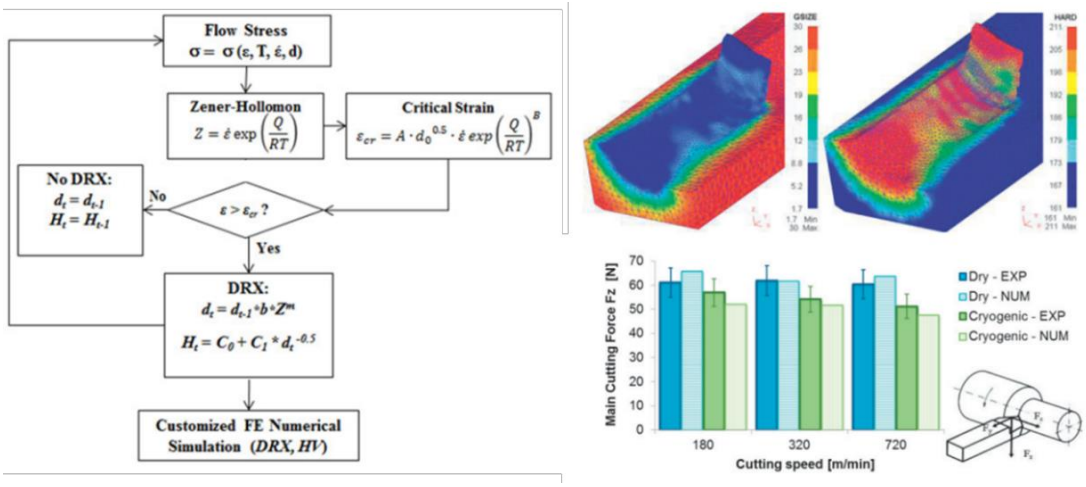

Figure 101: Prediction strategy of the microstructural changes and FE numerical results obtained in *AA7075-T6* turning simulation (Adapted from Rotella and Umbrello 2014).

The prediction starts with the computed Zener-Hollomon value, used to calculate the critical strain. If the strain induced by the tool exceed the critical one, the dynamic recrystallization starts and a new value of grain size is computed. The hardness variation due to the grain size changes is predicted by the Hall-Petch relation. The adopted strategy was calibrated and validated by comparison with the experimental results and the developed models are able to successfully predict the main fundamental variables, microstructural and hardness changes at varying cutting speed, feed rate and cooling strategies (Figure 101 and Figure 102). Rotella and Umbrello 2014 applied this prediction strategy to simulate the orthogonal cutting of the titanium alloy *Ti6Al4V* under dry and cryogenic condition. They obtained very good results in terms of cutting forces, grain sizes and hardness (Figure 102).

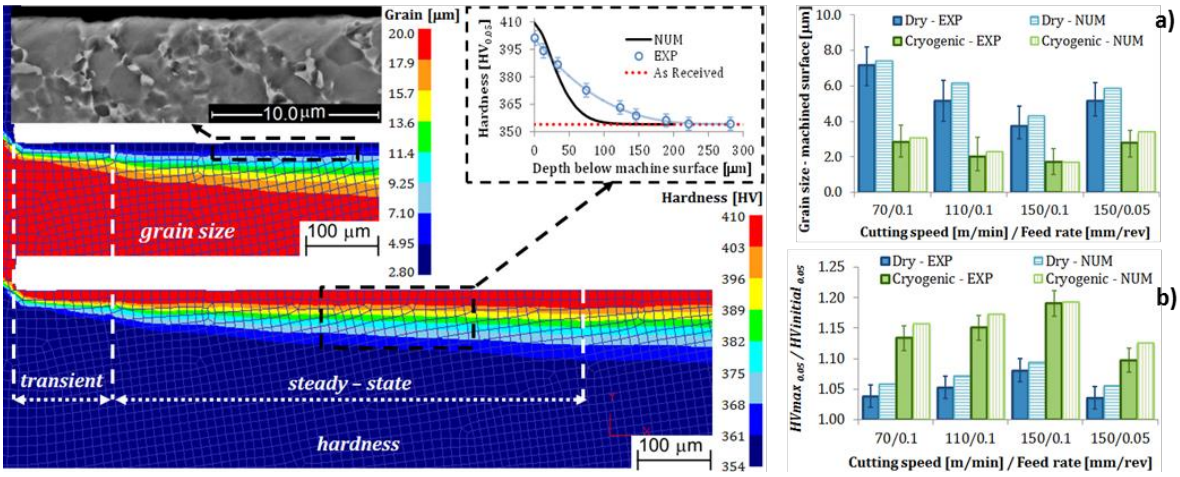

Figure 102: Numerical prediction of microstructural changes on machined *Ti6Al4V*; a) grain size, b) hardness (Adapted from Rotella and Umbrello 2014).

The empirical approaches to model the mechanical behavior of a material during dynamic loading conditions coupling the metallurgical phenomena are quite complex. Indeed, a high number of equations and unknown numerical constants are involved and need to be implemented or calibrated.

In contrast, generally a physics based unified model considers the microstructure and describes the full strain-microstructure-stress relationship. As such, a physics-based unified model provides a mechanistic tool to analyze the observed inelastic behavior and understand the effects of the micro-scale mechanisms. They mathematically describe the flow stress of a metal material as a function of microscale phenomena responsible of the strengthening (e.g. interaction between mobile and immobile dislocations) or softening (e.g. dynamic recovery, grain recrystallization or grain boundary sliding). It is fundamental tenet of materials science that the material properties depend on its current metallurgical structure, the changes in properties result from changes in structure (Mecking and Kocks 1981). In the machining operations, the microstructural evolutions are characterized by the interaction between mobile dislocations and short or long range obstacles (e.g. solute atoms, precipitates, forest dislocations (ρ) or grain boundaries (l)). In that case, the strengthening or softening phenomena are always governed by strain, strain rate and temperature. Due to their complexity in determining the material and microstructural constants, the physics based constitutive models have limited application in metal cutting simulation. However, they are more attractive than phenomenological models since they intrinsically permit to simulate the microstructure effects on the mechanical properties and to understand their evolution during the machining processes and their effect on the material properties. Some examples of physically-based constitutive models used in metal cutting modelling and simulation are given in Table 14.

Table 14: Material constitutive model proposed by Zerilli and Armstrong 1987, Follansbee and Kocks 1988.

Physics based material behavior model	
$\sigma = \sigma_a + Be^{-\beta T} + B_0\sqrt{\varepsilon_p}e^{-\alpha T}, \sigma_a = \sigma_G + k_d l^{-0.5}, \beta, \alpha = f(\dot{\varepsilon}_p)$	(Zerilli and Armstrong 1987)
$\sigma = \sigma_a + \sigma_{th}, \sigma_a = \sigma G b\sqrt{\rho}, \sigma_a = \sigma_0\left[1 - \left(\frac{kT}{g_0 G b^3} ln\frac{\dot{\varepsilon}_0}{\dot{\varepsilon}}\right)^{1/q}\right]^{1/p}$	(Follansbee and Kocks 1988)

σ_G is the athermal stress due to the dislocation-grain boundary interaction, ε_p is the plastic strain, $\dot{\varepsilon}_p$ is the plastic strain rate, G is the shear modulus, b is the Burger's vector, ρ is the dislocation density, k is the Boltzmann's constant, g_0 is the normalized activation energy, l is the average grain size, T is the absolute temperature while the other terms are model calibration parameters. Among the physics-based model, the most famous is the Zerilli-Armstrong (ZA) constitutive model (Zerilli and Armstrong 1987). This latter is based on the well-known theory of thermal activation of dislocations. The flow stress is basically modelled as the superposition of two main components that are athermal and thermal stress. They are both function of the strain, strain rate and temperature. ZA model provides different flow stress behavior formulations that take into account the strain-hardening or thermal softening depending on the crystal structure e.g. bcc, fcc and hcp. Liu et al. 2013 have proposed an enhanced ZA model including the failure function proposed by Calamaz et al 2008, Calamaz et al. 2010, Calamaz et al. 2011 and Sima and Özel 2010 to accurately simulate the adiabatic shear band formation in machining. The proposed model is able to successfully predict the cutting force components and frequency of chip segmentation at varying cutting speeds and feed rates. Paturi et al. 2014 developed two modified models namely JC and ZA. They applied the developed model to simulate turning process on aluminum alloy *AA7075-T6* to predict the chip thickness, shear plane angle and tool-chip contact temperatures at varying cutting speed. The proposed models show numerical results that are in good agreement with the experimental observations (Figure 103).

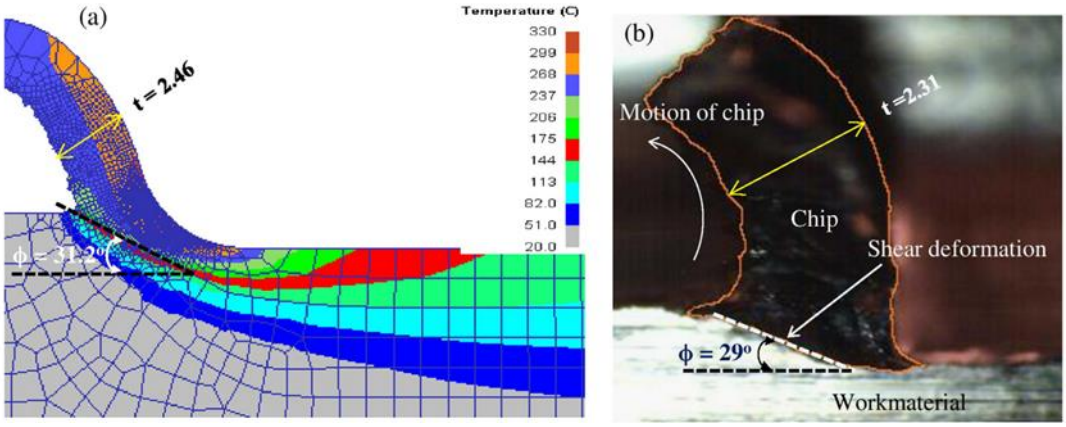

Figure 103: Comparison of simulated a), and experimental results b) of chip morphology and shear plane deformation at low speed machining (V_c =100 m/min, f=0.25 mm/rev) (Paturi et al. 2014).

Most of the physically based material behavior models related to the aluminum alloy are generally applied to forming or severe plastic deformation processes such as ECAP (Hallberg et al. 2010, Baik et al. 2003). It is clear that a lack of knowledge regarding the existence of a reliable physics based model able to simulate the material behavior under machining conditions is evident.

Analyzing other interesting researches proposed by the literature, Melkote et al. 2015, presented an enhanced physically based material model that accounts for microstructure evolution induced flow softening due to inverse Hall-Petch below a critical grain size.

The model has been developed for commercially pure titanium and it was implemented into FE software to simulate cutting operations. Conversely to what observed in the ZA model, the modeling approach is based on the thermal activation theory; therefore, the flow stress is formulated as a linear superposition of separate terms that are thermally or not thermally dependent. The plastic instability of the material due to the cutting operation was well predicted by the model developed (Figure 104). The model also takes into account the metallurgical phenomena such as dislocation density and grain size changes and their effect on the flow stress (Figure 105).

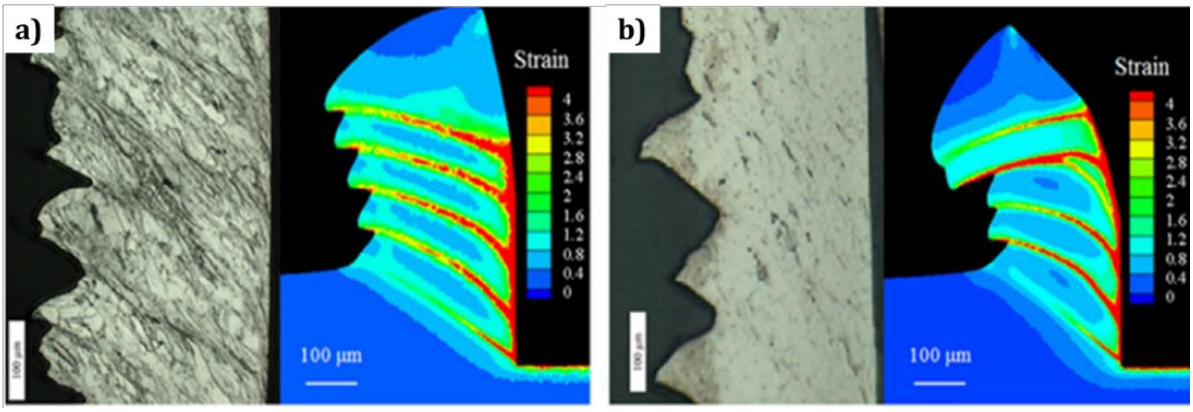

Figure 104: Comparison of measured and simulated chip shapes (Melkote et al. 2015).

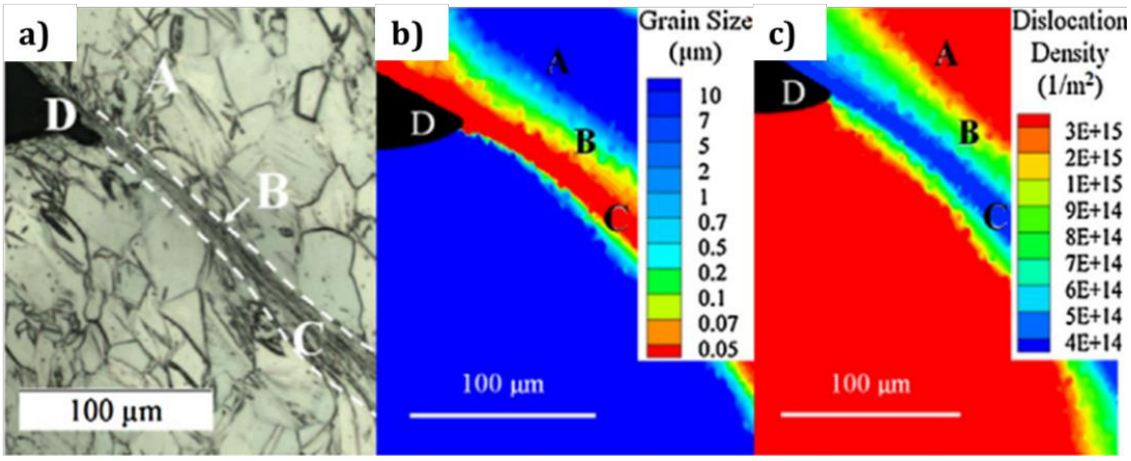

Figure 105: a) optical micrograph of the chip microstructure in shear band region and simulated b) grain size and c) dislocation density distribution (Melkote et al. 2015).

A new physics-based model, proposed by Liu et al. 2014 has been implemented to simulate the hardness variation induced by machining process on Oxygen Free High Conductivity (OFHC) Copper. This model explicitly incorporates microstructure evolution due to hardening, dynamic recovery and dynamic recrystallization into the constitutive law, describing the macroscale plastic deformation response of the material during severe plastic deformation process (Figure 106).

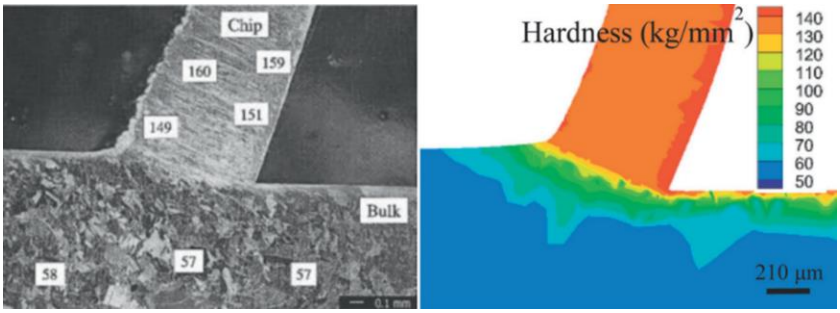

Figure 106: Comparison between the measured and predicted cutting-induced hardness changes (Liu et al. 2014).

Other different approaches in developing physics based model were proposed by other researchers (Estrin et al. 1998) in metal plasticity. Their theory was based in formulating discrete dislocation density model to compute the shear stress. This approach consists to split dislocations into low dislocation density channels (ρ_c) and high dislocation density walls (ρ_w) that follow two separate evolution equations. Consequently, the total dislocation density (ρ_{tot}) is computed taking into account the single contribution of the evolution of dislocation forming a cell structure, and those contained within the cell interiors (Equation 7). These two dislocation densities are internal variables that contribute to the shear stress.

$$\rho_{tot} = f\rho_w + (1-f)\rho_c \tag{7}$$

Where *f* denote the volume fraction of the cell walls. Each contribution of the dislocation affects a distinct stress component representative of the stress field inside the cell interiors (τ_c^r) and in the cell walls (τ_w^r).

Equation 8 shows the combination of these single contributions:

$$\tau^r = f\tau_w^r + (1-f)\tau_c^r \tag{8}$$

This physics based model was applied to simulate cutting operation on OFHC Copper by Atmani et al. 2016 in order to predict the cutting forces and to study the dislocation densities and grains size evolution (Figure 107).

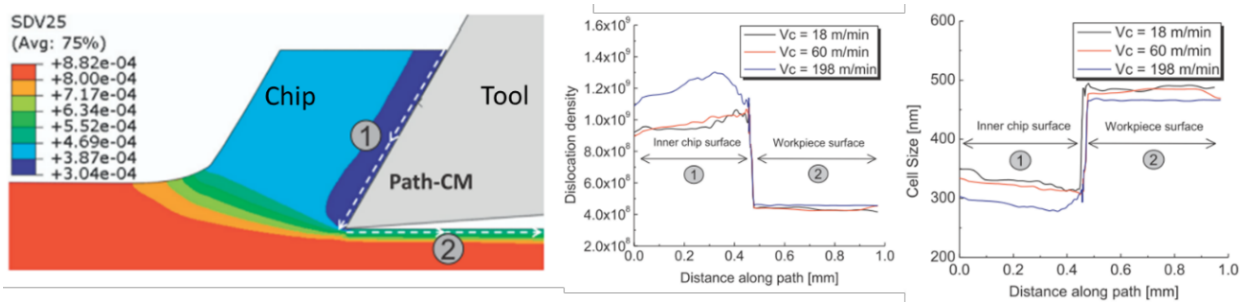

Figure 107: Cutting simulation of OFHC CU, dislocation density and grain size evolutions (Atmani et al. 2016).

Based on the same modeling approach, Ding and Shin 2013, developed a multi-physic model to simulate the surface microstructural alterations during hard turning of AISI 52100 steel (Figure 108). They also used the dislocation density evolution law presented by Estrin et al. 1998 and Tòth et al. 2002 taking into account the rule of mixture to combine the single effect of the dislocation cell walls and cell interiors.

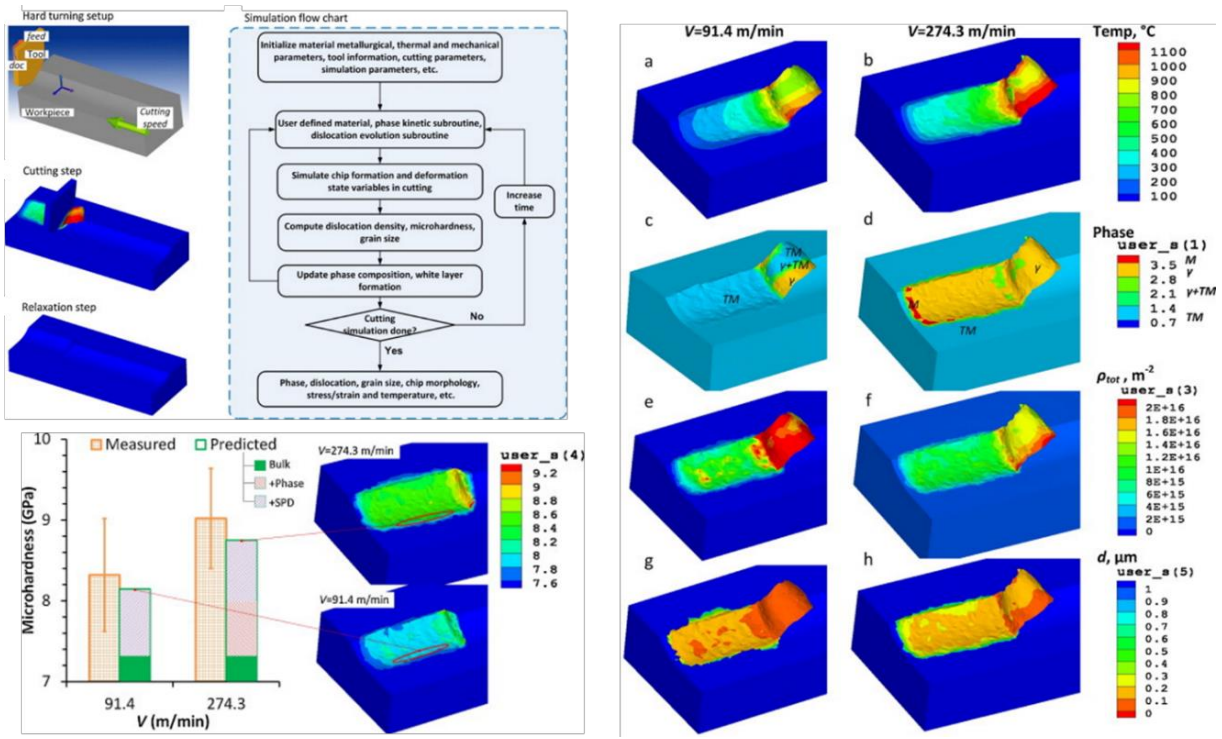

Figure 108: Adapted by Ding and Hing 2013, simulation flow chart and numerical prediction of temperature, phase transformation, dislocation density, grain size and microhardness.

Moreover, they also implemented a physics hardness based model depending on physics material constants and total density dislocation density in order to predict the hardness changes on surface due to the machining operation. The results were also compared with the experimental outcomes to show the reliability of the model in predicting physics state variables (Figure 108). In literature are presented other research works that shows the same physics based model approach previously explained to describe the behavior of many other materials during machining. The authors used the simulations to predict cutting forces and temperature as well as grain size and other metallurgical phenomena (Shen and Ding 2014, Ding et al. 2014, Ding et al. 2011).

Lindgren et al. 2017 presents a new material behavior model based on dislocation density evolution. The flow stress was assumed to consist of additive long-range and short-range contributions. The long-range contribution to the material resistance was due to the interaction between the mobile and immobile dislocations, therefore the dislocation substructure. In presence of small particles, precipitations or very small disturbance of the lattice, these interactions are considered of short range, and the material resistance to plastic deformation was also due to the short-range interactions. In this case, the thermal activated mechanisms assist the applied stress in moving dislocations. The total stress was defined as the superposition of each single contribution (short or long-range) to the stress field (Equation 9).

$$\sigma_Y = \sigma_G + \sigma_{HP} + \sigma_{SR} \quad (9)$$

Where the σ_G represents the material resistance due to the dislocations density variation, the σ_{HP} represents the material resistance contribution due to the grain size changes (Hall-Petch effect) and the σ_{SR} that represents the material resistance contribution due to the short-range interactions of the mobile dislocations with the small obstacles. The total stress field was computed as showed also by Melkote et al. 2015, but on the contrary, the dislocation density evolution was computed differently. In fact, Lindgren et al. 2017 affirm that the ρ_i represents the total dislocation density of the immobile dislocation and it can be computed taking into account its differential equation (Equation 10).

$$\dot{\rho}_i = \dot{\rho}_i{}^{+} - \dot{\rho}_i{}^{-} \tag{10}$$

This equation describes the evolution of the immobile dislocation density and it is composed by two parts: hardening ($\dot{\rho}_i{}^{+}$) and restoration/recovery or softening ($\dot{\rho}_i{}^{-}$) (Lindgren et al. 2017; Babu and Lindgren 2013). The hardening term is computed taking into account the average distance that the dislocations have to go through before to be immobilized or annihilated. On the contrary, different processes may contribute to the reduction in dislocation density and are divided in static and dynamic recovery. The static recovery is generally due to climb that is the motion of dislocations perpendicular to its glide plane, while the dynamic recovery is due to the glide dislocations and it implies that moving dislocation annihilates the immobile ones. It is possible to understand that in this modeling approach, the dislocation density is considered in a different meaning and takes into account the effects of the presence of mobile and immobile dislocations and their interactions during the plastic deformation. In other words, the modeling of dislocation density is different from the one described by Estrin et al. 1998.

Svodoba et al. 2010 and Kalhori et al. 2010 implemented this physics numerical approach in FE software to simulate the mechanical behavior of steel 316L. Svodoba et al. 2010 implemented also the JC model and compared the reliability in prediction cutting forces and temperature. They concluded that the new dislocation density model was able to better predict the results with very low error values (Figure 109). Kalhori et al. 2010 obtained similar results in predicting chip morphology. Moreover, they observed from the cutting simulations that in the primary shear zone, the highly localized plastic deformation causes the temperature to rise sharply, well above the neighboring regions, which in turn, causes the yield stress to decrease. This corresponds to increasing in dislocation density and vacancies.

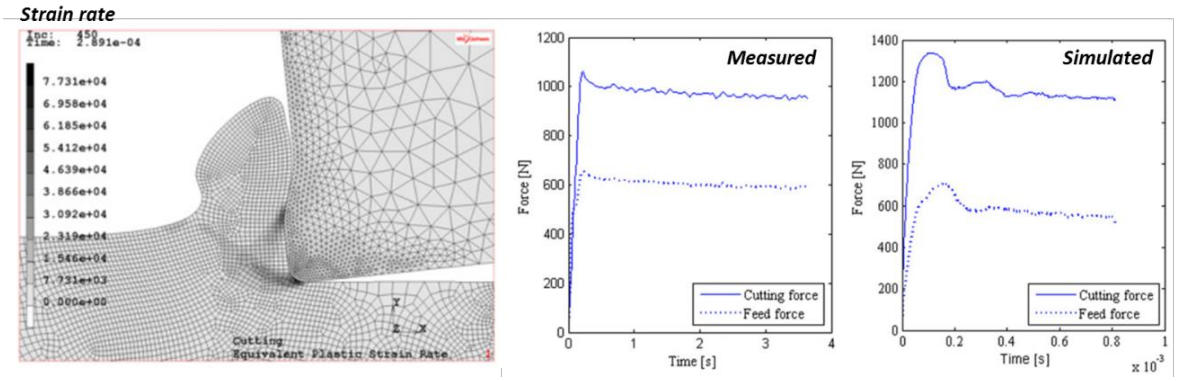

Figure 109: Strain rate predicted and comparison between experimental and numerical cutting forces (Adapted from Svodoba et al. 2010).

At the end of this brief state-of-the-art about the material modeling in machining simulations, it is possible to understand that there are some lack of knowledge in modeling the material behavior.

In particular, the daily growing interest in printing metal parts by Additive Manufacturing technology is still studying new solutions to describe the material behavior of the printed metal parts. The possibility to know constitutive models could be useful to simulate the finishing process in order to optimize the production process. This knowledge can contribute to study and to improve the surface and subsurface quality through the post-processing procedures. Additionally, the aluminum alloy being the most machined metal material due to its applicability and flexibility in many engineering applications still shows some limits in machinability due to particular and strong requirements as high quality surface integrity (Campbel 2006, MacKenzie 2006). From the literature analysis, it is evident that a clear physics based model of the *AA7075-T6* to simulate the high speed machining operations was not proposed so far. It could represent a fundamental tool to help the designer in decisions about the cutting parameters and the machining strategy. The right selection of the manufacturing parameters is fundamental to achieve the quality requirements and the simulations can contribute to build a machining strategy in order to save time and reducing costs to perform long experimental campaigns.

5.2 3D FE model of semi-finishing of *Ti6Al4V* produced via EBM and DMLS technology

In Section 5.2 are described all the main procedures used to set up the numerical model implemented in order to simulate the semi-finishing turning operation of *Ti6Al4V* produced by EBM and DMLS technology on a commercial FE software, namely SFTC DEFORM 2D/3D. In detail, the first section describes the procedure employed to select the appropriate material constitutive model available from those reported in literature, its modification to match the mechanical properties of the Ti alloys produced via AM processes. The following sections describe the development of the FE model, the choice of the friction model and its calibration and the prediction of the main fundamental and surface integrity variables. Finally, the validation of the model through comparison with the experimental results is also showed and discussed.

5.2.1 Material constitutive model

In literature, most of the material constitutive models for simulating thermo-mechanical behavior of the *Ti6Al4V* material are empirically obtained. The JC is mainly used in machining simulation to predict cutting forces as well as temperature and metallurgical changes (Zhang et al. 2017, Arisoy and Özel 2015, Calamaz et al. 2008, Calamaz et al. 2010, Rotella and Umbrello 2014). Imbrogno et al. 2014 provided a comprehensive analysis on prediction capability of JC model in machining simulation testing also several group coefficients for the *Ti6Al4V*. At the end of all the simulations, a selection procedure with the aim to select the model that could provide the best results in terms of cutting forces, temperature and chip morphology prediction was carried out. The selected material constitutive flow stress was the modified JC model proposed by Calamaz et al. 2008 with coupled Lee and Lin 1998 and Özel et al. 2010 proposed constants (Equation 11). Subsequently, the material constitutive flow stress suggested by this procedure (Imbrogno et al. 2014) has been applied and implemented to simulate the material behavior during turning operation of the *Ti6Al4V* produced via EBM.

$$\begin{cases} \sigma = \left(A + B{\varepsilon_p}^n\right)\left(1 + C ln\left(\frac{\dot{\varepsilon}_p}{\dot{\varepsilon}_0}\right)\right)\left(1 - \left(\frac{T - T_r}{T_m - T_0}\right)^m\right)\left(D + (1 - D)\left(tanh\left(\frac{1}{(\varepsilon + P)^r}\right)\right)^S\right) \\ D = 1 - \frac{T}{T_m} \quad P = \left(\frac{T}{T_m}\right)^S \end{cases} \tag{11}$$

where the constants *A*, *B*, *C*, *n* and *m* are listed in the Lee and Lin 1998, while *r* and *S* are the material parameters introduced by Özel et al. 2010. The numerical values of the material constants are summarized in Table 15.

It is important to highlight that to take into account the higher mechanical properties showed by Ti alloy produced via EBM, the "*A*" numerical constant representative of the yield strength was modified. The Lee and Lin 1998 proposed value referred to A constant was equal to 724.7 MPa, after the calibration this value was increased to 940 MPa in according with the higher yield and ultimate strength measured by Facchini et al. 2010 on the *Ti6Al4V* EBM material.

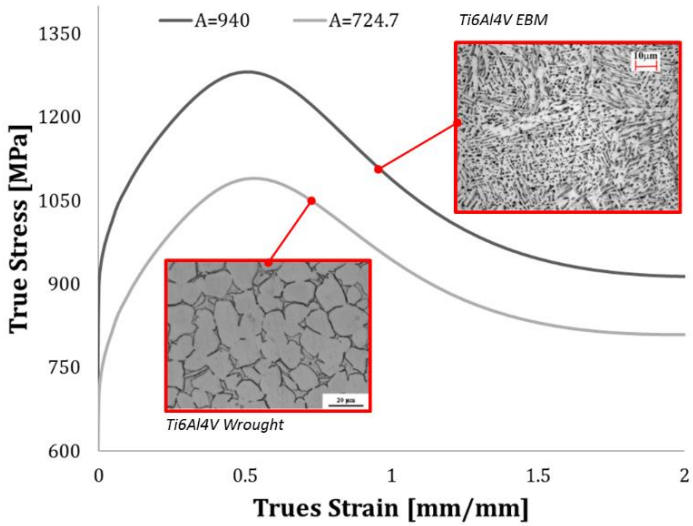

Figure 110: Comparison of the material constitutive flow stress with different numerical constants. The red pictures represent the microstructures.

As showed by Figure 110, the *A* numerical coefficient modified permitted to model a higher strength material, in fact as observed in Chapter III, the *Ti6Al4V* produced via EBM manifested an higher mechanical response compared with the wrought one in terms of yield strength and ultimate tensile strength.

Table 15: Set of coefficient for the material constitutive model adopted in the FE analysis for the *Ti6Al4V* EBM (Lee and Lin 1998, Özel et al. 2010).

A_{EBM} [MPa]	B	C	n	m	r	S
940	683.1	0.035	0.47	1	1.2	2.7

Recently, new interesting studies available in literature regarding the mechanical properties characterization coupled with the microstructure investigations on the *Ti6Al4V* produced via DMSL were carried out. In many of these research works, the experimental flow stress curves, micrographs of the microstructure and its characterization are reported. Nevertheless, empirical material flow stress able to represent the dynamic mechanical response is still missing. However, more information about the mechanical properties of the *Ti6Al4V* produced via DMLS are available in literature, therefore a detailed research on the best empirical material flow stress to fit the stress-strain curves and then the material behavior was carried out.

Regarding the DMLS titanium, the adopted approach was based on researching the experimental stress-strain curves related to the *Ti6Al4V* that was characterized quantitatively and qualitatively by the same microstructure of the material used in the turning test performed on this Ph.D. activity. As described previously in Chapter III, the *Ti6Al4V* DMLS had a lamellar microstructure and the average value of the lamellae thickness into the bulk region was equal to 3.77± 0.82μm.

The material investigated by Mower Todd and Long 2016 was a *Ti6Al4V* produced via AM process and the morphology microstructure (lamellae thickness of 3.50μm) was similar to the one observed in the machined parts (Figure 111).

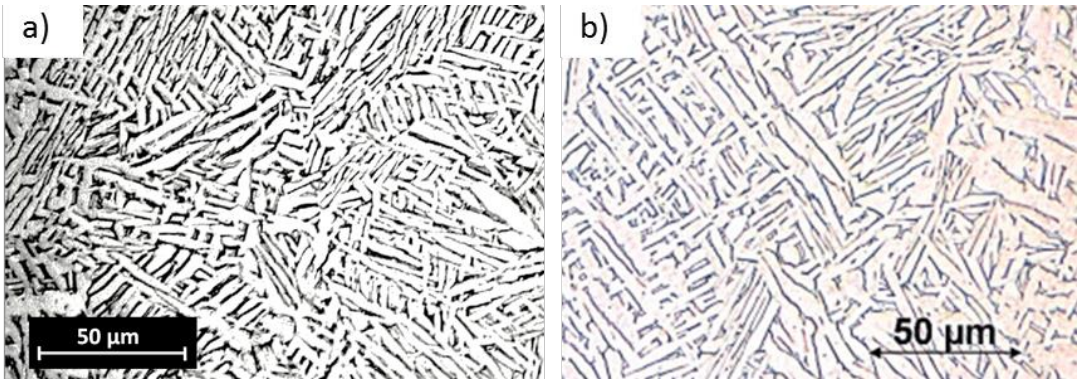

Figure 111: a) *Ti6Al4V* DMLS microstructure of the as-built material, b) Mower Todd and Long 2016.

Furthermore, because the mechanical properties are strongly related to the microstructure of the material, the stress-strain curves provided by Mower Todd and Long 2016 were collected and compared with the empirical ones obtained by computing all the material flow stress available in literature (Table 17). The mechanical properties of the *Ti6Al4V* DMLS obtained by Mower Todd and Long 2016 are reported in Table 16 and the experimental curve is showed in Figure 112.

Table 16: Mechanical properties of Ti6Al4V DMLS (Mower Todd and Long 2016).

Material	E [GPa]	UTS [MPa]	σ_y [MPa]
Ti6Al4V DMLS	111.7	931	862

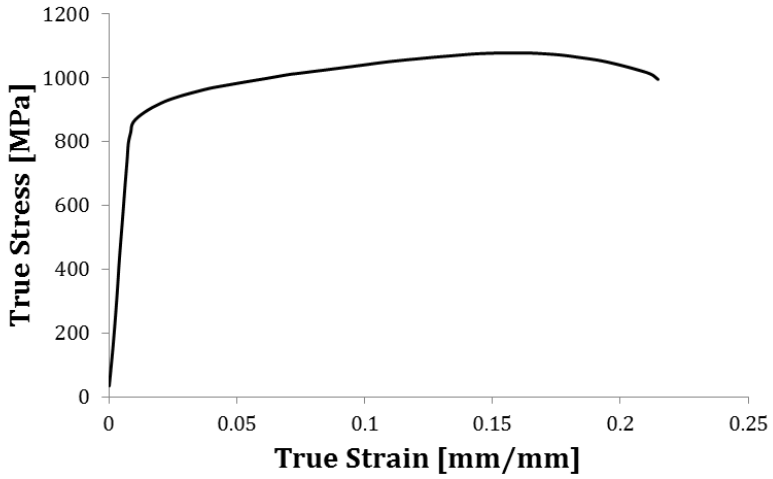

Figure 112: True Stress-True Strain experimental curve of Ti6Al4V DMLS (Mower Todd and Long 2016).

Table 17: Material constitutive model of Ti6Al4V tested.

Material constitutive model - Modified Johnson-Cook
Calamaz et al. 2008: $\sigma = \left(A + B\varepsilon^n\left(\frac{1}{\exp(\varepsilon^n)}\right)\right)\left(1 + C ln\left(\frac{\dot{\varepsilon}}{\dot{\varepsilon}_0}\right)\right)\left(1 - \left(\frac{T - T_0}{T_m - T_0}\right)^m\right)\left(D + (1 - D)\, tanh\left(\frac{1}{(\varepsilon + S)^c}\right)\right)$ $D = 1 - \left(\frac{T}{T_m}\right)^d \quad S = \left(\frac{T}{T_m}\right)^b$
Calamaz et al. 2011: $\sigma = \left(A + B\left(\frac{1}{\dot{\varepsilon}}\right)^a \varepsilon^{(n - 0.12(\varepsilon\dot{\varepsilon})^a)}\right)\left(1 + C \ln\left(\frac{\dot{\varepsilon}}{\dot{\varepsilon}_0}\right)\right)\left(1 - \left(\frac{T - T_0}{T_m - T_0}\right)^m\right)$
Sima et Özel. 2010 (Model 1): $\sigma = (A + B\varepsilon^n)\left[1 + C \ln\left(\frac{\dot{\varepsilon}}{\dot{\varepsilon}_0}\right)\right]\left[1 - \left(\frac{T - T_0}{T_m - T_0}\right)^m\right]\left[D + D\left[\tanh\left(\frac{1}{(\varepsilon + p)^r}\right)\right]^S\right]$
Sima et Özel. 2010 (Model 2): $\sigma = (A + B\varepsilon^n)\left(1 + C ln\left(\frac{\dot{\varepsilon}}{\dot{\varepsilon}_0}\right)\right)\left(1 - \left(\frac{T - T_0}{T_m - T_0}\right)^m\right)\left(D + (1 - D)\, tanh\left(\frac{1}{(\varepsilon + p)^r}\right)^S\right)$ $D = 1 - \left(\frac{T}{T_m}\right)^d \quad p = \left(\frac{T}{T_m}\right)^b$
Sima et Özel. 2010 (Model 3): $\sigma = \left(A + B\varepsilon^n\left(\frac{1}{\exp \varepsilon^n}\right)\right)\left(1 + C ln\left(\frac{\dot{\varepsilon}}{\dot{\varepsilon}_0}\right)\right)\left(1 - \left(\frac{T - T_0}{T_m - T_0}\right)^m\right)\left(D + (1 - D)\, tanh\left(\frac{1}{(\varepsilon + p)^r}\right)^S\right)$ $D = 1 - \left(\frac{T}{T_m}\right)^d \quad p = \left(\frac{T}{T_m}\right)^b$

The material constants used in all the models are reported in

Table 18.

Table 18: Material constants used in the models reported in Table 17.

			Coefficienti JC										
N.	**Modello**	**Ref.**	**A**	**B**	**C**	**n**	**m**	**D**	**P**	**r**	**S**	**a**	**c**
M1		(Lee and He 2006)	968	380	0.02	0.421	0.58	f(T)	-	-	f(T)	1.6	6
M2		(Lee and Lin 1998)	783	498	0.028	0.28	1	f(T)	-	-	f(T)	1.6	6
M3	**Calamaz et al. 2011**	(Shivpuri and Hua 2001)	870	990	0.011	0.25	1	f(T)	-	-	f(T)	1.6	6
M4	d = 1	(Lee and Lin 1998)	724	683	0.035	0.47	1	f(T)	-	-	f(T)	1.6	6
M5	b = 0.4	(Özel and Zeren 2004)	859	640	0.22	2.20E-05	1.1	f(T)	-	-	f(T)	1.6	6
M6		(Meyer and Kleponis 2004)	863	331	0.012	0.34	0.8	f(T)	-	-	f(T)	1.6	6
M7		(Lee and He 2006)	968	380	0.02	0.421	0.58	-	-	-	-	0.1	-
M8		(Lee and Lin 1998)	783	498	0.028	0.28	1	-	-	-	-	0.1	-
M9		(Shivpuri and Hua 2001)	870	990	0.011	0.25	1	-	-	-	-	0.1	-
M10	**Calamaz et al. 2008**	(Lee and Lin 1998)	724	683	0.035	0.47	1	-	-	-	-	0.1	-
M11		(Özel and Zeren 2004)	859	640	0.22	2.20E-05	1.1	-	-	-	-	0.1	-
M12		(Meyer and Kleponis 2004)	863	331	0.012	0.34	0.8	-	-	-	-	0.1	
M13		(Lee and He 2006)	968	380	0.02	0.421	0.58	0.5	0	1	7	-	-
M14		(Lee and Lin 1998)	783	498	0.028	0.28	1	0.5	0	1	7	-	-
M15		(Shivpuri and Hua 2001)	870	990	0.011	0.25	1	0.5	0	1	7	-	-
M16	**Model 1 (Sima and Özel 2010)**	(Lee and Lin 1998)	724	683	0.035	0.47	1	0.5	0	1	7	-	-
M17		(Özel and Zeren 2004)	859	640	0.22	2.20E-05	1.1	0.5	0	1	7	-	-
M18		(Meyer and Kleponis 2004)	863	331	0.012	0.34	0.8	0.5	0	1	7	-	-
M19		(Lee and He 2006)	968	380	0.02	0.421	0.58	f(T)	f(T)	2	1.5	-	-
M20		(Lee and Lin 1998)	783	498	0.028	0.28	1	f(T)	f(T)	2	1.5	-	-
M21	**Model 2 (Sima and Özel 2010)**	(Shivpuri and Hua 2001)	870	990	0.011	0.25	1	f(T)	f(T)	2	1.5	-	-
M22	d = 1	(Lee and Lin 1998)	724	683	0.035	0.47	1	f(T)	f(T)	2	1.5	-	-
M23	b = 2	(Özel and Zeren 2004)	859	640	0.22	2.20E-05	1.1	f(T)	f(T)	2	1.5	-	-
M24		(Meyer and Kleponis 2004)	863	331	0.012	0.34	0.8	f(T)	f(T)	2	1.5	-	-
M25		(Lee and He 2006)	968	380	0.02	0.421	0.58	f(T)	f(T)	2	0.1	-	-
M26		(Lee and Lin 1998)	783	498	0.028	0.28	1	f(T)	f(T)	2	0.1	-	-
M27	**Model 3 (Sima and Özel 2010)**	(Shivpuri and Hua 2001)	870	990	0.011	0.25	1	f(T)	f(T)	2	0.1	-	-
M28	d = 1	(Lee and Lin 1998)	724	683	0.035	0.47	1	f(T)	f(T)	2	0.1	-	-
M29	b = 5	(Özel and Zeren 2004)	859	640	0.22	2.20E-05	1.1	f(T)	f(T)	2	0.1	-	-

M30	(Meyer and Kleponis 2004)	863	331	0.012	0.34	0.8	f(T)	f(T)	2	0.1	-	-

Due to the numerous empirical flow stress curves (6 curves for each material model), a first comparison between the experimental stress-strain curve and the predicted via mathematical models was conducted as showed by Figure 113. From this first analysis, it is possible to observe that for each model there was a group of constants that permitted to fit the experimental curve. From this first step, four models successfully approximated the experimental curve in quasi-static conditions (T= 20°C and $\dot{\varepsilon}$=0.001s^{-1}) and they were M4, M16, M22 and M28.

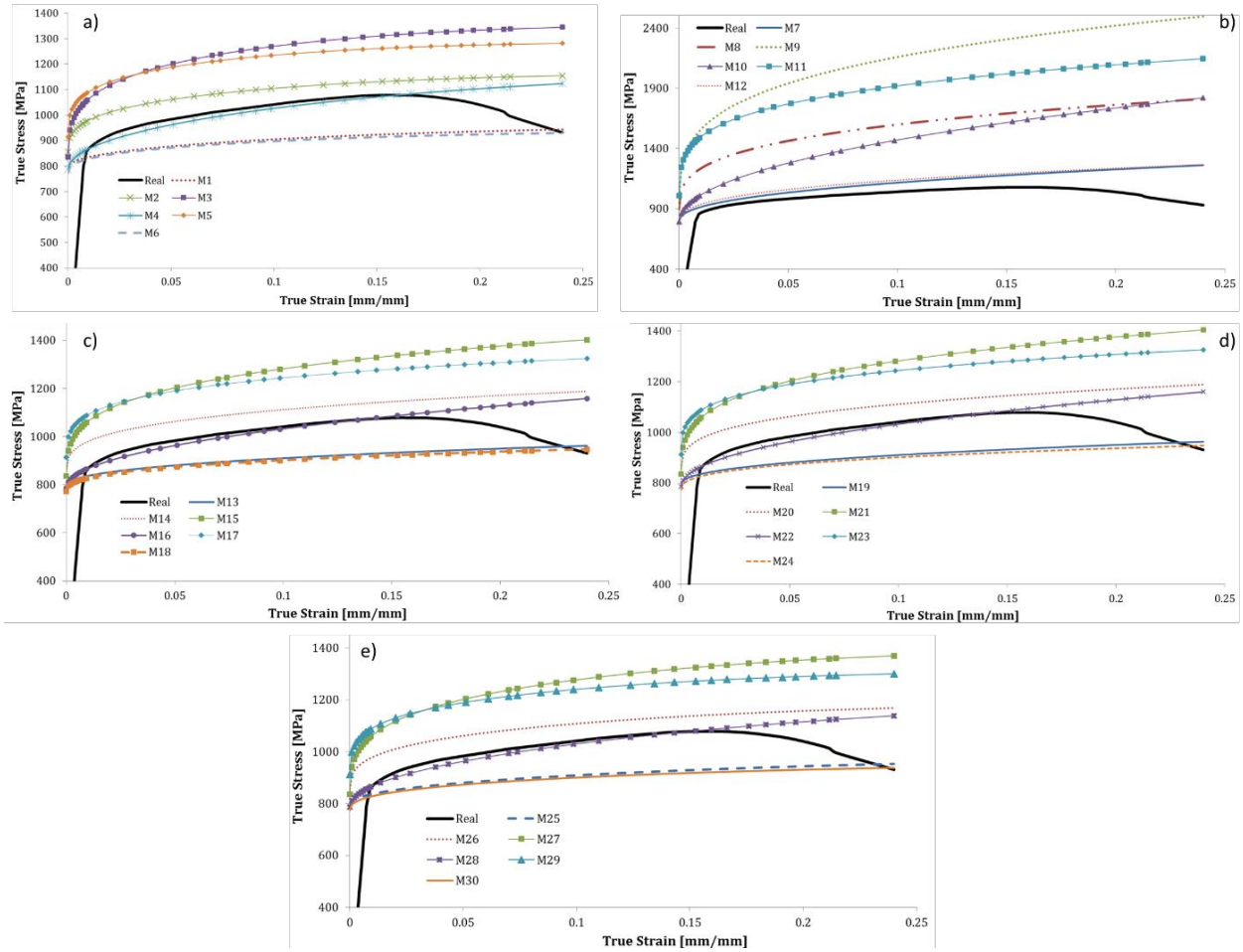

Figure 113: Comparison between all the empirical models and the experimental curve, a) Calamaz et al.2011, b) Calamaz et al. 2008, c) Sima and Özel. 2010 (Model 1), d) Sima and Özel. 2010 (Model 2), e) Sima and Özel. 2010 (Model 3).

These four models were implemented via sub-routine into the FE software to simulate the semi-finishing turning operation. The simulated case studies were characterized by the lowest and the highest cutting parameters, namely cutting speed of 50m/min, feed rate of 0.1mm/rev and cutting speed of 110m/min and feed rate of 0.2mm/rev respectively. The FE simulations were carried out to select the material behavior that minimize the average total error between the predicted cutting forces and temperature and the experimental ones. As showed by Table 19, the selection procedure showed the best model that provided the lowest total average error that was the M4 and the material constants are reported in Table 20.

Table 19: Comparison between numerical and experimental results, total average error.

Model	50/0.1				110/0.2			
	Ft	Fa	T(°C)	Err. % Tot.	Ft	Fa	T (°C)	Err. % Tot.
M4	-1.85%	-18.88%	30.84%	***17.19%***	3.64%	13.59%	22.11%	***13.12%***
M16	22.36%	-15.29%	53.36%	***30.34%***	32.32%	28.82%	45.94%	***35.70%***
M22	38.59%	5.10%	71.25%	***38.31%***	48.08%	53.68%	57.76%	***53.18%***
M28	13.39%	-13.42%	44.40%	***23.74%***	29.22%	31.31%	37.47%	***32.67%***

Table 20: Coefficients of the selected model to simulate the material behavior of the Ti6Al4V DMLS.

A_{DMLS} [MPa]	B [Mpa]	n	C	m	D	S	a	c	d	b
724	683.1	0.47	0.035	1	f(T)	f(T)	1.6	6	1	0.4

In Figure 114a and Figure 114b are reported the predicted flow stress at varying temperature and strain rate of the selected model.

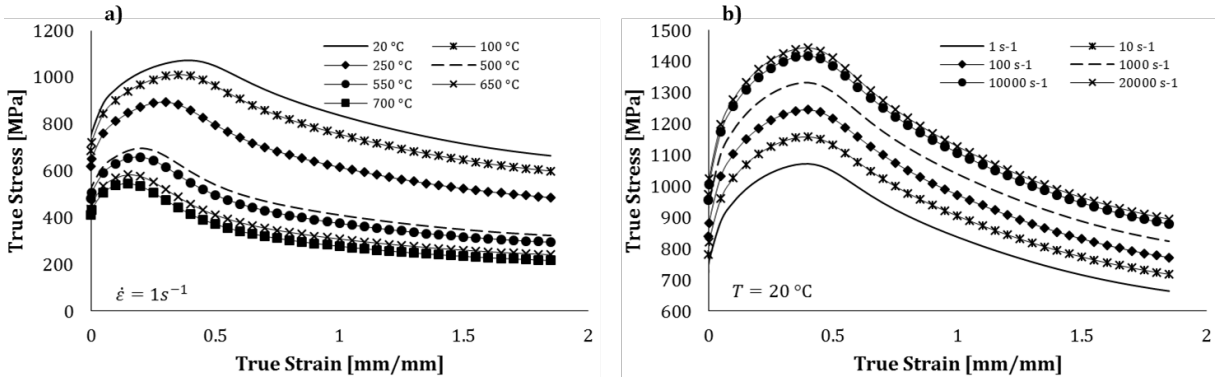

Figure 114: a) Flow stress at vary temperatures and fixed strain rate, b) flow stress at vary strain-rate and fixed temperature.

It is possible to observe that the strain corresponding to the peak stress value decreases when increasing the temperature. Moreover, the stress always increases at very low strain values and subsequently, once the peak stress is reached, the stress starts to decrease until to reach a constant value while the strain increases. This evolution corresponds to the recovery and/or dynamic recrystallization mechanisms. Therefore, this new material law takes into account the influence of the strain, strain rate, temperature on the flow stress and the hypothesis of metallurgical transformation mechanisms (Calamaz et al. 2011, Calamaz et al. 2008).

Generally, typical surface alterations induced by machining operations are plastic deformation, phase transformation, hardness and microstructure variation, residual stress distribution. These modifications drastically affect the functional performance and quality of the machined products as their fatigue life, thermo-mechanical or corrosion strength. Consequently, the FE models have to take into account these metallurgical phenomena and their effect on the mechanical properties of the material to prevent in advance possible deviation from the production process requirements. Moreover, the FE simulations can help to reduce at the same time the waste material rate because few experimental activities are required. Additionally, the simulations lead to a comprehensive understanding of the triggering and the evolution of the metallurgical phenomena that are impossible to catch and observe during the experimental tests. Taking into account the investigated material (*Ti6Al4*V), particularly, the lamellae thickness represents an important feature (Figure 115) in defining the mechanical properties of the material (Tan et al. 2015, Xu et al. 2015, Al- Bermani et al. 2010, Baufeld et al. 2010) as well as its fatigue life (Wu et al. 2013).

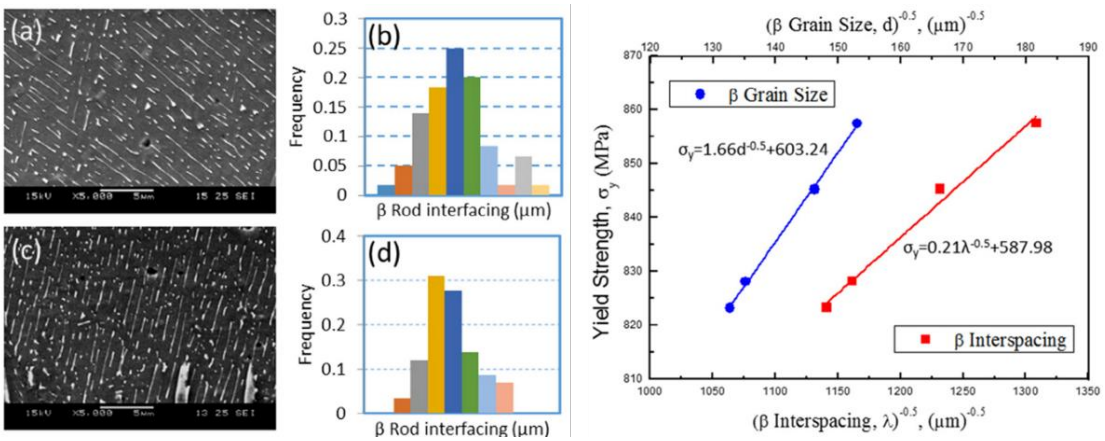

Figure 115: a), b), c), d) measurements of the α-lamellae thickness (or β-interspacing) and correlation between the yield stress and α-lamellae thickness on *Ti6Al4V* produced by EBM (Adapted by Tan et al. 2015).

Therefore, the proper correlations among manufacturing processes parameters set, microstructure and material properties changes are important in order to achieve the desired final properties required for the produced parts (Sha and Malinov 2009). In this work, the numerical model of the microstructural changes (lamellae thickness) was developed and validated based on the experimental data obtained by analyzing several micrographs of the machined surfaces samples. The alpha lamellae thickness variation is mainly provoked by the severe plastic deformation induced by the tool action. Some researches (Tan et al. 2015, Xu et al. 2015, Al-Bermani et al. 2010) showed that the microstructure dimensions and in this case the lamellae thickness affects the yield and ultimate stress. In particular, the increasing of the material strength is inversely proportional to the lamellae thickness. By fitting the data available in literature (Al-Bermani et al. 2010, Baufeld et al. 2010) the empirical model between the yield strength and the microstructure size has been set and implemented into the material flow stress by modifying the *A* constants with the Equation 12 and Equation 13. This modification was carried out with both the flow stresses representative of the material behavior of the *Ti6Al4V* EBM and DMLS.

$$A_{EBM} = 708.73\ MPa + \frac{265.57MPa \cdot \sqrt{\mu m}}{\sqrt{t_{EBM}}} \quad (12)$$

$$A_{DMLS} = 743\ MPa + \frac{239.29MPa \cdot \sqrt{\mu m}}{\sqrt{t_{DMLS}}} \quad (13)$$

The customized user-subroutine takes into account the numerical model to predict the lamellae thickness coupling the state variables, temperature and strain rate by a second order polynomial equation. The model was developed by fitting the strain rate and temperature values predicted by FE software with the experimental measurements, due to the lack of physical models referred to lamellae thickness variation. The numerical constants of the model were calibrated by Matlab non linear regression scripts. The models developed to predict the lamellae variations on the *Ti6Al4V* EBM and DMLS are showed by Equation 14 and Equation 15.

$$\begin{cases} t_{EBM} = 0.873 + 1.5 \cdot 10^{-6} A - 2.3 \cdot 10^{-4} T^* + 3.7 \cdot 10^{-10} A^2 + \\ +1.9 \cdot 10^{-8} A T^* + 5.1 \cdot 10^{-6} T^{*2} \\ A = \dot{\varepsilon} - 36530; \;\; T^* = T - 199 \end{cases} \quad (14)$$

$$\begin{cases} t_{DMLS} = 1.509 - 1.518B + 1.189C - 1.365B^2 + 2.165BC - 0.5671C^2 \\ B = \frac{\dot{\varepsilon} - 1.081E+4}{5470}; \;\; C = \frac{T - 402.7}{34.13} \end{cases} \quad (15)$$

The equations coupled the microstructural alteration, namely the thickness of the alpha lamellae *t*, with the main state variables that described the dynamic plastic behavior such as the strain-rate and the temperature. The microstructure was predicted by the FE model on the machined surface and sub-surface. In this manner, the numerical model could compute the value of *t* for each node of the mesh at any step during the deformation according to the level of temperature and strain-rate induced by the machining process. This value, continuously updated the flow stress referred to *Ti6Al4V* EBM and DMLS. Generally, this microstructural modification led to hardness changes in surface and subsurface; this other aspect was experimentally investigated and then an empirical model was also implemented via sub-routine to simulate the hardness variation during the machining process. Murr et al. 2009 investigated the mechanical properties of *Ti6Al4V* bars produced by additive manufacturing processes and they measured the hardness taking into account different regions on the samples. They also evaluated the microstructure shapes and sizes and they observed that a relation between hardness and microstructure size existed and could be well described by Hall-Petch equation. Al-Bermani et al. 2010 characterized the *Ti6Al4V* samples obtained by EBM process and observed that the yield stress measured on their samples increased with decreasing of the lamellae thickness of the alpha phase. Same results were showed in other interesting research works (Tan et al. 2015, Xu et al. 2015). Based on the scientific outcomes reported in literature, a relation between the lamellae thickness and hardness experimentally measured was defined. The empirical models that correlate the microstructure and the hardness related to the machined titanium samples are represented by Equation 16 and Equation 17.

$$Nanohardness_{EBM} = 1.419\ GPa + \frac{1.747\ GPa \cdot \sqrt{\mu m}}{\sqrt{t_{EBM}}} \quad (16)$$

$$Nanohardness_{DMLS} = 3.344\ GPa + \frac{2.436\ GPa \cdot \sqrt{\mu m}}{\sqrt{t_{DMLS}}} \quad (17)$$

Subsequently, the empirical models developed were implemented into the FE software via subroutine in order to study the hardness changes depending on the cutting parameters and cooling conditions. The comprehensive logic that describes the numerical prediction strategy is showed in Figure 116. The simulation started with the initial set of the cutting parameters, workpiece and tool geometry modeling as well as the friction model and its constants definition. Subsequently, the thermo-mechanical equilibrium was computed and all the state variables as well as the stress field were upgraded.

The microstructure was computed depending on the strain-rate and temperature results and its effect was considered by the flow stress step by step. Moreover, the lamellae thickness modification led to hardness changes that was computed into the sub-routine by the Hall-Petch relation developed and implemented. The numerical results were compared with the experimental ones to validate the numerical predictive strategy and to estimate the reliability of the material behavior and the FE developed models.

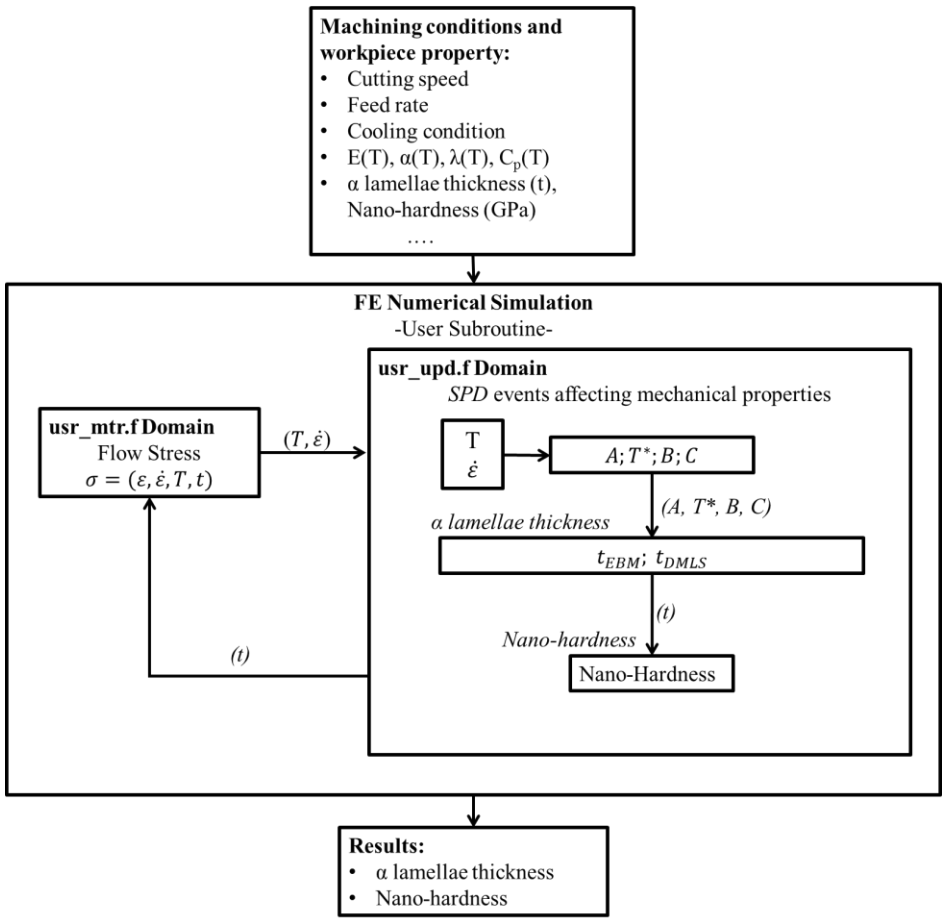

Figure 116: Numerical strategy to predict the α-lamellae thickness, the nano-hardness and to update the flow stress during the machining simulation.

5.2.2 3D FE model of Ti6Al4V semi-finishing machining process

This section reports in detail the modeling procedure used in DEFORM 3D FE environment. Initially, the tool and workpiece geometries were modeled by a CAD software. In Figure 117 is reported the 3D domain of the tool and workpiece.

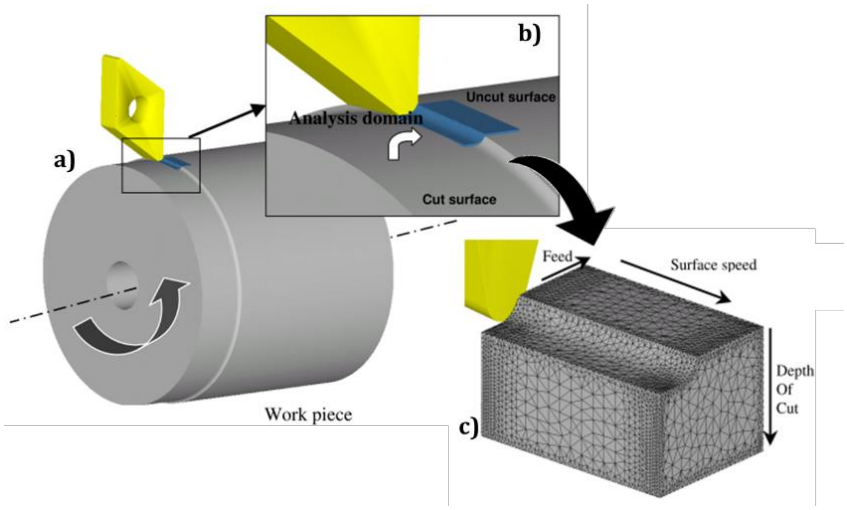

Figure 117: a), b) CAD models and c) FE domain of the turning process (adapted by DEFORM SFTC MANUAL).

In Figure 117a are reported the entire tool and workpiece with the real dimensions. As showed by Figure 117b and Figure 117c, in order to reduce the computational time, a very small portion of workpiece was considered as well as the small region of the tool that was in contact with the workpiece. Moreover, the considered domain (Figure 117b) was very small thus, the curvature of the workpiece piece could be neglected, and a prismatic workpiece was considered (Figure 117c). Once this geometric simplification was clarified, the second step of the modeling procedure was the definition of the workpiece dimensions and the relative position of the tool with the workpiece in the FE environment. In Figure 118 are reported the workpiece dimensions and the tool positioned on the workpiece based on the measurement carried out on the real set-up.

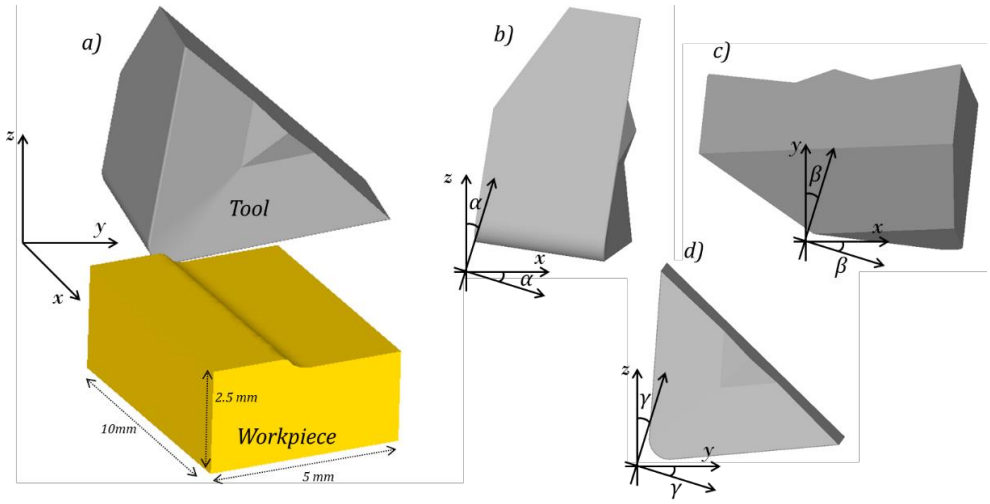

Figure 118: Dimensions of the workpiece and position of the tool in the space simulation; b) α=8°; c) β=7°; d) γ=5°.

Once defined the three-dimensional geometry, the kinematic and thermal boundary conditions were set on the tool and workpiece. In Figure 119 the surfaces with the kinematic-thermal boundary conditions are reported. The left picture represents the kinematic boundary conditions on the tool and workpiece; in particular, the bottom and side surfaces of the tool were fixed in x, y and z directions while the tool was completely free to move.

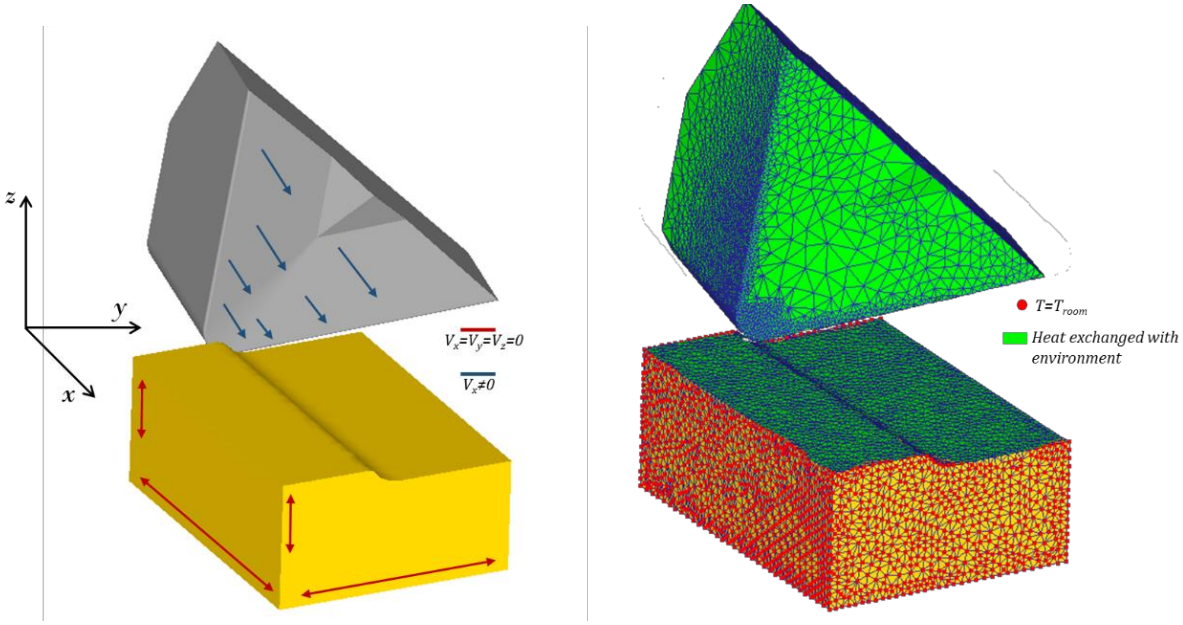

Figure 119: Kinematic and thermal boundary conditions.

The cutting speed and the feed rate were set on the tool in according with the ones used during the experimental tests. The cutting speed was set taking into account the x direction. Regarding the thermal boundary conditions, on the right picture (Figure 119) the upper surface of the workpiece was in contact with the air, therefore, it was able to exchange heat with the environment as the rake and flank face of the tool (green color). The bottom and side faces of the workpiece were at room temperature since represented the inner material as well as the back part of the tool (red color). The Ti alloy produced by EBM was also machined under cryogenic conditions. Therefore, taking into account the cryogenic effect, a further environmental window, that thermally represents the region in which the liquid nitrogen was delivered, was considered. Inside this customized window (Figure 120), the temperature was set equal to -196 °C (liquid nitrogen boiling temperature) while the heat transfer convective coefficient h_{cryo} (W/m²K) was computed by the Equation 18 (Astakhov and Joksch 2012).

$$h_{cryo} = \frac{0.20}{b^{0.35} g^{0.33}} \frac{V_f{}^{0.65} k_f{}^{0.67} c_p{}^{0.33} \gamma_f{}^{0.33}}{v_f{}^{0.32}} \tag{18}$$

where; b is the equivalent length (m), g is the gravitational acceleration (m/s²), and the remaining parameters are properties of the fluid, namely: V_f is the velocity (m/s), k_f is the thermal conductivity (W/m K), γ_f is the specific weight (kg/m³), v_f is the dynamic viscosity (Pa*s) and c_p is the specific heat capacity (J/kg K).

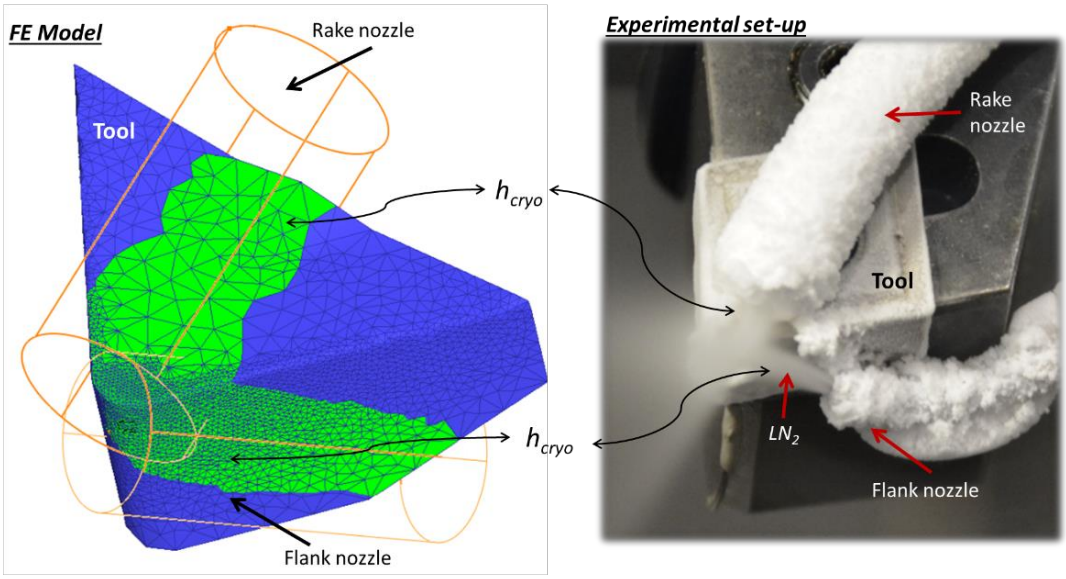

Figure 120: Customized heat exchange windows to model the thermal effect of liquid nitrogen during machining simulation.

Based on this equation and considering the physical and thermal properties of the liquid nitrogen, the Equation 19 was determined depending on the temperature (Figure 121) and implemented in the FE software. The shape of the curve represented in Figure 121a was due to the presence of transition of the nitrogen from liquid to gas (in corresponding to the -196 °C). As reported by Pušavec et al. 2016, the knowledge of the condition of nitrogen is fundamental to better understand its physic characteristics such as density, specific heat capacity, viscosity and therefore its ability to provide benefits into the cutting zone. In Figure 121b are reported the nitrogen properties depending on the temperature. There are huge difference before and after the boiling temperature, consequently the cryogenic characteristics are strongly affected by the liquid or gas nitrogen phase. Correlating these aspects with the cooling capacity/capability, of different nitrogen phases, it has to be taken into account that when nitrogen is delivered to the cutting zone in the liquid phase, a larger amount of the heat is used due to its more favorable physical properties (Pušavec et al. 2016).

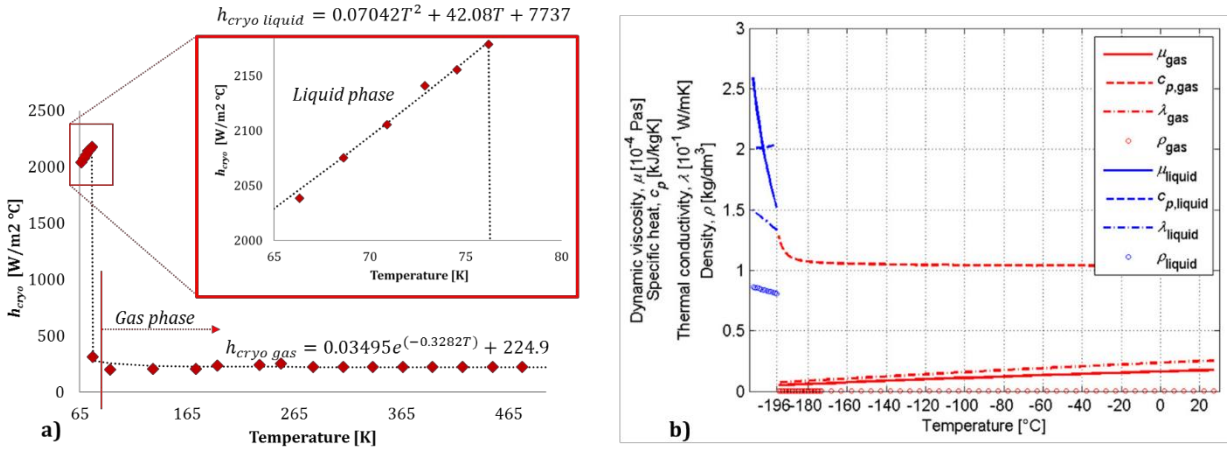

Figure 121: a) heat transfer coefficient implemented in the FE software, b) Nitrogen properties at 10^5 Pa isobar (Pušavec et al. 2016).

Depending on the temperature and consequently on the liquid or gas phase the heat transfer coefficient set into the customized heat exchange window is described by the following equations.

$$h_{cryo} = \begin{cases} 0.07042T^2 + 42.08T + 7737, \ T < -196\,°C \ (Liquid\ phase) \\ 0.03495e^{-0.3282T} + 224.9, \ T \geq -196\,°C \ (Gas\ phase) \end{cases} \quad (19)$$

5.2.3 FE Calibration

The calibration phase aims to determine the right coefficients of the implemented friction model. As demonstrated by Özel 2006, different friction definitions can lead to obtain different simulation outputs. For this reason, to properly simulate the cutting process, a hybrid friction model representative of a combination of sticking-sliding phenomena that occur into the tool-chip contact zone was employed (Figure 122).

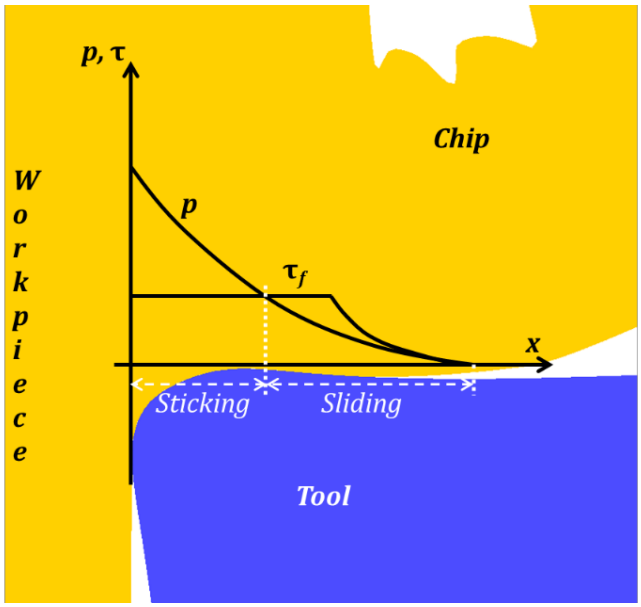

Figure 122: Representation of the sticking-sliding hybrid friction model used in machining simulation.

Focusing on the tribology that characterizes the tool-chip interface zone, several researches showed results of experimental and numerical studies about the shear (due to the friction) and normal stresses (due to the pressure) distribution on tool face (Melkote et al. 2017, Arrazola et al. 2010, Filice et al. 2007). Generally, these distributions are not linear, however while the pressures show a monotonous trend increasing exponentially, from zero (at the point of separation of the tool of the chip) to a maximum value located at the edge of the cutting edge, the shear stresses have a complex trend (Figure 122). In a first section the distribution grows exponentially (following a Coulomb model $\tau = \mu p$, where μ is a constant that needs to be calibrated and p is the interface pressure existing between chip and tool face). However, when it equals the value of the tangential stress of the plastic flow of the chip's material, the tangential stresses follow this model $\tau = m\tau_f$ (where m is a constants that needs to be calibrated and τ_f is the tangential stress of the plastic flow). This observation has led researchers to hypothesize the existence of two zones with different characteristics: in the farthest area from the cutting edge, the contact pressures are still relatively low, so the chip slides on the tool face (sliding conditions) and stresses due to friction follow the $\tau = \mu p$ law.

In the closest area to the cutting edge, however, the contact pressures are so high that, the chip tends to adhere to the surface of the tool (sticking condition): in this zone, the stresses follow the $\tau = m\tau_f$ law, due to the sticking of the chip with respect to the contact layer (Gabrielli et al. 2008). The calibration rule used in this numerical procedure, reported in Figure 123, is based on an iterative analysis that aims to minimize the total average error of predicted cutting forces and temperature. This procedure ends when the average total error is lower than 10%.

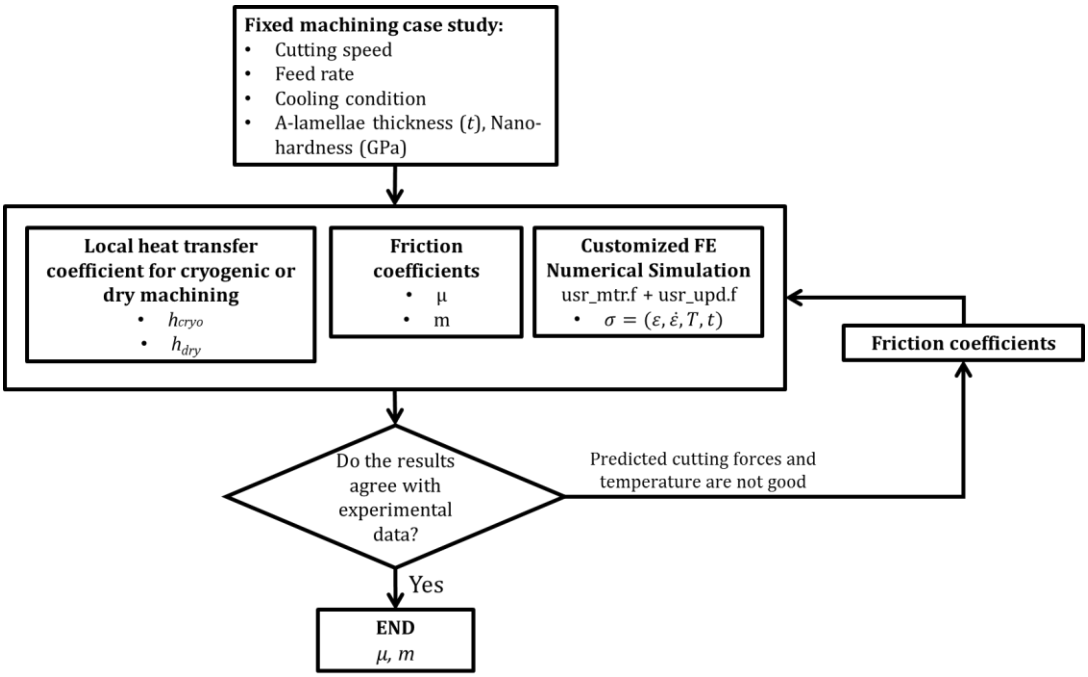

Figure 123: Calibration procedure to determine the friction coefficients of the hybrid friction model.

The calibration procedure was carried out for two cutting conditions corresponding to the following cutting parameters: V_c=50m/min and f=0.1mm/rev, V_c=110m/min and f=0.2 mm/rev. At the end of the calibration phase, the friction coefficients resulted of being equal to 0.2 and 0.3 for μ and m respectively for the machining simulations under dry conditions. On the other side, the friction coefficients calibrated under cryogenic conditions were slightly higher than the ones obtained under dry conditions and are 0.3 and 0.4 for μ and m respectively.

5.2.4 FE Validation

Once the calibration step was concluded, the validation phase was carried out with the aim to evaluate the reliability of the FE developed model in predicting the experimental cutting forces and temperature as well as metallurgical modifications. In particular, in this section, the main results of the predicted cutting forces and temperature under dry and cryogenic turning compared with the experimental outcomes of *Ti6Al4V* EBM and DMLS are reported. In detail, the numerical average values of the main cutting and feed forces were computed by calculating the average values of the data into the steady state region as done during the analysis of the experimental results. For what concern the temperature, a straight line composed by 40 points was considered to extrapolate the predicted temperature on the material region that was in contact with the tool nose (Figure 124). The measured data were considered taking into account the steps of the simulations inside the steady state regions.

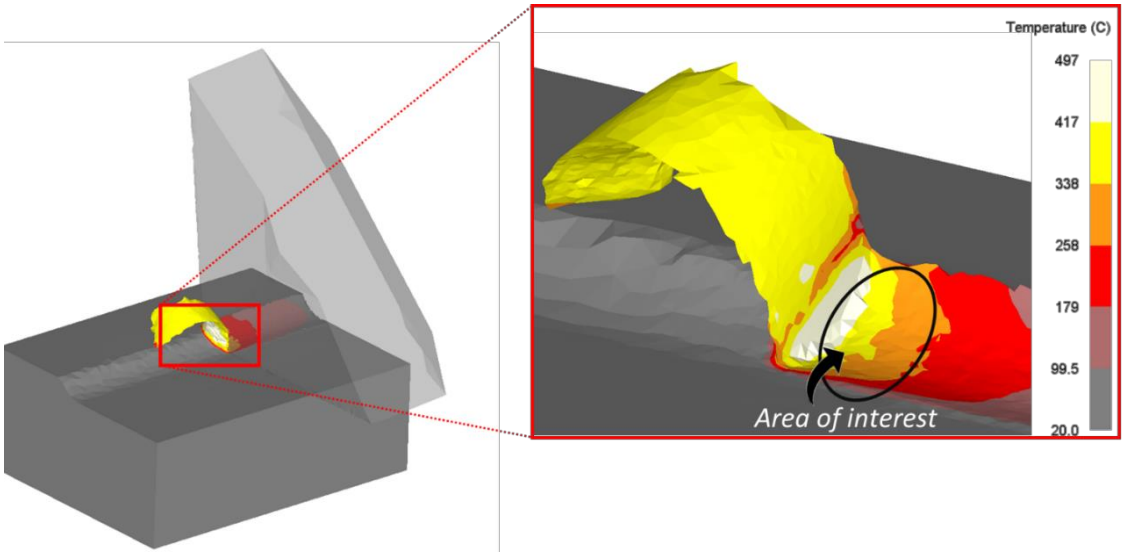

Figure 124: Numerical prediction of temperature and area of interest in which the data were collected.

In Figure 125, Figure 126, Figure 127 and Figure 128 are reported the comparison between the experimental and the predicted results in terms of cutting forces and temperatures. The predicted main cutting forces (Figure 125a, Figure 126a and Figure 127a) fitted correctly the experimental results showing also the same trend at varying cutting speed and feed rate. On the contrary, considering the feed force component (Figure 125b, Figure 126b and Figure 127b), the predicted one was lower than the experimental one. The reason of this result was probably due to the friction model that did not properly fit the real friction conditions on the flank face when semi-finishing operations were simulated. In fact, the feed force prediction when small parts of material were in contact each other was related to the number of elements used to increase the contact among the nodes. A higher number of elements into the cutting zone and on the tool nose were employed to solve this problem nose (better approximation of the cutting edge), but this led to increase the computational time. However, the trend depending on the cutting parameters was always predicted and the most important force component was the Main Cutting Force (Fz) that was directly related to the power consumption of the machine.

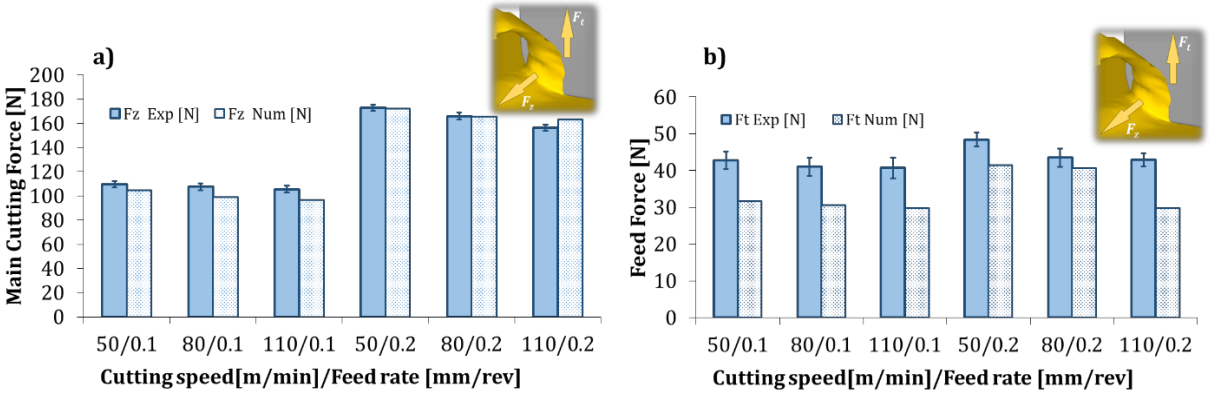

Figure 125: Comparison between experimental and numerical cutting forces; a) main cutting force (Fz) and b) feed forces (Ft) of turning tests on Ti6Al4V EBM under dry conditions.

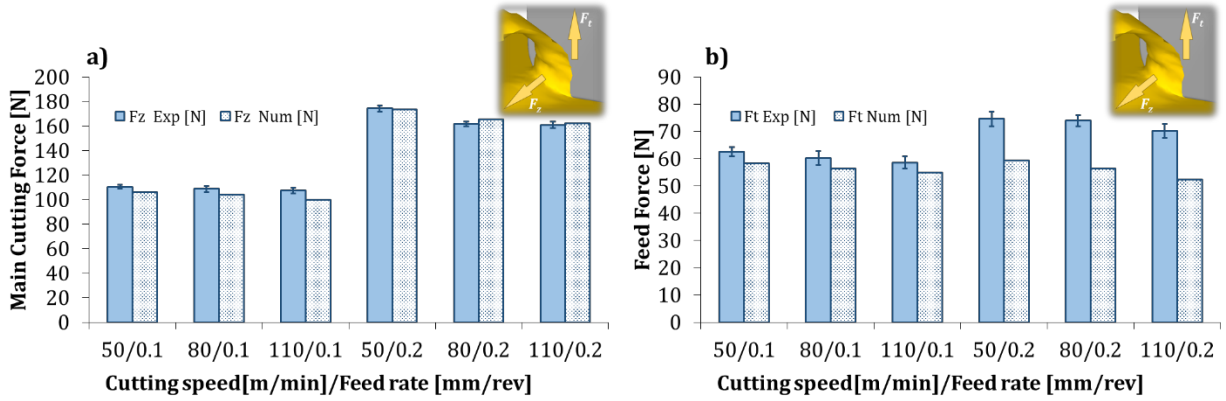

Figure 126: Comparison between experimental and numerical cutting forces; a) main cutting force (Fz) and b) feed forces (Ft) of turning tests on Ti6Al4V EBM under cryogenic conditions.

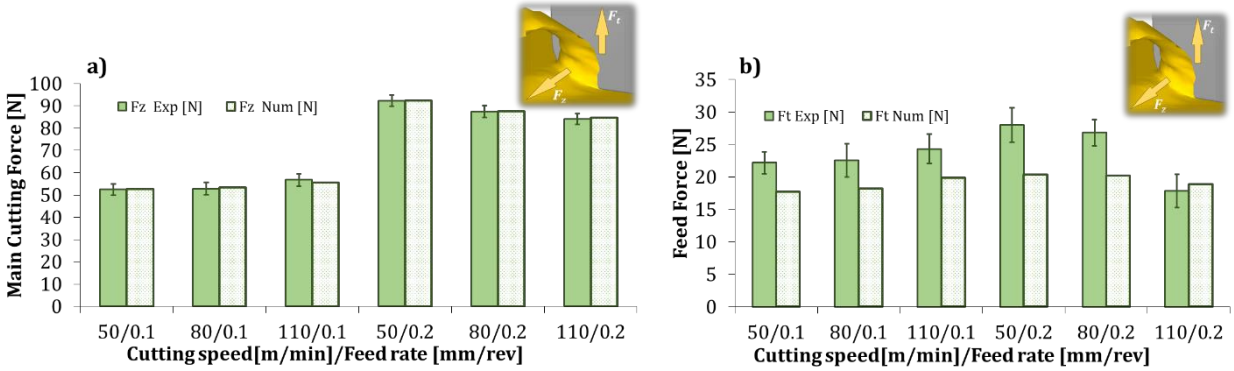

Figure 127: Comparison between experimental and numerical cutting forces; a) main cutting force (Fz) and b) feed forces (Ft) of turning tests on Ti6Al4V DMLS under cryogenic conditions.

In Figure 128 are reported the numerical and experimental results of the cutting temperature. Generally, the numerical model slightly overestimated the temperature and this result could be conservative from the tool wear point of view. Moreover, it is possible to observe that at varying cutting speed and feed rate the experimental trend was well predicted. Another important positive aspect of the FE developed model was the ability to predict the temperature during the cryogenic machining conditions. This result confirmed the accurate model strategy related to the heat transfer convective coefficient proposed in Section 5.2.2. Although the heat transfer during the machining operation with coolant was complex to study, the proposed approach was easy to implement into the FE software and it permitted to predict with a very small error the thermal gradient into the cutting zone. It is possible to confirm the correct material modeling strategy used to define the material behavior of these new class of materials (metal printed). The results showed that even though the material investigated was *Ti6Al4V* alloy, the additive production process modified its metallurgy and consequently its material behavior. In fact, the conventional material model available in literature were slightly modified to achieve the mechanical properties of the *Ti6Al4V* produced via EBM and DMLS.

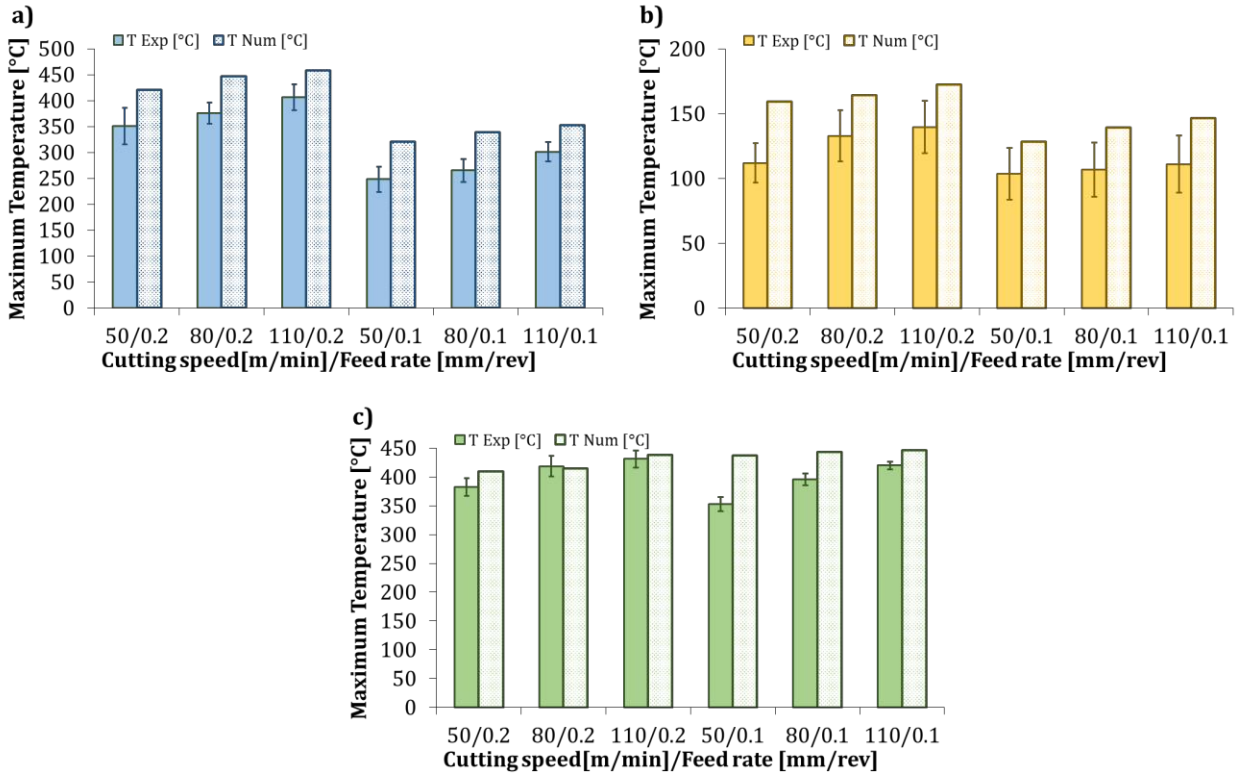

Figure 128: Comparison between experimental and numerical maximum temperature; a) Ti6Al4V EBM dry machining, b) Ti6Al4V EBM cryogenic machining, c) Ti6Al4V DMLS dry machining.

5.2.5 Surface Integrity Analysis

The proposed FE model aims to predict important information of industrial interest such as cutting forces, temperature on the tool nose and machined surfaces as well as to describe the evolution of the main state variables like plastic strain, strain rate and the metallurgical changes (lamellae thickness and hardness variations induced by plastic deformations). The model permits also to evaluate the influence of the cooling strategy on the surface integrity to better understand its role on the surface and subsurface quality of the machined parts. The numerical analysis was carried out only on the *Ti6Al4V* alloy produced by EBM due to the interesting outcomes observed during the experimental activity (Chapter III). In Figure 129 are reported the transversal section of the machined parts and the results of the simulated state variables related to *Ti6Al4V* EBM at cutting speed of 80m/min and feed rate of 0.1mm/rev. Figure 129a, Figure 129c and Figure 129e are referred to the numerical prediction. A cutting plane in the transversal direction sectioned the workpiece in order to show the strain, α-lamellae thickness and nano-hardness surface and subsurface predictions. Figure 129b, Figure 129d and Figure 129f represent the micrographs of the machined material. In particular, Figure 129b represents the plastically deformed microstructure and the parameter measured to quantify the plastic deformation amount inside the affected layer. Figure 129d shows the deformed lamellae and its thickness variation from the surface into the depth induced by plastic deformation. Figure 129f shows the nano-hardness tips carried out on the transversal section of the machined material. The depth of the affected material (Figure 129a and Figure 129c) was comparable to what observed experimentally (Figure 129b and Figure 129d).

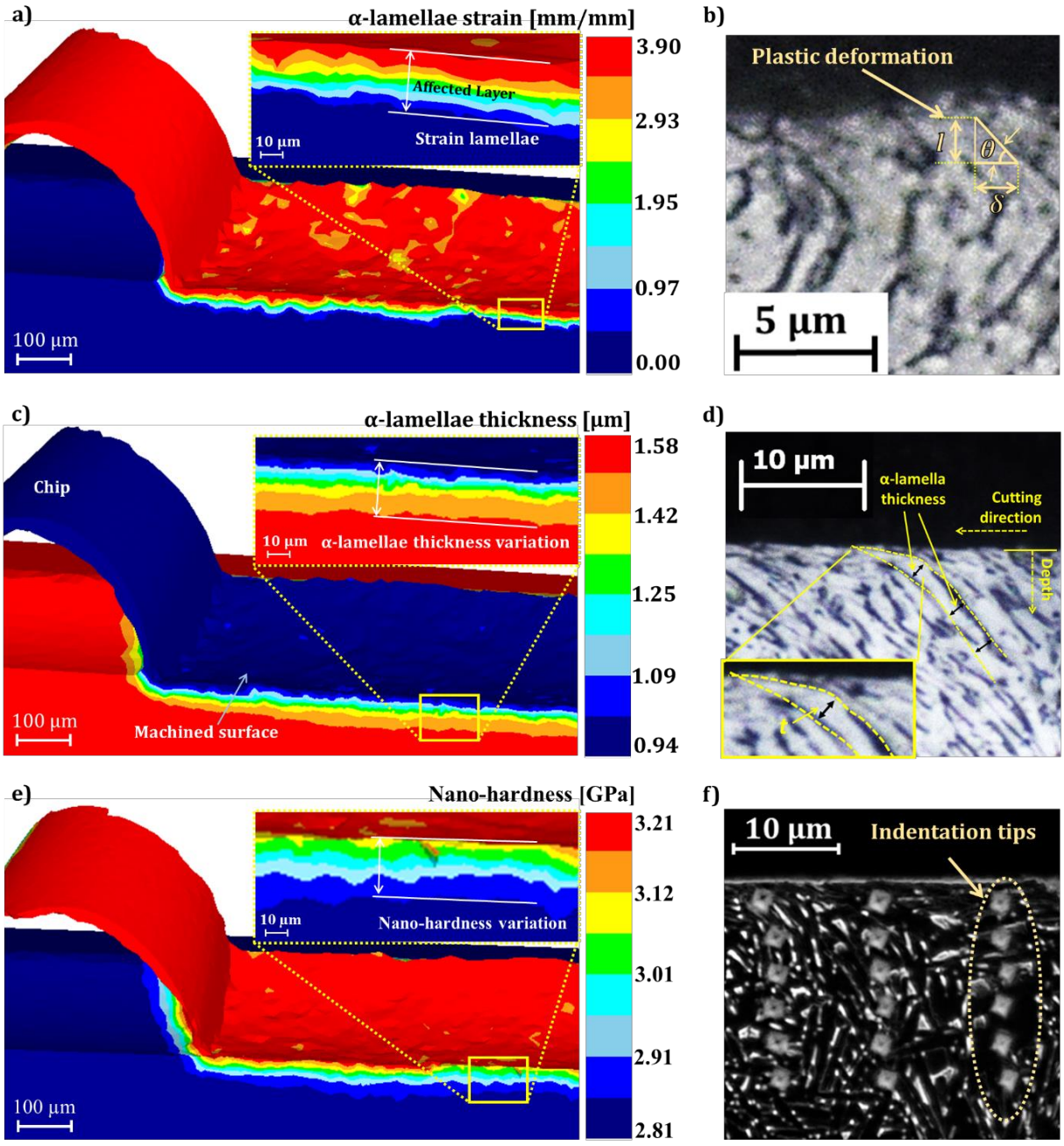

Figure 129: a) α-lamellae thickness predicted by FE simulation on *Ti6Al4V* EBM; b) micrograph of *Ti6Al4V* EBM microstructure in which α-lamellae is deformed due to the machining operation (V_c= 80m/min, f=0.1mm/rev dry conditions).

In Figure 130a and Figure 130b are reported the comparison between the α-lamellae thickness numerically predicted and experimentally measured approximately 2µm beneath the machined surface referred to *Ti6Al4V* EBM.

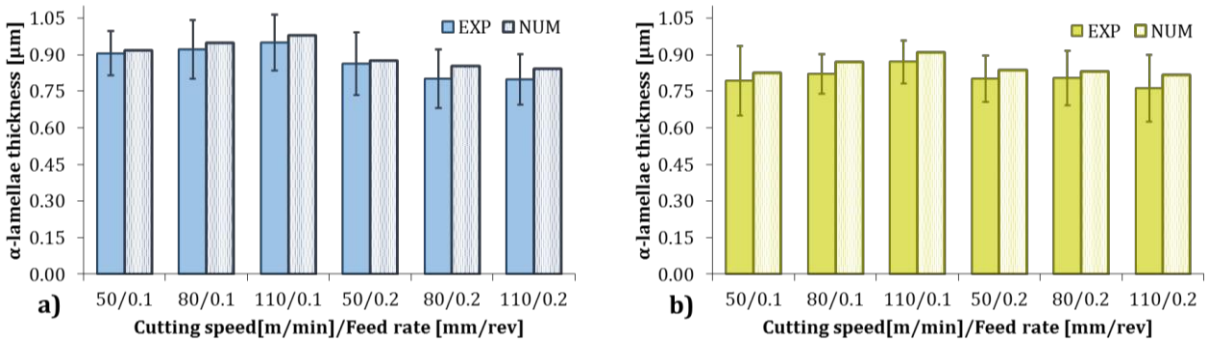

Figure 130: Comparison between numerical prediction and experimental measurements of α-lamellae thickness of machined *Ti6Al4V* EBM; a) dry conditions, b) cryogenic conditions.

Focusing on the results obtained with feed rate equal to 0.1 mm/rev, the liquid nitrogen had a predominant effect respect to the cutting speed in the reduction the lamellae thickness. The numerical model predicted this variation suggesting that the cryogenic conditions was well defined into the software. Therefore, the FE developed model could be used to study the cooling effect provided by the LN_2 on the microstructure setting new cutting speed and feed rate to study the metallurgical evolution of the α-lamellae. The higher feed rate (0.2 mm/rev) induced more plastic deformation that was represented by more bended lamellae and consequently smaller lamellae thickness close to the machined surface. In this case, the presence of LN_2 led also to a more evident effect on the microstructure (thinner lamellae thickness). This latter aspect was well predicted by the FE model and the results was well represented in Figure 129c and Figure 129d. Thus, the ability of the cryogenic cooling to stop the regrowth phase plays the major role in the grain refinement process (Jawahir et al. 2016, Rotella et al. 2014, Rotella and Umbrello 2014). All these aspects also led to higher yield strength and hardness (Figure 131).

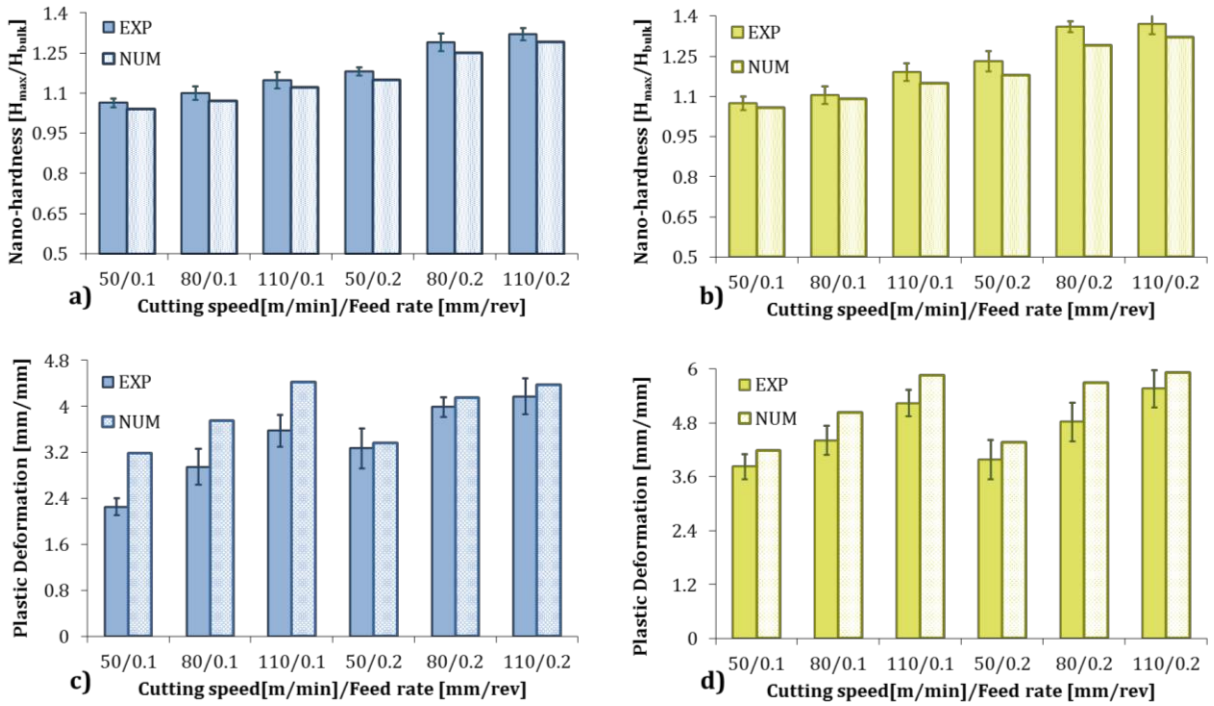

Figure 131: Comparison between numerical prediction and experimental measurements on *Ti6Al4V* EBM; a) nano-hardness dry condition; b) nano-hardness cryogenic condition; c) plastic deformation dry condition; d) plastic deformation cryogenic condition.

Finally, in Figure 131a and Figure 131b are reported the comparison between the nano-hardness measured on the machined surface and the related prediction by the FEM under dry and cryogenic conditions respectively, while in Figure 131c and Figure 131d the plastic deformation entities. The nano-hardness near the machined surface (Figure 131a and Figure 131b) was particularly influenced by both thickness and strain hardening effect. It is possible to observe that both under dry and cryogenic machining, the increase of the cutting speed led to an increase of the hardness close to the surface and higher feed rate produced higher hardness. Although the high cutting speeds produced more heat into the cutting zone, the measured amount of plastic deformation (Figure 131c) was higher respect to the one measured at lower cutting speeds. This means that the temperature and the recovery phenomena were not predominant even though were present. Therefore, the higher hardness was justified by the dislocation density accumulation into the texture. As also observed by Lee and Lin 1998, the microstructure of the room temperature deformed sample was characterized by high density of randomly-tangled dislocation networks that were lower when the material was deformed at higher temperature. The recovery phenomena due to the higher temperature may lead to softening and decrease in hardening rate. Therefore, by these observations it is possible to affirm that the dislocation density accumulation during deformation at lower temperature is higher and therefore the hardness is higher as well. Hence, the cryogenic fluid has a positive effect in increasing the hardness because avoid any recovery effect due to high temperature especially at higher feed rate. Moreover, the higher plastic deformation showed by Figure 131d clearly supports what previously affirmed, therefore, higher hardness under cryogenic were mainly due to the higher work hardening and more density dislocations accumulated. The FE model clearly predicted this behavior depending on the cooling condition adopted during the machining operation. As overall, the obtained results highlight the beneficial and positive effects of the cryogenic application when AM metal parts made in *Ti6Al4*V alloy are machined. Furthermore, the newly developed FE model permits to predict and numerically analyze the microstructural changes and surface integrity details varying the cooling conditions (dry and cryogenic) and the cutting parameters conventionally adopted in semi-finishing cutting operations.

5.3 3D FE model of high speed machining of *AA7075-T6*

This paragraph describes the development of 3D Finite Element model coupled with a physically based constitutive behavior model of the *AA7075-T6* in order to simulate the machining process under different cooling conditions. The choice to implement a physics based model is justified by some important reasons. Indeed, from the literature review, analyzing the numerical models of the constitutive behavior previously reported (Section 5.1), it is possible to understand that the mechanical behavior described by empirical laws is easier to develop and to implement into FE software compared with a physics-based law. On the other hand, the information related to the surface integrity is not always clear and its modification has no physics foundation due to the empirical nature of the equations. Therefore, a physic modeling approach is obviously required, due to the severe manufacturing process adopted. In fact, several metallurgical alterations (grain size and hardness changes, dislocation density evolution and precipitation formations) are involved and the understanding of their evolution, through numerical simulation, can surely help the analysis of the experimentally obtained results. Moreover, the surface integrity interpretation will be more reliable due to the physics foundation of the equations implemented and it could be used to make some design decisions about the process parameters that need to be set in production.

5.3.1 Material constitutive model

The constitutive law developed to simulate the material behavior during machining processes was built up taking into account the experimental observation of Ma et al. 2014, Dixit et al. 2008 and Zhao et al. 2004. In order to develop a physics based model it is fundamental the understanding of the material characteristics and all the physics variables that can contribute to describe the mechanical strengthening phenomena. Taking into account the aluminum alloy 7xxx series, the elements Zn, Mg and Cu form precipitates of various ternary and quaternary compositions following solution heat treatment and aging. The strengthening effects of these precipitates depend on their size, spacing and distribution. Other mechanisms like grain boundary strengthening, solid solution strengthening and strengthening due to work hardening contribute to increase the strength (Dixit et al. 2008). Therefore, regarding the analyzed aluminum alloy *7075-T6*, the following mechanisms strengthening were taken into account during the formulation of the physically-based material behavior model. As stated by Kocks 1966 and subsequently used from many other researchers (Melkote et al. 2015, Sabirov et al, 2013, Topping et al. 2012, Asghrzadeh et al. 2011, Gubicza et. al 2007) the yield strength can be reasonably assumed as a linear additivity of the different strengthening contributions previously mentioned (Equation 19).

$$\sigma = \sigma_{th} + \sigma_{dis} + \sigma_{hp} + \sigma_{or} + \sigma_{ss} \tag{19}$$

Where σ_{th} is representative of the short-range contribution and is thermally activated. It is the stress needed for a dislocation to pass short-range obstacles and to move it through the lattice (also known as the general term for dislocation glide) (Frost and Ashby 1977b). The thermal vibrations can assist the stress to overcome these obstacles. σ_{dis} denotes the long-range and it is often called strain hardening due to the forest dislocations (dislocation strengthening), σ_{hp} is representative of the Hall-Petch effect (long-range contribution), namely the grain size strengthening effect (i.e. grain size contribution to the flow stress). The σ_{or} is representative of the precipitation hardening (short-range contribution) and the σ_{ss} of the solid solution hardening (short-range contribution). The long-range contribution are sometimes considered as athermal contribution because the thermal vibrations cannot assist a moving dislocation to pass the region subjected to long-range distortion of lattice (Conrad 1970).

Long-range contribution - strain hardening

The interaction between moving dislocations and immobile dislocations is a long-range interaction (if it cuts orthogonal to the dislocation is of short-range). This interaction is the physical basis of the strain-hardening of a metal. The long-range contribution to the material resistance is represented by Equation 20 (σ_{dis}). This mechanical resistence is due to the interactions with the dislocation substructure (Artz 1998, Seeger 1956).

$$\sigma_{dis} = M\alpha G b\sqrt{\rho_i}\,;\left(G = 28815 - \frac{3440}{e^{\frac{210}{T}}-1}\right) \tag{20}$$

In Equation 20, α is a proportional fraction, ρ_i is the density of immobile dislocations and *G* is the temperature dependent shear modulus, *b* is the Burger's vector and *M* is the Taylor factor computed as (G/G_0). The immobile dislocation density evolution is described by Equation 21 (density dislocation evolution) (Bergström 1983). It is important to highlight that the mobile dislocation is assumed to be much smaller than the immobile one. The evolution equation consists of two terms: $\dot{\rho}_i^{(+)}$ that is representative of the hardening and $\dot{\rho}_i^{(-)}$ that is representative of the softening due to the recovery.

$$\dot{\rho}_i = \dot{\rho}_i^{(+)} - \dot{\rho}_i^{(-)} \tag{21}$$

Hardening contribution

The mobile dislocations may encounter obstacles that prevent further movement and become immobilized due to the trapping effect of the obstacles. Moreover, when dislocations are moving next to the grain boundaries can be annihilated due to the interactions with dislocations of opposite sign. The increase in dislocation density is assumed to be proportional to the plastic strain rate (Equation 22).

$$\dot{\rho}_i^{(+)} = \left(\frac{1}{s} + \frac{1}{D}\right)\frac{M}{b}\dot{\varepsilon}^p = \frac{M}{b\Lambda}\dot{\varepsilon}^p \tag{22}$$

M is the Taylor, *b* is the Burger's vector, $\dot{\varepsilon}^p$ is the plastic strain rate and Λ interpret the mean free path of a moving dislocation until it is immobilized. In the Equation 22, *D* and *s* represents the grain size and the cell size respectively. The cell size is assumed to be inversely proportional to the square root of the immobile dislocation according to Equation 23 (Holt 1970).

$$s = \frac{K_c}{\sqrt{\rho_i}} \tag{23}$$

where K_c is a calibration parameter.

Softening contribution

Different processes may contribute to the reduction in the dislocation density. They are separated into static and dynamic recover as showed by Equation 24.

$$\dot{\rho}_i^{(-)} = \dot{\rho}_{sr}^{(-)} - \dot{\rho}_{dr}^{(-)} \tag{24}$$

The $\dot{\rho}_{sr}^{(-)}$ represents the static recovery. This formulation is depending on some physics constants as Boltzamnn's constants and self-diffusivity models. It is also depending on grown of dislocation density that is used in the model to prevent that the dislocation density become zero when very long times are considered in the process. In the machining simulation, a very short interval time proportional to $\propto$ 1e-7s is considered, consequently its contribution ($\dot{\rho}_{sr}^{(-)}$) was neglected. On the contrary, the dynamic recovery terms is proportional to the immobile dislocation density and the plastic strain rate (Equation 25). The dynamic recovery implies that moving dislocation annihilates the immobile ones.

$$\dot{\rho}_{dr}^{(-)} = \Omega \rho_i \dot{\bar{\varepsilon}}^p \tag{25}$$

where Ω is a recovery function and its expression is reported in Equation 26

$$\Omega = \Omega_0 + \Omega_{r0} \left(\frac{1}{\dot{\bar{\varepsilon}}^p} \frac{D}{b^2} \right)^{1/3} \tag{26}$$

Where D is a diffusivity, while Ω_0 and Ω_{r0} are two calibration parameters (Bergstrom 1983). As reported by Bergstrom 1983, the recovery for the dislocations takes place mainly in the cell walls and this process is due to climb controlled by excess vacancies created during deformation.

Long-range contribution – the Hall-Petch effect

The Hall-Petch effect is due to the resistance to dislocation motion offered by grain boundaries. In detail, this effect is due to pile-up of dislocations at grain boundaries leading to the activation of other slip systems in the surrounding grains (Johnson and Feltner 1971). The equation representative of the Hall-Petch contribution to the flow stress was computed as showed by Equation 27.

$$\sigma_{hp} = \sigma_0 + \frac{k_{hp}}{\sqrt{D}} \tag{27}$$

Where σ_0 is the frictional or Peierls stress and its value has been taken from Vlado 2007, D is the grain size and k_{hp} is a coefficient. As grains are refined progressively, once they decrease under a critical value the material strength starts to decrease. This phenomenon is commonly referred to the inverse Hall-Petch effect and different physical explanations are available in literature (Takeuchi 2001, Scattergood and Kock 1992, Thomas et al. 1990). The coefficient k_{hp} catches the physics phenomenon that is particularly evident as a grain boundary sliding coupled with extreme grain refinement. This results in a softening effect on the material constitutive behavior and this effect is captured by the Equation 28 (Melkote et al. 2015):

$$\begin{cases} k_{hp} = \alpha_G^0 tanh\left(\frac{d}{D^{-0.5}}\right)^{\nu} \\ \nu = 0.000475T + 1.2455 \end{cases} \quad (28)$$

Where *d* and α_G^0 are calibration parameters while *D* is the grain size due to continuous grain refinements. The ν is a calibration parameter depending on the temperature.

Grain size evolution

The grain size *D* was computed based on the Equation 29 reported by Hallberg et al. 2010. The model was developed taking into account the inelastic deformation defined by the formation and annihilation of dislocations together with grain refinement due to continuous dynamic recrystallization. This latter occurs due to plastic deformation also without the aid of elevated temperature.

$$D = D_0 - \left(D_0 - D_f\right)\left[1 - e^{\left(-k_x\left(\varepsilon_{eff} - \varepsilon_c\right)^{c_x}\right)}\right], D_f \leq D \leq D_0 \quad (29)$$

$$\varepsilon_c = 0.058556\left(\frac{Z}{A}\right)^{0.00645} \quad (30)$$

$$Z = \dot{\varepsilon}_{eff} e^{\left(\frac{Q}{RT}\right)} \quad (31)$$

Where D_0 is the initial grain size (4.85 μm), D_f is the final grain size (in this case is the smallest grain size measured from all the case analyzed and its value is equal to 1.54 μm) and k_x and c_x are numerical constants. The Equation 29 is also depending on effective plastic strain ε, ε_{cr} is the critical strain for the nucleation of the recrystallization (Equation 30) and its formulation has been taken from Quan et al 2012. The critical strain physically represents the strain point at which the dynamic recrystallization usually starts and the Equation 30 depends on Z that is the Zener-Hollomon parameters. The Z parameter was computed as shown by Equation 31 and the coefficient A is a numerical constant also reported in Quan et al 2012. Q is the activation energy that is function of strain rate and temperature as reported by Shi et al. 2013.

Short-range contribution

The σ_{th} term, showed by Equation 32 represents the material resistance to plastic deformation due to the short-range interactions where thermal activated mechanisms assist the applied stress in moving dislocations (Caillard and Martin 2003). Short-range obstacle is a general classification of any disturbance of the lattice that is "small enough" so that thermal vibrations can, together with the effective stress, move the affected part of a dislocation through that region.

$$\sigma_{th} = M\sigma_i\left(1 - \left(\frac{k_b T}{g_{0i} G b^3} ln\left(\frac{\dot{\varepsilon}_{ref}}{\dot{\varepsilon}^p}\right)\right)^{2/q}\right)^{1/p} \quad (32)$$

where k_b is the Boltzmann constant, T is the temperature, Δf_0 , *q* and *p* are calibration parameter and $\dot{\varepsilon}_{ref}$ is typically taken as 10^6 or 10^{11} (Frost and Ashby 1982).

The σ_{or} represents the strengthening effect due to the precipitation hardening in the Al alloy of very small particles that usually are not sheared during the mechanical tests at yield stress (Equation 33).

$$\sigma_{or} = 0.3MG\frac{b}{R}\sqrt{f_v} \tag{33}$$

σ_{or} is depending on *G* that is the shear modulus, *R* is the mean particle radius of the precipitates, *M* that is the Taylor factor computed as (G/G_0), *b* is the Burger's and f_v is the precipitate volume fraction (Nicolas and Deschamps 2003).

The σ_{ss} term is representative of the solid solution strengthening and generally, in metals it depends on the concentration of solute atoms dissolved in the matrix *C* as showed by Equation 34

$$\sigma_{ss} = HC^n \tag{34}$$

Where *H* is computed as showed by Equation 35 and *n* is a constant. The parameter *n* can be in the range of 0.5-0.75 (Ryen et al. 2006).

$$H = -1.2004T + 885.11 \tag{35}$$

As previously mentioned, there are some numerical constants that are unknown, as a results their value were calibrated by fitting the experimental true stress-true strain curve experimentally obtained. In particular, some compression tests at different temperature values and at strain-rate 0.1 s^{-1} and 0.5 s^{-1} were carried out. Subsequently, the numerical prediction provided by the physically-based model were plotted together with the experimental curves and a fitting procedure was initialized. Once the fitting procedure provided an average error lower than 1%, the unknown numerical constants were finally determined. Subsequently, the model has been elaborated through excel and the numerical unknown constants were obtained after calibration procedure.

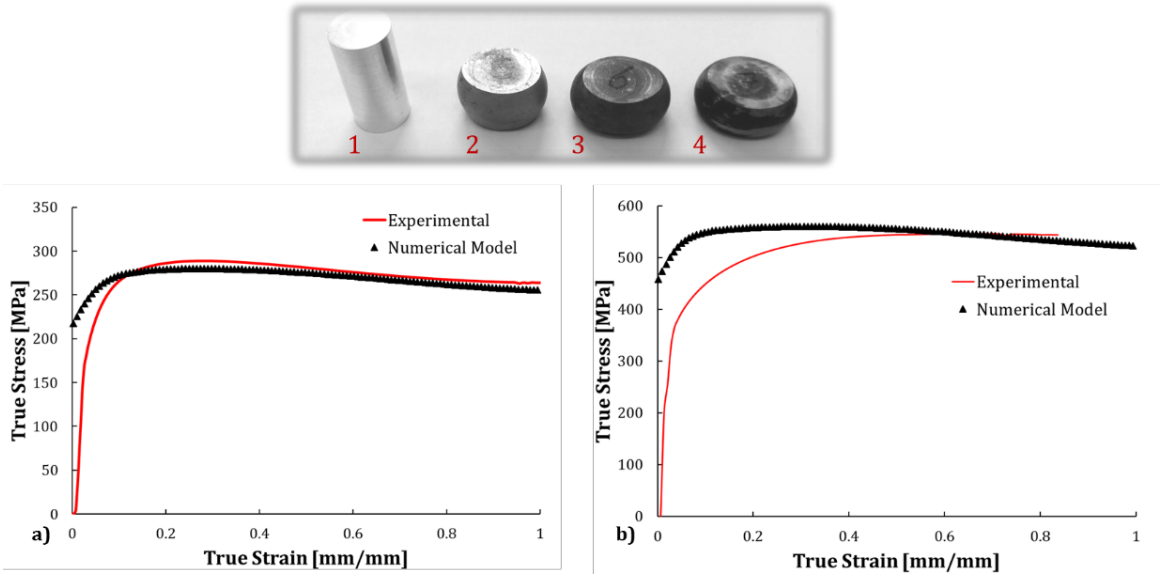

Figure 132: Comparison between the experimental and predicted true stress-strain curves of the aluminum alloy *7075-T6* at varying temperature and strain rate; a) strain-rate 0.1s^{-1} T= 200°C, b) strain-rate 0.5s^{-1} T= 150°C.

In Figure 132 are reported the simulated curve and the experimental representative of the true stress-true strain curves. The model was able to match the experimental curves at varying temperature and strain rate. All the numerical and physics constants are reported in Table 21. It is important to highlight that the model was able to correctly replicate the mechanical behavior at large plastic deformation values (higher than 0.3) in the region that characterizes the machining process.

Table 21: Numerical constants of the physics based model developed (calibrated or reported in literature).

Numerical constants	Value
α	0.2
b [m]	2.86^{-10}
K_c	21
Ω_0	4.43
Ω_{r0}	0.33
ϱ_0 [m^{-2}]	10^{10}
σ_0 [MPa]	0.01
σ_i [MPa]	615
α^0_G	3300
d	1
D_0 [μm]	4.85
D_f [μm]	1.55
k_x	3.8
c_x	2
k_b [J/K]	1.38^{-23}
g_{0i}	0.55
q	1.5
p	0.678
R [m]	1.50^{-09}
f_v	0.085
n	0.67
C	0.081

Figure 133 shows the prediction strategy implemented by sub-routine into the FE software DEFORM in order to simulate the constitutive material behavior of the aluminum alloy *AA7075-T6* during machining operations. The routine was developed in FORTRAN code, the FE software computed the routine step after step upgrading the state variable as strain, strain rate and temperature. Subsequently all the equations that represent the model were computed and the flow stress was upgraded at the end of each step. The routine returned the stress, strain, strain rate, temperature and the metallurgical variables at the end of each step.

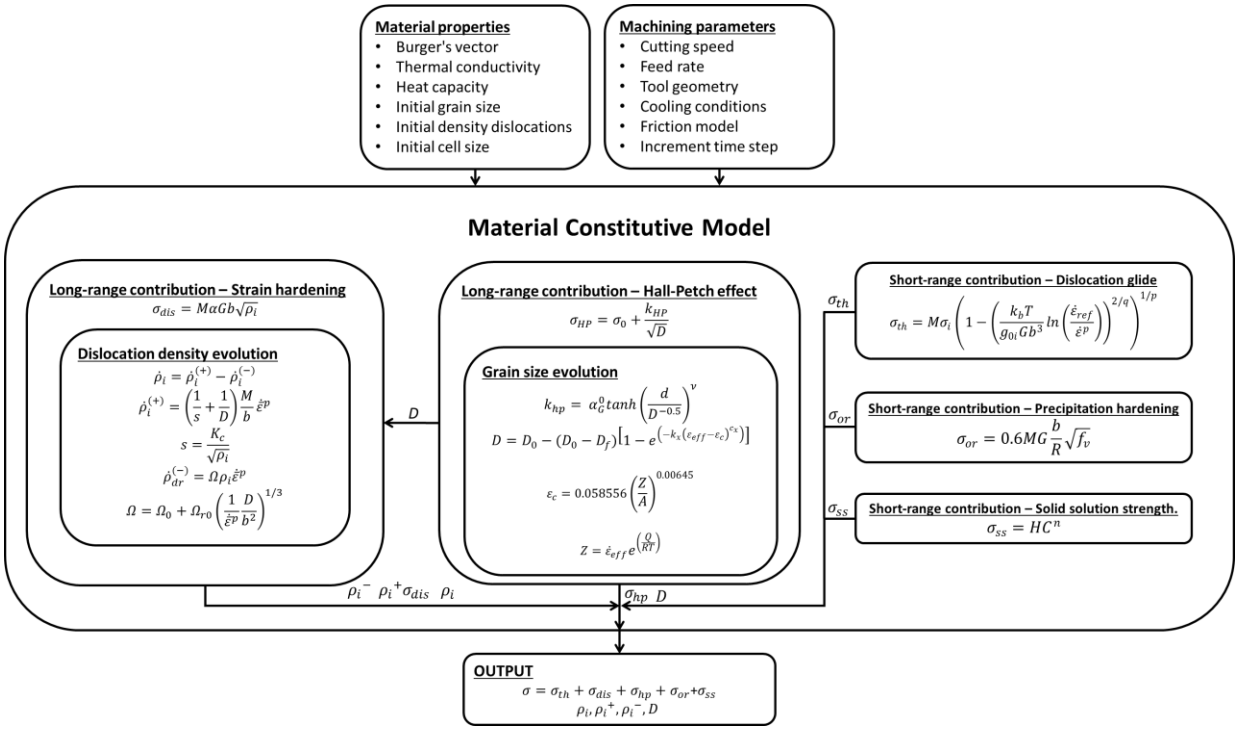

Figure 133: Numerical strategy developed to model the mechanical behavior of the *AA7075-T6* through physically based modeling approach.

5.3.2 FE Calibration

The calibration procedure aims to determine the friction coefficients of the hybrid model previously explained in Section 5.2.3. The friction model was the same adopted to simulate the friction conditions during the machining simulation of semi-finishing turning on *Ti6Al4V* (Figure 122). The calibration procedure adopted in the *7075-T76* machining simulation is reported in Figure 134. The strategy was based on an iterative analysis that aims to minimize the total average error of predicted cutting forces and temperature. This procedure stopped when the total average error was lower than 10%.

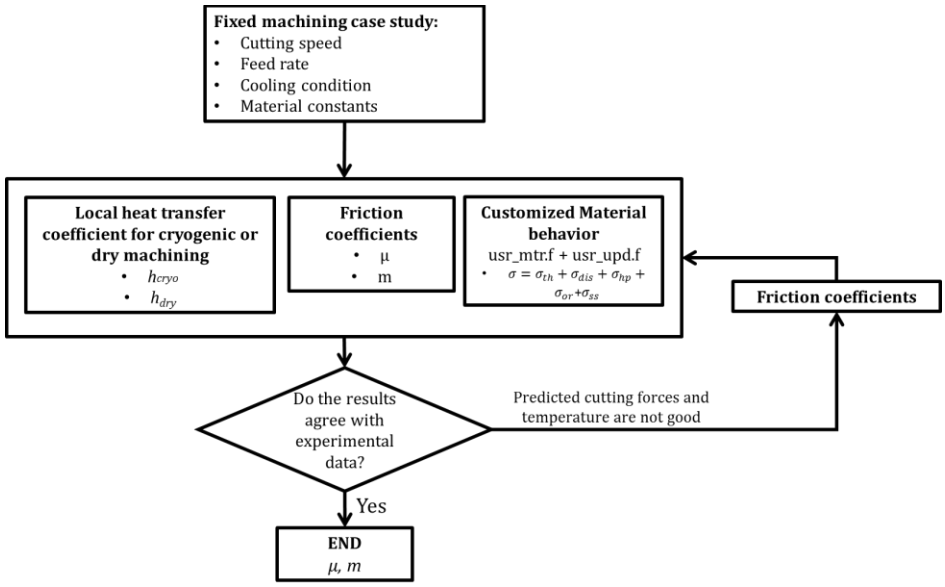

Figure 134: Calibration procedure to determine the friction coefficients of the hybrid friction model.

The calibration procedure was carried out for two cutting conditions corresponding to the following cutting parameters: Vc=1000m/min and Vc=1500m/min with f=0.1mm/rev, and Vc=1500m/min with f=0.3 mm/rev and both the cooling strategy, namely dry and cryogenic were taken into account during the calibration. At the end of the calibration procedure, through fitting procedure, the general polynomial models representative of m and μ friction coefficients depending on cutting speed and feed rate were determined by Matlab. Equation 36, 37and 38 permitted to calculate the friction coefficients referred to all the case studied.

$$m_{dry} = 2.625 + 0.25f - 0.0033V_c + 3.432e-17fV_c + 1.2e-06{V_c}^2 \quad (36)$$

$$\mu_{dry} = 2.612 + 0.9917f - 0.00335V_c - 0.0005fV_c + 1.24e-06{V_c}^2 \quad (37)$$

$$m_{cryo,}\ \mu_{cryo} = 0.2533 + 0.8583f - 0.00031V_c - 0.0003fV_c + 1.2e-07{V_c}^2 \quad (38)$$

The m and μ computed values related to the dry and cryogenic machining conditions are reported in **Errore. 'origine riferimento non è stata trovata.**.

Vc / f	m	μ
1000/0.1	0.55	0.55
1250/0.1	0.4	0.4
1500/0.1	0.4	0.4
1000/0.3	0.6	0.65
1250/0.3	0.45	0.47
1500/0.3	0.45	0.45

As showed by **Errore. L'origine riferimento non è stata trovata.**, the friction coefficients related to the ry machining were affected by the cutting speed and the feed rate. In detail, the high feed rate led to higher friction coefficients while at fixed feed rate, when the cutting speed increased the friction coefficients decreased. The friction coefficients referred to the cryogenic machining were lower than the ones calibrated in dry conditions. The feed rate and cutting speed played the same role observed in dry machining simulations. These numerical results referred to the dry and cryogenic conditions showed similar trends reported also by Cabanettes et al. 2016 operating under dry and lubricated conditions. They observed a decreasing of the friction coefficient when cutting speed increased. The lower friction coefficients reported for cryogenic machining were in agreement with the experimental observations, in fact lower cutting forces as well as rake face wear due to the reduced tool-chip contact were observed.

5.3.3 FE Validation

Once the friction coefficients were determined, the validation phase was carried out in order to understand the reliability rate of the developed and proposed FE model. The validation was performed taking into account all the case studied, therefore all the machining tests were simulated. The friction coefficients, namely, m and μ, were obtained using the polynomial expressions (Equation 38).

The obtained results and their comparison with the experimental ones in terms of cutting forces and temperatures inside the cutting zone are reported in Figure 135, Figure 136 and Figure 137 for different cutting parameters and cooling conditions.

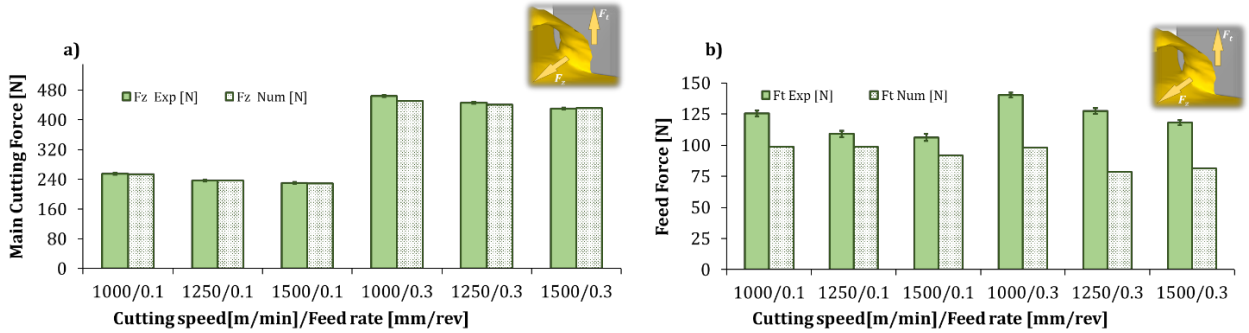

Figure 135: Comparison between experimental and numerical cutting forces; a) main cutting force (F_z) and b) feed forces (F_t) under dry conditions.

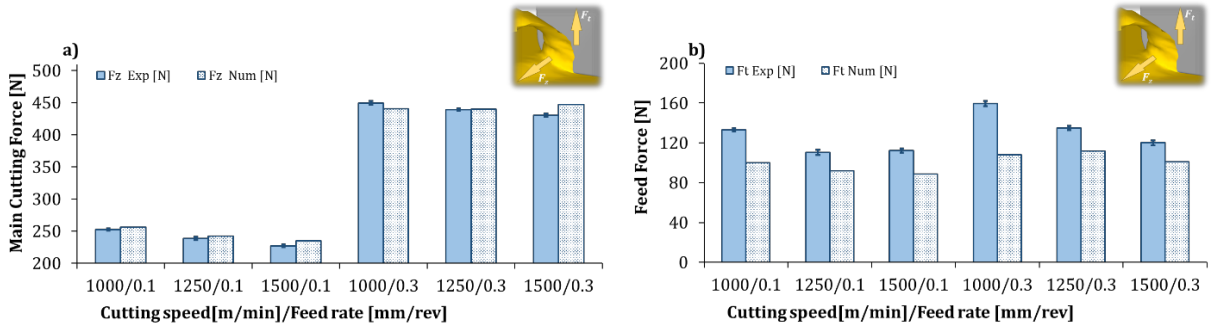

Figure 136: Comparison between experimental and numerical cutting forces; a) main cutting force (F_z) and b) feed forces (F_t) under cryogenic conditions.

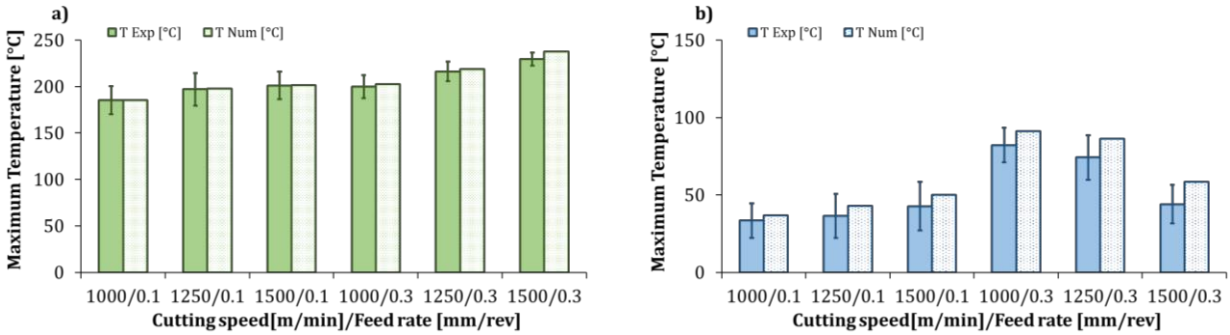

Figure 137: Comparison between experimental and numerical temperature; a) dry machining and b) cryogenic machining.

The developed physics based model was able to successfully predict the main fundamental variables as cutting forces and temperatures as showed by the figures. Between the cutting forces, the main cutting components that is directly related with the power consumption was correctly predicted at varying cutting parameters and cooling conditions. The highest errors in predicting the main cutting components were 2.89% and 3.93% obtained in dry and cryogenic machining simulations respectively, while the other comparison provided an error lower than 1%.

The predicted feed components (Figure 135b, Figure 136b) were always smaller than the experimental measurements. This problem was mainly due to the cutting edge approximation. Indeed, the cutting edge radius was very small, close to 40 μm, and the elements number required to properly approximate the round

shape in 3D dimension was high leading to longer computational time. However, machining parameters as energy or power requirements are mainly related to the main cutting components that were properly predicted, therefore, the poor prediction capability of the feed components is abundantly accepted. Moreover, the error in predicting the feed force did not exceed the 25% and the trend variation at varying cutting parameters and cooling strategy was well predicted. To improve the prediction of this other cutting component, more elements are necessary to approximate the cutting edge round shape, drastically increasing the duration of the simulations. Figure 137 shows the comparison between the predicted and experimentally measured thermal gradient inside the cutting zone. The FE developed model correctly predicted the experimental results as well as the trends at varying cutting speeds, feed rate and cooling strategy. This result is very important because the temperature plays an important role in tool wear phenomena, therefore, the right prediction of this state variable might be used to suggest if the machining strategy is critical for the tool life without performing long and expensive experimental tests.

5.3.4 Surface Integrity Analysis

The developed FE model aims to predict the main fundamental results (cutting forces and temperatures) that are particularly interesting from the industrial point of view. Indeed, the industries interested in exploring new manufacturing strategies, have to perform several tests usually not economically affordable. Therefore, the FE simulations and the implemented models once validated, represent valid alternatives to explore new cutting parameters and improve the machining process. However, due to the physics equations involved into the material behavior model, the FE simulations provide valuable information about the metallurgical alterations induced by the machining. Therefore, the surface integrity of the machined parts can be also investigated by the developed FE model. It is important to highlight that the metallurgical variables, such as dislocation densities predicted by the developed model, were not compared with experimental observations (no TEM analysis was performed during the experimental activity), but they could be used to qualitatively explain the hardening or softening phenomena that occurred during high speed machining. The FE developed model permitted to simulate other important aspects of the machining process. Taking into account the chip formation, the experimental cases represented by continuous chip formation (low feed rate and some isolated cases in dry conditions with high feed rate) were well simulated by the. As showed by Figure 138, the curling shape of the chip numerically predicted by the FE simulation is almost equal to the one obtained during the machining test.

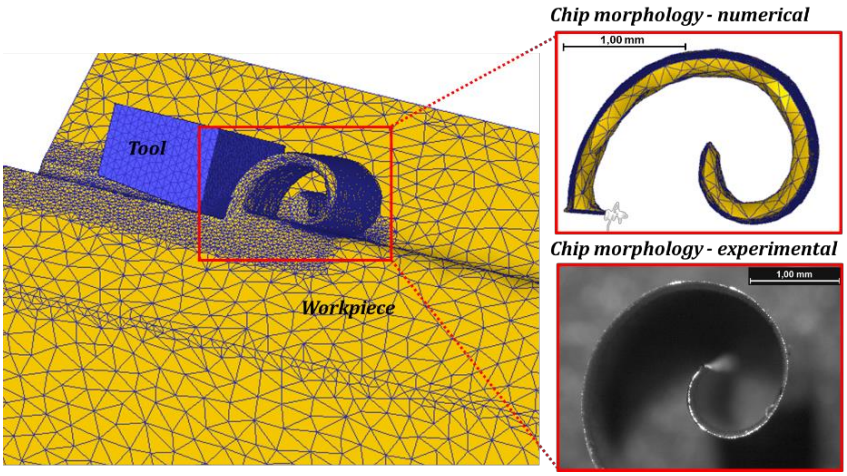

Figure 138: Comparison between the numerical and experimental chip shape (V_c=1000m/min, f=0.3mm/rev, dry conditions).

Moreover, the dimensions are also comparable suggesting that the developed model was quite reliable. The possibility to predict the real dynamic of chip formation can be used to predict other important

information as cutting lengths to approximately estimate the tool wear regions related to the tool-chip contact.

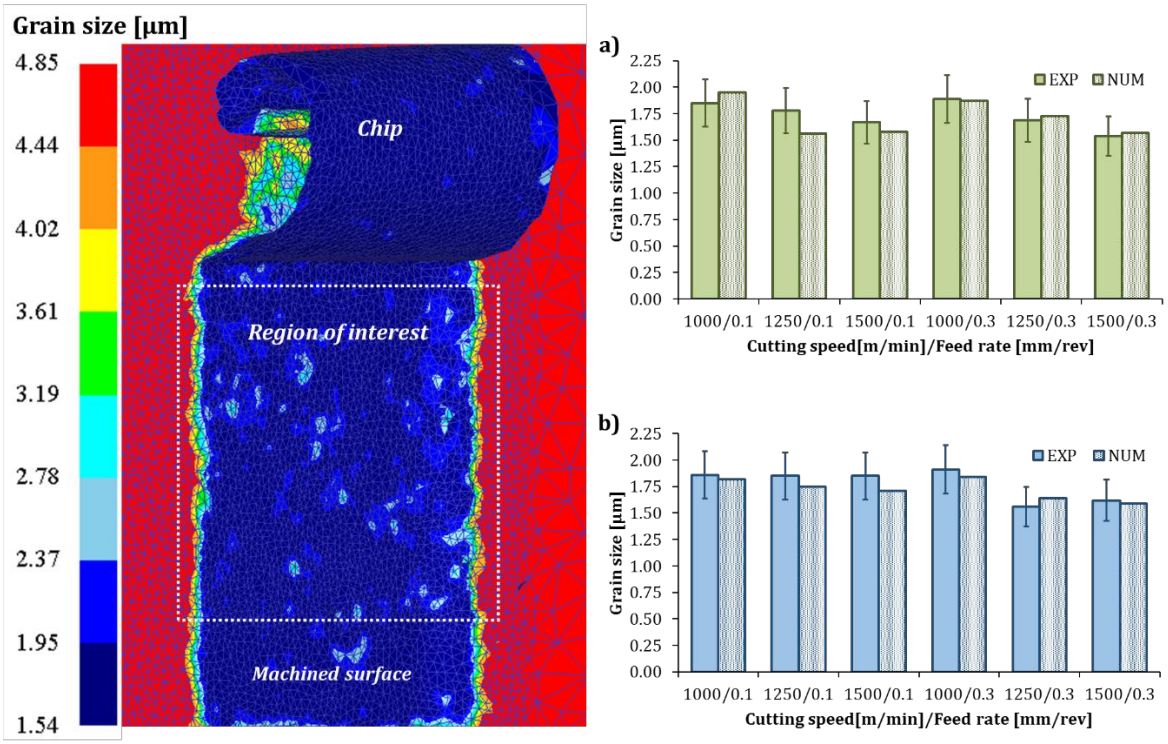

Figure 139: Predicted microstructure under dry conditions (V_c=1500m/min, f=0.3mm/rev); a) comparison of numerical and experimental grain size measured on machined surface (dry conditions); b) comparison of numerical and experimental grain size measured on machined surface (cryogenic conditions).

The microstructural alteration was predicted on machined surface and inside the workpiece at varying cutting parameters and cooling conditions. In Figure 139 is showed the top view of the machined surface and the grain size prediction. The white box represents the region in which the grain size was evaluated. 60 measurements were carried out and the average value are showed in Figure 139a and Figure 139b. The developed model was able to correctly predict the grain refinement due to the machining process. In fact, the grain size numerically predicted was very close to the experimental measured and at varying cutting parameters as well as cooling conditions, the trend was well predicted. The FE model can be used to estimate the amount of grain refinement modifying the cutting parameters depending on the machining strategy.

As previously mentioned, the FE model can predict the grain refinement gradient into the subsurface as showed by Figure 140. A transversal plane cut the machined components, consequently, the internal grain refinement predicted was visible. The metallurgical alteration was well described by the model, since the dislocation density variation was also predicted. Furthermore, the grain refinement in subsurface permitted to understand the amount of the affected layer. Therefore, considering the grain size changes in depth, the thickness of the altered material can be also evaluated and compared with the experimental results.

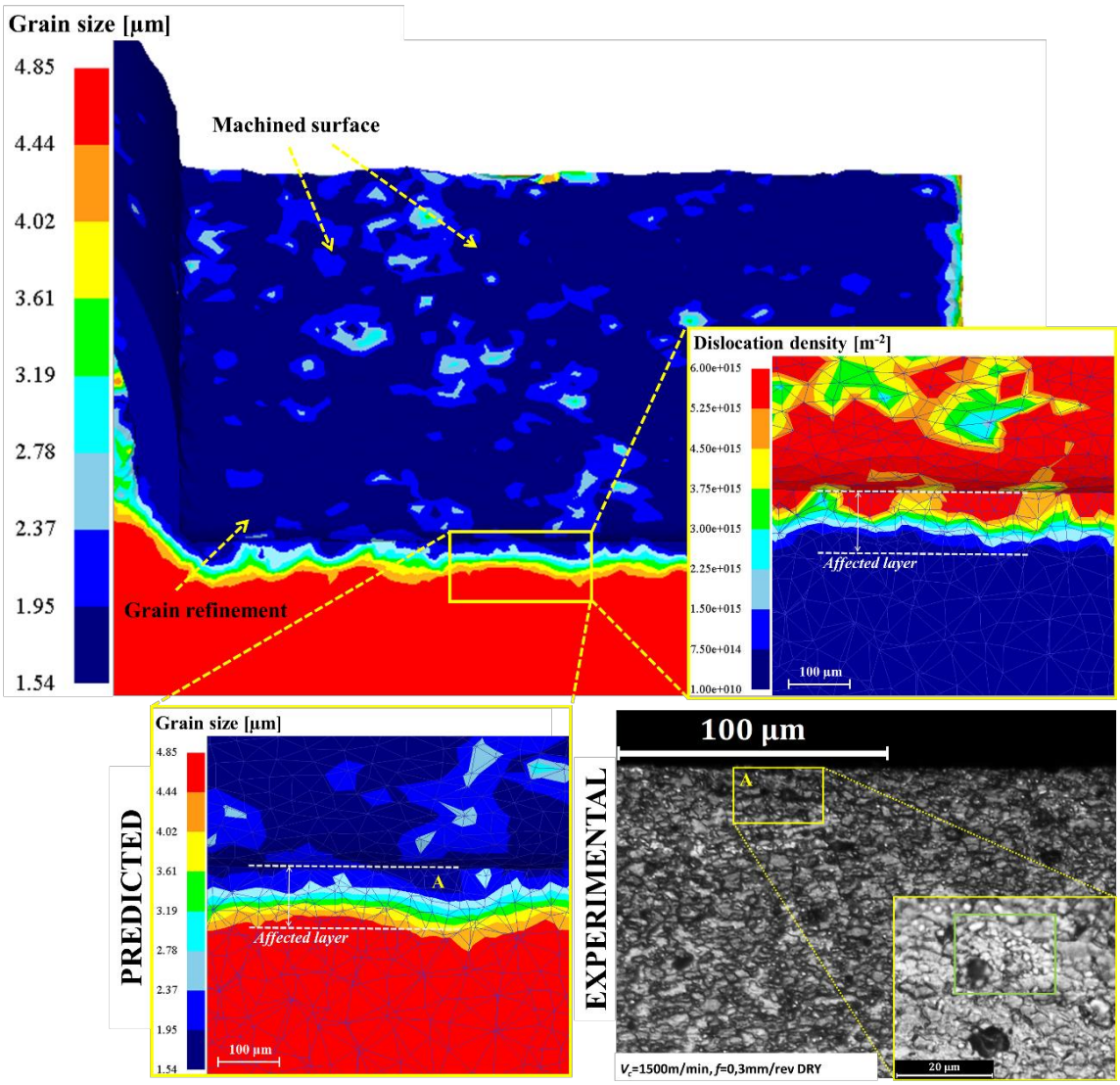

Figure 140: Grain refinement and dislocation density variations from the machined surface and in depth into the part (V_c=1500m/min, f=0.3mm/rev, dry condition)

As reported in Chapter IV, the cooling conditions coupled with the cutting parameters play a key role in changing the hardness of the machined parts. The analyses showed that the cryogenic fluids promoted the presence of precipitates. As reported by Gubicza et al. 2007, the regions with high dislocations density, due to the plastic deformation accumulation, represent nucleation sites for precipitates. Therefore, higher percentage of precipitate suggests high dislocation density accumulation. Moreover, the cryogenic temperature annihilated the recovery phenomena, therefore the size of the new recrystallized grains was smaller compared with the one observed on the dry machined samples. The FE developed model permitted to observe the previously mentioned metallurgical phenomena. Indeed, in Figure 141 the density of the smaller grains in the cryogenic machined part is higher than the one observed on the dry machined one. Moreover, in Figure 142 the higher dislocation density was predicted on the cryogenic machined sample. The metallurgical phenomena and their evolution can be studied through the FE developed model as well as their contribution to the strengthening of the alloy. The higher dislocation density predicted by the cryogenic simulation, even if not compared with the experimental results, clearly suggests that the low temperature on the machined surface can prevent the presence of recovery effects.

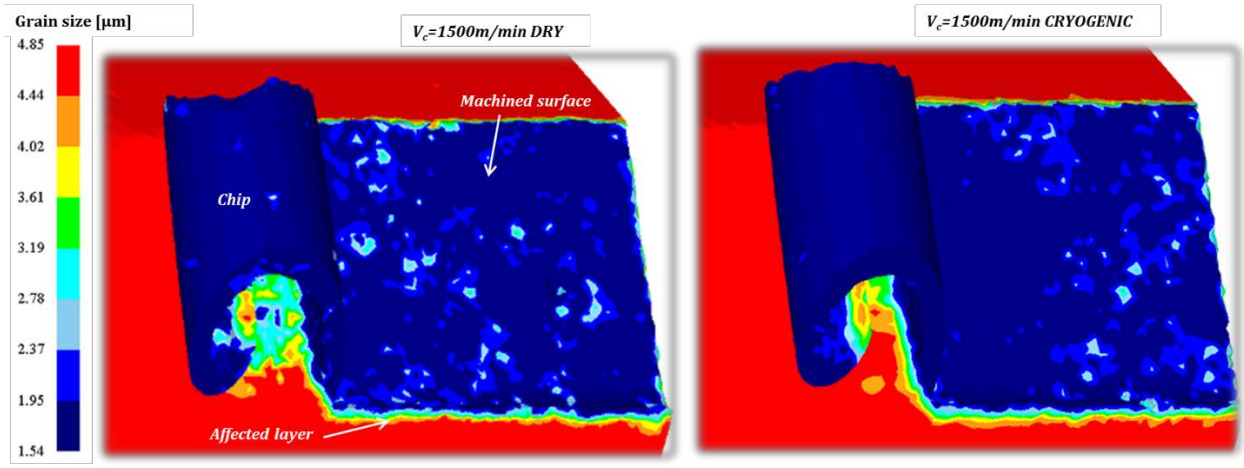

Figure 141: Recrystallized grain size prediction at varying cooling conditions (f=0.3mm/rev).

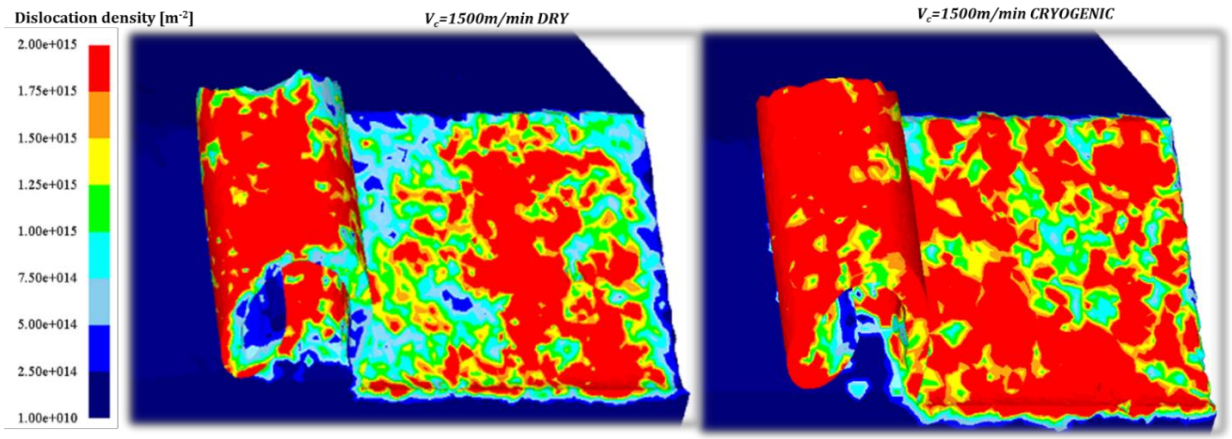

Figure 142: Dislocation density prediction at varying cooling conditions (f=0.3mm/rev).

Concluding Remarks

The semi-finishing operation on additive manufactured *Ti6Al4V* titanium alloy and high speed machining on *7075-T6* aluminum alloy with the application of liquid nitrogen during the process were conducted. The aims of this Ph.D. thesis were to investigate the possibility to enhance the surface integrity of the machined aerospace alloys devoted to engines and structural applications and to study the effects of the innovative cryogenic cooling technique.

The titanium components were produced through different additive manufacturing techniques, namely Electron Beam Melting and Direct Metal Laser Sintering. The as received conditions were studied and the surface quality was analyzed in terms of microstructural characterization, surface roughness measurements and X-Ray Diffraction analysis.

Although the material is chemically the same (titanium alloy), the additive manufacturing process significantly modifies the mechanical properties and surface quality of the parts. Indeed, the microstructure of the materials produced by EBM and DMLS was lamellar and the EBM produced thinner grains than the DMLS process. Furthermore, due to the poor roughness and inaccurate geometric tolerances, the produced parts required further post-processing treatments; therefore, the semi-finishing turning tests were conducted. The results collected showed that the machinability of the alloy was affected by the different mechanical properties due to the AM processes. In particular, the EBM produced parts which resulted more difficult to machine, in fact higher cutting forces and temperature were measured. The cryogenic fluid delivered during the machining tests did not provide benefits in terms of cutting forces reduction and roughness. The material behavior at low temperature was more brittle and the ductility was drastically reduced. Conversely, the cutting temperatures were significantly reduced, reducing tool wear and improving tool life.

The surface integrity of the titanium alloy additively manufactured and subjected to semi-finishing operation was generally improved. The surface roughness was reduced to values usually lower than 1μm and this contributes to improve the fatigue life of the machined components, reducing the possibility to failure due to the presence of surface defects. The microstructure was always affected and refined while the material beneath the machined surface was plastically deformed. The cryogenic machining led to increase the plastic deformation in the manufactured parts. The surface and sub-surface hardness were always increased and the cryogenic manufacturing provided parts with higher hardness because of the annihilation of recovery phenomena.

The aluminum alloy *7075-T6* was manufactured by high speed turning with the application of liquid nitrogen in order to investigate the machinability and to improve the surface integrity. The surface quality was analyzed in terms of microstructural characterization, surface roughness measurements and X-Ray Diffraction analysis.

The high cutting speeds permitted a fast chip removal avoiding high temperature concentration in the cutting zone. The thermal gradients were considerably reduced with the application of liquid nitrogen. The cutting force trends decreased with higher cutting speed because of the thermal-softening effect.

The surface roughness was better with low feed rate (0.1mm/rev) while it resulted poor when higher feed rate (0.3mm/rev) was adopted. The microstructure was always altered and new recrystallized equiaxed grains were produced close to the machined surface. The affected layers were deep from 90μm to 150μm and were characterized by plastic deformed material, recrystallized grains and precipitates. The cryogenic fluids permitted to cool the machined surface leading to the annihilation of recovery phenomena. In fact, the microstructure in the cryogenically machined sample was more refined while the affected layers were smaller. The surface hardness was always higher than the not machined material. In detail, the cryogenically machined materials showed higher hardness as well as higher presence of precipitate confirmed by XRD analysis.

The hardness change was defined as a combination of two main contributions that were the grain refinement and the presence or not of precipitates (GP zones, $MgZn_2$). At lower feed rate, both dry and cryogenic machining led to higher surface hardness due to the presence of the grain refinement and precipitates effects, but at higher feed rate only the cryogenic machined samples still revealed the presence of precipitates and this explained the higher surface hardness compared to the one measured on dry machined samples.

Finally, the material behavior models of the titanium alloy additively manufactured and aluminum alloy were developed. The Ti6Al4V AMed was modeled via empirical approach while the aluminum alloy material behavior was described by a physics based model. The constitutive models were implemented in a FE software to simulate the material behavior during machining operations. The cryogenic conditions were also modeled through the definition of the convective heat transfer model. The numerical results in terms of main fundamental variables as cutting forces and temperature were in agreement with the experimental ones. These developed models can be used to investigate new machining parameters in order to study new manufacturing strategies avoiding costly experimental tests.

The models that describe the metallurgical changes of titanium and aluminum alloys were also implemented into the FE software and their evolutions were predicted, and the results were very close to the experimental ones. Moreover, the surface integrity was well predicted varying the cutting parameters as well as the cooling conditions; therefore, the FE developed models were able to quantitatively describe the metallurgical alterations and their evolutions in the cutting zone and on the machined surface.

Future research directions

The effect of lubricant delivered by MQL (Minimum Quantity Lubricant) could be investigated on titanium and aluminum alloy in order to study its benefits in reducing cutting forces and temperature due to the lubricant effect, and to investigate its effect on the surface integrity, in particular on the surface roughness.

The cryogenic cooling apparatus could be improved; in detail, accurate orientable nozzles should be developed to direct the LN_2 jet between the tool and the chip and on the machined surface. This improvement can help to reduce the cutting forces due to smaller cutting length and constantly cool the machined surface to prevent coarsening phenomena of the microstructure.

The developed FE code to simulate the turning process of EBM and DMLS *Ti6Al4V* alloy can be optimized by characterizing the material constitutive model through experimental tests instead of testing several models available in literature. The material behavior should be tested also in cryogenic conditions to extend the knowledge of the titanium behavior at very low temperature under dynamic loads.

A more complex friction model calibrated for 3D machining should be developed depending on the sliding velocity. Some experimental pin-to-workpiece tests could be performed to develop the required friction model.

References

M. Abbasi-Baharanchi, F. Karimzadeh, M. H. Enayati, (2017), Mechanical and tribological behavior of severely plastic deformed Al6061 at cryogenic temperatures, Materials Science and Engineering A, 683: 56-63.

N.T. Aboulkhair, C. Tuck, I. Ashcroft, I. Maskery, N.M. Everitt, (2015), On the precipitation hardening of selective laser melted AlSi10Mg, Metallurgical and Materials Transactions. A, 46: 3337-3341.

S.S. Al-Bermani, M.L. Blackmore, W. Zhang, I. Todd, (2010), The Origin of Microstructural Diversity, Texture, and Mechanical Properties in Electron Beam Melted Ti-6Al-4V, Metallurgical and Material Transaction A, 41A: 3422-3434.

F. Ambrosy, F. Zanger, V. Schulze, I.S. Jawahir, (2014), An Experimental Study of Cryogenic Machining on Nanocrystalline Surface Layer Generation, 2nd CIRP Conference on Surface Integrity (CSI), Procedia CIRP, 13: 169-174.

Y. M. Arisoy, T. Özel, (2015), Prediction of machining induced microstructure in Ti–6Al–4V alloy using 3-D FE-based simulations: Effects of tool micro-geometry, coating and cutting conditions, Journal of Materials Processing Technology, 220: 1-26.

P. J. Arrazola, T. Özel, D. Umbrello, M. Davies, I. S. Jawahir, (2013), Recent advances in modelling of metal machining processes, Cirp Annals, 62: 695-718.

P. J. Arrazola, T. Özel, (2010), Investigations on the effects of friction modeling in finite element simulation of machining, International Journal of Mechanical Sciences, 52: 31-42.

E. Arzt, (1998), Size effects in materials due to microstructural and dimensional con- straints: a comparative review, Acta Materialia, 46: 5611–5626.

H. Asgharzadeh, A. Simchi, H.S. Kim, (2011), Microstructural features, texture and strengthening mechanisms of nanostructured AA6063 alloy processed by powder metallurgy, Materials Science and Engineering A, 528: 3981-3989.

V. P. Astakhov, S. Joksch, (2012), Metalworking fluids (MWFs) for cutting and grinding – fundamentals and recent advances: 147–151; Cambridge, UK, Woodhead Publishing Limited, 1.

Z. Atmani, B. Haddag, M. Nouari, M. Zenasni, (2016), Combined microstructure-based flow stress and grain size evolution models for multi-physics modelling of metal machining, International Journal of Mechanical Sciences, 118: 77-90.

A. Azushima, R. Kopp, A.Korhonen, D. Y. Yang, F. Micari, G. D. Lahoti, P. Groche, J. Yanagimoto, N. Tsuji A. Rosochowski, A. Yanagida, (2008), Severe plastic deformation (SPD) processes for metals, Cirp Annals, 57: 716-735.

B. Babu, L. E. Lindgren, (2013), Dislocation density based model for plastic deformation and globularization of Ti-6Al-4V, International Journal of Plasticity, 50: 94-108.

S. C. Baik, Y. Estrin, H. S. Kim, R. J. Hellmig, (2003), Dislocation density-based modeling of deformation behavior of aluminium under equal channel angular pressing, Materials Science and Engineering A, 351: 86-97.

B. Baufeld, O. Van der Biest, R. Gault, (2010), Additive manufacturing of Ti–6Al–4V components by shaped metal deposition: Microstructure and mechanical properties, Materials and Design, 31: S106-S111.

J. Beddoes M. Bibby, (1999), Principles of manufacturing processes, Elsevier Butterworth-Heinemann, Linacre House, Jordan Hill, Oxford OX2 8DP 200 Wheelers Road, Burlington, MA 01803.

Y. Bergström, (1983), The plastic deformation of metals - A dislocation model and its applicability. Reviews on powder metallurgy and physical ceramics 2/3: 79–265.

M.J.Bermingham, J.Kirsch, S.Sun, S.Palanisamy, M.S.Dargusch, (2011), New observations on tool life, cutting forces and chip morphology in cryogenic machining Ti-6Al-4V, International Journal of Machine Tools and Manufacture, 51: 500-511.

B. Binesh, M. Aghaie-Khafri, (2016), Phase Evolution and Mechanical Behavior of the Semi-Solid SIMA Processed 7075 Aluminum Alloy, Metals, 6: 1-23.

A. Bordin, S. Bruschi, A. Ghiotti, P. F. Bariani, (2015), Analysis of tool wear in cryogenic machining of additive manufactured Ti6Al4V alloy, Wear, 328-329: 89-99.

A. Bordin, S. Bruschi, A. Ghiotti, (2014), The Effect of Cutting Speed and Feed Rate on the Surface Integrity in Dry Turning of CoCrMo Alloy, 2nd CIRP Conference on Surface Integrity (CSI), Procedia CIRP, 13: 219-224.

A. Bordin, S. Bruschi, A. Ghiotti, F. Bucciotti, L. Facchini, (2014), Comparison between Wrought and EBM Ti6Al4V Machinability Characteristics, Key Engineering Materials, 611: 1186-1193.

S. Bruschi, G. Tristo, Z. Rysava, P.F. Bariani, D. Umbrello, L. De Chiffre, (2016), Environmentally clean micromilling of electron beam melted Ti6Al4V, Journal of Cleaner Production, 133: 932-941.

F. Cabanettes, J. Rolland, F. Dumont, J. Rech, Z. Dimkovski, (2016), Influence of Minimum Quantity Lubrication on friction characterizing tool-aluminum alloy contact, Journal of Tribology, 138: 1-10.

D. Caillard, J. L. Martin, (2003), Thermally Activated Mechanisms in Crystal Plasticity, Pergamon, Oxford.

M. Calamaz, D. Coupard, F. A. Girot, (2008), A New Material Model for 2D Numerical Simulation of Serrated Chip Formation When Machining Titanium Alloy Ti–6Al–4 V, International Journal of Machine Tools and Manufacture, 48: 275-288.

M. Calamaz, D. Coupard, F. Girot, (2010), Numerical simulation of titanium alloy dry machining with a strain softening constitutive law, Machining Science and Technology, 14: 244–257.

M. Calamaz, D. Coupard, M. Nouari, F. Girot, (2011), Numerical analysis of chip formation and shear localization processes in machining the Ti–6Al–4V titanium alloy. International Journal of Advanced Manufacturing Technology, 52: 887–895.

F. C. Campbell, (2008), Elements of Metallurgy and Engineering Alloys, ASM International, Materials Park, Ohio, USA.

F. C. Campbell, (2006), Manufacturing technology of aerospace structural materials, Elsevier B. V. Radarweg 29, P. O. Box 211, 1000 AE, Amsterdam Netherlands.

K. R. Cardoso, D. N. Travessa, W. J. Botta, A. M. Jorge Jr, (2011), High Strength AA7050 Al alloy processed by ECAP: Microstructure and mechanical properties, Materials Science and Engineering A, 528: 5804-5811.

C. M. Cepeda-Jiménez, J.M.García-Infanta, O. A. Ruano, F.Carreño, (2011), Mechanical properties at room temperature of an Al–Zn–Mg–Cu alloy processed by equal channel angular pressing, Journal of Alloys and Compounds, 509: 8649-8656.8

C. M. Cepeda-Jiménez, J.M.García-Infanta, E. F. Rauch, J. J. Blandin, O. A. Ruano, F.Carreño, (2012), Influence of Processing Severity During Equal-Channel Angular Pressing on the Microstructure of an Al-Zn-Mg-Cu Alloy, Metallurgical and Materials Transactions A, 43: 4224-4236.

K. S. Chan, (2010), Changes in fatigue life mechanism due to soft grains and hard particles, International Journal of Fatigue, 32: 526-534.

K. S. Chan, (2010), Roles of microstructure in fatigue crack initiation, International Journal of Fatigue, 32: 1428-1447.

Y. Chen, Y. Yang, Z. Feng, B. Huang, X. Luo, (2017), Surface gradient nanostructures in high speed machined 7055 aluminum alloy, Journal of Alloys and Compounds, 726: 367-377.

P. C. Collins, B. Welk, T. Searles, J. Tiley, J. C. Russ, H. L. Fraser, (2009) Development of methods for the quantification of microstructural features in α+β-processed α/β titanium alloys, Materials Science and Engineering A, 508: 174-182.

H. Conrad, (1970), The athermal component of the flow stress in crystalline solids, Material Science and Engineering A, 6: 265–273.

P. J. T. Conradie, D. Dimitrov, G. A. Oosthuizen, P. Hugo, M. Saxer, (2017), Comparative assessment of process combination for Ti6Al4V components, Rapid Prototyping Journal, 23 Issue: 3: 624-632.

M. Danish, T. L. Ginta, K. Habib, D. Carou, A. M. A. Rani, B. B. Saha, (2017), Thermal analysis during turning of AZ31 magnesium alloy under dry and cryogenic conditions, International Journal of Advanced Manufacturing Technology, 91: 2855–2868.

J. P. Davim, (2010), Surface Integrity in Machining, Springer: 1-7.

J.P. Davim,(2014), Machining of Titanium Alloys, Springer: 6:11.

R. DeIasi, P. N. Adler, (1977), Calorimetric Studies of 7000 Series Aluminum Alloys: I. Matrix Precipitate Characterization of 7075, Metallurgical Transactions A, 8: 1177-1183.

J. J. M. De Rijck, J. J. Homan, J. Schijve, R. Benedictus, (2007), The driven rivet head dimensions as an indication of the fatigue performance of aircraft lap joints, (International Journal of Fatigue, 29: 2208-2218.

L. Ding, X. Zhang, R. Liu, (2014), Dislocation Density and Grain Size Evolution in the Machining of Al6061-T6 Alloys, Journal of Manufacturing Science and Engineering, 136: 1-10.

H. Ding, Y. C. Shin, (2013), Multi-physics modeling and simulations of surface microstructure alteration in hard turning, 213: 877-886.

H. Ding, N. Shen, Y. C. Schin, (2011), Modeling of grain refinement in aluminum and copper subjected to cutting, Computational Materials Science, 50: 3016-3025.

M. Dixit, R. S. Mishra, K. K. Sankaran, (2008), Structure–property correlations in Al 7050 and Al 7055 high-strength aluminum alloys, Materials Science and Engineering A, 478: 163–172.

M.J. Donachie Jr, (2000), Titanium a Technical Guide, ASM International, Materials Park, OH 44073-0002: 1-25.

B. Dutta, F. H. Froes, (2016), Additive Manufacturing of Titanium alloys. State of the Art, Challenges and Opportunities, Elsevier Butterworth-Heinemann, The Boulevard, Langford Lane, Kidlington, Oxford OX5 1GB.

E. A. El-Danaf, (2008), Mechanical properties and microstructure evolution of 1050 aluminum severely deformed by ECAP to 16 passes, Materials Science and Engineering: A, 487: 189-200.

Y. Estrin, L. S. Tòth, A. Molinari, Y. Bréchet, (1998), A dislocation-based model for all hardening stages in large strain deformation, Acta Materialia, 46: 5509-5522.

Y. Estrin, A. Vinogradov, (2013), Extreme grain refinement by severe plastic deformation: A wealth of challenging science, Acta Materialia, 61: 782-817.

L. Facchini, E. Magalini, P. Robotti, A. Molinari, (2010),Microstructure and mechanical properties of Ti-6Al-4V produced by electron beam melting of pre-alloyed powders, Rapid Prototyping Journal,15 Issue 3: 171-178.

L. Facchini, E. Magalini, P. Robotti, A. Molinari, S. Höges, K. Wissenbach, (2010), Ductility of Ti6Al4V alloy produced by selective laser melting of prealloyed powders, Rapid Prototyping Journal, 16/6: 450-459.

A. Fatemi, R. Molaei, S. Sharifimehr, N. Shamsaei, N. Phan, (2017), Torsional fatigue behavior of wrought and additive manufactured Ti-6Al-4V by powder bed fusion including surface finish effect, International Journal of Fatigue, 99: 187-201.

L. Filice, F. Micari, S.Rizzuti, D.Umbrello, (2007), A critical analysis on the friction modelling in orthogonal machining, International Journal of Machine Tools and Manufacture, 47: 709-714.

H. M. Flower, (1995), High Performance Materials in Aerospace, Springer Science+Business Media Dordrecht.

P. Follansbee, U. Kocks, (1988), A constitutive description of the deformation of copper based on the use of the mechanical threshold stress as an internal state variable, Scripta Metallurgica Materialia, 36: 81-93.

S. Fritsch, M. Scholze, M.F.X. Wagner, (2012), Cryogenic Forming of AA7075 by Equal-Channel Angular Pressing, Materialwissenschaft und Werkstofftechnik, 43: 561-566.

H. Frost, M. Ashby, (1982), Deformation-mechanism maps - the plasticity and creep of metals and ceramics, Pergamon Press, Oxford.

H. Frost, M. Ashby, (1977b), Deformation-mechanism maps for pure iron, two austenitic stainless steels and a low-alloy ferritic steel. In: Jaffee, R.I., Wilcox, B.A. (Eds.), Fundamental Aspects of Structural Alloy Design. Plenum Press, pp. 26–65.

F. Gabrielli, R. Ippolito, F. Micari, (2008), Analisi e tecnologia delle lavorazioni meccaniche, McGraw-Hill pp. 407-409; pp. 427-429.

L.M. Gammon, R.D. Briggs, J.M. Packard, K.W. Batson, R. Boyer, C.W. Domby, (2004), Metallography and Microstructures of Titanium and Its Alloys, Metallography and Microstructures, ASM Handbook, ASM International, 9: 899–917.

M. Gebler, A. J. M. S. Uiterkamp, C. Visser, (2014), A global sustainability perspective on 3D printing technologies, Energy Policy, 74:158-167.

I. Gibson, D. W. Rosen, B. Stucker, (2010), Additive Manufacturing Technologies. Rapid prototyping to Direct Digital Manufacturing, Springer.

D. Greitemeier, F. Palm, F. Syassen, T. Melz, (2017), Fatigue performance of additive manufactured TiAl6V4 using electron and laser beam melting, International Journal of Fatigue, 94: 211-217.

D. Greitemeier, C. Dalle Donne, F. Syassen, J. Eufinger & T. Melz, (2016), Effect of surface roughness on fatigue performance of additive manufactured Ti–6Al–4V, Materials Science and Technology, 32:7, 629-634.

W. Grzesik, K. Zak, M. Prazmowski, B. Storch, T. Palka, (2012), Effects of Cryogenic Cooling on Surface Layer Characteristics Produced by Hard Turning, Archives of Materials Science and Engineering, 54: 5-12.

R. Guinebretière, (2007), X-Ray Diffraction by Polycrystalline Materials, ISTE Ltd, London.

J. Gubicza, I. Schiller, N.Q. Chinh, J. Illy, Z. Horita, T.G. Langdon, (2007), The effect of severe plastic deformation on precipitation in supersaturated Al–Zn–Mg alloys, Materials Science and Engineering A: 461: 77–85.

Y. B. Guo, D. W. Yen, (2004), A FEM study on mechanisms of discontinuous chip formation in hard machining, Journal of Materials Processing Technology, 156: 1350-1356.

E. O. Hall, (1951), The Deformation and Ageing of Mild Steel: III Discussion of Results, Proceedings of the Physical Society. Section B, 74: 747-753.

H. Hallberg, M. Wallin, M. Ristinmaa, (2010), Modeling of continuous dynamic recrystallization in commercial-purity aluminum, Materials Science and Engineering A, 527: 1126–1134.

D. Herzog, V. Seyda, E. Wycisk, C. Emmelmann, (2016), Additive manufacturing of metals, Acta Materialia, 117: 371-392.

D. Holt, (1970), Dislocation cell formation in metals, Journal of Applied Physics, 41: 3197-3201.

S. Y. Hong, Y. Ding, W. Jeong, (2001), Friction and cutting forces in cryogenic machining of Ti–6Al–4V, International Journal of Machine Tools and Manufacture, 41: 2271-2285.

S. Y. Hong, (2006), Lubrication mechanism of LN2 in ecological cryogenic machining, Material Science and Technology, 10: 133-155.

H. E. Hu, X. Y. Wang, (2016), A high-temperature deformation model based on dislocation movement for wrought aluminium alloys, Materials Science and Technology, 33: 712-718.

R. Huang, M. Riddle, D. Graziano, J. Warren, S. Das, S. Nimbalkar, J. Cresko, E. Masanet, (2016), Energy and emissions saving potential of additive manufacturing: the case of lightweight aircraft components, Journal of Cleaner Production, 135: 1559-1570.

X. Huang, X. Zhang, H. Mou, X. Zhang, H. Ding, (2014), The influence of cryogenic cooling on milling stability, Journal of Materials Processing Technology, 214: 3169-3178.

Z. Hussain, A. Ahmed, O. M. Irfan, F. Al-Mufadi, (2017), Severe Plastic Deformation and Its Application on Processing Titanium: A Review, International Journal of Engineering and Technology, 9: 426-431.

S. Imbrogno, G. Rotella, D. Umbrello, (2014), On the Flow Stress Model Selection for Finite Element Simulations of Machining of Ti6Al4V, Key Engineering Materials, 612: 1274-1281.

Y. Iwahashi, J. Wang, Z. Horita, M. Nemoto. T. G. Langdon, (1996) Principle of equal-channel angular pressing for the processing of ultra-fine grained materials, Scripta Materialia, 35: 143-146.

I. S. Jawahir, E. Brinksmeier, R. M'Saoubi, D. K. Aspinwall, J. C. Outeiro, D. Meyer, D. Umbrello, A. D. Jayala, (2011), Surface integrity in material removal processes: Recent advances, Cirp Annals, 60: 603-626.

I. S. Jawahir, H. Attia, D. Biermann, J. Duflou, F. Klocke, D. Meyer, S. T. Newman, F. Pušavec, M. Putz, J.Rech, V. Schulze, D. Umbrello, (2016), Cryogenic manufacturing processes, Cirp Annals, 65: 713-736.

G.R. Johnson, W.H. Cook, (1983), A constitutive model and data for metals subjected to large strains, high strain rates and high temperatures. Proceedings of the 7th International Symposium on Ballistics, 54: 1-7.

S. Joshi, P. Pawar, A. Tewari, S. S. Joshi, (2014), Influence of b Phase Fraction on Deformation of Grains in and Around Shear Bands in Machining of Titanium Alloys, Materials Science & Engineering A, 618: 71–85.

V. Kalhori, D. Wedberg, L. E. Lindgren, (2010), Simulation of mechanical cutting using a physical based material model, International Journal of Material Forming, 3: 511-514.

N. Kamikawa, X. Huang, N. Tsuji, N. Hansen, (2009), Strengthening mechanisms in nanostructured high-purity aluminium deformed to high strain and annealed, Acta Materialia, 57: 4198-4208.

S. Kar, T. Searles, E. Lee, G.B. Viswanathan, J. Tiley, R. Banerjee, H.L. Fraser, (2006), Modeling the Tensile Properties in β-Processed α/β Ti Alloys, Metallurgical and Material Transaction, 37A: 559-566.

Y. Karpat, (2010), A modified material model for the finite element simulation of machining titanium alloy Ti6Al4V, Machining Science and Technology, 14: 390-410.

G. Kasperovich, J. Hausmann, (2015), Improvement of fatigue resistance and ductility of Ti6Al4V processed by selective laser melting, Journal fo Materials Processing Technology, 220: 202-214.

J. G. Kaufman, (2000), Introduction to Aluminum Alloys and Tempers, ASM Internation, Materials Park, OH 44073-0002: 49-50.

D. R. Klenosky, D. R. Johnson, S. Chandrasekar, K. P. Trumble, (2017), Characterization of Large Strain Extrusion Machining (LSEM) of AA7050: 301-304 in: Ratvik A. (eds) Light Metals 2017. The Minerals, Metals & Materials Series. Springer, Cham.

R. Komanduri, B. F. Von Turkovich, (1981), New observations on the mechanism of chip formation when machining titanium alloys, Wear, 69: 179-188

A. Krämer, F. Klocke, H. Sangermann, D. Lung, (2014), Influence of the lubricoolant strategy on thermo-mechanical tool load, CIRP Journal of Manufacturing Science and Technology, 7 Issue 1: 40-47.

T. G. Langdon, (2011), Processing by Severe Plastic Deformation: Historical Developments and Current Impact, Materials Science Forum, 669: 9-14.

L. Laperrire, G. Reinhart, (2014), CIRP Encyclopedia of Production Engineering, Springer Publishing Company.

W. Lee, C. Lin, (2016), Deformation behavior and microstructural evolution of 7075-T6 aluminum alloy at cryogenic temperatures, Cryogenics, 79:26-34.

W. S. Lee, C. F. Lin, (1998), Plastic deformation and fracture behaviour of Ti–6Al–4V alloy loaded with high strain rate under various temperatures, Materials Science and Engineering A: 241: 48-59.

W.-S. Lee, C.-F. Lin, (1998), High-temperature deformation behavior of Ti6Al4V alloy evaluated by high strain-rate compression tests, Journal of Materials Processing Technology, 75: 127–136.

C. Leyens, M. Peters, (2003), Titanium and titanium alloys: fundamental and applications, Weinheim: Wiley-VCH.

A. Li, J. Zhao, Y. Zhou, X. Chen, D. Wang, (2012), Experimental investigation on chip morphologies in high-speed dry milling of titanium alloy Ti-6Al-4V, Internation Journal of Advacned Manufacturing Technology, 62: 933-942.

R. Li, L. Riester, T. R. Watkins, P. J. Blau, A. J. Shih, (2008), Metallurgical analysis and nanoindentation characterization of Ti6Al4V workpiece and chips in high-throughput drilling, Materials Science & Engineering A, 472: 115-124.

L. Li, N. He, (2006), A FEA study on mechanisms of saw-tooth chip deformation in high speed cutting of Ti–6–Al–4V alloy, in: Fifth International Conference on High Speed Machining HSM: 759–767.

S. Li, B. Hou, (2013), Material Behavior Modeling in Machining Simulation of 7075-T651 Aluminum alloy, Journal of Engineering Materials and Technology, 136:1-14.

L. E. Lindgren, Q. Hao, D. Wedberg, (2017), Improved and simplified dislocation density based plasticity model for AISI 316 L, Mechanics of Materials, 108: 68-76.

L. E. Lindgren, A. Svodoba, D. Wedberg, M. Lundblad, (2016), Towards predictive simulations of machining, Comptes Rendus Mecanique, 344: 284-295.

R. Liu, M. Salahshoor, S. N. Melkote, T. Maurish, (2014), The prediction of machined surface hardness using a new physics-based material model, 2nd CIRP Conference on Surface Integrity (CSI), Procedia Cirp, 13: 249-256.

G. A. Longhitano, M. A. Larosa, A. L. J. Munhoza, C. A. de Carvalho Zavaglia, M. C. F. Ierardia, (2015), Surface Finishes for Ti-6Al-4V Alloy Produced by Direct Metal Laser Sintering, Materials Research, 18: 838-842.

V. A. Lubarda, (2007), On atomic disregistry, misfit energy and the Peierls stress of a crystalline dislocation, The Montenegrin Academy Of Science and Arts, Proceedings of the section of Natural Sciences, 17: 2-27.

G. Lütjering, J. C. Williams, (2007), Titanium, 2nd edition, Springer-Verlag Berlin Heidelberg 2007.

R. M'Saoubi, D. Axinte, S. L. Soo, C. Nobel, H. Attia, G. Kappmeyer, S. Engin, W. M. Sim, (2015), High performance cutting of advanced aerospace alloys and composite materials, CIRP Annals, 64: 557-580.

K. Ma, H. Wen, T. Hu, T. D. Topping, D. Isheim, D. N. Seidman, E. J. Lavernia, J. M. Schoenung, (2014), Mechanical behavior and strengthening mechanisms in ultrafine grain precipitation-strengthened aluminum alloy, Acta Materialia, 61: 141-155.

D. S. MacKenzie, G. E. Totten, (2006), Analytical Characterization of Aluminum, Steel, and Superalloys, Taylor & Francis Group, 6000 Broken Sound Parkway NW, Suite 300 Boca Raton, FL 33487-2742H.

H. Mecking, U. F. Kocks, (1981), Kinetics of flow and strain-hardening, Acta Metallurgica, 29: 1865-1875.

H.W. Meyer, D.S. Kleponis, (2001), Modeling the high strain rate behavior of titanium undergoing ballistic impact and penetration, International Journal of Impact Engineering, 26: 509–521.

S. N. Melkote, R. Liu, P. F. Zelaia, T. Marusich, (2015), A physically based constitutive model for simulation of segmented chip formation in orthogonal cutting of commercially pure titanium, Cirp Annals, 64: 65-68.

S. N. Melkote, W. Grzesik, J. Outeiro, J. Rech, V. Schulze, H. Attia, P. J. Arrazola, R. M'Saoubi, C. Saldana, (2017), Advances in material and friction data for modelling of metal machining, Cirp Annals, 66: 731-754.

K. Mohan, J. A. Suresh, P, Ramu, R. Jayaganthan, (2016), Microstructure and Mechanical Behavior of Al 7075-T6 Subjected to Shallow Cryogenic Treatment, Journal of Materials Engineering and Performance, 25: 2185-2194.

V. N. Moiseyev, (2006), Titanium alloys: Russian Aircraft and Aerospace Applications; Taylor & Francis Group 6000 Broken Sound Parkway NW, Suite 300, Boca Raton, FL 33487-2742.

A. P. Mouritz, (2012), Introduction to aerospace materials, Woodhead Publishing Limited, 80 High Street, Sawston, Cambridge CB22 3HJ, UK

T. M. Mower, M. J. Long, (2016), Mechanical behavior of additive manufactured, powder-bed laser-fused materials, Materials Science & Engineering A, 651: 198-213.

L. E. Murr, E. Martinez, K. N. Amato, S. M. Gaytan, J. Hernandez, D. A. Ramirez, P. W. Shindo, F. Medina, R. B. Wicker, (2012), Fabrication of Metal and Alloy Components by Additive Manufacturing: Examples of 3D Materials Science, Journal of Materials Research and Technology, 1: 42-54.

L. E. Murr, E. V. Esquivel, S. A. Quinones, S. M. Gaytan, M. I. Lopez, E. Y. Martinez, F. Medina, D. H. Hernandez, E. Martinez, J. L. Martinez, S. W. Stafford, D. K. Brown, T. Hoppe, W. Meyers, U. Lindhe, R. B. Wicker, (2009), Microstructures and mechanical properties of electron beam-rapid manufactured Ti–6Al–4V biomedical prototypes compared to wrought Ti–6Al–4V, Material Characterization, 60: 96-105.

K. Nakashima, Z. Horita, M. Nemoto, T. Langdon, (1998), Influence of channel angle on the development of ultrafine grains in Equal Channel Angular Pressing, Acta Materialia, 46: 1589-1599.

R. Neugebauer, K. D. Bouzakis, B. Denkena, F. Klocke, A. Sterzing, A.E. Tekkaya, R. Wertheim, (2011), Velocity effects in metal forming and machining processes, Cirp Annals, 60: 627-650.

M. Nicolas, A. Deschamps, (2003), Precipitate Microstructures and Resulting Properties of Al-Zn-Mg Metal Inert Gas–Weld Heat-Affected Zones, Metallurgical and Materials Transactions A, 35: 1437-1448

E. A. Ott, J. R. Groh, A. Banik, I. Dempster, T. P. Gabb, R. Helmink, X. Liu, A. Mitchell, G. P. Sjöberg, A. Wusatowska-Sarnek, (2010), Superalloy 718 and Derivates, Proceedings of the 7th International Symposium on SUPERALLOY 718 and DERIVATIVES, John Wiley & Sons, Inc., Hoboken, New Jersey.

T. Özel, M. Sima, A. K. Srivastava, B. Kaftanoglu, (2010), Investigations on the effects of multi-layered coated inserts in machining Ti–6Al–4V alloy with experiments and finite element simulations, Cirp Annals, 59: 77-82.

T. Özel, E. Zeren, (2004) Determination of work material flow stress and friction properties for FEA of machining using orthogonal cutting tests, Journal of Materials Processing Technology, 153: 1019–1025.

T. Özel, (2006), The influence of friction models on finite element simulations of machining, International Journal of Machine Tools and Manufacture, 46: 518–530.

U. M. R. Paturi, S. K. R. Narala, R. S. Pundir, (2014), Constitutive flow stress formulation, model validation and FE cutting simulation for AA7075-T6 aluminum alloy, Materials Science & Engineering A, 605: 176-185.

R. S. Pawade, S. S. Joshi, (2011), Mechanism of chip formation in high-speed turning of Inconel 718, Machining Science and Technology, 15: 132-152.

N. J. Petch, (1953), The Cleavage Strength of Polycrystals, Journal of the Iron and Steel Institute, 174: 25-28.

N. E. Prasad, R.J.H. Wanhill, (2017), Aerospace Materials and Material Technologies Volume 1: Aerospace Materials, Springer Nature Singapore Pte Ltd.

N. E. Prasad, R.J.H. Wanhill, (2017), Aerospace Materials and Material Technologies Volume 2: Aerospace Material Technology, Springer Nature Singapore Pte Ltd.

Z.Pu, S.Yang, G.-L.Song, O.W.DillonJr., D.A.Puleo, I.S.Jawahir, (2011), Ultrafine-grained surface layer on Mg–Al–Zn alloy produced by cryogenic burnishing for enhanced corrosion resistance, Scripta Materialia, 65:520-523.

Z. Pu, J.C. Outeiro, A.C. Batista, O.W. Dillon Jr, D.A. Puleo, I.S. Jawahir, (2012), Enhanced surface integrity of AZ31B Mg alloy by cryogenic machining towards improved functional performance of machined components, International Journal of Machine Tools & Manufacture, 56: 17-27.

F. Pušavec, T. Lu, C. Courbon, J. Rech, U. Aljancic, J. Kopac, I. S. Jawahir, (2016), Analysis of the influence of nitrogen phase and surface heat transfer coefficient on cryogenic machining performance, Journal of Materials Processing Technology, 233: 19-28.

F. Pušavec, H. Hamdi, J. Kopac, I. S. Jawahir, (2011), Surface integrity in cryogenic machining of nickel based alloy—Inconel 718, Journal of Materials Processing Technology, 211: 773-783.

F. Pušavec, E. Govekar, J. Kopač, I.S. Jawahir, (2011), The influence of cryogenic cooling on process stability in turning operations, Cirp Annals, 60: 101-104.

G. Z. Quan, Y. P. Mao, G. S. Li, W. Q. Lv, Y. Wang, J. Zhou, (2012), A characterization for the dynamic recrystallization kinetics of as-extruded 7075 aluminum alloy based on true stress–strain curves, Computational Material Science, 55: 65-72.

N. X. Randall, (2010), Applications of the ConScan Surface Profilometer, Advanced Mechanical Surface Testing, Application Bulletin, 33 (CSM Instrument).

B. Rao, Y. C. Shin, (2001), Analysis on high-speed face-milling of 7075-T6 aluminum using carbide and diamond cutters, International Journal of Machine Tools and Manufacture, 41: 1763-1781.

S. Rinaldi, S. Caruso, D. Umbrello, L. Filice, R. Franchi, A. Del Prete, (2017), Machinability of Waspaloy under different cutting and lubri-cooling conditions, The International Journal of Advanced Manufacturing Technology, 1-10.

G. Rotella, O. W. Dillon Jr., D. Umbrello, L. Settineri, I. S. Jawahir, (2013), Finite element modeling of microstructural changes in turning of AA7075-T651 Alloy, Journal of Manufacturing Processes, 15: 87-95.

G. Rotella, O. W. Dillon Jr., D. Umbrello, L. Settineri, I. S. Jawahir, (2014), The effects of cooling conditions on surface integrity in machining of Ti6Al4V alloy, The International Journal of Advanced Manufacturing Technology, 71, Issue 1-4: 47-55.

G. Rotella, D. Umbrello, (2014), Numerical simulation of surface modification in dry and cryogenic machining of AA7075 alloy, 2nd CIRP Conference on Surface Integrity (CSI), Procedia CIRP, 13: 327-332.

G. Rotella, D. Umbrello, (2014), Finite element modeling of microstructural changes in dry and cryogenic cutting of Ti6Al4V alloy, Cirp Annals, 63: 69-72.

G. Rotella, (2013), Sustainable Machining of Aerospace Alloys for Improved Product and Process Sustainability: Evaluation of Dry, Near-dry (MQL) and Cryogenic Machining Processes, Ph.D. Dissertation, Politecnico di Torino.

O. Ryen, O. Nijs, E. Sjolander, B. Holmedal, H.E. Ekstrom, E. Nes, (2006), Strengthening mechanisms in solid solution aluminum alloys, Metallurgical and Materials Transactions A, 37: 1999-2006.

I. Sabirov, M. Y. Murashkin, R. Z. Valiev, (2013), Nanostructured aluminium alloys produced by severe plastic deformation: New horizons in development, Materials Science and Engineering A, 560: 1-24.

A. Sahai, K. H. Raj, N. K. Gupta, (2017), Mechanical behaviour and surface profile analysis of Al 6061 alloy processed by Equal Channel Angular Extrusion, Procedia Engineering 173: 956-963.

K. O. Sanusi, O. D. Makinde, G. J. Oliver, (2012), Equal channel angular pressing technique for the formation of ultra-fine grained structures, South African Journal of Science, 103: 38-44.

S. Sartori, A. Ghiotti, S. Bruschi, (2017), Temperature effects on the Ti6Al4V machinability using cooled gaseous nitrogen in semi-finishing turning, Journal of Manufacturing Processes, 30: 187-194.

S. Sartori, A. Bordin, A. Ghiotti, S. Bruschi, (2016), Analysis of the Surface Integrity in Cryogenic Turning of Ti6Al4 V Produced by Direct Melting Laser Sintering, 3rd CIRP Conference on Surface Integrity (CIRP CSI), Procedia CIRP, 45: 123-126.

R. O. Scattergood, C. C. Kock, (1992), A modified model for Hall-Petch behavior in nanocrystalline materials, Scripta Metallurgica et Materialia, 27: 1195-1200.

I. Schiller, J. Gubicza, Zs. Kovàcs, N. Q. Chinh, J. Illy, (2016), Precipitation and mechanical properties of supersaturated Al-Zn-Mg alloys processed by severe plastic deformation, Materials Science Forum, 521: 833-840.

M. Schmidt, M. Merklein, D. Bourell, D. Dimitrov, T. Hausotte, K. Wegener, L. Overmeyer, F. Vollertsen, G. N. Levy, (2017), Laser based additive manufacturing in industry and academia, Cirp Annals, 66: 561-583.

H. Schulz, T. Moriwaki, (1992), High-Speed Machining, Cirp Annals, 2: 637-643.

V. Schulze, F. Bleicher, P. Groche, Y. B. Guo, Y. S. Pyun, (2016), Surface modification by machine hammer peening and burnishing, Cirp Annals, 65: 809-832.

A. Seeger, (1956) The mechanism of Glide and Work Hardening in FCC and HCP Metals. In: Fisher, J., Johnston, W.G., Thomson, R., Vreeland, T.J. (Eds.), Dislocations and Mechanical Properties of Crystals, pp. 243–329.

SFTC, Deform®-User Manual, Columbus (OH), USA, 2010.

W. Sha, S. Malinov, (2009), Titanium alloys: modeling of microstructure, properties and applications, Woodhead Publishing Limited and CRC Press LLC.

M. Shaeri, M. Ebrahimi, (2016), Effect of ECAP temperature on microstructure and mechanical properties of Al–Zn–Mg–Cu alloy, Progress in Natural Science: Materials International, 26: 182-191.

M. H. Shaeri, M.T.Salehi, S. H. Seyyedein, M. R. Abutalebi, (2015), Effect of equal channel angular pressing on aging treatment of Al-7075 alloy, Progress in Natural Science: Materials International, 25:159-168.

N. Shen, H. Ding, (2014), Physics-Based Microstructure Simulation for Drilled Hole Surface in Hardened Steel, Journal of Manufacturing Science and Engineering, 136: 1-5.

C. Shi, W. Mao, X. G. Chen, (2013), Evolution of activation energy during hot deformation of AA7150 aluminum alloy, Materials Science and Engineering A 571: 83-91.

R. Shivpuri, J. Hua, (2001), Microstructure-mechanics interactions in modeling chip segmentation during titanium machining, CIRP Annals, 51: 85–89.

M Sima, T. Özel, (2010), Modified material constitutive models for serrated chip formation simulations and experimental validation in machining of titanium alloy Ti–6Al–4V, International Journal of Machine Tools and Manufacture, 50: 943-960.

A. Starke, J. T. Staley, (1996), Application of modern aluminum alloys to aircraft, Progress in Aerospace Science, 32: 131–172.

T. Stichel, T. Frick, T. Laumer, F. Tenner, T. Hausotte, M. Merklein, M. Schmidt, (2017), A Round Robin Study for Selective Laser Sintering of Polyamide 12, Microstructural Origin of the Mechanical Properties. Optics & Laser Technology, 89:31–40.

S. Sun, M. Brandt, M. S. Dargusch, (2009), Characteristics of cutting forces and chip formation in machining of titanium alloys, International Journal of Machine Tools & Manufacture, 49: 561–568.

S. Sun, M. Brandt, M. S. Dargusch, (2010), Machining Ti–6Al–4V alloy with cryogenic compressed air cooling, International Journal of Machine Tools & Manufacture, 50: 933-942.

A. Svodoba, D. Wedberg, L. E. Lindgren, (2010), Simulation of metal cutting using a physically based plasticity model, Modeling and Simulation in Materials Science and Engineering, 18: 1-19.

A. Tabei, D. S. Shih, H. Germestani, S. Y. Liang, (2016), Dynamic Recrystallization of Al alloy 7075 in Turning, Journal of Manufacturing Science and Technology, 138: 071010-1 – 7.

H. Takeyama, R. Murata, (1963), Basic Investigation of Tool Wear. Journal of Engineering for Industry, 85: 33-37.

S. Takeuchi, (2001), The mechanism of the inverse Hall-Petch relation of nanocrystals, Scripta Materialia, 44: 1483-1487.

X. Tan, Y. Kok, Y.J. Tan, M. Descoins, D. Mangelinck, S. B. Tor, K. F. Leong, C. K. Chua, (2015), Graded microstructure and mechanical properties of additive manufactured Ti–6Al–4V via electron beam melting, Acta Materialia, 97: 1-16.

S. V. Telrandhe, A. K. Saxena, S. Mishra, (2017), Effect of microstructure and cutting speed on machining behavior of Ti6Al4V alloy, Journal of Mechanical Science and Technology, 31: 2177-2184.

G. J. Thomas, R.W. Siegel, J.A. Eastman, (1990), Grain boundaries in nanophase palladium: high resolution electron microscopy and image simulation, Scripta Metallurgica et Materialia, 24: 201-206.

T.D. Topping, B. Ahn, Y. Li, S.R. Nutt, E.J. Lavernia, (2012), Influence of Process Parameters on the Mechanical Behavior of an Ultrafine-Grained Al Alloy, Metallurgical and Materials Transactions A, 43: 505-519.

L. S. Tóth, A. Molinari, Y. Estrin, (2000), Strain Hardening at Large Strains as Predicted by Dislocation Based Polycrystal Plasticity Model, Journal of Engineering Materials and Technology, 124: 71-77.

G. E. Totten, D. S. MacKeinzie, (2003), Handbook of Aluminum, Volume 1 Physical Metallurgy and Processes, Marcel Dekker, Inc. 270 Madison Avenue, New York, NY 10016.

N. Tsuji, T. Maki, (2009), Enhanced structural refinement by combining phase transformation and plastic deformation in steels, Scripta Materialia, 60: 1044-1049.

D. Umbrello, S. Caruso, S. Imbrogno, (2016), Finite element modelling of microstructural changes in dry and cryogenic machining AISI 52100 steel, Materials Science and Technology, 32: 1062-1070.

D. Umbrello, (2008), Finite element simulation of conventional and high speed machining of Ti6Al4V alloy, Journal of Materials Processing Technology, 196: 79-87.

J. D. P. Velásquez, B.Bolle, P.Chevrier, G.Geandier, A.Tidu, (2007), Metallurgical study on chips obtained by high speed machining of a Ti–6 wt.%Al–4 wt.%V alloy, Materials Science and Engineering: A, 452: 469-474.

M. Vetterli, M. Schmid, K. Wegener, (2014) Comprehensive Investigation of Surface Characterization Methods for Laser Sintered Parts. Proceedings of the Fraunhofer Direct Digital Manufacturing Conference 1–6.

P. Wang, W. J. Sin, M. L. S. Nai, J. Wei, (2017), Effects of Processing Parameters on Surface Roughness of Additive Manufactured Ti-6Al-4V via Electron Beam Melting, Materials, 10, 1121.

B. Wang, Z. Liu, (2016), Investigations on deformation and fracture behavior of workpiece material during high speed machining of 7050-T7451 aluminum alloy, CIRP Journal of Manufacturing Science and Technology, 14: 43–54.

M. Warmuzek, (2004), Metallographic Techniques for Aluminum and Its Alloys, Metallography and Microstructures, ASM Handbook, ASM International, 9: 711–751.

G. Q. Wu, C. L. Shi, W. Sha, A. X. Sha, H. R. Jiang, (2013), Effect of the microstructure on the fatigue properties of the Ti6Al4V titanium alloys, Material and Design, 46: 668-674.

W. Xu, M. Brandt, S. Sun, J. Elambasseril, Q. Liu, K. Latham, K. Xia , M. Qian, (2015), Additive manufacturing of strong and ductile Ti–6Al–4V by selective laser melting via in situ martensite decomposition, Acta Materialia, 85: 74-84.

W. Xu, E.W. Lui, A. Pateras, M. Qian, M. Brandt, (2017), In situ tailoring microstructure in additively manufactured Ti-6Al-4V for superior mechanical performance, Acta Materialia, 125: 390-400.

J. Yanagimoto, K. Karhausen, (1998), Incremental Formulation for the Prediction of Flow Stress and Microstructural Change in Hot Forming, Journal of manufacturing science and engineering, 120: 316- 322.

S. Yang, O. W. Jr. Dillon, D. A. Puleo, I. S. Jawahir, (2013), Effect of cryogenic burnishing on surface integrity modifications of Co-Cr-Mo biomedical alloy, Journal of Biomedical Materials Research Part B, Applied Biomaterials, 101: 139-152.

X. Yang, C. R. Liu, (1999), Machining titanium and its alloys, Machining Science and Technology, 3: 107-139.

F. J. Zerilli, R. W. Armstrong, (1987), Dislocation-mechanics-based constitutive relations for material dynamics calculations, Journal of Applied Physics, 61: 1816-1825.

X. P. Zhang, R. Shivpuri, A. K. Srivastava, (2017), A New Microstructure-Sensitive Flow Stress Model for the High-Speed Machining of Titanium Alloy Ti–6Al–4V, Journal of Manufacturing Science and Engineering, 139: 1-17.

S. Zhang, D. Zhao, (2013), Aerospace Materials Handbook. CRC Press Taylor & Francis Group, 6000 Broken Sound Parkway NW, Boca Raton, FL 33487-274.

Y. H. Zhao, X. Z. Liao, Z. Jin, R. Z. Valiev, Y. T. Zhu, (2004), Microstructures and mechanical properties of ultrafine grained 7075 Al alloy processed by ECAP and their evolutions during annealing, Acta Materialia, 52: 4589-4599.